

## ABSTRACT

DUFFICY, MARTIN KYLE. Binders and Hosts for High-Capacity Lithium-ion Battery Anodes. (Under the direction of Dr. Peter S. Fedkiw and Dr. Saad A. Khan).

Lithium-ion batteries (LIBs) are universal electrochemical energy storage devices that have revolutionized our mobile society. Nonetheless, societal and technological advances drive consumer demand for LIBs with enhanced electrochemical performance, such as higher charge capacity and longer life, compared to conventional LIBs. One method to enhance LIB performance is to replace graphite, the industry standard anode since commercialization of LIBs in 1991, with high-charge capacity materials. Implementing high-capacity anode materials such as tin, silicon, and manganese vanadates, to LIBs presents challenges; Li-insertion is destructive to anode framework, and increasing capacity increases structural strains that pulverize anode materials and results in a short-cycle life. This thesis reports on various methods to extend the cycle life of high-capacity materials. Most of the work is conducted on nano-sized anode materials to reduce Li and electron transport pathway length (facilitating charge-transfer) and reduce strains from volume expansions (preserving anode structure).

The first method involves encapsulating tin particles into a graphene-containing carbon nanofiber (CNF) matrix. The composite-CNF matrix houses tin particles to assume strains from tin-volume expansions and produces favorable surface-electrolyte chemistries for stable charge-discharge cycling. Before tin addition, graphene-containing CNFs are produced and assessed as anode materials for LIBs. Graphene addition to CNFs improves electronic and mechanical properties of CNFs. Furthermore, the 2-D nature of graphene provides Li-binding sites to enhance composite-CNF both first-cycle and high-rate capacities > 150% when compared to CNFs in the absence of graphene. With addition of Sn, we vary loadings and thermal production temperature to elucidate structure-composition relationships of tin and

graphene-containing CNF electrodes that lead to increased capacity retention. Of note, electrodes containing  $\leq 20$  wt% tin result in small tin (metallic and tin oxide) particles ( $\leq 15$  nm) within the composite-CNF matrix, which yield long cycle-lives; large reversible capacities of  $\sim 600$  mAh  $g^{-1}$  are observed at 0.2-C rates, while capacities of  $\sim 400$  mAh  $g^{-1}$  (double the capacity of CNFs) are observed after hundreds of cycles at 2-C rates.

The second method comprises an approach to enhance the cycle life of silicon anodes. Many researchers believe that Si is the future anode material of LIBs, and Si is capable of providing a much needed boost in overall cell performance. Silicon has the highest known charge capacity at  $\sim 3579$  mAh  $g^{-1}$ , nearly an order of magnitude larger than graphite (372 mAh  $g^{-1}$ ). In attempt to realize the entire capacity of Si anodes, we use binding agents to prolong cycle life. Binding agents enhance capacity retention via favorable interactions with cell components such as active materials and electrolytes. In this study, we introduce galactomannans (specifically, guar) as viable, inexpensive, biopolymer binders for Si electrodes. In attempt to elucidate the role of the binder in Si electrodes, we study guar-electrode and -electrolyte interactions that lead to electrochemical performance enhancements. We recognize that there are deficiencies in guar-silicon systems, which we address in our following approach. Notably, we develop a guar-derived binder to increase the strength and conductivity of Si-based electrodes by crosslinking guar and carbon black dispersions. The crosslinked binders, in effect, enhance electrode adhesion and hinder electrode cracking by self-healing. This study monitors gelation via rheological methods and assesses effects of crosslinking density on physical and electrochemical properties.

Lastly, we consider a vacancy-induced manganese vanadate as high-capacity, high-power anodes for LIBs. Rather than assessing nanoparticles, we tailored molecular structure

to enhance electrochemical performances. X-ray diffraction studies enable us to suggest a Li-insertion mechanism, where Li travels through large channels created by defects in the crystal structure. The ensuing manganese vanadate structure produces a stable framework that results in stable cycling of hundreds of cycles.

© Copyright 2016 Martin Kyle Dufficy

All Rights Reserved

Binders and Hosts for High-Capacity Lithium-ion Battery Anodes

by  
Martin Kyle Dufficy

A dissertation submitted to the Graduate Faculty of  
North Carolina State University  
in partial fulfillment of the  
requirements for the degree of  
Doctor of Philosophy

Chemical Engineering

Raleigh, North Carolina

2016

APPROVED BY:

---

Dr. Peter S. Fedkiw  
Committee Co-Chair

---

Dr. Saad A. Khan  
Committee Co-Chair

---

Dr. Gregory N. Parsons

---

Dr. Linyou Cao

## **DEDICATION**

I dedicate this work to my father, Joe Dufficy, who taught me to push the boundaries of the human body and mind.

## **BIOGRAPHY**

Martin Kyle Dufficy was born just outside of Chicago in Evanston, Illinois. He grew up in the suburb of Skokie and spent much of his childhood traveling around the Chicagoland Area playing soccer matches. Upon realization that a career in professional soccer was not in the cards, Marty turned towards the books. His favorite high school classes were calculus and chemistry, which influenced his decision to pursue a degree in Chemical Engineering.

Marty enrolled at Iowa State University, located in the lovely town of Ames. While at Iowa State, Marty took on a nine month co-op as a process engineer with International Paper in Cedar Rapids, Iowa. Interested in exploring other career paths of chemical engineer, Marty decided to pick up undergraduate research. Under the direction of Robert Brown and Brett Shanks, Marty characterized and assessed the performance of catalysts for steam reforming and deoxygenation of biomaterials for biorenewable chemical production. Marty worked in many different laboratory settings including Ames National Lab, Iowa State University, and even a stint at Fritz Haber Institute of the Max Plank Society in Berlin, Germany. His passion to advance science and question the status quo brought him to graduate school.

Marty joined the groups of Saad Khan and Peter Fedkiw at North Carolina State University in 2012.

## ACKNOWLEDGMENTS

I would like to thank my advisors Saad Khan and Peter Fedkiw for their guidance throughout graduate school. Their tutelage taught me to communicate in clear and concise manner, and to see the work of myself and others in a new light. I would also like to thank my group members, past and present: Andrew Loebl for teaching me the basics of battery assembly and analysis early into my Ph.D., Shengyang Huang for assisting in materials characterization, Mackenzie Geiger for many fruitful discussions on rheology, and Kimberly Dennis for her arduous work in the lab. I would also like to thank the folks at the Analytical Instrumentation Facility for assisting with materials characterization, notably Fred Stevie for running XPS and Li Liu for his wizardry with TEM. I would like to thank the professors in this department for allowing me to use their equipment: Greg Parsons and Jan Genzer. I would also like to thank our collaborators in the Department of Chemistry, Lan Luo and Paul Maggard, for broadening my horizons and introducing me to new Li-ion chemistries.

My friends and colleagues at NC State have been a tremendous source of innovation, inspiration, and invitation. Graduate school would not have been the same without all the amazing people I have met. I would like to thank the people with whom I share a roof: Matt Melillo and Ryan Barton for their camaraderie through the journey of graduate school; Cody Addington for footing the Netflix bill and encouraging engineering around the house; Ellie the dog for being a happy oversized lap and exercise companion. I would also like to thank the cycling crew for providing me an outlet to experience the beauty of the Carolinas—from mountains to coast—and an outlet to clear my mind in times of need.

I would like to give thanks to my family: to my parents Judy and Joe, thank you for stressing the importance of education and balance in life; to my brother Nick for instilling in me a competitive spirit; and to my sister Annie for her support and always putting a smile on my face.

Last, but certainly not least, I would like to thank my girlfriend, Margaret Spinks, for being a truly great partner-in-crime, for sharing my interests and making life fun. Also, many thanks for making the coffee to fuel my mornings and for making some of the best lunches to fuel my days.

## TABLE OF CONTENTS

<b>List of Tables</b> .....	<b>x</b>
<b>List of Figures</b> .....	<b>xi</b>
<b>Chapter 1. Introduction</b> .....	<b>1</b>
1.1. Opening Remarks.....	2
1.2. Document Organization.....	4
1.3. References.....	6
<b>Chapter 2. Background</b> .....	<b>7</b>
2.1. The Li-ion Battery.....	8
2.1.1. Electrochemistry of Li-ion anodes.....	10
2.1.2. Carbon Anodes.....	16
2.1.3. Manganese Vanadate Anodes .....	21
2.1.4. Tin-based Anodes .....	22
2.1.5. Silicon Anodes .....	25
2.1.6. Binding agents .....	27
2.2. Galactomannans .....	30
2.2.1. Guar solution and gels .....	32
2.2.2. Oscillatory rheology and gel formation .....	33
2.3. Electrospinning .....	35
2.3.1. The Process .....	36
2.3.2. Electrospinning parameters.....	38
2.3.3. Steady-shear rheology and fiber morphology.....	40
2.3.4. Polymer and carbon fibers via polyacrylonitrile.....	41
2.3.5. Composite carbon nanofibers .....	44
2.4 References .....	45
<b>Chapter 3. Hierarchical graphene-containing carbon nanofibers for lithium-ion battery anodes</b> .....	<b>55</b>
3.1. Introduction.....	56
3.2. Materials and Methods.....	59
3.2.1. Graphite oxide preparation .....	59
3.2.2. GO-PAN suspension preparation.....	60
3.2.3. Characterization of Electrospinning Suspension .....	60

3.2.4. Graphene-containing nanofibers preparation.....	60
3.2.5. Composite polymer and CNF characterization.....	61
3.2.6. Electrochemical performance characterization.....	62
3.3. Results and Discussion .....	63
3.3.1. GO/PAN nanofibers by electrospinning .....	63
3.3.2. TRGO/CNF characterization .....	68
3.3.3. TRGO/CNF electrochemical characterization.....	73
3.4. Summary .....	82
3.5. References.....	83
<b>Chapter 4. Effects of Composition and Structure on Performance of Tin/Graphene-Containing Carbon Nanofibers for Li-ion Anodes .....</b>	<b>88</b>
4.1. Introduction.....	90
4.2. Experimental .....	92
4.2.1 Preparation of electrospinning solution .....	92
4.2.2 Preparation of Sn-containing fibers .....	92
4.2.3 Characterization of Sn-containing fibers .....	93
4.2.4 Electrochemical characterization .....	94
4.3. Results and Discussion .....	95
4.3.1 Characterization of Sn-fibers .....	95
4.3.2 Electrochemical characterization of Sn-containing fibers .....	105
4.4. Summary .....	115
4.5. References.....	117
<b>Chapter 5. Galactomannan binding agents for silicon anodes in Li-ion batteries.....</b>	<b>120</b>
5.1. Introduction.....	121
5.2. Experimental .....	124
5.2.1. Materials .....	124
5.2.2. Binder purification and dissolution.....	125
5.2.3. Half-cell fabrication.....	125
5.2.4. Electrochemical testing.....	126
5.2.5. Solvent Uptake.....	127
5.2.6. Physical Characterization.....	127
5.3. Results and Discussion .....	128

5.4. Summary .....	142
5.5. References .....	143
<b>Chapter 6. Guar hydrogel binders for silicon nanoparticle anodes: a case study of binder rheology on electrode performance .....</b>	<b>146</b>
6.1. Introduction .....	148
6.2. Materials and Methods .....	150
6.2.1. Guar purification .....	150
6.2.2. Hydrogel preparation .....	151
6.2.3. Hydrogel characterization .....	153
6.2.4. Electrochemical characterization .....	154
6.3. Results .....	155
6.3.1. Gelation rheology .....	155
6.3.2. Materials characterization .....	163
6.3.3 Electrochemical characterization .....	169
6.4. Summary .....	177
6.5. References .....	179
<b>Chapter 7. Vacancy-Induced Manganese Vanadates and Their Potential Application to Li-ion Batteries .....</b>	<b>184</b>
7.1. Introduction .....	185
7.2. Experimental Section .....	186
7.2.1. Materials and Instrumentation .....	186
7.2.2. Synthetic Procedures .....	187
7.2.3. Electrode Fabrication and Characterization .....	188
7.2.4. Ex-Situ Electrode Characterization .....	188
7.3. Results .....	189
7.3.1. Crystallographic characterization .....	189
7.3.2. Electrochemical characterization .....	191
7.4. Summary .....	199
7.5. References .....	200
<b>Chapter 8. Conclusions and Recommendations for Future Work .....</b>	<b>202</b>
8.1. Chapter Summaries .....	203
8.2. Recommendations .....	206

8.2.1. Electrospun carbon nanofiber anodes .....	206
8.2.2. Tin anodes .....	212
8.2.3. Coating nano-Si anodes .....	212
8.2.4. Binders for Si anodes .....	213
8.2.5. Manganese vanadate anodes .....	221
8.3. References .....	223
<b>Appendices .....</b>	<b>227</b>
<b>Appendix A: Supporting Information for Chapter 4 .....</b>	<b>228</b>
<b>Appendix B: Supporting Information for Chapter 5 .....</b>	<b>238</b>
<b>Appendix C. Supporting Information for Chapter 6 .....</b>	<b>248</b>
<b>Appendix D: Supporting Information for Chapter 7 .....</b>	<b>257</b>
D.1. Data Analysis .....	258
D.1.1. Estimating mols Li on first lithiation .....	258
D.1.2. Thermogravimetric analysis .....	258
D.1.3. Infrared spectra .....	258
D.2. Figures and Tables .....	259
D.4. References .....	268

## LIST OF TABLES

<b>Table 3.1.</b> Properties of GO/PAN-DMF electrospinning suspensions; <sup>‡</sup> not measurable....	63
<b>Table 3.2.</b> Electrical conductivity and fiber diameter for CNFs and TRGO/CNFs. ....	69
<b>Table 4.1:</b> List of calculated and experimentally found (actual) first-cycle lithiation capacities and coulombic efficiencies (CEs) in parentheses; calculated capacities were determined using Sn content from EDS. The table also shows the Sn(IV) content that was added to the fiber precursor solution and corresponding Sn content in the carbonized fibers. ....	109
<b>Table A1.</b> Coulombic efficiencies, averaged per 100 cycles, corresponding to <b>Figure 4.6c</b> .....	237
<b>Table A2.</b> Coulombic efficiencies, averaged per 100 cycles, corresponding to <b>Figure 4.6d</b> .....	237
<b>Table B1.</b> Carbon bond composition as determined via integrating the peaks of the spectra in <b>Figure B1</b> . The original atomic bond content of guar that we measured is close to the expected composition of guar gum. However, the mannose-to-galactose ratio was never determined, so exact composition remains unknown. Of importance in this table is the stark difference in the C 1s spectra when SiNPs are coated with GG, as compared to pure GG. Notably a decrease in C-O and O-C-O content and an increased C-C content. This change in composition may be caused by interactions or reactions between SiNPs and GG. ....	239
<b>Table D1.</b> Selected bond distances, angles, and bond valence sums for <b>I</b> <sup>a</sup> .....	267
<b>Table D2:</b> A review of Mn-V anodes in Li-ion half-cells, showing the superior cycling performance of <b>I</b> in this study compared to similarly prepared electrodes in literature .....	267

## LIST OF FIGURES

<b>Figure 2.1.</b> Cartoon of LIB showing the three major active components (anode, cathode, and electrolyte), as well as the non-active components: Cu/Al-foil current collectors, binders to adhere electrodes to the current collectors, a separator to prevent short-circuiting, and carbon black (CB) as a conductive additive to reduce internal cell limitations .....	10
<b>Figure 2.2.</b> The basics of chronopotentiometry: an excitation (current) is applied to a cell and the response (change in voltage) is measured within a voltage limit. The time to span the voltage window is used to calculate electrode capacity. Symmetrical or asymmetrical currents may be applied, where charge and discharge current is constant or varied, respectively.....	13
<b>Figure 2.3.</b> Nyquist plot and equivalent circuit for typical Li-ion half-cell (left) and the physical interpretation of the model (right). .....	15
<b>Figure 2.4.</b> Simplified structures for two galactomannans, guar and locust bean gum. ....	31
<b>Figure 2.5.</b> Two extreme situations in gelation: frequency dependence of a viscous-like fluid (left) is observed prior to gelation ( $G'' > G'$ ), and frequency independence of a fully crosslinked gel (right) where $G'' < G'$ . .....	35
<b>Figure 2.6.</b> Schematic of horizontal electrospinning setup. ....	37
<b>Figure 2.7.</b> Idealization of the stabilization heat-treatment reaction, which essentially crosslinks PAN.....	42
<b>Figure 2.8.</b> Three potential reactions that occur during carbonization of stabilized-PAN. <sup>[125]</sup> .....	43
<b>Figure 3.1.</b> Unidirectional, steady-shear (a) viscosity and (b) shear stress/rate results for an 8 wt% PAN-DMF suspension with various GO concentrations. Data points for pure PAN and PAN containing 1 wt% GO overlap.....	65
<b>Figure 3.2.</b> Images of composite GO-PAN electrospun fibers with (i) 0 (ii) 1 (iii) 5 (iv) 10 and (v) 20 wt% GO. As GO loading increases, the fiber mats darken. ....	66
<b>Figure 3.3.</b> (a) FT-IR spectra of graphite oxide, PAN nanofibers, and the composite GO-PAN nanofibers; (b) An idealization of proposed GO structure; (c) XRD diffractograms of graphite oxide, PAN, and composite GO-PAN nanofibers. ....	68
<b>Figure 3.4.</b> SEM images of (a) CNFs and, (b) 1, (c) 5, (d) 10, (e) 20 wt% TRGO/CNFs and f) a typical porous carbon bead formed in 20 wt% TRGO/CNFs. ....	70
<b>Figure 3.5.</b> TEM images of (a, b) CNFs and (c,d) 5, (e) 10 and, (f) 20 wt% TRGO/CNFs. .	71
<b>Figure 3.6.</b> (a) XRD spectra of CNFs and TRGO/CNFs with 5 and 20 wt% GO; (b) The ratio (R) of D to G absorption peak intensity measured by Raman spectroscopy and estimated crystallite size ( $L_a$ ) for CNFs, TRGO/CNFs, and heat-treated GO.....	73
<b>Figure 3.7.</b> (a) The formation charge/discharge profiles for CNFs and TRGO/CNFs. The discharge of 1 and 10 wt% TRGO/CNFs coincide; (b) the derivatives ( $dQ/dV$ ) during charge. ....	76
<b>Figure 3.8.</b> The charge/discharge profiles for the first 20 cycles of (a) CNFs and (b) 5 wt% TRGO/CNFs at $75 \text{ mA g}^{-1}$ (C/5).....	77
<b>Figure 3.9.</b> Rate dependence on discharge capacities of CNF and TRGO/CNF electrodes, averaged over first 10 cycles.....	78

<b>Figure 3.10.</b> (a) Discharge capacities of CNF and TRGO/CNF electrodes over 200 cycles at 750 mA g <sup>-1</sup> (2-C) and (b) corresponding Coulombic efficiencies. ....	79
<b>Figure 3.11.</b> Post-mortem SEM images of working electrodes after 200 cycles at 750 mA g <sup>-1</sup> (2C) of (a) CNFs and (b) 20 wt% GO shows the nonwoven fiber structure is retained. High-resolution images of TRGO/CNFs shows a (c) stable and (d) porous SEI film on the fiber surface. ....	80
<b>Figure 3.12.</b> The (a) film resistance and (b) charge-transfer resistance over 20 cycles for delithiated CNF and TRGO/CNF electrodes cycled at 75 mA g <sup>-1</sup> . The inset in Figure 3.11a shows the equivalent circuit used to model the system. ....	82
<b>Figure 4.1.</b> SEM images of nonwoven GO/PAN mats with (a) 0, (b) 5, (c) 10, (d) 15, and (e) 30 wt% Sn(IV). The scale bars represent 20 μm. The insets show high-resolution SEM images of a typical fiber. Scale bars of insets represent 500 nm; (f) Fiber diameter plotted against ionic conductivity of electrospinning solution, with Sn(IV) loading [wt%] labeled on the plot. ....	97
<b>Figure 4.2.</b> SEM images of TRGO/CNFs carbonized at 850°C with (a, b) 5, (c, d) 10, (e, f) 15, and (g, h) 30 wt% Sn(IV). Scale bars represent (a, c, e, and g) 10 μm and (b, d, f, and h) 500 nm. ....	99
<b>Figure 4.3.</b> Surface and bulk characterization of Sn-containing fibers; XPS data of as-spun GO/PAN fibers containing 10 wt% Sn(IV), along with the ensuing spectra of fibers carbonized at 650 and 850°C showing (a) the survey and (b) high-resolution Sn 3d transition. XRD profiles for tin-TRGO/CNFs carbonized at (c) 650°C and (d) 850°C with Sn loadings labeled on the plot. The location of the strongest peaks associated with SnO <sub>2</sub> , if present, are labeled in (c) ....	102
<b>Figure 4.4.</b> TEM images of (a) 10Sn650 (b,c) 10Sn850 (d) STEM image and corresponding EDS maps of 10Sn650. The element pertaining to each map is labeled in the lower left. Scale bars for EDS represent 1 μm. ....	105
<b>Figure 4.5.</b> Typical CV profiles using scan rates of 0.1 mV s <sup>-1</sup> for (a) 10Sn650 and (b) 10Sn850 with phase transitions labeled. <sup>31</sup> ....	107
<b>Figure 4.6.</b> Rate capability measurements of tin-TRGO/CNFs carbonized at (a) 650°C and (b) 850°C; Symmetrical Li-extraction cycling data of tin-TRGO/CNFs carbonized at (c) 650°C and (d) 850°C cycled at 2-C rates. ....	112
<b>Figure 4.7.</b> Post cycle SEM images of (a) 5Sn650 after 900 cycles at 2-C, (b) 5Sn850 after 500 cycles at 2-C, and (c) 15Sn850 after 500 cycles at 2-C with EDS mapping of the individual elements. The scale bars represent 1 μm. ....	115
<b>Figure 5.1.</b> The chemical composition of guar gum (GG) and locust bean gum (LBG). Galactomannans are polysaccharides comprised of a mannose backbone and galactose side-chains, which can be distributed randomly or in blocks throughout the molecule. ....	123
<b>Figure 5.2.</b> a) FT-IR spectra of GG, SiNPs, and the composite electrodes. Hydroxyl groups are observed on the surface of both GG and SiNPs; b) Depiction of H-bonding that may contribute to the good cyclability of electrodes using GG binders. The grey circles correspond to the galactose side-groups on the GG backbone. ....	130
<b>Figure 5.3.</b> SEM images of (a, b) pre-cycled SiNP/GG electrodes and (c, d) post-cycled delithiated SiNP/GG electrodes. The porous structure is maintained after 50 cycles. The size	

of the SiNPs increase after cycling. Electrode composition is 85:10:5, SiNPs:C:Binder wt%.	132
<b>Figure 5.4.</b> (a) Steady-state swelling of polymer-only films in 1 M LiPF <sub>6</sub> salt with EC:EMC (1:1 wt) solvents shows PVDF and galactomannans uptake more electrolyte than Na-CMC; (b) The EIS spectra of electrolyte-swelled PVDF, Na-CMC, LBG, and GG films deposited on Cu foil in the absence of Si and C show resistances that can be attributed to the binder material. The symbols represent the measured data and the lines correspond to an equivalent-circuit model. The inset shows the high-frequency data. EIS measurements were conducted at 10 mV vs Li/Li <sup>+</sup> .	134
<b>Figure 5.5.</b> The delithiation capacities of SiNP/GG and SiNP/LBG electrodes using a symmetric charge/discharge rate of 0.05-C and electrode composition of 85:10:5, SiNPs:C:Binder wt%.	135
<b>Figure 5.6.</b> Cyclic voltammograms of (a) SiNP/GG and (b) SiNP/LBG electrodes. The half-cells were scanned between 1 V and 0.01 V vs Li/Li <sup>+</sup> using a scan rate of 0.2 mV s <sup>-1</sup> . Electrode composition is 85:10:5, SiNPs:C:Binder wt%.	137
<b>Figure 5.7.</b> a) The symmetrical cycling performance of SiNPs with GG, LBG, Na-CMC and PVDF binders. After 250 cycles at 3.6 A g <sup>-1</sup> , both SiNP/LBG and GG show superior capacity to SiNP/CMC and PVDF. The columbic efficiency (CE) of all SiNP electrodes using biopolymer binders remains >99% throughout cycling; b) Rate capability of the SiNPs electrodes using biopolymer binders at symmetric 0.5, 1 and 2-C rates; c) Delithiation capacities of SiNP electrodes from asymmetric charge-discharge using various binders. All Li-insertion was performed at 0.05-C to ensure full electrode lithiation while Li-extraction was performed at an increasing C-rate. The GG binder is capable of allowing Li to extract at high rates, i.e. 2300 mAh g <sup>-1</sup> at 18 A g <sup>-1</sup> . Electrode composition is 85:10:5, SiNPs:C:Binder wt%.	140
<b>Figure 5.8.</b> Rate performance for biopolymer binders reveal that SiNP/GG electrodes are capable of the highest capacities while SiNP/LBG electrodes suffer large capacity losses at elevated currents. Electrodes composition is 75:10:15, SiNP:C:binder.	141
<b>Figure 6.1.</b> a) Molecular structure of glutaraldehyde (GA) and typical representation of guar gum; b) cartoon of crosslinked guar showing GA (orange) attacking the galactose side chain (blue). The mannose backbone is pictured in green; c) proposed crosslink, where GA reacts with the primary hydroxyl on two separate galactose side-chains (in acidic conditions) to form a hemiacetal linkage. Other hydroxyl sites are capable of crosslinking, including those on the mannan backbone. Acetal linkage (not shown) is also possible with the remaining hydroxyl on the GA and galactose hydroxyl.	152
<b>Figure 6.2.</b> Dynamic rheology of 1 wt% guar solutions at different crosslinking reaction times; a) frequency sweeps show that the guar structure breaks down within the first day, but begins to build after 24 hours; b) strain sweeps show that guar gels crosslinked for > 1 day did not enter the nonlinear viscoelastic regime at high (> 100%) strains; c) loss tangent for guar samples that were used to assess the extent of the crosslinking reaction (gelation).	158
<b>Figure 6.3.</b> Dynamic rheology of guar + CB ( $\phi = 0.05$ ) solutions at different crosslinking reaction times; a) frequency sweeps show that the guar structure breaks down within the first day, but begins to build after 24 hours to a gel with near frequency-independent moduli; b)	

strain sweeps show that guar + CB deviate from the linear viscoelastic regime at high (> 40%) strains; c) loss tangent for guar + CB samples that were used to assess the crosslinking reaction (gelation). ..... 161

**Figure 6.4.** Elastic modulus as a function of CB loadings using of 1 wt% guar gels crosslinked for 2 days and dialyzed for 3 days with various loadings of CB. The addition of CB enhances the strength of the gels. .... 163

**Figure 6.5.** (a-c) Cross-sectional, cryo-SEM images of hydrated guar + CB gels (crosslinked for 2 days and  $\phi_{CB} = 0.05$ ); Field emission SEM images of the same dehydrated guar + CB gels showing (d, e) the surface and (f) cross section; (g) cartoon of: the guar + CB mixture before high-shear mixing and crosslinking; the structure of guar + CB gel after high-shear mixing and crosslinking; the dehydrated guar + CB gel structure. The aggregation of CB after dehydration coats the CB surface with crosslinked guar to create a durable binding material. .... 166

**Figure 6.6.** (a) Mass uptake as a function of crosslinking time (b) Nyquist plot of Cu foil, and guar films crosslinked for 0-3 days on Cu foil at 10 mV vs Li/Li<sup>+</sup>. The inset in (b) shows high-frequency impedance data..... 168

**Figure 6.7.** Typical first-cycle capacities at 180 mA g<sup>-1</sup> (0.05-C) for SiNP electrodes using crosslinked guar + CB binders; first-cycle coulombic efficiencies (CEs) are reported on the plot ..... 170

**Figure 6.8.** Effect of crosslinking density on electrochemical cycling performance of SiNP electrodes using guar + CB binders with various crosslinking time; typical symmetrical cycling of a) rate capability performances and 2) performances over 300 cycles..... 172

**Figure 6.9.** (a-c) Images of (a) guar + CB gel with the razor blade used to produce (b) a fragmented gel. The gel was (c) placed in a scintillation vial and H<sub>2</sub>SO<sub>4</sub> was added to yield a concentration of 75 mM. The gel was given 24 hours to swell; Changes in network structure before and after acid treatment were assessed via (d) frequency and (e) stress sweeps. .... 175

**Figure 6.10.** (a) Capacity over 300 cycles for SiNP electrodes using guar + CB binders that have been crosslinked for 0, 1, and 2 days. Electrodes were lithiated using a constant-current, constant-voltage technique and delithiated at 3.6 A g<sup>-1</sup>; (b) Nyquist plots at select cycles for lithiated electrodes at 10 mV vs. Li/Li<sup>+</sup>; (c) equivalent circuit used to fit impedance data; (d) the high-frequency solution resistance and (e) the charge-transfer resistance, determined by fitting impedance data to the equivalent circuit..... 177

**Figure 7.1.** Polyhedral view of **I** showing (a) the unit cell down the *b*-axis; Edge-sharing VO<sub>5</sub> square pyramidal chains along the *b*-axis, bridged through corner oxygen atoms by (b) MnO<sub>6</sub> octahedral chains and (c) disordered MnO<sub>4</sub>(H<sub>2</sub>O)<sub>2</sub><sup>2+</sup>/2NH<sub>4</sub><sup>+</sup>. .... 190

**Figure 7.2.** (a) Initial charge/discharge profile for **I** electrodes at 10 mA g<sup>-1</sup>; the lettering refers to potentials where Li-ion (de)intercalate; (b) PXRD patterns of **I** electrodes at (de)intercalation voltages lettered in (a); Proposed crystal structures of **I** after (c) 1 mol per formula Li-ion intercalate at **B** and (d) 3 mol per formula Li-ion intercalate at **C**. .... 193

**Figure 7.3.** Electrochemical characterization of **I** electrodes in Li-ion half-cells showing (a) capacities for 300 cycles cycled at 0.5 A g<sup>-1</sup> along with the corresponding coulombic efficiencies (CEs) with an areal loading = 2 mg cm<sup>-2</sup>; (b) capacities as a function of current density with varied areal loading. .... 197

<b>Figure 7.4.</b> SEM images showing the top surface of <b>I</b> electrodes (a, b) before cycling and (c, d) after 300 cycles; (e,f) cross-section of electrodes after 300 cycles; inset of (f) reveals high-magnification image of a cycled <b>I</b> particle. ....	199
<b>Figure 8.1.</b> Discharge capacities of Li-ion half-cells using SnO <sub>2</sub> -TRGO/CNF working electrodes with Sn(IV) loadings of (a) 5 and (b) 10 wt%. The electrolyte comprises 1 M LiPF <sub>6</sub> in 1:1 wt ethylene carbonate: ethylmethyl carbonate with FEC concentration labeled on the plots.....	210
<b>Figure 8.2.</b> Discharge capacities as a function of symmetrical charge-discharge rate with various areal loadings of SiNP electrodes using guar binders. Capacities on the plot represent the 10 <sup>th</sup> symmetric cycle at a specific rate. Basis rate: 1-C = 3.6 A g <sup>-1</sup> ; Electrode composition: SiNP:CB:GG = 8:1:1 wt%; Electrolyte composition: 1 M LiPF <sub>6</sub> in 1:1 wt ethylene carbonate: ethylmethyl carbonate. ....	216
<b>Figure A1.</b> Steady-shear rheology of PAN systems; Experiments were performed to observe the influence of SnCl <sub>4</sub> and EG on the viscosity of electrospinning precursor solution. All experiments were conducted with 8 wt% polymer; EG concentration was 4:1 mol EG:SnCl <sub>4</sub> .....	229
<b>Figure A2.</b> Box plots of fiber diameters for tin-TRGO/CNFs. The dot in each samples represents the mean diameter, which is also written above each individual box plot. ....	229
<b>Figure A3.</b> Images of SnO <sub>2</sub> -TRGO/CNFs carbonized at 650°C containing a Sn (IV) loadings of (a-c) 5 wt% and (d-f) 10 wt% .....	230
<b>Figure A4.</b> SEM image of TRGO/CNFs carbonized at 850°C .....	230
<b>Figure A5.</b> TGA and DTG of GO/PAN fibers. The technique (temperature, heating ramp-rate, and gaseous environment) used for TGA was analogous to stabilization and carbonization of PAN that was used in this study. ....	231
<b>Figure A6.</b> High-resolution XPS transitions of <i>as-spun</i> fibers with Sn (IV) loading of 10 wt%, 10Sn650, and 10Sn850 showing (a) Cl 2p and (b) N 1s; the inset of (b) magnifies the N 1s transition of heat treated samples.....	232
<b>Figure A7.</b> (a) EDS maps overlain on an SEM image of 15Sn850, with individual elemental maps below the overlay. The scale bar represents 10 μm; (b) EDS spectrum of the above sample. ....	233
<b>Figure A8.</b> SEM image of 10Sn850 on carbon tape with EDS maps overlain, and the respective elemental maps; Scale bar represents 2.5 μm .....	234
<b>Figure A9.</b> CV of TRGO/CNFs in the absence of tin that were carbonized at (a) 650°C and (b) 850°C.....	234
<b>Figure A10.</b> Ratios of Li-reversible to Li-irreversible host materials as measured via EDS. ....	235
<b>Figure A11.</b> (a) Galvanostatic cycling with potential limitation technique used to calculate C-rates as a function of current density; (b) Charge/discharge curves of highly loaded tin electrodes that were carbonized at 650°C.....	235
<b>Figure A12.</b> (a) Raman spectra for TRGO/CNFs carbonized at various HTTs; the two peaks in the spectrum above represent the defective (D peak ~1330 cm <sup>-1</sup> ) and graphitic (G peak ~1580 cm <sup>-1</sup> ) nature of TRGO/CNFs. An increased intensity ratio of the two peaks (I <sub>D</sub> /I <sub>G</sub> ) suggests increased disorder in the carbon structure. The I <sub>D</sub> /I <sub>G</sub> ratios for TRGO/CNFs carbonized at 650,	

850, and 1050°C, are 1.65, 1.42, and 1.15, respectively; disorder decreases with HTT. (b) Electrical conductivity of TRGO/CNFs carbonized at different temperatures..... 236

**Figure A13.** SEM image of 30Sn850 after 500 cycles at 2-C at (a) low and (b) high magnification. At low magnifications, we notice that Sn particles aggregate upon cycling, which likely occurred after recurrent pulverizations. After 500 cycles, capacities of TRGO/CNFs with high Sn loadings are equal to capacities in the absence of Sn, which suggests that the Sn deactivates and the fiber structure maintains electrochemical activity..... 236

**Figure B1.** XPS data showing the C 1s transitions for (a) GG and (b) guar + SiNPs; the Si 2p transition for (c) SiNPs and (d) guar + SiNPs; The red circles are measured data, green peaks were fit using XPSEAK41 with a Shirley background, and the black line is the sum of calculated peaks. The guar used in this thesis was purified via centrifugation at 5000 RPM for 30 mins and decantation of the supernatant. A slight shift towards higher binding energies was observed in SiNP after they were coated with GG (0.1 eV shift), possibly due to oxidation. .... 239

**Figure B2.** Steady-shear rheology of (a) galactomannan and (b) CMC and PVDF solutions; the concentration of each solution is labeled on the plots. As evident from comparison of the two graphs, galactomannans have a much higher viscosity than PVDF and CMC solutions. .... 240

**Figure B3.** (a) XRD spectrum of the SiNP/GG electrodes used to determine the crystallite size of the SiNPs; (b) SEM image of the SiNPs on carbon tape and (c) the corresponding size distribution of the SiNPs as measured by HR-SEM images with average bi-modal particle size of 58 nm. .... 240

**Figure B4.** SEM images of SiNP/GG electrodes with (a) 10 wt% binder and (b) 15 wt% binder. As the concentration of binder increases, no dramatic decrease in film porosity is observed. Additionally, the size of the SiNPs encapsulated in the binder does not appear to increase as the binder loading increases. The same effect can be seen when the LBG concentration in the electrode increases from (c) 5 wt% to (d) 15 wt%..... 241

**Figure B5.** SEM images of pre-cycled (a) SiNP/PVDF and (d) SiNP/CMC electrodes. SiNP/PVDF electrodes appear to lose porosity and fuse together (b,c) upon cycling. A similar loss in pre-cycled electrode structure is observed in SiNP/CMC electrodes (e, f). Post-mortem images were captured after 50 charge/discharge cycles at 3.6 A g<sup>-1</sup>. .... 241

**Figure B6.** Cyclic voltammograms of (a) GG, (b) LBG, (c) CMC, and (d) PVDF polymer-only films on Cu foil indicate little current is produced with the binder materials. Additionally, given their electrochemical stability at potentials higher than 2 V vs Li/Li<sup>+</sup>, GG and LBG may be candidates for alternative cathode binding materials. .... 242

**Figure B7.** Cycling of SiNP electrodes in the absence of carbon with 100 mV cut-off voltage. The half-cells were lithiated to 1200 mAh g<sup>-1</sup> at 0.1-C (360 mA g<sup>-1</sup>) on the first cycle. On ensuing cycles the electrodes were lithiated under constant current to 100 mV at 0.1-C (360 mA g<sup>-1</sup>) and held under constant voltage conditions until 0.01-C (36 mA g<sup>-1</sup>). The binders allow for stable cycling at 0.1-C rates. The electrode contains 90 wt% SiNPs and 10 wt% binder. .... 242

**Figure B8.** (a) Typical charge/discharge profiles of SiNP electrodes using various polymer binders. In the first lithiation the crystalline Si is converted to amorphous Si and the native-

oxide layer is reduced to  $\text{Si}^0$ ; (b) Average coulombic efficiencies of SiNP electrodes on the formation cycle. The galactomannan binders operate with the highest initial CEs. The electrodes composition is 85:10:5, SiNPs:C:Binder wt%. ..... 243

**Figure B9.** CV cycles 11-20 of a SiNP/LBG electrode. A maximum peak current density is attained after the 13<sup>th</sup> cycle. The half-cell was cycled between 1 V and 0.01 V vs Li/Li<sup>+</sup> using a scan rate of 0.2 mV s<sup>-1</sup>. Electrode composition is 85:10:5, SiNPs:C:LBG wt%. ..... 243

**Figure B10.** Discharge capacity as a function of cycle life using SiNP electrodes using guar binders. Each electrode contained various amounts of electrolyte additive fluoroethylene carbonate (FEC), and the amount of FEC is labeled on the figure. Half-cells were cycled symmetrically with electrode composition 80:10:10, SiNPs:C:Guar wt%. ..... 244

**Figure B11.** Nyquist plots from electrochemical impedance spectroscopy (EIS) from half-cells in Figure B9. Impedance values were measure on lithiated electrodes. The cells were charged at 1-C rates (corresponding to the values seen in Figure B9) to 10 mV vs. Li/Li<sup>+</sup> and let rest for 4 hours before EIS was run. Nyquist plots in this figure represent the impedance values after select cycle numbers: (a) 10 (b) 60 (c) 120, and (d) 200 cycles. From these plots, we can infer that electrodes in the absence of FEC have the largest resistance after 200 cycles, as Nyquist plots reveal largest high-frequency values and the largest semi-circles. .... 245

**Figure B12.** Asymmetric charge-discharge profile curves of SiNP electrodes using (a) GG (b) LBG and (c) CMC electrodes, as well as the corresponding differential capacities for the delithiation curve for the electrodes using (d) GG and (e) LBG and (f) CMC binders. All lithiation rates are 0.05-C to ensure full lithiation. .... 246

**Figure B13.** Typical (a) charge/discharge profiles of the formation cycle when binder loading is increased to 15 wt% and the (b) corresponding CEs reveal high CEs of ~88% (b). Electrode composition is 75:10:15, SiNPs:C:Binder wt%. ..... 246

**Figure B14.** (a) Delithiation capacity and coulombic efficiency of SiNP electrodes using 10 and 15 wt% GG and LBG over 100 cycles at 1-C rate and (b) the capacity retention corresponding to (a). The capacity data from 5 wt% can be seen in Figure 7a in the text. As the amount of binder increases, so too does the irreverble capacity loss. .... 247

**Figure C1.** Dynamic rheology of 1 wt% guar in H<sub>2</sub>O before and after high-shear mixing (HSM) at 7500 RPM for 15 minutes; insignificant differences between pre- and post-sheared samples revealed that changes in microstructure occurred after high-shear mixing quickly rebuilt before sample loading..... 249

**Figure C2.** a) Decrease in the viscous and elastic moduli in a 0.70 wt% guar solution with 75 mM H<sub>2</sub>SO<sub>4</sub>. Values were obtained from the linear viscoelastic regime of a stress sweep with  $\omega = 1 \text{ rad s}^{-1}$ ; b) steady flow rheology values showing the decrease in viscosity of 0.70 wt% guar solutions with time. No significant decrease in viscosity was observed when glutaraldehyde (GA) was added to guar solutions (1 mol OH from GA to 1 repeat unit) because GA is a biocide and inhibits the breakdown of guar. A large decrease in viscosity of the guar + H<sub>2</sub>SO<sub>4</sub> (75 mM H<sub>2</sub>SO<sub>4</sub>) was observed. .... 249

**Figure C3.** Frequency sweeps showing the elastic modulus (left) and viscous modulus (right) for guar solutions that have been crosslinked for 2 days with various volume fractions of CB. .... 250

<b>Figure C4.</b> Elastic modulus for guar systems that were not crosslinked. Values represent those collected from frequency sweeps (within the linear viscoelastic regime) and at $\omega = 1 \text{ rad s}^{-1}$ . The slope of the line is 0.5. ....	250
<b>Figure C5.</b> Nyquist plots of hydrated guar hydrogels crosslinked for 2 days and containing various amounts of CB (labeled on the plot). The gels were dialyzed for 3 days prior to measurements to leach out $\text{H}_2\text{SO}_4$ and unreacted GA. Measurements were taken at open circuit from 1 GHz to 1 Hz with a voltage amplitude of 10 mV. The zoomed-in Nyquist plot (right) reveals that no difference in high-frequency resistance can be determined, which indicates no significant difference in electronic or ionic conductivities. Also, the high impedance values (values of plots on the kilo-ohm scale) indicate little conductivity, and thus percolation....	251
<b>Figure C6.</b> Cryo-SEM images of guar gel crosslinked for 2 days; (a) macrostructure at low-resolution, and (b) microstructure at high-resolution. The scale in (a) is 20 $\mu\text{m}$ and the scale in (b) is 1 $\mu\text{m}$ . ....	251
<b>Figure C7.</b> Nyquist plots of hydrated guar hydrogels crosslinked for 2 days and containing various amounts of CB (labeled on the plot). The gels were dialyzed for 3 days prior to measurements to leach out $\text{H}_2\text{SO}_4$ and unreacted GA. The solids concentration of each sample was then determined by drying the contents overnight in a vacuum oven. Then, $\text{H}_2\text{SO}_4$ was added to gels to make a 0.1 M sample and the gel was given 16 hours to swell. Measurements were taken at open circuit from 1 GHz to 1 Hz with a voltage amplitude of 10 mV. Cell constant = 0.69 $\text{cm}^{-1}$ . ....	252
<b>Figure C8.</b> (a) FTIR spectra of guar and guar crosslinked for 1 and 3 days.....	252
<b>Figure C9.</b> a) Thermal gravimetric analysis (TGA) of components in the guar + CB gels, as well as gels that had been crosslinked for 2 days. TGA was used to determine solids composition after dialysis; b) derivatives of (a), which show no significant difference in degradation temperature when crosslinked. ....	253
<b>Figure C10.</b> (a) Coulombic efficiencies (CEs) as a function of cycle number, which correspond to <b>Figure 6.9</b> . Average CEs for SiNP electrodes using guar + CB binders crosslinked for 0, 1, 2, and 3 days were 99.8, 99.9, 99.9., and 99.8%; (b) Capacity retention of SiNP electrodes using guar + CB binders, also corresponding to <b>Figure 6.9</b> ; values are normalized to the second-cycle discharge capacity. ....	254
<b>Figure C11.</b> Characterization of SiNP electrode using guar + CB binder crosslinked for 2 days; (a) SEM image of top surface (inset shows porosity of the microstructure); (b) EDS analysis of the electrode with chemical symbol in bottom left.....	255
<b>Figure C12.</b> Photograph of films cast in Teflon molds showing guar crosslinked for 1 (top left), 2 (center), and 3 (bottom right) days.....	256
<b>Figure D1.</b> Thermogravimetric analysis for <b>I</b> in air plotted as weight (%) versus temperature ( $^{\circ}\text{C}$ ). ....	259
<b>Figure D2.</b> Infrared spectra of <b>I</b> (black), $\text{H}_2\text{O}$ (blue), and $\text{NH}_3\text{H}_2\text{O}$ (red). ....	260
<b>Figure D3.</b> Typical (dis)charge capacity curve derivative profile from constant-current cycling at 10 mA $\text{g}^{-1}$ . Peaks denote phase changes that were used for <i>ex-situ</i> PXRD studies. ....	260
<b>Figure D4.</b> The calculated XRD spectrum of <b>I</b> , which agrees with the synthesized structure and proves we created a high-purity, single phase material. ....	261

**Figure D5.** The empirical and simulated low-angle PXRD patterns for **I** electrodes that were lithiated to points **C** and **D**, as described in Chapter 7..... 261

**Figure D6.** Powder XRD pattern of the thermogravimetric analysis residue for **I** electrodes after charge/discharge cycling and stopped at different voltages, and their assignments. The XRD pattern of **D** revealed a larger presence of  $\text{Li}_2\text{CO}_3$  (decomposed SEI material) at 10 mV than 270 mV, indicating that SEI formation occurred at low potentials vs.  $\text{Li}/\text{Li}^+$ . ..... 262

**Figure D7.** Cyclic voltammetry (CV) on **I** electrodes showing the initial cycling (top) and later cycles (bottom). The first cycle shows single cathodic polarization peak (intercalation) at a potentials near the onset of Li-ion reduction and a single anodic polarization peak (deintercalation) at 2.38 V vs.  $\text{Li}/\text{Li}^+$ . As the cycling progresses, we see a changing voltammogram, as evidence of irreversible reactions and structural rearrangement within **I**; new cathodic peaks arise at  $\sim 1.71$  and  $0.65$  V vs.  $\text{Li}/\text{Li}^+$  and new anodic peaks arise at  $\sim 0.93$  vs.  $\text{Li}/\text{Li}^+$ . We also see a decrease in cathodic peak current as cycling progresses, which we attribute to Mn dissolution. Peak position becomes constant in later cycles (cycles 8-10) as **I** rearranges into a structure that is stable for (de)intercalation. A scan rate of  $0.1 \text{ mV s}^{-1}$  was used. .... 263

**Figure D8.** Select half-cell cycling profiles of **I** electrodes, showing (a) the charge/discharge curves and the corresponding (b) derivatives of the charge/discharge curves over 300 cycles. Low-voltage intercalation peaks in (b) decrease in magnitude due to Mn dissolution, however, we observed no significant decrease in low-voltage peak magnitude between cycles 100 and 300..... 264

**Figure D9.** Impedance data for **I** electrodes showing a) Nyquist plots as a function of state-of-charge (SOC) with the equivalent circuit used to fit impedance data; b) values for the resistors when fitting the Nyquist plot to the model equivalent circuit. During the first cycle, the high-frequency resistance values stay constant, which indicates that Mn-ion that may have dissolved in the electrolyte, do not increase the solution resistance. The mid-frequency resistance, corresponding to film resistance from the SEI, decreased in half from points **C** to **D**, or from  $\sim 50 \Omega$  at 250 mV to  $\sim 19 \Omega$  at 10 mV. The reduction in  $R_2$  value with SOC may be associated with decomposition of electrolyte to form a more conductive SEI, as seen in graphite electrodes with similar electrolyte. <sup>2</sup> Upon delithiation, the SEI values do not increase beyond the fully charged state, indicating that a stable SEI has formed. Values of the low-frequency resistance,  $R_3$ , correspond to the charge transfer resistance. The charge transfer resistance is dependent on mols Li in **I** and diffusivity of Li in **I**. Since the concentration of Li in **I** is high at **D** (near full lithiation after chronoamperometry at 10 mV until C/100), we see the charge transfer resistance increase due to a lower driving force from the concentration gradient. Charge transfer resistances are large before major Li-insertion at **C** and near full Li-extraction at **G**, and therefore not shown in (b). ..... 265

**Figure D10.** Powder XRD pattern of the TGA residue of **I** after heating in nitrogen (blue), and the calculated  $\text{MnV}_2\text{O}_6$  pattern (red) and the calculated  $\text{V}_2\text{O}_5$  pattern (green)..... 266

# **Chapter 1. Introduction**

## 1.1. Opening Remarks

Rechargeable batteries were first invented in 1859, when Gaston Planté devised the lead acid battery. At the time, Planté used cloth to separate lead sheets that he submerged in sulfuric acid. Throughout the years, technological developments led to the modern lead acid battery found in many internal combustion engine vehicles, and exploration of new chemistries led to Ni-Cd and Ni-H rechargeable batteries. However, these early battery chemistries did not compare to the specific energy and electrochemical potential of lithium. Short-circuiting in metallic lithium anodes plagued early renditions of Li-batteries. Major contributions headed by Goodenough, Whittingham, and Yazami in the 1970-80s led to a battery where Li-ions reversibly shuttled across two electrodes that did not comprise metallic lithium. <sup>[1]</sup> With successful commercialization of Li-ion batteries (LIBs) in 1991, Sony revolutionized our mobile society. Today, LIBs power many mobile devices such as phones, laptops, and more recently, electric vehicles. Nonetheless, an increased energy density is needed for electric vehicles to competitively compete with the internal combustion engine market.

Since commercialization 25 years ago, the cycle life of LIBs has significantly improved and the cost to produce LIBs has significantly decreased, <sup>[2]</sup> which is advantageous for stationary applications. However, the gravimetric energy density (advantageous for mobile applications) has only increased ~ 2.5 times in the same 25-year period; LIBs in 1991 contained energy densities of ~ 100 Wh kg<sup>-1</sup>, whereas today's state-of-the-art LIBs contain ~ 250 Wh kg<sup>-1</sup>. Performance enhancements are largely attributed to discovery of novel cathode materials. The anode found in today's LIB comprises the same active component as in 1991: graphite.

Promising high-charge capacity materials such as tin, silicon, and metal oxides provide alternatives to graphite anodes. Incorporating these high-capacity anode materials in LIBs may increase energy density as high as 30 %, rendering the range of an electric vehicle comparable to a full tank of gas. <sup>[3]</sup> However, high-capacity materials suffer from a short cycle life. Here, we investigate means to enhance the cycle life of high-capacity anode materials.

The work comprised in this thesis largely focuses on implementing high-capacity Si- and Sn-based anode materials on the nano-scale to enhance the cycle life of next-generation anodes. We consider nanomaterials as replacements for conventional micron-sized active materials in Li-ion batteries because they improve redox kinetics, charge-transfer, and structural integrity. We couple use of nanomaterials with approaches to vary: 1) architecture, by using structures such as nanofibers, nanoparticles, or nanowires; 2) composition, by forming nano-composites with carbon, a material known to exhibit stable electrochemical performance in LIBs; 3) binding agent, which may favorably associate with electrode materials. Unique, multifaceted methods to enhance electrochemical performances arise from our combinatorial approach. Notably, we investigate composite-carbon nanofiber/tin and Si/binder systems to extend the cycle life of high-capacity anodes in LIBs. The last study in the document investigates a less-considered, high-capacity transition metal oxide for potential high-power anodes: manganese vanadates. Unlike the aforementioned methods used to prolong the cycle life of Si- and Sn-based anodes, here we assess how defects in molecular structure may be used to enhance anode performance.

## 1.2. Document Organization

This dissertation begins with a background section (**Chapter 2**), in which we review LIB electrochemistry and survey present and future electrode materials for next-generation LIBs: from Li-active hosts to binding agents. This chapter highlights electrochemical methods used to characterize these electrode materials. Proceeding sections summarize the electrospinning fiber-formation process and present recent developments from nanofiber literature. Subsequent chapters (**Chapters 3 - 7**) provide results from various approaches used to extend the cycle life of promising, high-capacity anode materials. All studies aim to correlate physical with electrochemical properties to produce next-generation Li-ion anodes.

The first approach involves encapsulating tin nanoparticles within a graphene-containing carbon nanofiber matrix. Tin has a capacity three times greater than commercial graphite anodes, but suffers from a short life due to particle pulverization. In this study, we used carbon nanofibers to provide scaffolding and prevent cracking of tin particles during cycling. Graphene, an electronically conductive and flexible two-dimensional carbon, was added to the carbon nanofibers to enhance electronic properties of the composite electrode for high-rate capabilities. Before introduction of tin, graphene-containing carbon nanofibers were produced and assessed as conductive, high-capacity anodes (**Chapter 3**). Here, we scrutinized effects of graphene concentration on fiber morphology and structure. The aforementioned physical properties were correlated with electrochemical performance. Incorporation of tin in the aforementioned graphene-containing carbon nanofibers follows in **Chapter 4**, with supporting information in **Appendix A**. Here, we investigated the influence of process

parameters, such as tin concentration and thermal treatment temperature, on composite-nanofiber morphology and tin oxidation state. The goal of this study was to produce an electrode capable of high-capacity, stable cycling in Li-ion batteries by encapsulating tin nanoparticles into graphene-containing carbon nanofibers.

Next, we shift attention to Si-based systems. Silicon has the highest charge capacity of any known material, but suffers from particle pulverization that ends in cell failure (similar to tin). Unlike the first approach, where we used carbon composites to increase the cycle life, a novel biopolymer binding agent is used to increase the cycle life of silicon nanoparticle (SiNP) systems. Binding agents bond with electrode components to preserve microstructure and decrease internal resistances across the electrode. **Chapter 5** showcases galactomannans as novel binding agents for SiNP electrodes. Here, we examine galactomannan-electrode and -electrolyte interactions that lead to electrochemical performance enhancements in Si-based anodes. **Appendix B** contains supplemental information on Si-galactomannan systems, including further assessment on Si-binder interactions. We recognized that galactomannans (specifically guar gum) did not make perfect binders, and in **Chapter 6**, we showcase crosslinked guar-carbon black hydrogel binders, which were developed to build upon shortcomings in our previous study. Notably, we attempt to increase the strength and conductivity of Si-based electrodes. The crosslinked binders, in effect, enhance electrode cohesion and hinder cracking by self-healing. This study monitors gelation via rheological methods and assesses effects of crosslinking density on physical and electrochemical properties. Supporting information is presented in **Appendix C**.

Our final study, reported in **Chapter 7**, comprises a preliminary investigation on a novel manganese vanadate, which has potential application as anode material in LIBs (**Appendix D** contains supplementary information). Typical manganese vanadate anodes suffer from a short cycle life and poor electronic conductivity, and thus, researchers overlook manganese vanadates for carbon, Si, and Sn. To enhance the cycling performance of manganese vanadates, we investigate a novel crystal conformation with induced structural vacancies. We assess structure as a function of state-of-charge and the electrochemical performance of the novel vacancy-induced anode.

The dissertation concludes (**Chapter 8**) with a summary of major findings in each chapter and a prospective means to progress work presented in this document. In this chapter, we address the viability of carbon nanofiber anodes, Si-based systems, and manganese vanadate anodes in LIBs. This chapter proposes extensions to studies in **Chapters 3 – 7**, with aim to extend the cycle life of high-capacity anode materials. We hope our studies will encourage use of multifaceted approaches for incorporation of high-capacity LIB anode materials, and in effect, enhance battery technology and the quality of our mobile society.

### **1.3. References**

- (1) D. Deng. *Energy Science & Engineering*, 3, 2015, 385-418.
- (2) B. Nykvist, M. Nilsson. *Nature Climate Change*, 5, 2015, 329-332.
- (3) E. C. Evarts. *Nature*, 526, 2015, S93-S95.

## **Chapter 2. Background**

## 2.1. The Li-ion Battery

Li-ion batteries (LIBs) are ubiquitous electrochemical energy storage devices. The vast appeal for LIBs, be it for mobile or stationary storage, lies in the high-energy and power density. <sup>[1]</sup> Energy density in batteries, or charge per unit mass or volume, is the product of nominal operating voltage and specific capacity. <sup>[2]</sup> The high-voltage of LIBs, at 3.6 V/cell, decreases the necessary amount of cells in a battery. Lightweight small Li-ions make favorable charge carriers, while favorable electrodes chemistries boost specific capacities. Modern cells boast energy densities  $> 250 \text{ Wh kg}^{-1}$ , <sup>[3]</sup> which is over twice the energy density of other rechargeable battery chemistries such Ni-Cd and Ni-MH. High-power density (rapid withdraw of current) is also an advantageous property of LIBs, and is related to internal battery resistance. A high-power density allows for quick acceleration in electric vehicles and adoption in mobile power tools. Despite the growing usage of LIBs, advancements in consumer electronics technology drive demand for batteries with enhanced electrochemical performance.

LIB cells comprise three major components: anode, cathode, and electrolyte. Electrodes are fabricated in a roll-to-roll process, where slurries of binding agents and composite materials (active material and conductive additive) are cast on a current collector (metal foil). A cartoon of a Li-ion full cell is shown in **Figure 2.1**. During a charge cycle, Li-ions transport from cathode to anode through electrolyte (Li-ion flow reverses during discharge). Current state-of-art LIBs use graphite anodes, Li-rich metal oxide cathodes, and electrolyte containing lithium hexafluorophosphate ( $\text{LiPF}_6$ ) salt in a mixture of linear and cyclic carbonate (ethylene carbonate, ethylmethyl carbonate, etc.) solvents. There are many

different approaches to enhance the performance of LIBs such as use of high-voltage, high-capacity cathode materials <sup>[4]</sup> or electrolyte additives. <sup>[5]</sup> This thesis focuses on a different approach to enhance the performance of LIB: development of energy-dense anodes. The following subsections provide a literature survey on novel anode components ranging from the active materials to the binding agents. Since the Li-graphite intercalation reaction occurs at voltages close to the reduction of Li (deep charging may occur at 0 V vs. Li/Li<sup>+</sup>), investigating materials with reduction potentials lower than graphite would render little improvement. Rather, novel active materials that have larger charge capacities than graphite (372 mAh g<sup>-1</sup>), such as manganese vanadates (~900 mAh g<sup>-1</sup>), tin (1000 mAh g<sup>-1</sup>), and silicon (3600 mAh g<sup>-1</sup>), are analyzed and assessed. High-capacity anodes usually suffer from a short cycle life. To increase cycle life, electrodes with various architectures and binding agents are investigated. However, before a literature survey on current and promising anode material for LIB is presented, Li-ion anode electrochemistry is highlighted.

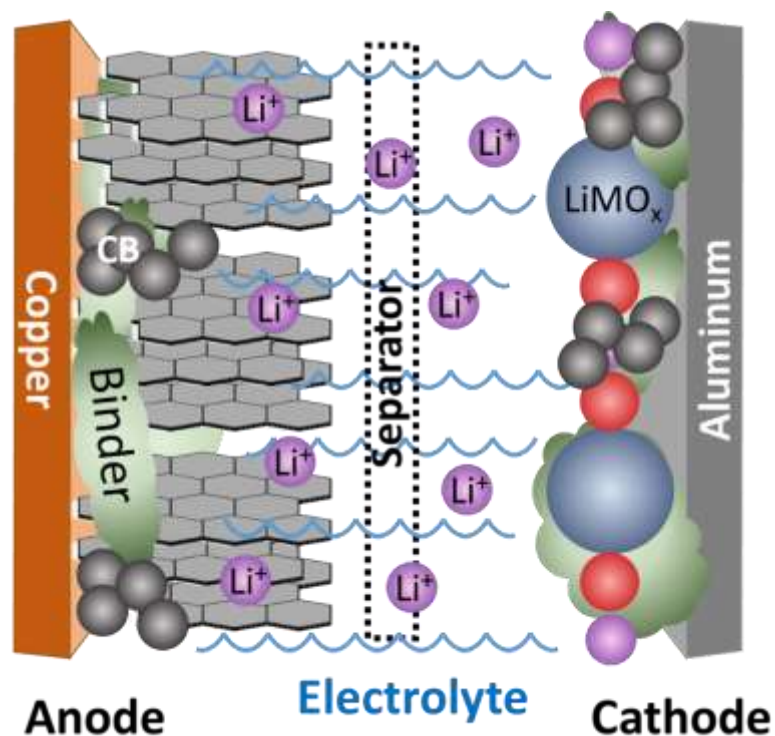
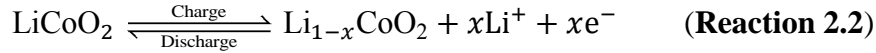
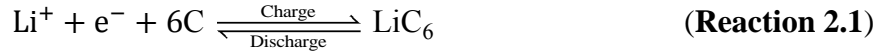


**Figure 2.1.** Cartoon of LIB showing the three major active components (anode, cathode, and electrolyte), as well as the non-active components: Cu/Al-foil current collectors, binders to adhere electrodes to the current collectors, a separator to prevent short-circuiting, and carbon black (CB) as a conductive additive to reduce internal cell limitations

### 2.1.1. Electrochemistry of Li-ion anodes

Anodes in LIBs store charge, in the form of Li, through redox reactions. Anodes are defined as electrodes that are oxidized by the flow of electrons in an external circuit. By definition, LIB anodes vary in polarity from charge to discharge; the anode is the positive electrode during charge and negative electrode during discharge. While this section focuses on the electrochemistry of negative electrodes (hereafter referred to as anodes), fundamentals of cathodes are analogous. The half-cell reactions for industrial-standard graphite anode (**Reaction 2.1**) and lithium-cobalt oxide cathode (**Reaction 2.2**) are presented below. In the

forward reactions, Li-ions transport through electrolyte in the cell and are met by electrons that transports through an external circuit.



Unlike capacitors where charge builds on the surface, Li-ions in batteries insert into Li-active hosts. For example, Li intercalates into layers of graphite in **Reaction 2.1**. Both **Reactions 2.1** and **2.2** are reversible and progress forward on charge cycles and backward on discharge. Since the forward reactions require electrical energy to occur (charge), the system is an electrolytic cell. An electrolytic cell is defined as a cell having a positive Gibbs free energy (**Equation 2.1**):

$$\Delta G = -nFE^\circ \quad \text{(Equation 2.1)}$$

where  $G$  is the Gibbs free energy,  $n$  is the number of electrons in the redox reaction,  $F$  is Faraday's constant, and  $E^\circ$  is cell voltage that is defined by the species in the reaction ( $E^\circ = E_{\text{Cathode}} - E_{\text{Anode}}$ ). If  $E^\circ > 0$  and  $\Delta G < 0$ , the cell is considered galvanic, the redox reaction occurs spontaneously, and work is done on the system (i.e. powering a device). Dividing **Equation 2.1** by molecular weight of the species yields the cell-specific theoretical energy density. Thus, for energy dense anodes, it is imperative to study materials with 1) low-reduction potentials to increase  $E^\circ$  and 2) high-capacity to increase  $n$ .

Throughout this dissertation, electrochemical performance of anode materials are assessed using two-electrode half-cells. The working electrodes of two-electrode cells comprises active anode material (carbon, Si, Sn, etc.) while the combined counter/reference

electrode comprises metallic Li ( $E^\circ \approx -3.05$  V vs. SHE). Chronopotentiometry, or constant-current cycling, is used to charge and discharge the half-cells. In a sample test, the user chooses a certain current (charge/discharge rate) and measures the voltage within a material-specific potential window. **Figure 2.2** shows sample data obtained by chronopotentiometry. Because one electron is needed to reduce one Li-ion, as shown in **Reaction 2.1**, the capacity is calculated by integrating current over the time needed to scan the potential window from one voltage cut-off at  $t_o$  to the other, at  $t_f$ .

$$\text{Capacity} = \int_{t_o}^{t_f} i \cdot dt \quad \text{(Equation 2.2)}$$

Slow currents may be applied to determine a maximum, or theoretical, capacity of electrodes. Slow currents reduce mass transfer and kinetic limitations. Fast currents may be applied to assess power capacities of working electrodes. Charging and discharging currents are expressed as *C*-rates, and calculated as the quotient of theoretical capacity divided by total time necessary to obtain full charge or discharge. For example, a 0.5-*C* rate for a battery with 3600 mAh of capacity would charge in 2 hours at a current of 1800 mA, and a 2-*C* rate would charge the same battery in 0.5 hr at 7200 mA. Chronopotentiometry is the first charging step in commercial LIBs, and is followed by chronoamperometry, where a DC bias is applied until the current falls below a specified threshold (typically *C*/100). The efficiency of the anode (also known as coulombic efficiency) at each cycle is defined as the discharge capacity over the charge capacity. A coulombic efficiency > 99.9% over a thousand cycles is required <sup>[6]</sup> for anodes to be deemed acceptable for commercial applications. One cause for low coulombic efficiency is Li lost to formation of the solid-electrolyte interphase, which is defined below.

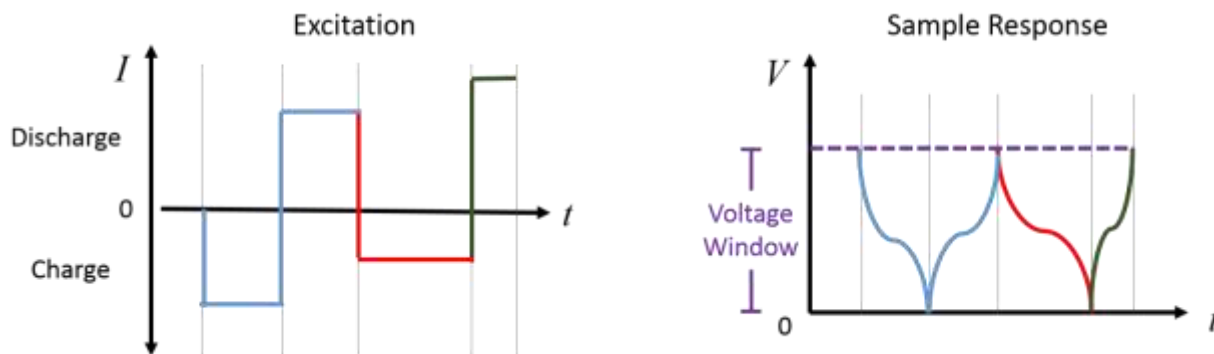


**Figure 2.2.** The basics of chronopotentiometry: an excitation (current) is applied to a cell and the response (change in voltage) is measured within a voltage limit. The time to span the voltage window is used to calculate electrode capacity. Symmetrical or asymmetrical currents may be applied, where charge and discharge current is constant or varied, respectively.

Graphite is a good candidate for high-energy anodes because Li-ions intercalate near, but positive to, the potential of Li reduction. However, common electrolyte components are not thermodynamically stable at the low potentials needed to achieve full intercalation in graphite electrodes. The electrolyte undergoes a series of reduction and polymerization reactions below a certain potential ( $\sim 0.8$  V vs. Li/Li<sup>+</sup> for commercial electrolytes), which forms a passivating film on the electrode surface about 1-10 nm thick.<sup>[7]</sup> The passivating film is known as the solid-electrolyte interphase (SEI),<sup>[8]</sup> and allows for operation of LIBs outside the thermodynamically stable voltage window of electrolytes. Li-ions are able to penetrate through the SEI because it is ionically conductive. Using impedance spectroscopy, researchers proposed that the ionically conductive properties of the SEI form at potentials below 250 mV vs Li/Li<sup>+</sup>.<sup>[9]</sup> Electrons, however, have difficulty transporting through the SEI because it is an electronic insulator. The SEI is typically formed on the first cycle, termed a “formation cycle,” and results in irreversible loss of Li-ions in the electrolyte. Formation of a stable SEI upon the first cycle(s) is crucial to retain capacity of materials. Recurrent SEI formation results in large

irreversible capacity loss and electronic isolation of Li-active particles, both of which lead to premature cell failure. High-capacity and -surface area anodes (porous materials, nanoparticles, etc) suffer from large irreversible capacity loss. Many approaches are being taken to limit these capacity losses, such as formation of an artificial SEI <sup>[10]</sup>, or changing the composition of electrode <sup>[11]</sup> and electrolyte <sup>[12]</sup>. However, short cycle life and poor capacity retention still hinder these high-capacity and -surface area electrodes from appearing in the LIB market. A common method used to study SEIs, working electrodes, and interfaces between the two is electrochemical impedance spectroscopy.

Electrochemical impedance spectroscopy (EIS) is an interfacial technique used to study the Li-insertion mechanism in batteries. <sup>[13]</sup> Impedance,  $Z$ , is a complex measure of resistance to electron flow in a circuit. It may be thought as an alternating current extension of Ohm's law ( $E = I \cdot R$ , where  $E$  is the voltage,  $I$  is the current, and  $R$  is the resistance). In a typical potentiometric-EIS experiment, a sinusoidal voltage is applied to a steady-state electrode with varying frequency. The corresponding phase change and amplitude of current are measured at each frequency to determine the impedance.

The magnitude of impedance and phase angle may be plotted against log frequency, called a Bode plot, or the imaginary impedance may be plotted against the real component, called a Nyquist plot. Both plots enable relation of impedance data with electrochemical phenomena by fitting to equivalent circuits. More specifically, equivalent circuits (i.e. placing resistors, capacitors, and inductors in series or parallel) allow the user to model Li-insertion by taking advantage of time constants associated with each interfacial process. For example,

faradaic events such as charge transfer do not occur at the same frequencies (time constants)<sup>[14]</sup> as solid-state diffusion. A cartoon of a Nyquist plot and typical equivalent circuit for a Li-ion half-cell is shown in **Figure 2.3**. The Nyquist plot below comprises a high-frequency semi-circle, a mid-frequency semi-circle, and a diagonal line at low frequencies. Semi-circles are typically modeled as parallel  $QR$  circuits and diagonal lines are modeled as  $Q$ , where  $Q$  is a constant-phase element (non-ideal capacitor). Each component of the equivalent circuit is related to an electrochemical process; ohmic resistances (dominated by the solution resistances of the electrolyte, and thus termed  $R_{Soln}$ ) are measured at high frequencies, a film resistance from the SEI ( $R_{SEI}$ ) and charge-transfer ( $R_{CT}$ ) at mid-frequency ranges, followed by diffusion at low frequencies.

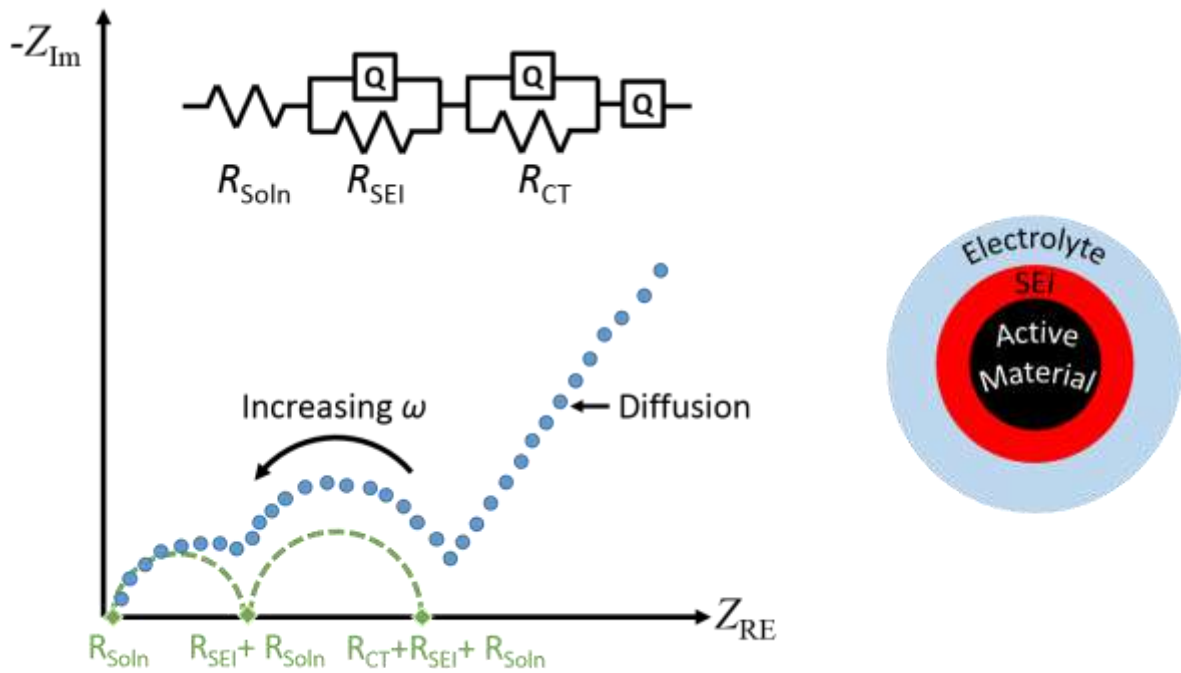


**Figure 2.3.** Nyquist plot and equivalent circuit for typical Li-ion half-cell (left) and the physical interpretation of the model (right).

An interpretation of the Nyquist plot and equivalent circuit in **Figure 2.3** is the following: ohmic resistances from the solution, copper current collector, and electronic connections are experienced at short times, followed by the flow to the SEI. Li-ions de-solvate before entering the SEI. <sup>[15]</sup> Once through the SEI, the electron meets a Li-ion and undergoes charge transfer at the surface of the active material. Li(0) then diffuses through the active material, which occurs at long time scales, and can be the rate-determining step. <sup>[16]</sup> It is important to note that all values (resistances, diffusion coefficients, etc.) obtained via EIS are potential-dependent, as working electrode composition varies with lithiation. When looking at new materials for LIB anodes, especially those for electric vehicle application, it is important to minimize internal cell resistances. Realizing a physical interpretation of EIS data suggests that novel, high-performance anodes must 1) allow the formation of a stable SEI with the electrolyte, 2) provide ample electronic and ionic conductivity for rapid charge transfer, and 3) contain short diffusion pathways. The next sections highlight conventional and promising anode materials for Li-ion batteries, beginning with carbons.

### *2.1.2. Carbon Anodes*

Since commercialization of LIBs in 1991, carbon-based materials remain the preferred choice of anode. The type of carbon (graphitic, amorphous, etc.) heavily impacts the electrochemical performance of the electrode. While carbon electrodes have been extensively studied, <sup>14-16</sup> with an emphasis on graphite, current research aims to discover and investigate novel, high-capacity carbons as active anode material. Herein, attention is given to ordered (crystalline) and disordered (amorphous) carbon electrodes.

*Graphite*—a layered, crystalline allotrope of carbon—was first discovered as a reversible anode material for Li-ion batteries by Rachid Yazami in 1983<sup>[17]</sup> and is still used in most LIB anodes today. Success of the graphite anode is attributed to four main features: 1) Li-insertion near, but positive to, reduction of Li<sup>+</sup> to Li(0), 2) structural stability 3) high-electronic conductivity and 4) favorable reaction kinetics. Graphite has a low-intercalation potential with Li; the fully lithiated stage of carbon occurs at < 0.1 V vs. Li/Li<sup>+</sup> while deep charging occurs at the reduction potential of Li.<sup>[18]</sup> The low Li-insertion potential and minimal voltage hysteresis on charge/discharge profiles contribute to the high-energy and power density of LIBs. Intercalation at potentials lower than graphite-insertion (< 0 V vs Li/Li<sup>+</sup>) raise safety concerns, as Li plating on the surface of graphite may lead to dendrite formation and cell failure. The low (relative to alloying materials such as Si and Sn) theoretical charge capacity of graphite, LiC<sub>6</sub> = 372 mAh g<sup>-1</sup>, results in low volume expansions of 10.3% during Li-intercalation. The van der Waals forces that preserve graphite's layered structure are able to withstand the volume expansions of intercalation, which leads to a mechanically durable electrode and contribute to a long cycle life. Graphite also has anisotropic electronic conductivity properties, which minimizes ohmic resistances for fast cycling.<sup>[16, 19]</sup> Graphite electrodes also have high-coulombic efficiency and low-capacity fade, which are attributed to 1) reversibility of the lithium-carbon complex (**Reaction 2.1**), and 2) formation of a stable solid-electrolyte interphase (SEI) with carbonate electrolyte solvents,<sup>[2]</sup> preventing further electrolyte decomposition and allowing for favorable kinetics. Despite the many advantages

that graphite electrodes offer, new forms of carbon materials with enhanced charge capacity are being explored as alternative anodes. One such material is graphene.

*Graphene*, an  $sp^2$  hybridized two-dimensional (2-D) carbon, has gained a great deal of attention for electrochemical energy storage. Researchers attempt to exploit enticing physical, chemical, and mechanical properties of graphene for nanoscale electronic materials. These properties include, but are not limited to, a high-electrical conductivity, specific surface area, strength, and flexibility. Notably, near-ballistic electron transport <sup>[20]</sup> in high-quality graphene at room temperatures minimizes the ohmic resistance across electrodes, while high-specific surface area provides Li more binding sites. Additionally, flexible and mechanically robust electrodes are able to withstand mechanical stresses of Li-insertion and permit use in wearable devices. <sup>[21]</sup> Early reports <sup>[22]</sup> on graphene anodes revealed a reversible charge capacity of 540 mAh  $g^{-1}$ , leading the authors to conclude that lithium does not bind to graphene in the same  $LiC_6$  orientation as graphite. Researchers <sup>[23]</sup> used first-principles calculations to predict a  $LiC_3$  stoichiometry for pristine graphene sheets, which increase the specific capacity from the 372 mAh  $g^{-1}$  of graphite to 754 mAh  $g^{-1}$ ; the 2-D nature of graphene allows Li-ion to bind to both sides of graphene sheets and doubles capacity. Additionally, the 2-D nature of graphene makes it an ideal candidate for producing composite electrodes to further enhance capacity. Graphene composites with high-capacity materials such as tin and silicon have been produced promising results, and are discussed in the following subsections. However, mass production of high-quality graphene has bottlenecked commercial battery application.

Graphene is commonly produced via a modified Hummer's method,<sup>[24]</sup> which involves oxidation of graphite to increase inter-layer distance ( $d$ -spacing), followed by exfoliation and chemical or thermal reduction of the ensuing single-layer sheets. Artifacts from graphene production introduce limitations for LIB electrodes. Structural defects are common in the final product, which reduces electronic conductivity and mechanical strength. Presence of oxygen-containing functional groups (remaining from graphene production), coupled with the inherently high specific surface area of graphene, result in large irreversible capacity losses (~60% CE on the first cycle).<sup>[25]</sup> Additionally, the oxygen-containing functional groups and carbon cracking that occurs during graphene production creates voids in the sheets and further increases electronic resistance. Doping of graphene with nitrogen has been proposed to increase the electronic conductivity of graphene produced via the Hummers method.<sup>[26]</sup> Development of high-throughput methods that produce high-quality graphene, such as modified-chemical vapor deposition,<sup>[27]</sup> is a major research thrust. Efforts by Samsung SDI to incorporate CVD-derived graphene into LIB anodes have resulted promising, energy dense materials.<sup>[28]</sup> Contrary to production challenges of graphene, numerous approaches exist to create amorphous carbon materials.

*Amorphous carbons*, or non-graphitizable carbons, are the final carbon-based material surveyed for Li-ion anodes. These materials usually comprise both crystalline and amorphous regions. The size of each region is dependent on the precursor material and heat-treatment temperature used to produce the amorphous carbon. Facile and inexpensive synthesis of amorphous carbons typically involves pyrolysis of precursor material. A common precursor

material for amorphous carbon is polyacrylonitrile, <sup>[29]</sup> however, other materials such as sugars, <sup>[30]</sup> carbon-backbone polymers, <sup>[31]</sup> and aromatic molecules <sup>[32]</sup> have recently been studied. In addition to their ease of production, amorphous carbons are attractive LIB anode material because of their high-specific capacity (first-cycle capacity  $\sim 500\text{-}1200\text{ mAh g}^{-1}$ ).

The large capacity, relative to graphite, is attributed to molecular structure. Unlike graphitic carbons, where Li intercalates between graphene sheets at zigzags and armchairs and defects in the basal plane, the amorphous structure provides more Li-insertion and Li-binding sites. Using <sup>7</sup>Li NMR on disordered carbons, it was determined that Li is able to bind to the nearest neighboring carbon ring to yield the LiC<sub>2</sub> conformation <sup>[33]</sup> with capacities  $\sim 1000\text{ mAh g}^{-1}$ . Accompanied with the large capacities, amorphous carbon anodes exhibit larger irreversible capacity losses on the first cycle than graphite. Amorphous carbons also exhibit a larger voltage hysteresis than graphite electrodes. Hence, the intercalation mechanism in amorphous carbons is different than graphite and graphene. Notably, graphite undergoes distinct phase changes during Li-insertion, whereas amorphous carbons do not. <sup>[34]</sup> Phase changes in the Li-graphite complex decrease diffusion coefficients two-to-four orders of magnitude as compared to amorphous carbon material <sup>[16]</sup>. Increased Li-diffusivity in anodes is desired. After the initial cycle, many binding sites are lost due to SEI formation. However, amorphous carbons, especially those produced at low temperatures, have low electronic conductivities and contain tortuous diffusion pathways that hinder rapid Li-diffusion. Current research focuses on methods to enhance reversible capacity beyond that of carbon-based materials.

### 2.1.3. Manganese Vanadate Anodes

Metal oxide anodes, such as lithium titanate (LTO), are possible alternatives to graphite for high-power applications. The low-capacity of LTO ( $\sim 175 \text{ mAh g}^{-1}$ ) and high-operating potential ( $\sim 1.5 \text{ V vs. Li/Li}^+$ ), relative to graphite, yields a low-energy dense battery. However, the operating potential of LTO is advantageous for high-power applications because it decreases the possibility of Li-plating and cell failure. Additionally, the electrolyte is thermodynamically stable at the positive operating potentials, which decreases irreversible capacity from SEI formation. Due to the low capacity of LTO, other metal oxides, such as manganese vanadates, are being considered as potential anode material for high-power applications.

Manganese vanadates are prepared hydrothermally from precursor salts to form  $\text{MnV}_2\text{O}_x$ , where typically  $x = 6$ . The particles are rod-like, with a layered crystal structure.<sup>[35]</sup> The highly ordered structure produces large capacities ( $\sim 900 \text{ mAh g}^{-1}$ ) on the first charge cycle.<sup>[36]</sup> Manganese vanadates have been investigated as cathodes ( $\sim 200 \text{ mAh g}^{-1}$  with voltage limits  $2 - 3.5 \text{ V vs. Li/Li}^+$ ),<sup>[37]</sup> where vanadium is reduced from  $\text{V}^{5+}$  to  $\text{V}^{3+}$ .<sup>[38]</sup> However, most of the Li inserts at potentials slightly positive to Li-ion reduction, giving the possibility for energy-dense anodes; Li inserts into manganese oxide anodes at  $\sim 0.5 \text{ V vs. Li}$  with a capacity  $\sim 700 \text{ mAh g}^{-1}$ .<sup>[39]</sup> Deintercalation, on the other hand, occurs at high potentials ( $\sim 2 \text{ V vs. Li/Li}^+$ ). The large charge/discharge polarization led researchers to speculate that Li is reversibly stored via Li-O bonds.<sup>[40]</sup> The  $\text{MnV}_2\text{O}_x$  structure becomes amorphous after deintercalation on the first cycle, which lowers the capacity to  $\sim 400 - 600 \text{ mAh g}^{-1}$ .<sup>[41]</sup> One

possible reason for amorphization after initial cycling of  $\text{MnV}_2\text{O}_x$  anodes is Mn(II) dissolution in  $\text{LiPF}_6$ -containing electrolytes. Dissolution of Mn(II) stymied development of Mn-based cathode materials, <sup>[42]</sup> and required a Mn oxide-based cathode with different structure and composition to limit dissolution and thus capacity fade. <sup>[43]</sup> A novel structure and composition of manganese vanadates for LIBs is the focus of *Chapter 7*.

To enhance the electrochemical performance of  $\text{MnV}_2\text{O}_x$  anodes, research is needed to 1) retain initial capacity (i.e. implementing voltage limits) and 2) understand the Li-binding mechanism (i.e. in situ spectroscopy) to prevent amorphization and drive the deintercalation potential to a more negative value. Other opportunities for electrochemical performance improvements in  $\text{MnV}_2\text{O}_x$  systems include increasing the rate capability and cycle life. Manganese vanadates have semi-conducting properties, and no attempts (to our knowledge) have been implemented to increase the electronic conductivity. One method to improve conductivity involves coating particles with carbon, which has been shown to decrease the charge/discharge overpotential in LTO electrodes. <sup>[44]</sup> Researchers have attempted to enhance the cycle life by decreasing grain size, however, no studies have reported data beyond 130 charge/discharge cycles. <sup>[41b]</sup> Compared to the aforementioned carbon anodes, manganese vanadate anodes are still in their infancy.

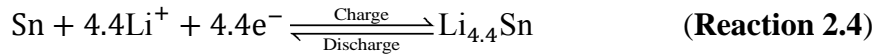
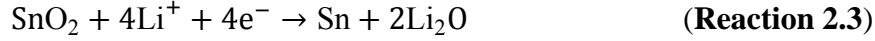
#### *2.1.4. Tin-based Anodes*

Tin attracts attention as anode material because it offers a larger charge capacity than graphite; full lithiation at room temperature inserts 4.25 Li atoms per Sn atom ( $\text{Li}_{17}\text{Sn}_4 = 959.5 \text{ mAh g}^{-1}$  or  $1991 \text{ mAh cm}^{-3}$ ). Despite the large capacity, Li-insertion in Sn particles occurs at

more positive potentials ( $\sim 0.5$  V vs Li/Li<sup>+</sup>) than graphite. While a more positive insertion potential decreases the energy density in Li-ion full cells, it mitigates the possibility of plating lithium, thus, creating a safer cell. The major limitation facing tin anodes is the short cycle life, which is a result of material cracking and pulverization. Volume expansions in Sn particles  $> 300\%$  accompany large capacities. Sn particles pulverize because they cannot withstand the large mechanical strains of volume expansions during charge cycles. The low melting point of Sn ( $273^\circ\text{C}$ ) is thought to facilitate crystallization and produce a brittle Li<sub>17</sub>Sn<sub>4</sub> complex.<sup>[45]</sup> Additional SEI forms on the surface of newly exposed Sn particles upon cracking, which leads to electronic isolation and ultimately cell-failure. Herein, we focus on two methods to increase cycle life of Sn anodes: using the oxide and forming carbon composites.

Anodes composed of SnO<sub>2</sub> typically experience larger capacity retentions than metallic Sn anodes. The electrochemical reduction of SnO<sub>2</sub> to Sn forms Li<sub>2</sub>O, as shown in **Reaction 2.3**. Formation of inert Li<sub>2</sub>O around Sn particles is thought to hinder Sn aggregation upon cracking<sup>[46]</sup> and to retain a small particle size. Small particles in electrodes are advantageous because they reduce strains on the particle and prolong cycle life. However, the reduction of SnO<sub>2</sub> to Sn is largely irreversible, resulting in the irreversible loss of 4 Li-ions per SnO<sub>2</sub> atom on the first cycle (irreversible capacity of **Reaction 2.3**  $\sim 500$  mAh g<sup>-1</sup>). Recent studies have shown that electrochemically reduced SnO<sub>2</sub> particles on the order of 1 nm may re-oxidize to form SnO<sub>x</sub>.<sup>[47]</sup> Unfortunately, the oxidation occurs  $> 1.25$  V vs. Li/Li<sup>+</sup>, which is a Li-extraction potential beyond the potential limits of cathodes in current Li-ion cells. Sole use of small SnO<sub>2</sub> particles seldom renders electrodes with long cycle lives; lithia regions surrounding

electrochemically reduced Sn(0) fail to buffer the volume expansions experienced during **Reaction 2.4**. Fuji introduced batteries with tin-composite oxide anodes under the name Stalion,<sup>[48]</sup> which never reached commercialization due to large capacity fade. Formation of nanoscale carbon-tin oxide composites has been the most successful approach to prolonging cycle life of tin and tin oxide anodes.



Carbon nanocomposites have long been a common method to enhance electrode cycle life<sup>[49]</sup> because they provide fast Li-diffusion and high-rate capabilities.<sup>[50]</sup> Carbon nanocomposites are durable materials, and thus composite materials (e.g. SnO<sub>2</sub> particles) may impart strains onto the carbon matrix during volume expansions to withstand pulverization; volume expansions in the LiC<sub>x</sub> complex are small (~10% graphene layer expansion) relative to the Li<sub>x</sub>Sn complex (~300% volume expansion).<sup>[18]</sup> While lithia-rich regions reduce Sn aggregation, anchoring or encapsulating SnO<sub>2</sub> to carbon has been demonstrated to further prevent tin aggregation and cell failure: binding SnO<sub>2</sub> to the surface of graphene sheets produced capacities > 1200 mAh g<sup>-1</sup> over 500 cycles using a symmetrical current of 500 mA g<sup>-1</sup>;<sup>[26b]</sup> encapsulating Sn in hollow spheres produced capacities of 500 mAh g<sup>-1</sup> over 100 cycles at symmetrical 0.2-C rates;<sup>[51]</sup> SnO<sub>2</sub> particles incorporated in carbon nanofibers produced ~500 mAh g<sup>-1</sup> after 40 cycles using a symmetrical current of 50 mA g<sup>-1</sup>.<sup>[52]</sup> While the aforementioned studies provide promise for commercial Sn-based anodes, improvements are still needed to maximize Sn capacity and capacity retention within a more negative voltage window.

### 2.1.5. Silicon Anodes

Silicon has the largest theoretical Li-alloying charge capacity of any material ( $\text{Li}_{4.4}\text{Si} = 4200 \text{ mAh g}^{-1}$ ). Maximum capacity at standard temperatures and pressures is obtained in the  $\text{Li}_{3.75}\text{Si}$  phase ( $\sim 3600 \text{ mAh g}^{-1}$ ). Lithiation reactions with Si occur at low potentials (slightly more positive than graphite), making Si the ideal energy-dense anode material. Silicon readily oxidizes in dry-air<sup>[53]</sup> (commercial cell-production atmosphere) to form a native-oxide surface layer that contains silanol and hydrogen-terminated moieties. While these moieties contribute to capacity loss on the first cycle,<sup>[54]</sup> they enhance capacity retention, as described in the following section. Despite the appeal of Si anodes, integration into commercial anodes has proved challenging; Si- and Sn-based anodes face similar issues retaining capacity. Si pulverizes as a result of  $> 300\%$  volume expansion, which causes recurrent SEI formation. Formation of the electronically resistive SEI results in electronic isolation of Si particles and premature cell failure. Thus, many researchers (in particular Cui's lab at Stanford,<sup>[55]</sup> and his start-up Amprius) have explored different nanoscale Si architectures such as nanowires,<sup>[56]</sup> nanoparticles,<sup>[57]</sup> and core-shell nanoparticles<sup>[58]</sup> to preserve structure during cycling and combat the destructive nature of Li-insertion.

The destructive nature of Li-insertion transforms crystalline Si (*c*-Si) to amorphous (*a*-Si) during charge. Either slow constant-current cycling below 50 mV vs Li/Li<sup>+</sup> or low potential constant-voltage cycling (standard practice in commercial LIB) may revert *a*-Si to the undesired crystalline state.<sup>[59]</sup> Converting *a*-Si back to *c*-Si is undesired because lithiation into *c*-Si increases stress on Si particles and decrease the cycle life of Si-based anodes.<sup>[60]</sup>

Crystalline Si lithiates anisotropically about the  $\langle 110 \rangle$  direction <sup>[61]</sup>, which induces more cracking than the isotropic lithiation of *a*-Si. <sup>[62]</sup> Thus, one common approach to increase Si-anode cycle life is to limit the cut-off voltage to potentials  $> 50$  mV vs Li/Li<sup>+</sup>. <sup>[59]</sup> While limiting the cut-off voltage decreases full cell energy density, it improves 1) cycle life by decreasing volume expansions, and 2) cell safety by reducing the chance of dendrite formation.

Blending silicon with carbon to form Si-nanocomposite also increases the performance of anodes by buffering volume expansions (similar to Sn/C composites) and increasing electrode conductivity. Silicon is a semi-conductor that lacks the necessary electron transport properties to operate at fast rates. Mixtures of amorphous carbons <sup>[63]</sup>, graphene, <sup>[64]</sup>, and carbon coatings <sup>[65]</sup> have been demonstrated to increase the capacity retention in Si-based electrodes and provide an electronically conductive network for rapid charge-discharge. Recently, Samsung SDI achieved energy densities 50% larger than current commercial cells via graphene growth on Si nanoparticles. <sup>[28]</sup> However, the electrodes attained  $\sim 60\%$  of Si theoretical capacity. Researchers strive to achieve the full  $3600 \text{ mAh g}^{-1}$  capacity of Si.

Research on electrolyte additives has been conducted in an attempt to retain the full capacity of Si electrodes. Incorporation of molecules such as fluoroethylene carbonate <sup>[66]</sup> (FEC) and vinylene carbonate <sup>[67]</sup> (VC), are proven to increase capacity and capacity retention in Si-based systems. In general, performance enhancements from electrolyte additives are attributed to their reduction products on the surface of Si, which create a thinner (or possibly less electronically resistive) SEI. <sup>[68]</sup> Researchers revealed that 1 wt% VC in ethylene carbonate:dimethyl carbonate reduced the amount of degraded LiPF<sub>6</sub> in the SEI and did not

increase impedance during the first five cycles in Si half-cells. <sup>[67b]</sup> Studies using FEC in Si half-cells revealed a larger presence of LiF compared to half-cells in the absence of FEC. <sup>[66a]</sup> A reduction in impedance accompanied LiF formation (LiF is a depolymerization and defluorination product of FEC). <sup>[66a]</sup> FEC is also thought to create an SEI that uniformly coats the surface of Si and minimizes decomposition of LiPF<sub>6</sub>. <sup>[69]</sup> While electrolyte additives boost performance, electronic isolation stymies Si-anodes after repeated cycling.

The final approach (discussed in this dissertation) that researchers use to enhance the cycle life of Si-based anodes is modification to the binding agent. The next section discusses binding agents, with an emphasis on binding agents for Si-based electrodes.

#### *2.1.6. Binding agents*

Electrodes consist of three components: active material, conductive additive, and binder. To fabricate commercial electrodes, the conductive additive and active material are mixed with binder solution and slurry-cast onto the current collector. Commercial slurry casting is a roll-to-roll process; to comply with commercial standards, binding agents must be dissolved in a solvent that yields a viscosity and stable dispersion conducive to homogenous film formation.

Binding agents have many roles in LIB electrodes, such as promoting ionic conductivity and preserving electrode microstructure. To begin, a good binding agent provides sufficient ionic conductivity for rapid charge transfer. Transport of Li-ions through the binder is the main mechanism of Li-transport from the electrolyte to the active material. The ionic transport of a binder is correlated with electrolyte uptake. Since the electrolyte contains

solvated Li-ions, increased electrolyte uptake in the binder enhances the amount of Li-ions that readily transport to and from active material. The binder should also preserve the pre-cycled microstructure of composite electrodes during cycling. If active particles dislodge from the electrode, fresh SEI forms on newly exposed active surface and the electrode suffers from electronic isolation. Similarly, if the binding agent does not adhere to the current collector, delamination occurs. Delamination produces SEI at the current collector-electrode interface and greatly increases ohmic resistance.

The binder should also sufficiently cover the electrode surface. Excess binder content ohmically limits cells (binders are typically electronic insulators). Insufficient binder content fails to protect the active material from SEI formation on the surface. Low coulombic efficiencies result from recurrent SEI formation, which decrease capacity retention. Insufficient binder content also produces a mechanically weak microstructure that cannot withstand restructuring during lithiation. Restructuring breaks electronic pathways in electrodes and increases cell resistance. Due to their critical importance in LIBs, novel binding agents that increase capacity and conductivity are a major research thrust. Interesting interfacial chemistry between binding agents and silicon have resulted in anodes with enhanced electrochemical performance.

Studies on Si anodes revealed that bonding (interactions and reactions) between the native surface oxide layer of Si and the binding agent greatly increase the cycle life of Si-based anodes. Researchers first observed that using carboxyl methylcellulose (CMC) as a binding agent in Si nanoparticle electrodes enhanced capacity retention <sup>[70]</sup> beyond that of the

conventional binding material polyvinylidene fluoride (PVDF). Performance enhancements were attributed to the polar carboxyl moieties of CMC, which undergo a condensation reaction<sup>[70]</sup> and hydrogen bond<sup>[54]</sup> with the native-surface oxide layer of Si. A self-healing effect (ability to reform bonds between Si and CMC that broke during Si volume expansion) was also observed upon cycling.<sup>[71]</sup> The strong interactions between Si and the binder keep inter-particle (Si-Si, Si-conductive additive) distances small and preserve electronic pathways. Prior to studies on CMC binders, polyvinylidene fluoride (PVDF) was the standard binder for carbon anodes. PVDF is more elastic and allows for more electrolyte uptake than CMC, yet Si/CMC electrodes display ample ionic conductivity. Polyvinylidene fluoride  $-(C_2H_2F_2)_n-$  is not used in Si-based systems because it does not bond with the surface of Si, and thus, makes a poor binder; Si/PVDF electrodes typically fail after 10 cycles.<sup>[72]</sup> CMC, and other biopolymers, are more environmentally benign than PVDF. CMC is water soluble, whereas PVDF uses harsh, toxic solvents for dissolution.

The enhanced electrochemical performance of Si/CMC electrodes fueled investigations of novel Si electrode binding agents, many with carboxyl functionalization. Binders such as alginate,<sup>[73]</sup> polyacrylic acid,<sup>[74]</sup> and a mixture of polyacrylic acid and CMC<sup>[72]</sup> all reported great cycling performances in Si-based anodes. However, like CMC, these materials failed to preserve the electrode microstructure over hundreds of cycles and required electrolyte additives such as FEC to achieve good cyclability.<sup>[75]</sup> Additionally, these materials required a large concentration of binder and conductive additive to achieve large capacities with appreciable capacity retention. Large concentrations of Li-inactive materials increase “dead

weight” and reduce the energy density in electrodes. Efforts to preserve Si electrode microstructure while minimizing binder content is still a major research thrust. Efforts to functionalize to binders, such as use of electrically conductive polymers, <sup>[57a, 76]</sup> have gained attention. Electronically conductive polymers are usually more rigid, which results in cracking (cracking then increases SEI formation and leads to low coulombic efficiencies). Rigid polymers also have reduced molecule mobility, which limits favorable interactions with other polymers, the Si surface, and the electrolyte. Researchers have also attempted to enhance Si-binder elasticity to better withstand volume expansions during lithiation. Researchers have crosslinked polymers to increase molecular weight, <sup>[77]</sup> utilize favorable properties from two polymers, <sup>[78]</sup> and enhance elastic-like properties <sup>[79]</sup> of binders. However, the fracture of Si in the electrodes still leads to short cycle lives. The next sections, and *Chapters 5-6* in this dissertations, focus on using galactomannans and galactomannan-derived materials as novel binding agents in Si nanoparticle electrodes.

## **2.2. Galactomannans**

Galactomannans are water soluble polysaccharides extracted from leguminous seeds. The name *galactomannan* is derived from their chemical composition: a galactose side-chain and mannose backbone. Four types of galactomannans exist in nature: fenugreek, guar, tara, and locust bean gums. Each type of galactomannan varies in galactose-to-mannose ratio, or degree of substitution; molecules of fenugreek, guar (GG), tara, and locust bean (LBG) gums have approximately 1:1, 1:2, 1:3, and 1:4 galactose:mannose ratios, respectively. Ratios may vary, depending on growing location and environmental conditions. <sup>[80]</sup> Substitution of the

galactose side-chain does not occur in repeating fashion; galactose side chains have been found in pairs, blocks, or randomly distributed throughout the backbone. <sup>[81]</sup> However, for convenience, galactomannans may be represented with repeating units, as in **Figure 2.4**, which shows two galactomannans that are investigated as novel binding agents for Si electrodes in *Chapter 5* (GG and LBG).

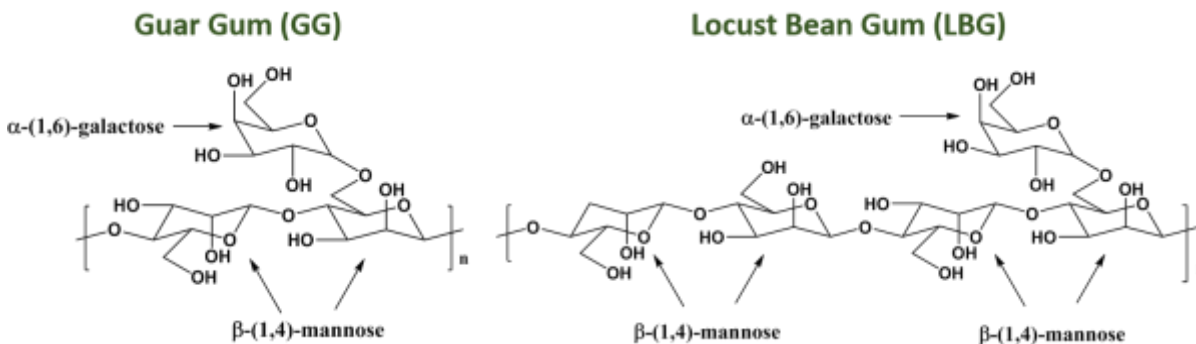


**Figure 2.4.** Simplified structures for two galactomannans, guar and locust bean gum.

The degree of substitution gives each galactomannan unique properties in solution, such as viscosity and microstructure strength, which are governed by biopolymer self-associations. <sup>[82]</sup> Galactomannans exhibit gel-like characteristics at concentrations < 1 wt % in water. The large viscosity is attributed, in part, to the large molecular weight (> 2,000,000 Da) of galactomannans found in nature. <sup>[83]</sup> Elastic properties originate from strong polymer-polymer interactions (H-bonding) between unsubstituted mannan-rich chains on the backbone. A larger degree of substitution produces weaker gels. Viscous-like properties originate from the galactose side-chains, which are more hydrophilic and sterically hinder inter-polymer interactions. Steric hindrance in the molecules promotes solvent-polymer interactions. Hence, a more substituted galactomannan has a higher solubility in water and lower viscosity. Galactomannans are currently used in the food industry as food stabilizers and thickening

agents, in natural gas industry as a proppant for fracking fluids, and in the paper industry to increase strength.<sup>[84]</sup> Herein, we focus on one type of galactomannan: guar gum.

### *2.2.1. Guar solution and gels*

Guar gum derives from the endosperm of guar seeds, which reside in pods. Purity of GG depends on methods used to separate the hull and germ. Typical processing conditions involve hydration and mechanical shearing to break the cell wall and separate the water-soluble GG. The hydrated sample is then dried and milled to a desired coarseness. It was found that guar contain 10-17 wt% debris,<sup>[80, 85]</sup> rendering the need for further purification to obtain high-quality GG samples. Many NMR studies have found the actual galactose-to-mannose ratio of GG to be ~1:1.7 and vary depending on growing conditions.

Industrial attraction associated with GG stems from its high viscosity (~20 Pa-s at 1 wt% in water for a 250 kDa sample), as a result of inter-polymer H-bonding and favorable associations with water. Despite the high viscosity, GG exhibits shear thinning at low strains due to disentanglements and disruptions in the H-bonding network,<sup>[86]</sup> which is ideal for processing highly viscous solutions. Degradations from heat,<sup>[87]</sup> acid hydrolysis,<sup>[88]</sup> and enzymatic depolymerization<sup>[89]</sup> reduce viscosity and stability in solution. To increase stability of GG solutions, biocides may be added to the solution or the solution may be crosslinked to form a hydrogel.

Hydrogels are crosslinked 3-D polymeric networks that comprise hydrophilic polymers. Guar hydrogels have been studied as potential drug carriers that exhibit sustained release profiles,<sup>[90]</sup> and as proppants for fracking fluids. Borate<sup>[91]</sup> and glutaraldehyde (GA)

<sup>[92]</sup> may be used to crosslink GG to form hydrogels. Borate ions attack *cis* hydroxyls to crosslink guar. The chemical crosslinking of GG and GA is assisted by the protonation of GA in acidic conditions, which also attack hydroxyl groups. However, the actual mechanism of GA-crosslinked guar is still unclear and research is needed to accurately tailor network strength. Dynamic rheological methods, which are detailed in the follow section, provide a powerful technique to study the formation and ensuing strength of hydrogels.

### 2.2.2. Oscillatory rheology and gel formation

Viscoelastic systems display both viscous and elastic-like behavior. A viscous material flows upon applied stress, whereas an elastic material strains upon applied stress but retains its original shape upon removal of stress. Contributions from viscous and elastic properties may be deconvoluted by using dynamic rheological experiments, or small amplitude oscillatory shear. This technique uses many of the same linear time-invariant principals as EIS (described in *Section 2.1.2.*). During an oscillatory strain experiment, a sinusoidal strain,  $\gamma$ , is applied with amplitude  $\gamma_o$  and angular frequency  $\omega$ , to a sample placed between two parallel plates. The resulting stress,  $\tau$ , and phase change,  $\delta$ , are measured by the rheometer, as shown in **Equations 2.5-6** below.

$$\gamma = \gamma_o \sin(\omega t) \quad \text{(Equation 2.5)}$$

$$\tau = \tau_o \sin(\omega t + \delta) \quad \text{(Equation 2.6)}$$

The measured stress wave is decomposed into two waves, in-phase ( $\delta = 0^\circ$ ) and out-of-phase ( $\delta = 90^\circ$ ) components. Trigonometric identities are used to obtain the following frequency dependent response: <sup>[93]</sup>

$$\tau(\omega) = \gamma_o [G' \sin(\omega t) + G'' \cos(\omega t)] \quad \text{(Equation 2.7)}$$

$$G' = \frac{\tau_o}{\gamma_o} \cos(\delta); G'' = \frac{\tau_o}{\gamma_o} \sin(\delta) \quad \text{(Equation 2.8, 9)}$$

where  $G'$  and  $G''$  represent the in-phase, elastic moduli and out-of-phase, viscous moduli, respectively. Analogous to EIS,  $G'$  and  $G''$  represent the real resistive and capacitive components, respectively.

The moduli measured in dynamic rheological experiments are crucial for studying the microstructure of a system. This dissertation uses two dynamic rheological tests to study and assess sample microstructure: strain sweeps and frequency sweeps. The former applies a gradually increasing oscillatory strain to the sample and measures the resulting stress while applying a constant frequency. Strain sweeps allow the user to measure gel strength or determine strains necessary to breakdown gel microstructure. The region where moduli are independent of strain (no microstructure breakdown) is called the linear viscoelastic (LVE) regime. The strain at which microstructure begins to breakdown is called the critical strain.

Frequency sweeps (the second dynamic rheology experiment discussed in this dissertation) may be performed upon determination of the LVE regime. In these experiments,  $\omega$  is varied and strain is kept constant and within the LVE such that sample microstructure remains intact. Frequency sweeps provide information on dynamic colloidal forces present in viscoelastic systems, such as particle-polymer interactions or structural changes. One such structural change is gelation. During gelation, a fluid converts into a solid via crosslinking. The rate at which gelation occurs, or the kinetics of a system, may be inferred by running frequency sweeps at various reaction times. Typically, the sample starts in a liquid-like state, with moduli dependent on frequency and  $G'' > G'$ . As the reaction progresses and networks continue to

form,  $G'$  in sample increases. Gelation occurs when the moduli are equal. <sup>[94]</sup> Physically, the crosslinked networks of the sample spans the gap of the rheometer plates (height of the sample). After the crossover (when  $G' > G''$ ), crosslinks may continue to form in the sample and increase network density. A fully crosslinked sample displays gel-like response, where the moduli are frequency independent,  $G'' \ll G'$ , and the elastic modulus plateaus. Idealized plots of frequency sweep are picture below (**Figure 2.5**).

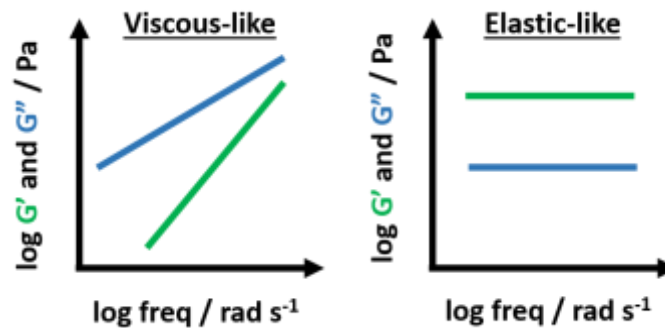


**Figure 2.5.** Two extreme situations in gelation: frequency dependence of a viscous-like fluid (left) is observed prior to gelation ( $G'' > G'$ ), and frequency independence of a fully crosslinked gel (right) where  $G'' < G'$ .

### 2.3. Electrospinning

Electrospinning is a fiber synthesis technology dating back to the early 1900s, when J.F. Cooley <sup>[95]</sup> and W.J. Morton <sup>[96]</sup> described formation of polymer fibers by exceeding surface tension with charge. The method remained dormant until its revival nearly a century later in the 1990s by the Reneker group. <sup>[97]</sup> Electrospinning produces 1-D polymer fibers, or composite fibers, with diameters on the order of 0.1 to 1- $\mu\text{m}$ . The process is continuous and ideal for scalability, with applications ranging from medicine to electronics to catalysis. Electrospinning is a complex process; many process variables (including humidity, electric field strength, tip-to-collector distance, feed rate) and polymer parameters (including

molecular weight, solvent, concentration, surface tension, viscosity, and conductivity) effect fiber quality. <sup>[98]</sup> Herein, we highlight the electrospinning process and examine the influence of process/material parameters on fiber morphology. We also introduce steady shear rheological methods as a means to relate solutions properties to fiber morphology. Attention is given to electrospun polyacrylonitrile fibers and their composites as carbon precursor material for LIB anodes.

### *2.3.1. The Process*

Electrospinning converts polymer solutions into nanofiber mats. **Figure 2.6** shows a schematic of a typical horizontal electrospinning setup, which contains 3 main components: a power supply, ground collector plate, and solution. The first step in the electrospinning process is to prepare the electrospinning precursor solution. Studies have shown that concentration of linear polymers in solution should be 2.5 times greater than the entanglement concentration <sup>[99]</sup> to obtain uniform fibers. Not all polymers can be electrospun; an electric field must induce a dipole in the polymer. Upon applying an electric field, the polymer exhibits both electrostatic surface charge repulsions and Coulombic forces from the electrical field, forming a Taylor cone. When the electric field reaches a critical point—where the electric field forces overcome the forces due to surface tension—a jet of charged polymer liquid extrudes and travels towards the ground collector plate.

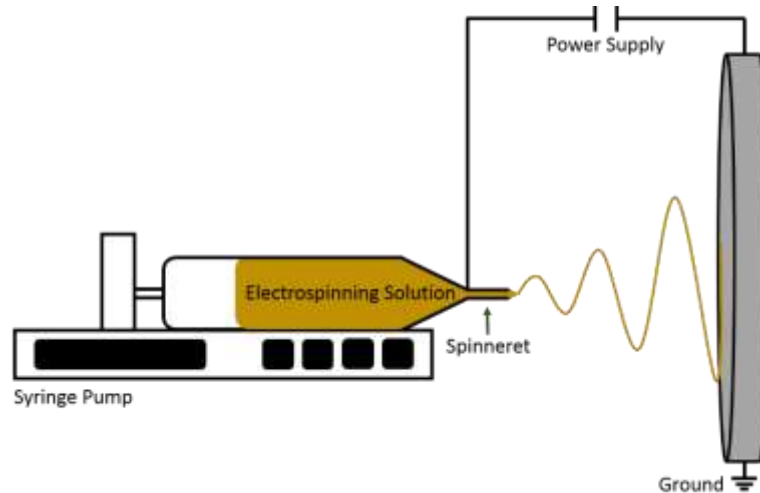


**Figure 2.6.** Schematic of horizontal electrospinning setup.

During post-extrusion flight, the polymer solution bends and whips due to charge instabilities. <sup>[100]</sup> To explain the bending, the system is modeled as a group of point charges operating under Coulomb's law. The observed instabilities are explained by Earnshaw's theorem, which states that electrostatic forces alone cannot equilibrate a static system. A perturbation in Coulombic forces causes a point charge to deviate perpendicular to its linear trajectory, thus bending and whipping the polymer. The polymer stretches as the charged jet is whipped towards the collector, increasing fiber surface area. Due to the increase in surface area, surface tension forces counteract the bending instabilities and regulate the system. <sup>[100]</sup> Bending instabilities cause solvent to evaporate and reduce fiber diameter. The polymer accumulates on a collector, forming a fiber mat. The type of collector plate dictates nanofiber orientation. For example, parallel dielectric plates <sup>[101]</sup> and mandrels <sup>[102]</sup> may be used to create aligned fibers, flat plates create nonwoven mats, and combination of a plate and mandrel may create yarns. <sup>[103]</sup>

### 2.3.2. *Electrospinning parameters*

To obtain uniform nanofibers, the influence of many process and solution parameters must be manipulated and assessed. A review of electrospinning literature on similar polymers may ease electrospinning novel polymers or polymer-composites. However, fine-tuning new systems is difficult since many parameters compete.<sup>[104]</sup> The purpose of this section is to give the reader an idea of the complexities of the electrospinning process and provide insight on select parameters that govern the process.

*Surface Tension* – The surface tension of a polymer solutions is generally thought as the main contributor to uniform fibers. Surface tension counters electrostatic charge repulsions to regulate whipping instabilities.<sup>[105]</sup> If the surface tension is too large, the polymer jet becomes instable and forms droplets (smallest surface area to volume ratio). Reducing the surface tension, by changing solvent, polymer concentration, or adding surfactants, may convert droplets to beaded fibers. Beads are unwanted in fibers because they lead to non-uniform regions of activity or performance for the desired fiber application.

*Viscosity* – The viscosity of the electrospinning solution may be correlated with fiber size and morphology. Increasing viscosity (i.e. polymer concentration or molecular weight) resists elongational forces during bending/whipping instabilities, which produces larger fibers. Fibers produced from high-viscosity fluids typically have a more uniform size distribution than the same lower-viscosity polymer solution.<sup>[104]</sup> Likewise, lower viscosity polymers lead to smaller fibers and possible beading. Thus, surface tension governs low-viscosity solutions.

More detail on the influence of viscosity on fiber morphology is presented in the following section (*Section 2.2.3*).

*Charge Density* – Electric fields may induce dipoles in polymer molecular structures, which migrate surface charges to the polymer-air interface. This increases surface charge density and whipping instabilities to create smaller fibers than a solution with lower surface charge density. Introducing salts to the electrospinning solutions similarly increases net surface charge, decreases fiber diameter, and enables smaller fiber formation at larger polymer concentrations. Conductivities below a certain polymer-specific value limit whipping instabilities, which results in beaded fibers or polymer droplets.

*Humidity* – Depending on the polymer system, humidity may have a large influence on fiber morphology. Thus, it is important to electrospin within a specific humidity range. It has been reported that low-moisture content reduces whipping instabilities in the polymer jet.<sup>[106]</sup> Water may be absorbed in the polymers at high-relative humidity, which may induce morphological changes such as pores within the fiber.<sup>[107]</sup> Humidity also alters the evaporation rate of solvent during electrospinning, inducing polymer-specific effects to nanofibers.<sup>[108]</sup>

*Electric Field* – The effect of electric field on fiber size and morphology is thought to be polymer specific,<sup>[104]</sup> and also depend on parameters such as solution conductivity, viscosity, and tip-to-collector distance. Electrospinning saline polymer solutions or conductive polymers reduce the amount of voltage required to produce uniform fibers. Researchers have reported that increasing electric field strength increased polymer flowrate and produced larger fibers.<sup>[109]</sup> Others have reported that higher voltages increase elongational forces and produce

smaller fibers or promote bead formation.<sup>[110]</sup> Beaded fibers tend to form if applied voltage is too large,<sup>[111]</sup> possibly because forces from surface tension cannot overcome forces from the electric field.

### 2.3.3. *Steady-shear rheology and fiber morphology*

We previously introduced dynamic rheology (*Section 2.2.2*), where an oscillating shear is applied to a sample and moduli are determined to assess the viscoelasticity of a material. Moduli may be used to study microstructure of a system, as experiments leave them intact. Steady-shear rheology is another type of rheological assessment that is performed on fluids under flow conditions. Large strains are imposed on the sample during steady-shear experiments, which disrupt sample microstructure (the microstructure may rebuild, and the time it takes to rebuild is associated with relaxation time). One common flow experiment is the strain sweep. In a typical strain sweep, a sample is placed between two plates. A monotonically increasing amount of strain (deformation) is applied to a sample to induce flow, and the corresponding stress (torque) is measured. Through an extension of Newton's Law of Viscosity, the apparent viscosity of the sample is determined, where apparent viscosity is a function of strain.

Polymers under flow conditions may exhibit different behavior that influence electrospinnability. The most elementary type of flow is Newtonian, where apparent viscosity is independent of strain. Many polymer systems, such as polyacrylonitrile, exhibit such flow at low strains. However, deviations from Newtonian behavior is quite common, notably in filled and colloidal systems. For example, a certain stress is needed to induce flow in fluids

such as ketchup and blood. This critical stress needed to induce flow is known as the yield stress. Yielding behavior is common in filled polymer systems due to colloidal interactions that form networks within the electrospinning precursor solution. <sup>[112]</sup> The bending and whipping instabilities of electrospinning yield high shears ( $> 10^2$  Pa), which is more than enough to induce flow in most filled polymer systems. However, the shears may not be large enough to break down all particle aggregates, causing regions of disproportionate stress in the extruding polymer jet, and producing a mat with non-uniform fibers. Capillary instabilities, as a result of particle aggregates, may also produce beaded fibers. <sup>[100]</sup> For example, Wu and researches discovered that beaded fibers formed in carbon nanotube-filled systems when the carbon nanotubes were not uniformly dispersed. <sup>[113]</sup> Shear thinning, or a decrease in viscosity at high shears, is another deviation from Newtonian behavior that is common in entangled polymer systems. Viscosity is reduced because polymer chains become oriented at high shears. Since whipping instabilities produce high shears, electrospinning systems that exhibits shear thinning behavior may induce changes to polymer structure and packing.

#### *2.3.4. Polymer and carbon fibers via polyacrylonitrile*

Polyacrylonitrile (PAN), is a polymer consisting of acrylonitrile monomers. The polymer is soluble in polar solvents such as dimethylformamide (DMF) in concentrations as high as 25 wt%. <sup>[114]</sup> Concentrations of PAN  $> 6$  wt% may be electrospun to produce fibers. <sup>[115]</sup> The dipole created on the nitrile moieties make PAN an ideal candidate for electrospinning. And thus, much work has been conducted on the electrospinning PAN for applications such as tissue engineering <sup>[116]</sup> and membrane. <sup>[117]</sup> However, most of the attention of PAN lies in the

carbon fibers that are produced upon thermal treatments. PAN is a thermoplastic that degrades prior to melting. The degradation products are of great importance, as they give rise to a carbon-rich material. The quality of the ensuing carbon depends on the decomposition products of the polymer. The highly polar nitrile moieties of PAN create coulomb interactions that repel other chains and prevent ordered packing. A coexistence<sup>[118]</sup> of ordered and amorphous phases exist in PAN fibers. PAN may be co-polymerized with acrylic acid or methacrylate monomers to obtain a more ordered carbon structure. Regardless of polymer composition, a two-step heat treatment is needed to convert PAN to carbon.

The first heat-treatment, stabilization, essentially crosslinks the polymer. Stabilization (**Figure 2.7**) is conducted between 250-300°C in air. Here, PAN undergoes cyclization and dehydrogenation to create a pyridine-like material with a “ladder” structure.<sup>[119]</sup> The reaction releases gasses such as HCN, and H<sub>2</sub> as byproducts. The oxidative conditions of the process introduce oxygen moieties into the structure.

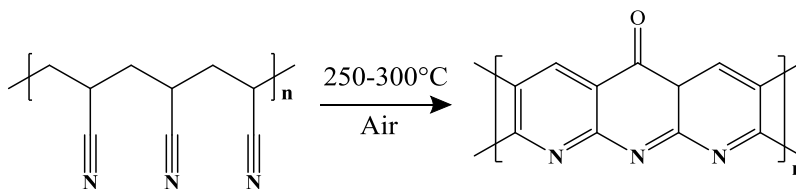


**Figure 2.7.** Idealization of the stabilization heat-treatment reaction, which essentially crosslinks PAN

The second heat-treatment process, carbonization, releases noncarbonaceous species to produce a carbon-rich material. Carbon composition > 95 wt% may be achieved. Carbonization occurs in an inert atmosphere (typically N<sub>2</sub> or Ar) above 600°C. PAN is a non-graphitizable carbon precursor,<sup>[120]</sup> and the ensuing molecular structure and composition is dependent on the heat-treatment temperature. Using Raman spectroscopy, researchers have

observed that crystalline size and  $sp^3$  carbon ordering in carbon nanofibers increase with heat treatment temperature. <sup>[121]</sup> Larger crystallites that form at high temperatures increase elastic modulus in the fibers. For example, increasing the carbonization temperature increased from 800 to 1700°C increased the elastic modulus from ~ 75 to 200 GPa. <sup>[122]</sup> PAN-derived CNFs may also exhibit near-superconducting electronic properties <sup>[123]</sup> and have been used for electrochemical energy storage techniques such as Li-ion batteries <sup>[50]</sup> and supercapacitors. <sup>[124]</sup> Recent computational studies conducted by Saha et al. <sup>[125]</sup> provided insight on likely elimination reactions that occur during thermal degradation of PAN. The researchers concluded that temperature-dependent reactions occur during the thermal degradation of stabilized PAN (**Figure 2.8**). <sup>[125]</sup> Because gases are released on a temperature-dependent basis, an understanding of environmental condition during carbonization is vital for in situ reduction of species (such as metal oxides) in composite fibers

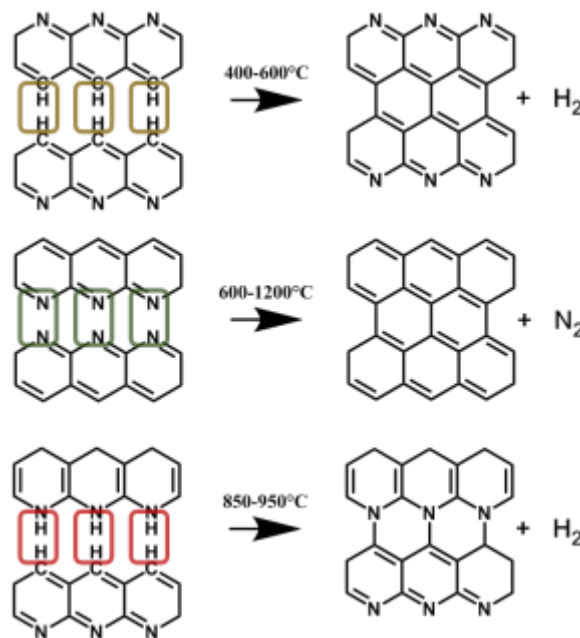


**Figure 2.8.** Three potential reactions that occur during carbonization of stabilized-PAN. <sup>[125]</sup>

### 2.3.5. Composite carbon nanofibers

The electrospinning process provides an easy method to produce carbon composite materials. Electrospinning blends (polymers) and fillers (particles) is one means of producing composite fibers. For example, electrospun PAN/tetraethyl orthosilicate blends yield composite carbon-silica fibers.<sup>[126]</sup> Likewise, adding fillers to PAN induces functionalization on CNFs: carbon nanotubes enhance the mechanical strength and electronic conductivity in CNF;<sup>[127]</sup> graphene-containing CNFs enhance the performance of super-capacitors beyond CNFs,<sup>[128]</sup> and also provide high-performance capacitive deionization materials for desalination.<sup>[129]</sup> Additionally, many composite CNFs have been used for Li-ion battery applications, as they increase Li-ion activity and provide a mechanically durable scaffolding for materials such as Si<sup>[130]</sup> and Sn.<sup>[52]</sup> While they have been applied to the cathode for high-conductivity and lightweight applications,<sup>[131]</sup> composite CNFs are more commonly assessed as a possible high-capacity scaffoldings for composite Li-ion anodes.

Carbon nanofibers (without fillers) display specific charge capacities in Li-ion half-cells similar to graphite electrodes; CNFs carbonized at 1000°C<sup>[50]</sup> displayed capacity ~350 mAh g<sup>-1</sup> using currents of 100 mA g<sup>-1</sup>. The nonwoven architecture and carbon-rich structure do not require binder and conductive additive, which reduces the amount of Li-inactive material in a cell and increases energy density. Researchers were able to enhance the capacity and electronic conductivity<sup>[132]</sup> of CNFs by increasing nitrogen content (N-doping). Blending polypyrrole with polyacrylonitrile enhanced the capacity of carbon nanofibers to ~450 mAh g<sup>-1</sup> at 100 mA g<sup>-1</sup>.<sup>[133]</sup> Despite the high-charge capacity of CNF anodes, a large voltage

hysteresis, high Li-extraction potential, and large irreversible capacity mar their viability in commercial cells. Thus, CNFs are commonly used as scaffolding for high-capacity materials to reduce the intercalation potential and buffer volume expansions. For example, Yan et al.<sup>[134]</sup> showed that electrospinning SnO<sub>2</sub>-precursor salts in a PAN solution, followed by carbonization at 700°C, creates stable and durable electrodes; the SnO<sub>2</sub>/CNFs exhibited capacities of ~550 mAh g<sup>-1</sup> at 200 mA g<sup>-1</sup> over 1,000 cycles. Similar performance enhancements were observed with the addition of SiNPs to CNF systems. Capacities ~800 mAh g<sup>-1</sup> after 100 cycles at 100 mA g<sup>-1</sup> have been observed in Si-containing CNFs.<sup>[135]</sup> However, Si/CNF composites exhibit poor capacity retention due to aggregation of SiNPs in the electrospinning solution and, thus, in the polymer-derived CNFs. Regions with aggregated SiNPs in fibers fracture during Li-insertion due to large volume expansions (as described in *Section 2.1.4*). Methods to increase capacity retention by manipulating the fiber microstructure of composite electrodes remain a worthy research thrust.<sup>[136]</sup>

## 2.4 References

- (1) C.-X. Zu, H. Li. *Energy & Environmental Science*, **4**, 2011, 2614-2624.
- (2) P. K.-S. Goodenough J. B. *Journal of the American Chemical Society*, **4**, 2013, 1167-1176.
- (3) R. Van Noorden. *Nature*, **507**, 2014, 26-28.
- (4) P. Rozier, J. M. Tarascon. *Journal of the Electrochemical Society*, **162**, 2015, A2490-A2499.
- (5) K. Xu. *Chemical reviews*, **114**, 2014, 11503-11618.
- (6) S. B. Peterson, J. Apt, J. Whitacre. *Journal of Power Sources*, **195**, 2010, 2385-2392.

- (7) S. J. Harris, A. Timmons, D. R. Baker, C. Monroe. *Chemical Physics Letters*, **485**, 2010, 265-274.
- (8) E. Peled. *Journal of the Electrochemical Society*, **126**, 1979, 2047-2051.
- (9) S. Zhang, M. S. Ding, K. Xu, J. Allen, T. R. Jow. *Electrochemical and Solid-State Letters*, **4**, 2001, A206-A208.
- (10) A. J. Loebl, C. J. Oldham, C. K. Devine, B. Gong, S. E. Atanasov, G. N. Parsons, P. S. Fedkiw. *Journal of the Electrochemical Society*, **160**, 2013, A1971-A1978.
- (11) M. B. Pinson, M. Z. Bazant. *Journal of the Electrochemical Society*, **160**, 2013, A243-A250.
- (12) S. Zhang, K. Xu, T. Jow. *Electrochimica Acta*, **51**, 2006, 1636-1640.
- (13) D. Aurbach. *Journal of Power Sources*, **89**, 2000, 206-218.
- (14) A. Lasia, *Electrochemical impedance spectroscopy and its applications*, Springer, **2014**, p.
- (15) T. Abe, H. Fukuda, Y. Iriyama, Z. Ogumi. *Journal of the Electrochemical Society*, **151**, 2004, A1120-A1123.
- (16) M. Park, X. Zhang, M. Chung, G. B. Less, A. M. Sastry. *Journal of Power Sources*, **195**, 2010, 7904-7929.
- (17) R. Yazami, P. Touzain. *Journal of Power Sources*, **9**, 1983, 365-371.
- (18) M. Winter, J. O. Besenhard, M. E. Spahr, P. Novak. *Advanced Materials*, **10**, 1998, 725-763.
- (19) P. R. Wallace. *Physical Review*, **71**, 1947, 622.
- (20) J. Baringhaus, M. Ruan, F. Edler, A. Tejada, M. Sicot, A. T. Ibrahimi, Z. Jiang, E. Conrad, C. Berger, C. Tegenkamp. *arXiv preprint arXiv:1301.5354*, 2013.
- (21) Y. Xu, Y. Wang, J. Liang, Y. Huang, Y. Ma, X. Wan, Y. Chen. *Nano Research*, **2**, 2009, 343-348.
- (22) E. Yoo, J. Kim, E. Hosono, H.-s. Zhou, T. Kudo, I. Honma. *Nano letters*, **8**, 2008, 2277-2282.
- (23) G. Wang, B. Wang, X. Wang, J. Park, S. Dou, H. Ahn, K. Kim. *Journal of Materials Chemistry*, **19**, 2009, 8378-8384.

- (24) S. Stankovich, D. A. Dikin, R. D. Piner, K. A. Kohlhaas, A. Kleinhammes, Y. Jia, Y. Wu, S. T. Nguyen, R. S. Ruoff. *Carbon*, **45**, 2007, 1558-1565.
- (25) P. Lian, X. Zhu, S. Liang, Z. Li, W. Yang, H. Wang. *Electrochimica Acta*, **55**, 2010, 3909-3914.
- (26) a) Z.-S. Wu, W. Ren, L. Xu, F. Li, H.-M. Cheng. *ACS nano*, **5**, 2011, 5463-5471; b) X. Zhou, L. J. Wan, Y. G. Guo. *Advanced Materials*, **25**, 2013, 2152-2157.
- (27) E. S. Polsen, D. Q. McNerny, B. Viswanath, S. W. Pattinson, A. J. Hart. *Scientific reports*, **5**, 2015.
- (28) I. H. Son, J. H. Park, S. Kwon, S. Park, M. H. Rummeli, A. Bachmatiuk, H. J. Song, J. Ku, J. W. Choi, J.-m. Choi. *Nature communications*, **6**, 2015.
- (29) J. K. Lee, K. W. An, J. B. Ju, B. W. Cho, W. I. Cho, D. Park, K. S. Yun. *Carbon*, **39**, 2001, 1299-1305.
- (30) a) B. Campbell, R. Ionescu, Z. Favors, C. S. Ozkan, M. Ozkan. *Scientific reports*, **5**, 2015; b) K. Tang, R. J. White, X. Mu, M. M. Titirici, P. A. van Aken, J. Maier. *ChemSusChem*, **5**, 2012, 400-403.
- (31) C. Li, X. Yin, L. Chen, Q. Li, T. Wang. *The Journal of Physical Chemistry C*, **113**, 2009, 13438-13442.
- (32) a) K. Tokumitsu, A. Mabuchi, H. Fujimoto, T. Kasuh. *Journal of the Electrochemical Society*, **143**, 1996, 2235-2239; b) C. H. Kim, D.-K. Lee, T. J. Pinnavaia. *Langmuir*, **20**, 2004, 5157-5159.
- (33) K. Sato, M. Noguchi, A. Demachi, N. Oki, M. Endo. *Science*, **264**, 1994, 556-557.
- (34) T. Ohzuku, Y. Iwakoshi, K. Sawai. *Journal of the Electrochemical Society*, **140**, 1993, 2490-2498.
- (35) T. Morishita, K. Nomura, T. Inamasu, M. Inagaki. *Solid State Ionics*, **176**, 2005, 2235-2241.
- (36) S. Zhang, R. Hu, L. Liu, D. Wang. *Materials Letters*, **124**, 2014, 57-60.
- (37) F. Zhang, M. S. Whittingham. *Electrochemistry Communications*, **2**, 2000, 69-71.
- (38) A. Doble, K. Ngala, S. Yang, P. Y. Zavalij, M. S. Whittingham. *Chemistry of Materials*, **13**, 2001, 4382-4386.

- (39) Y. Liu, X. Zhao, F. Li, D. Xia. *Electrochimica Acta*, **56**, 2011, 6448-6452.
- (40) F. Leroux, Y. Piffard, G. Ouvrard, J.-L. Mansot, D. Guyomard. *Chemistry of Materials*, **11**, 1999, 2948-2959.
- (41) a) Y. S. Mario Simoes, Songhak Yoon, Corsin Battaglia, Simone Pokrant, Anke Weidenkaff. *Journal of Power Sources*, **291**, 2015, 66-74; b) Y. Piffard, F. Leroux, D. Guyomard, J.-L. Mansot, M. Tournoux. *Journal of Power Sources*, **68**, 1997, 698-703.
- (42) N. Yabuuchi, T. Ohzuku. *Journal of Power Sources*, **119**, 2003, 171-174.
- (43) L. Jaber-Ansari, K. P. Puntambekar, S. Kim, M. Aykol, L. Luo, J. Wu, B. D. Myers, H. Iddir, J. T. Russell, S. J. Saldaña. *Advanced Energy Materials*, **5**, 2015.
- (44) E. Kang, Y. S. Jung, G. H. Kim, J. Chun, U. Wiesner, A. C. Dillon, J. K. Kim, J. Lee. *Advanced Functional Materials*, **21**, 2011, 4349-4357.
- (45) N. Nitta, G. Yushin. *Particle & Particle Systems Characterization*, **31**, 2014, 317-336.
- (46) I. A. Courtney, J. Dahn. *Journal of the Electrochemical Society*, **144**, 1997, 2045-2052.
- (47) Z. Chen, M. Zhou, Y. Cao, X. Ai, H. Yang, J. Liu. *Advanced Energy Materials*, **2**, 2012, 95-102.
- (48) Y. Idota, T. Kubota, A. Matsufuji, Y. Maekawa, T. Miyasaka. *Science*, **276**, 1997, 1395-1397.
- (49) V. Etacheri, R. Marom, R. Elazari, G. Salitra, D. Aurbach. *Energy & Environmental Science*, **4**, 2011, 3243-3262.
- (50) C. Kim, K. S. Yang, M. Kojima, K. Yoshida, Y. J. Kim, Y. A. Kim, M. Endo. *Advanced Functional Materials*, **16**, 2006, 2393-2397.
- (51) W. M. Zhang, J. S. Hu, Y. G. Guo, S. F. Zheng, L. S. Zhong, W. G. Song, L. J. Wan. *Advanced Materials*, **20**, 2008, 1160-1165.
- (52) C. Bonino, L. Ji, Z. Lin, O. Toprakci, X. Zhang, S. A. Khan. *ACS Applied Materials & Interfaces*, **3**, 2011, 2534-2542.
- (53) M. Morita, T. Ohmi, E. Hasegawa, M. Kawakami, M. Ohwada. *Journal of Applied Physics*, **68**, 1990, 1272-1281.

- (54) S. Xun, X. Song, L. Wang, M. Grass, Z. Liu, V. Battaglia, G. Liu. *Journal of the Electrochemical Society*, **158**, 2011, A1260-A1266.
- (55) H. Wu, Y. Cui. *Nano Today*, **7**, 2012, 414-429.
- (56) a) C. K. Chan, H. Peng, G. Liu, K. McIlwrath, X. F. Zhang, R. A. Huggins, Y. Cui. *Nature nanotechnology*, **3**, 2008, 31-35; b) K. Peng, J. Jie, W. Zhang, S.-T. Lee. *Applied Physics Letters*, **93**, 2008, 033105.
- (57) a) H. Wu, G. Yu, L. Pan, N. Liu, M. T. McDowell, Z. Bao, Y. Cui. *Nature communications*, **4**, 2013; b) X. H. Liu, L. Zhong, S. Huang, S. X. Mao, T. Zhu, J. Y. Huang. *ACS nano*, **6**, 2012, 1522-1531.
- (58) Y. Yao, M. T. McDowell, I. Ryu, H. Wu, N. Liu, L. Hu, W. D. Nix, Y. Cui. *Nano letters*, **11**, 2011, 2949-2954.
- (59) M. Obrovac, L. Krause. *Journal of the Electrochemical Society*, **154**, 2007, A103-A108.
- (60) M. Obrovac, L. Christensen. *Electrochemical and Solid-State Letters*, **7**, 2004, A93-A96.
- (61) S. W. Lee, M. T. McDowell, J. W. Choi, Y. Cui. *Nano letters*, **11**, 2011, 3034-3039.
- (62) V. Baranchugov, E. Markevich, E. Pollak, G. Salitra, D. Aurbach. *Electrochemistry Communications*, **9**, 2007, 796-800.
- (63) H. Li, X. Huang, L. Chen, Z. Wu, Y. Liang. *Electrochemical and Solid-State Letters*, **2**, 1999, 547-549.
- (64) J. K. Lee, K. B. Smith, C. M. Hayner, H. H. Kung. *Chemical communications*, **46**, 2010, 2025-2027.
- (65) H. Kim, J. Cho. *Nano letters*, **8**, 2008, 3688-3691.
- (66) a) V. Etacheri, O. Haik, Y. Goffer, G. A. Roberts, I. C. Stefan, R. Fasching, D. Aurbach. *Langmuir*, **28**, 2011, 965-976; b) Y.-M. Lin, K. C. Klavetter, P. R. Abel, N. C. Davy, J. L. Snider, A. Heller, C. B. Mullins. *Chemical communications*, **48**, 2012, 7268-7270.
- (67) a) L. Chen, K. Wang, X. Xie, J. Xie. *Electrochemical and Solid-State Letters*, **9**, 2006, A512-A515; b) L. Chen, K. Wang, X. Xie, J. Xie. *Journal of Power Sources*, **174**, 2007, 538-543.

- (68) H. Nakai, T. Kubota, A. Kita, A. Kawashima. *Journal of the Electrochemical Society*, **158**, 2011, A798-A801.
- (69) C. Xu, F. Lindgren, B. Philippe, M. Gorgoi, F. Björefors, K. Edström, T. r. Gustafsson. *Chemistry of Materials*, **27**, 2015, 2591-2599.
- (70) N. Hochgatterer, M. Schweiger, S. Koller, P. Raimann, T. Wöhrle, C. Wurm, M. Winter. *Electrochemical and Solid-State Letters*, **11**, 2008, A76-A80.
- (71) J.-S. Bridel, T. Azais, M. Morcrette, J.-M. Tarascon, D. Larcher. *Chemistry of Materials*, **22**, 2009, 1229-1241.
- (72) B. Koo, H. Kim, Y. Cho, K. T. Lee, N. S. Choi, J. Cho. *Angewandte Chemie International Edition*, **51**, 2012, 8762-8767.
- (73) I. Kovalenko, B. Zdyrko, A. Magasinski, B. Hertzberg, Z. Milicev, R. Burtovyy, I. Luzinov, G. Yushin. *Science*, **334**, 2011, 75-79.
- (74) A. Magasinski, B. Zdyrko, I. Kovalenko, B. Hertzberg, R. Burtovyy, C. F. Huebner, T. F. Fuller, I. Luzinov, G. Yushin. *ACS Applied Materials & Interfaces*, **2**, 2010, 3004-3010.
- (75) M. H. Ryou, J. Kim, I. Lee, S. Kim, Y. K. Jeong, S. Hong, J. H. Ryu, T. S. Kim, J. K. Park, H. Lee. *Advanced Materials*, **25**, 2013, 1571-1576.
- (76) a) M. Wu, X. Xiao, N. Vukmirovic, S. Xun, P. K. Das, X. Song, P. Olalde-Velasco, D. Wang, A. Z. Weber, L.-W. Wang. *Journal of the American Chemical Society*, **135**, 2013, 12048-12056; b) G. Liu, S. Xun, N. Vukmirovic, X. Song, P. Olalde-Velasco, H. Zheng, V. S. Battaglia, L. Wang, W. Yang. *Advanced Materials*, **23**, 2011, 4679-4683.
- (77) J. Lopez, Z. Chen, C. Wang, S. C. Andrews, Y. Cui, Z. Bao. *ACS Applied Materials & Interfaces*, 2015.
- (78) J. Song, M. Zhou, R. Yi, T. Xu, M. L. Gordin, D. Tang, Z. Yu, M. Regula, D. Wang. *Advanced Functional Materials*, **24**, 2014, 5904-5910.
- (79) N. Yuca, H. Zhao, X. Song, M. F. Dogdu, W. Yuan, Y. Fu, V. S. Battaglia, X. Xiao, G. Liu. *ACS Applied Materials & Interfaces*, **6**, 2014, 17111-17118.
- (80) Y. Cheng, K. M. Brown, R. K. Prud'homme. *Biomacromolecules*, **3**, 2002, 456-461.
- (81) Y. Wu, W. Li, W. Cui, N. Eskin, H. Goff. *Food Hydrocolloids*, **26**, 2012, 359-364.

- (82) a) I. C. Dea, E. R. Morris, D. A. Rees, E. J. Welsh, H. A. Barnes, J. Price. *Carbohydrate Research*, **57**, 1977, 249-272; b) M. A. Cerqueira, B. W. Souza, J. Simões, J. A. Teixeira, M. R. M. Domingues, M. A. Coimbra, A. A. Vicente. *Carbohydrate Polymers*, **83**, 2011, 179-185.
- (83) R. Brady, H. Cheng, A. Haandrikman, A. Moore, P.-K. Kuo, W. McNabola, C. Wheeler, Z.-F. Xu, R. Riehle, T. Nguyen in *Reduced molecular weight galactomannans oxidized by galactose oxidase*, Vol. Google Patents, **2001**.
- (84) R. Whistler, *Industrial gums: polysaccharides and their derivatives*, Elsevier, **2012**,
- (85) J. Chatterji, J. Borchardt. *Journal of Petroleum Technology*, **33**, 1981, 2,042-042,056.
- (86) W. W. Graessley, *The entanglement concept in polymer rheology*, Springer, **1974**, p.
- (87) M. Chaisawang, M. Suphantharika. *Carbohydrate Polymers*, **61**, 2005, 288-295.
- (88) Y. Cheng, K. M. Brown, R. K. Prud'homme. *International Journal of Biological Macromolecules*, **31**, 2002, 29-35.
- (89) A. Tayal, V. B. Pai, S. A. Khan. *Macromolecules*, **32**, 1999, 5567-5574.
- (90) a) T. R. Bhardwaj, M. Kanwar, R. Lal, A. Gupta. *Drug development and industrial pharmacy*, **26**, 2000, 1025-1038; b) M. George, T. Abraham. *International Journal of Pharmaceutics*, **335**, 2007, 123-129.
- (91) S. Kesavan, R. K. Prud'Homme. *Macromolecules*, **25**, 1992, 2026-2032.
- (92) a) I. Gliko-Kabir, B. Yagen, A. Penhasi, A. Rubinstein. *Pharmaceutical research*, **15**, 1998, 1019-1025; b) C. Sandolo, P. Matricardi, F. Alhaique, T. Coviello. *Food Hydrocolloids*, **23**, 2009, 210-220.
- (93) a) S. A. Khan, J. R. Royer, S. R. Raghavan, *Aviation fuels with improved fire safety: a proceedings* **1997**, pp. 31-46; b) C. W. Macosko, *Rheology: Principles, Measurements, and Applications*, Wiley-VCH, New York, **1994**, p.
- (94) H. Winter. *Polymer Engineering & Science*, **27**, 1987, 1698-1702.
- (95) J. F. Cooley in *Apparatus for electrically dispersing fluids*, Vol. Google Patents, **1902**.
- (96) W. J. Morton in *Method of dispersing fluids*, Vol. Google Patents, **1902**.

- (97) J. Doshi, D. H. Reneker, *Industry Applications Society Annual Meeting, 1993., Conference Record of the 1993 IEEE* **1993**, pp. 1698-1703.
- (98) D. Li, Y. Xia. *Advanced Materials*, **16**, 2004, 1151-1170.
- (99) M. G. McKee, G. L. Wilkes, R. H. Colby, T. E. Long. *Macromolecules*, **37**, 2004, 1760-1767.
- (100) D. H. Reneker, A. L. Yarin. *Polymer*, **49**, 2008, 2387-2425.
- (101) H. Yan, L. Liu, Z. Zhang. *Applied Physics Letters*, **95**, 2009, 143114.
- (102) J. A. Matthews, G. E. Wnek, D. G. Simpson, G. L. Bowlin. *Biomacromolecules*, **3**, 2002, 232-238.
- (103) E. Smit, U. Büttner, R. D. Sanderson. *Polymer*, **46**, 2005, 2419-2423.
- (104) N. Bhardwaj, S. C. Kundu. *Biotechnology advances*, **28**, 2010, 325-347.
- (105) A. L. Andrady, *Science and Technology of Polymer Nanofibers*, John Wiley & Sons, Inc, Hoboken, **2008**, p.
- (106) R. M. Nezarati, M. B. Eifert, E. Cosgriff-Hernandez. *Tissue Engineering Part C: Methods*, **19**, 2013, 810-819.
- (107) C. L. Casper, J. S. Stephens, N. G. Tassi, D. B. Chase, J. F. Rabolt. *Macromolecules*, **37**, 2004, 573-578.
- (108) S. De Vrieze, T. Van Camp, A. Nelvig, B. Hagström, P. Westbroek, K. De Clerck. *Journal of materials science*, **44**, 2009, 1357-1362.
- (109) M. M. Demir, I. Yilgor, E. Yilgor, B. Erman. *Polymer*, **43**, 2002, 3303-3309.
- (110) S. Megelski, J. S. Stephens, D. B. Chase, J. F. Rabolt. *Macromolecules*, **35**, 2002, 8456-8466.
- (111) J. Deitzel, J. Kleinmeyer, D. Harris, N. B. Tan. *Polymer*, **42**, 2001, 261-272.
- (112) a) M. K. Dufficy, S. A. Khan, P. S. Fedkiw. *ACS Applied Materials & Interfaces*, **8**, 2016, 1327-1336; b) M. K. Dufficy, M. T. Geiger, C. A. Bonino, S. A. Khan. *Langmuir*, **31**, 2015, 12455-12463.
- (113) D. Wu, T. Shi, T. Yang, Y. Sun, L. Zhai, W. Zhou, M. Zhang, J. Zhang. *European Polymer Journal*, **47**, 2011, 284-293.

- (114) C. H. See, A. T. Harris. *Industrial & engineering chemistry research*, **46**, 2007, 997-1012.
- (115) T. Wang, S. Kumar. *Journal of applied polymer science*, **102**, 2006, 1023-1029.
- (116) W. J. Li, C. T. Laurencin, E. J. Caterson, R. S. Tuan, F. K. Ko. *Journal of biomedical materials research*, **60**, 2002, 613-621.
- (117) P. Gibson, H. Schreuder-Gibson, D. Rivin. *AIChE journal*, **45**, 1999, 190-195.
- (118) Y.-J. Bai, C.-G. Wang, N. Lun, Y.-X. Wang, M.-J. Yu, B. Zhu. *Carbon*, **44**, 2006, 1773-1778.
- (119) A. Gupta, D. Paliwal, P. Bajaj. *Journal of Macromolecular Science, Part C: Polymer Reviews*, **31**, 1991, 1-89.
- (120) a) S.-S. Tzeng. *Carbon*, **44**, 2006, 1986-1993; b) I. Mochida, R. Ohtsubo, K. Takeshita, H. Marsh. *Carbon*, **18**, 1980, 117-123.
- (121) C. Kim, S. H. Park, J. I. Cho, D. Y. Lee, T. J. Park, W. J. Lee, K. S. Yang. *Journal of Raman Spectroscopy*, **35**, 2004, 928-933.
- (122) S. N. Arshad, M. Naraghi, I. Chasiotis. *Carbon*, **49**, 2011, 1710-1719.
- (123) Y. Wang, J. J. Santiago-Aviles. *Nanotechnology, IEEE Transactions on*, **3**, 2004, 221-224.
- (124) J. R. McDonough, J. W. Choi, Y. Yang, F. La Mantia, Y. Zhang, Y. Cui. *Applied Physics Letters*, **95**, 2009, 243109.
- (125) B. Saha, G. C. Schatz. *The Journal of Physical Chemistry B*, **116**, 2012, 4684-4692.
- (126) T. Pirzada, S. A. Arvidson, C. D. Saquing, S. S. Shah, S. A. Khan. *Langmuir*, **30**, 2014, 15504-15513.
- (127) J. J. Ge, H. Hou, Q. Li, M. J. Graham, A. Greiner, D. H. Reneker, F. W. Harris, S. Z. Cheng. *Journal of the American Chemical Society*, **126**, 2004, 15754-15761.
- (128) Z. Zhou, X.-F. Wu. *Journal of Power Sources*, **222**, 2013, 410-416.
- (129) Q. Dong, G. Wang, B. Qian, C. Hu, Y. Wang, J. Qiu. *Electrochimica Acta*, **137**, 2014, 388-394.
- (130) L. Ji, X. Zhang. *Carbon*, **47**, 2009, 3219-3226.

- (131) X. Fang, M. Ge, J. Rong, C. Zhou. *ACS nano*, **8**, 2014, 4876-4882.
- (132) L. Qie, W. M. Chen, Z. H. Wang, Q. G. Shao, X. Li, L. X. Yuan, X. L. Hu, W. X. Zhang, Y. H. Huang. *Advanced Materials*, **24**, 2012, 2047-2050.
- (133) L. Ji, Y. Yao, O. Toprakci, Z. Lin, Y. Liang, Q. Shi, A. J. Medford, C. R. Millns, X. Zhang. *Journal of Power Sources*, **195**, 2010, 2050-2056.
- (134) F. Yan, X. Tang, Y. Wei, L. Chen, G. Cao, M. Zhang, T. Wang. *Journal of Materials Chemistry A*, **3**, 2015, 12672-12679.
- (135) a) M.-S. Wang, W.-L. Song, J. Wang, L.-Z. Fan. *Carbon*, **82**, 2015, 337-345; b) J. Y. Howe, D. J. Burton, Y. Qi, H. M. Meyer, M. Nazri, G. A. Nazri, A. C. Palmer, P. D. Lake. *Journal of Power Sources*, **221**, 2013, 455-461.
- (136) S. Y. Kim, K. S. Yang, B.-H. Kim. *Journal of Power Sources*, **273**, 2015, 404-412.

### **Chapter 3. Hierarchical graphene-containing carbon nanofibers for lithium-ion battery anodes**

Chapter 3 is essentially a manuscript that is reprinted with permission from Martin K Dufficy, Saad A. Khan, and Peter S. Fedkiw, *ACS Applied Materials and Interfaces*, **2016**, 8 (2), pp 1327-1336. Copyright 2016 American Chemical Society.

## **Abstract**

We present a method to produce composite anodes consisting of thermally-reduced graphene oxide-containing carbon nanofibers (TRGO/CNFs) via electrospinning a dispersion of polyacrylonitrile (PAN) and graphene oxide (GO) sheets in dimethylformamide followed by heat treatment at 650°C. A range of GO (1-20 wt% GO relative to polymer concentration) was added to the polymer solution, with each sample comprising similar polymer chain packing and subsequent CNF microstructure, as assessed by x-ray diffraction. An increase from 0 to 20 wt% GO in the fibers led to carbonized nonwovens with enhanced electronic conductivity, as TRGO sheets conductively connected the CNFs. Galvanostatic half-cell cycling revealed that TRGO addition enhanced the specific discharge capacity of the fibers. The optimal GO concentration of 5 wt% GO enhanced first-cycle discharge capacities at C/24 rates (15.6 mA g<sup>-1</sup>) 150% compared to CNFs, with a 400% capacity increase at 2-C rates (750 mA g<sup>-1</sup>). We attribute the capacity enhancement to a high-degree of GO exfoliation. The TRGO/CNFs also experienced no capacity fade after 200 cycles at 2-C rates. Impedance spectroscopy of the composite anodes demonstrated that charge transfer resistances decreased as GO content increased, implying that high GO loadings result in more electrochemically active material.

## **3.1. Introduction**

The lithium-ion battery (LIB) is ubiquitous, ranging in applications from mobile phones to automobiles. Current research thrusts aim to increase the anode capacity beyond that of graphite (372 mAh g<sup>-1</sup>), a common component of commercial anodes. Researchers have attempted to increase anode capacity by incorporating Li-alloying materials such as iron oxide

<sup>1,2</sup>, tin <sup>3-6</sup>, and silicon <sup>7-10</sup>. While these materials demonstrate a charge capacity much greater than graphite, they suffer from large volume expansions upon lithiation and subsequent pulverization of the materials during charge-discharge cycling causing a loss in capacity not observed in carbon electrodes <sup>11</sup>.

Since commercialization of LIBs, carbon-based materials remain the preferred choice of anode. Carbon has a low-intercalation potential with Li; the fully lithiated stage of carbon occurs at ~0.1 V vs. Li/Li<sup>+</sup> while deep charging occurs at the reduction potential of Li <sup>12</sup>. Additionally, the lithium-carbon reaction is reversible, which contributes to high-coulombic efficiencies and low-capacity fade. Lithium intercalation into graphite results in a 10.3% increase in layer spacing, compared to >300% volume increases with host alloys <sup>12</sup>. The small volume expansion upon intercalation leads to a mechanically durable electrode. Furthermore, a stable solid-electrolyte interphase (SEI) forms on the surface of carbon with carbonate electrolyte solvents <sup>13</sup>, preventing further electrolyte decomposition and allowing for favorable kinetics. The type of carbon (graphitic, amorphous, etc.) used in the electrode greatly impacts the electrochemical performance.

While carbon electrodes have been extensively studied <sup>14-16</sup>, research has focused on newly discovered forms of carbon (*i.e.*, graphene) as alternative high-capacity electrodes to graphite. Graphene, a two-dimensional carbon, possesses a theoretical specific charge capacity twice that of graphite <sup>17-19</sup>. Graphene properties, such as large aspect ratio and specific surface area, allow for a highly conductive network and enhanced rate capabilities in LIB anodes. Graphene-containing composite electrodes may augment the beneficial properties of graphene,

and in the present work, composite electrospun nanofibers are studied. Electrospinning allows for the production of uniform fibers on the order of tens to hundreds of nanometers in diameter. The 1-D architecture of the fibers allows for rapid charge transfer, reduced Li-diffusion pathways, and large specific surface areas. Notably, electrospinning is a facile method to produce composite fibers <sup>20</sup>.

Herein, we present an approach to incorporate graphene oxide (GO) into a polyacrylonitrile (PAN) polymer nanofiber matrix via electrospinning to form nonwoven mats. These mats are heat treated to produce thermally reduced graphene oxide-containing carbon nanofibers (TRGO/CNFs) as LIB anodes. The novelty of this work lies in the enhanced capacity and conductivity of TRGO/CNFs carbonized at a low heat-treatment temperature when compared to CNFs. The CNFs in this study are carbonized at 650°C, resulting in a defective carbon structure, and amplifying the effects (increased conductivity, charge capacity, *etc.*) of carbon-rich TRGO in the composite mat. While graphene-containing nanofibers have been produced <sup>21,22</sup> and applied to super-capacitors <sup>23</sup>, to our knowledge they have not been applied to LIB anodes and their physical features not extensively characterized. This study examines the morphology and electrochemical effects of a range of GO concentrations (0 to 20 wt%) incorporated into CNFs. The results suggest that TRGO/CNFs mats provide a composite carbon electrode superior to CNF mats and capable of operating at high rates.

## 3.2. Materials and Methods

### 3.2.1. Graphite oxide preparation

Graphite oxide was synthesized via a modified Hummers method<sup>24</sup>. In a typical synthesis, 16.6 g of both  $K_2S_2O_8$  (99% A.C.S. Reagent, Sigma Aldrich) and  $P_2O_5$  (99.99% Purity, Sigma Aldrich) were added to a round bottom flask filled with 100 ml  $H_2SO_4$  (95-98% A.C.S. Reagent, Sigma Aldrich). The flask was heated and stirred until the temperature reached 80°C. Then 10 g graphite powder (99.99% purity, < 45  $\mu m$ , Sigma Aldrich) was added and the mixture was stirred for 10 min and allowed to cool to room temperature. The solution was slowly diluted with 200 ml water (DI, 18.2  $M\Omega\text{-cm}$ ) and again allowed to reach room temperature. The solid was filtered, washed, and dried overnight in a vacuum oven at 40°C. The aforementioned pre-oxidized graphite was added to 460 ml  $H_2SO_4$  in a 9L vessel in an ice bath and stirred for 20 min to reach 0°C. Then, 30 g  $KMnO_4$  (99% A.C.S. Reagent, Sigma Aldrich) was added to the mixture at a rate of  $\sim 1 \text{ g min}^{-1}$ . The vessel was removed from the ice bath and heated for 3 hours at 35°C. After allowing the vessel to reach room temperature, the sample was gradually diluted with 920 ml  $H_2O$ . Then, 80 ml  $H_2O_2$  (30%, Sigma Aldrich) was added, turning the solution yellow. After allowing the solids to settle, the excess liquid was decanted. The product was washed and centrifuged 12 times at 6,000 RPM for 20 min until the supernatant had a pH of 5.5 or greater. Now termed graphite oxide, the product was dried overnight in a vacuum oven at 40°C.

### *3.2.2. GO-PAN suspension preparation*

A range of graphite oxide concentrations (1, 5, 10, and 20 wt% relative to polymer concentration) were dispersed in anhydrous dimethylformamide (DMF, 99.8% purity, Sigma Aldrich) and sonicated to exfoliate into GO sheets (~1 hr). Immediately after sonication, polyacrylonitrile (PAN, 150 kDa, Scientific Polymer Products) was added to the GO dispersion resulting in an 8 wt% polymer dispersion. The dispersion was heated to 60°C and stirred overnight and was used as the solution for electrospinning the composite fibers.

### *3.2.3. Characterization of Electrospinning Suspension*

Rheology experiments were performed at 25°C on a stress-controlled rheometer (Discovery Hybrid Rheometer-2, TA Instruments) using 40-mm flat plates with a gap height of 0.5 mm. The zero-shear viscosity was determined by averaging steady-shear viscosity values in the Newtonian regime. Experiments were performed in triplicate to ensure reproducibility within 5%. Ionic conductivities were measured using a Mettler Toledo S47-K conductivity meter. Surface tension was measured using the pendant drop method (FTA1000, First Ten Angstroms). Both ionic conductivity and surface tension measurements were performed in triplicate.

### *3.2.4. Graphene-containing nanofibers preparation*

Prior to electrospinning, the GO-PAN/DMF suspensions described above were cooled to room temperature. The composite fibers were electrospun using an in-house setup described elsewhere<sup>25</sup>. In brief, a syringe pump (NE-300, New Era Pumps) fitted with a metallic needle (22-gauge) was used to pump the nanofiber precursor solution. A potential was applied to the

needle using a high-voltage power supply (Matsusada Precision, Inc. Model AU-60P0.5) resulting in the extrusion of a stable polymer jet, which was collected on a grounded collector plate. A typical sample was spun in an open-air environment between 11 and 13 kV at a volumetric rate of 1 ml hr<sup>-1</sup> with a fixed tip-to-collector distance of 15 cm. After electrospinning, the mats were stabilized in a quartz tube at 275°C with a heating ramp rate of 5°C min<sup>-1</sup> for 2 hrs under dry air. The stabilization process crosslinks PAN to form a ladder conformation<sup>26</sup>. The mats were allowed to cool to room temperature before purging the quartz tube furnace with N<sub>2</sub> at 90°C for 3 hrs and carbonizing at 650°C with a heating rate of 2°C min<sup>-1</sup>. The carbonization process evolves many of the non-carbonaceous compounds. The final carbonization temperature was held for 1 hr followed by uncontrolled cooling to room temperature.

### *3.2.5. Composite polymer and CNF characterization*

To determine the presence of oxygen functional groups on graphite oxide and the composite polymer fibers, FT-IR (Thermo Scientific Nicolet 6700) was employed. Microscopy images were taken with an FEI Verios XHR SEM (1 kV) and JEOL 2010F FR S/TEM (200 kV). Average nanofiber diameters were determined from SEM images using Image J software (National Institutes of Health) by measuring the diameters of 100 samples in three different locations on the mat. A Rigaku SmartLab X-ray diffractometer (Cu K<sub>α</sub>, λ = 1.5406 Angstrom) was used to study fiber structure. The mat conductivity was measured using an in-house 4-probe system<sup>27</sup>. To guarantee contact with the electrodes, a 200 g weight was placed atop the cell and conductivity of each side of the mat was measured 6 times and averaged. A Horiba-

Jobin Yvon LabRAM HS VIS Raman microscope equipped with a 632.8-nm laser was used to characterize the carbonized PAN structure. All samples were focused through a 100X objective lens. A D2 filter was used to decrease the intensity of the laser and protect the samples from degradation.

### *3.2.6. Electrochemical performance characterization*

The carbonized nanofiber mats were used as the working electrode in 2032 coin cells (MTI Corp) with Li metal (99%, 0.75 mm thick, Sigma Aldrich) as the counter and reference electrode. The cells were assembled in an argon-rich glove box. Approximately 50  $\mu\text{l}$  of electrolyte, 1M  $\text{LiPF}_6$  (>99% purity, BASF) in ethylene carbonate: ethyl methyl carbonate (EC:EMC 1:1 wt%, 99% purity, Sigma Aldrich), was added atop the working electrode and the Celgard separator. Half-cell anode performance was assessed (Arbin BT2000) between 2.5 V and 25 mV vs.  $\text{Li/Li}^+$ . The charge capacity of CNFs for calculating the reported C-rate was set at 375 mAh  $\text{g}^{-1}$ <sup>28</sup>. The current densities examined include C/24, C/10, C/5, C, and 2C, which correspond to 15.6, 37.5, 75, 375 and 750 mA  $\text{g}^{-1}$ , respectively. All cycling measurements were conducted on at least 3 half-cells to guarantee reproducibility within 10%. Electrochemical impedance spectroscopy (VersaSTAT 4, Princeton Applied Research) was conducted on delithiated cells at 1.7 V vs.  $\text{Li/Li}^+$  between 100 MHz - 10 mHz with an amplitude of 10 mV. Prior to each measurement, a potential bias of 1.7 V was applied to the half-cells until the current fell below 375  $\mu\text{A g}^{-1}$  (C/1000).

### 3.3. Results and Discussion

#### 3.3.1. GO/PAN nanofibers by electrospinning

Properties such as surface tension, ionic conductivity, and viscosity of the electrospinning solution are affected by the quality of dispersion <sup>29,30</sup>. The aforementioned material properties are shown in **Table 3.1** for 8 wt% PAN/DMF solutions containing 0, 1, 5, 10 and 20 wt% GO. As GO concentration in the polymer suspension increased, the ionic conductivity decreased. Based on previous work from our group <sup>31</sup>, we attribute the decreased ionic conductivity to the formation of 3-dimensional networks and the onset of the percolation threshold as well as particle aggregation. Steady-shear rheology measurements (**Figure 3.1**) were performed to study the formation of such networks and particle aggregation.

**Table 3.1.** Properties of GO/PAN-DMF electrospinning suspensions; <sup>‡</sup> not measureable

Wt% GO	Conductivity [ $\mu\text{S cm}^{-1}$ ]	Surface Tension [ $\text{mN m}^{-1}$ ]	Zero-Shear Viscosity [Pa s]
0	$210 \pm 2.0$	35.4	1
1	$204 \pm 0.7$	35.4	1.1
5	$198 \pm 2.3$	35.4	1.2
10	$182 \pm 4.0$	35.4	n/a <sup>‡</sup>
20	$154 \pm 2.2$	35.4	n/a <sup>‡</sup>

The addition of 1 wt% GO to PAN has no effect on the viscosity profile of the sample. This is evident from the overlapping data of neat PAN with that containing 1 wt% GO (**Figure 3.1a**). The zero-shear viscosity increases marginally at 5 wt% GO when compared to neat PAN. However, viscosity profiles start to increase and become different as the concentration of GO increases to 10 and 20 wt%. In particular, we observe a deviation from Newtonian behavior and an absence of the zero-shear plateau in PAN suspensions with 10 and 20 wt% GO. The increased viscosity with decreasing stress provides evidence for network

configuration <sup>32</sup> and particle aggregation, which corroborates the trend of decreasing ionic conductivity with increasing GO concentration. Non-spherical particles such as GO sheets may amplify deviations from Newtonian behavior because of their high packing densities, which result in more particle interactions than spherical particles and may lead to a yield stress. The stress-strain plot (**Figure 3.1b**) for the polymer dispersions shows the presence of an apparent “yield stress” for the PAN suspension containing 20 wt% GO. Using extrapolation methods <sup>33</sup>, we observe a yield stress of ~0.1 Pa for the aforementioned system. We observed shear thinning as shear stress increased in higher wt% GO samples, which is indicative of GO network cleavage or the mechanical exfoliation of GO sheets. Thus, single- to few-layer GO sheets should be present in the composite PAN/GO fibers as a result of high stresses (> 100 Pa) experienced during the electrospinning process. Moreover, the surface tension of the electrospinning suspensions was unaffected by GO addition, which suggests the hydrophilic nature of GO does not act as a surfactant and the surface properties of DMF dominate.

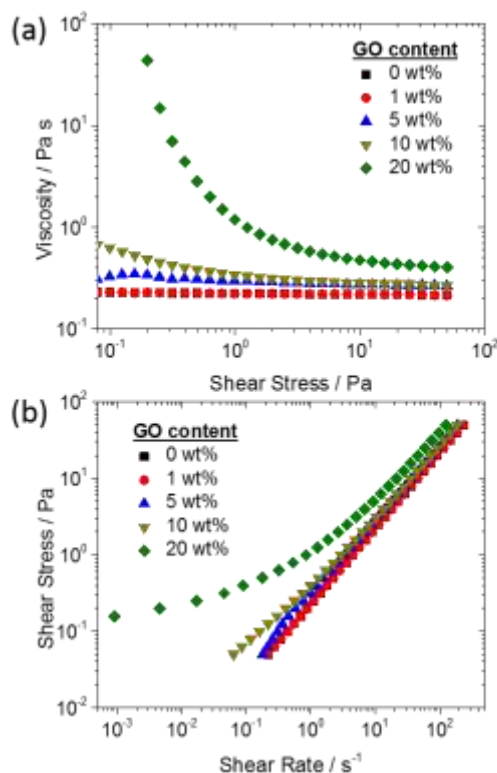


**Figure 3.1.** Unidirectional, steady-shear (a) viscosity and (b) shear stress/rate results for an 8 wt% PAN-DMF suspension with various GO concentrations. Data points for pure PAN and PAN containing 1 wt% GO overlap.

The GO/PAN fibers were electrospun in an open-air environment with different concentrations of GO. The hue of the GO/PAN fibers resembled the characteristic brown of GO as solids concentration increased (**Figure 3.2**). The color change in the samples provides preliminary evidence for GO incorporation in the fiber mats; the shears from electrospinning did not dislodge GO from the polymer jet. FT-IR analysis confirmed the presence of GO sheets in these composite polymer fibers. **Figure 3.3a** shows the FT-IR spectra of graphite oxide, PAN, as well as GO/PAN composite fibers. The spectrum for graphite oxide has many peaks. The peaks characteristic of the oxidation procedure are observed at  $\sim 3450$ ,  $1730$ , and  $1610 \text{ cm}^{-1}$

<sup>1</sup>, which correspond to hydroxyl (-OH) stretching, carbonyl (C=O) stretching, and the overlapping responses from vibrations of intercalated water and unoxidized carbon regions, respectively <sup>34</sup>. The peaks characteristic of PAN are located at 2240, 1660, and 1445  $\text{cm}^{-1}$  and correspond to the presence of nitrile ( $\text{C}\equiv\text{N}$ ) and the aliphatic CH groups, respectively <sup>35</sup>. The only peak that emerges from GO addition is the carbonyl stretching at 1730  $\text{cm}^{-1}$ . It is generally accepted that hydroxyl groups are present on the basal plane and the carbonyl groups are located on the edges of GO <sup>36</sup>. An idealization of the proposed GO structure is pictured in **Figure 3.3b**. Based on the FT-IR results, edges of GO may be protruding through the fibers. The absence of a broad hydroxyl peak in the composite fibers at 3450  $\text{cm}^{-1}$  suggests that PAN covers the basal plane of GO. The absence of the hydroxyl peak also suggests the formation of an exfoliated GO/PAN composite mat, with the water molecules either evaporated during the spinning process or below the detection threshold of the instrument. We employed XRD to gain a better understanding of the GO/PAN fiber structure.



**Figure 3.2.** Images of composite GO-PAN electrospun fibers with (i) 0 (ii) 1 (iii) 5 (iv) 10 and (v) 20 wt% GO. As GO loading increases, the fiber mats darken.

The x-ray diffractograms of PAN fibers and composite GO/PAN fibers presented in **Figure 3.3c** do not show a sharp peak at  $2\theta = 12^\circ$ , which is characteristic of the crystalline (002) phase in oxidized graphite structures also shown in **Figure 3.3c**. The absence of the sharp (002) peak characteristic of graphite oxide indicates that either GO has exfoliated in the fibers, which is consistent with the shear-thinning rheology of the electrospinning solution, or that

either graphite oxide or GO is embedded within the PAN fibers beyond the penetration depth of the XRD. Using Bragg's Law, we observed an increase in interlayer  $d$ -spacing from 0.335 nm (characteristic of graphite) to 0.737 nm in graphite oxide, which is attributed to intercalated water bound to oxygen functional groups<sup>37</sup>. The increased layer spacing facilitated graphite oxide exfoliation in DMF during sonication and led to dispersed suspensions.

The diffractograms of PAN nanofibers display two broad peaks, (100) at  $2\theta = 17^\circ$  and (110) at  $2\theta = 25^\circ$ , which indicates a defective PAN crystalline microstructure<sup>38</sup>. While the intensity of the (100) peak decreased with increasing GO concentration, the  $d_{(100)}/d_{(110)}$  ratio remains unchanged at 1.47, indicating the PAN chain packing remained unaffected as GO concentration increased. The similarities in chain packing should yield the same carbon structure after heat treatments and suggests the electrochemical enhancements in the composite CNFs, reported below, to be attributed to the addition of GO.

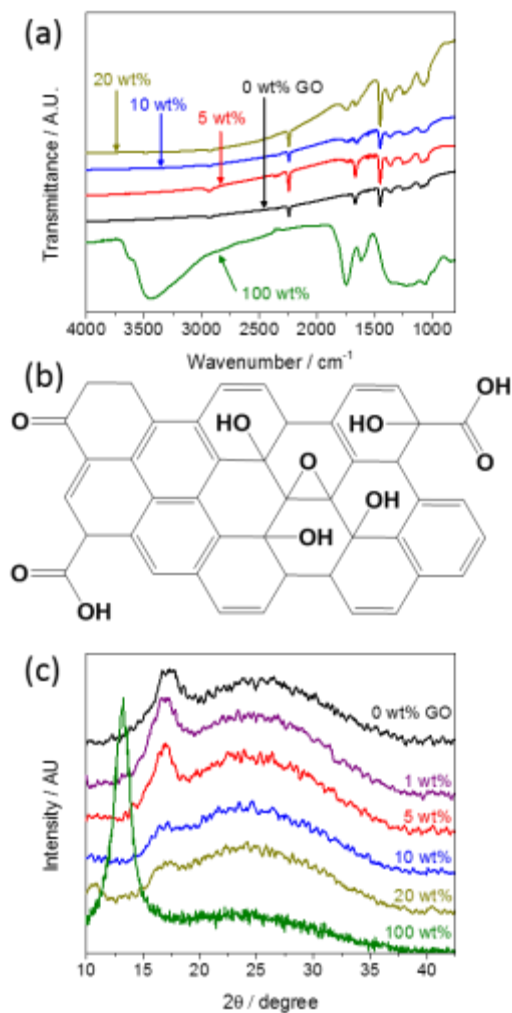


**Figure 3.3.** (a) FT-IR spectra of graphite oxide, PAN nanofibers, and the composite GO-PAN nanofibers; (b) An idealization of proposed GO structure; (c) XRD diffractograms of graphite oxide, PAN, and composite GO-PAN nanofibers.

### 3.3.2. TRGO/CNF characterization

Scanning electron microscopy was used to determine the effect of GO loading on the morphology of heat-treated fibers. The low PAN concentration (8 wt%), and resulting low viscosity in the electrospinning solution, caused minor beading of the CNFs (**Figure 3.4a**) and 1 wt% TRGO/CNFs (**Figure 3.4b**). We did not observe beading in the thermally-treated fibers

at GO loadings of 5 wt% (**Figure 3.4c**) and greater. Rather, at 5 wt% TRGO/CNFs, TRGO sheets appeared dispersed throughout the mat, and the diameter of the composite fibers decreased. Exfoliation of GO sheets from the high shear in the electrospinning process may have caused a fragmented jet during the electrospinning process. As the GO content increased to 10 wt% (**Figure 3.4d**) and 20 wt% (**Figure 3.4e**), the diameter of the composite fibers again increased (**Table 3.2**). The TRGO sheets become encased in the fibers (to give a bead-like effect) as a result of high GO concentration and aggregation in the polymer suspension; the shear from electrospinning was apparently insufficient to exfoliate the large concentration of GO. At 20 wt% GO, the encased TRGO sheets contain pores ~50 nm in diameter (**Figure 3.4f**), which may be caused by oxygen evolution or the loss of intercalated water during heat treatment. Average fiber diameters reported in **Table 3.2** show that TRGO/CNFs with 10 and 20 wt% GO have the largest diameter, which is consistent with the rheology findings (an increased viscosity contributes to larger fiber diameters).

**Table 3.2.** Electrical conductivity and fiber diameter for CNFs and TRGO/CNFs.

Wt% GO	Electrical Conductivity [S cm <sup>-1</sup> ]	Fiber Diameter [nm]
0	0.28 ± 0.06	319 ± 57
1	0.63 ± 0.09	282 ± 47
5	0.44 ± 0.08	240 ± 61
10	0.72 ± 0.10	338 ± 75
20	1.22 ± 0.12	491 ± 118

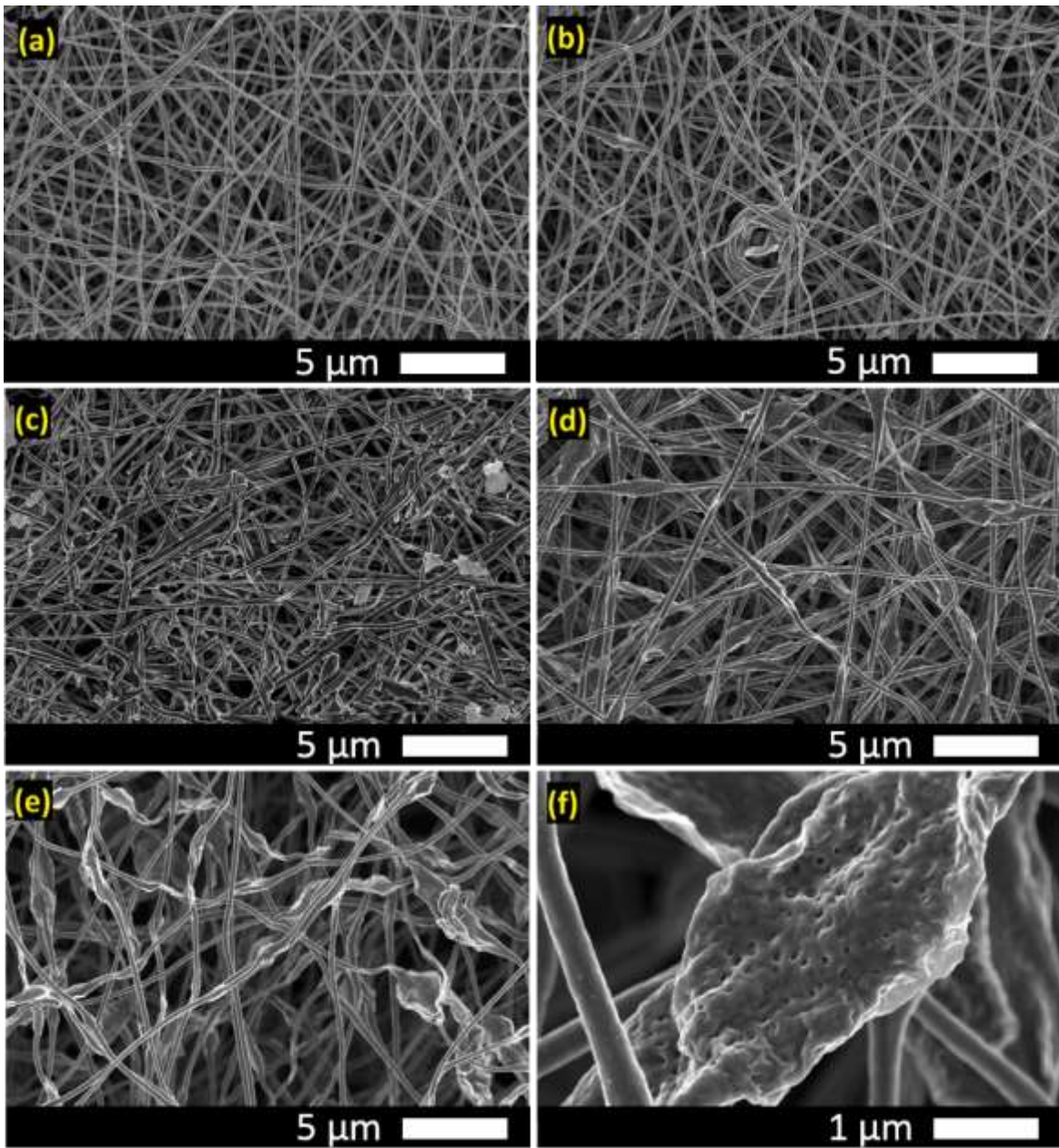


**Figure 3.4.** SEM images of (a) CNFs and, (b) 1, (c) 5, (d) 10, (e) 20 wt% TRGO/CNFs and (f) a typical porous carbon bead formed in 20 wt% TRGO/CNFs.

TEM of the composite fibers provided high-resolution images to determine the location of nanoscale GO sheets created during GO synthesis. The neat CNFs (**Figure 3.5a, b**) appear

to have little defects and negligible surface roughness. With the incorporation of GO to the electrospinning solution, TRGO sheets appeared in a number of locations; sheets of TRGO are interwoven into the nanofiber matrix (**Figure 3.5c**), protruding through the fiber surface, consistent with FT-IR data (**Figure 3.5d**), or folded within the fiber (**Figure 3.5e**). Additionally, the composite TRGO/CNFs appear incised (**Figure 3.5f**), caused as a result of GO deflagration during heat treatments.

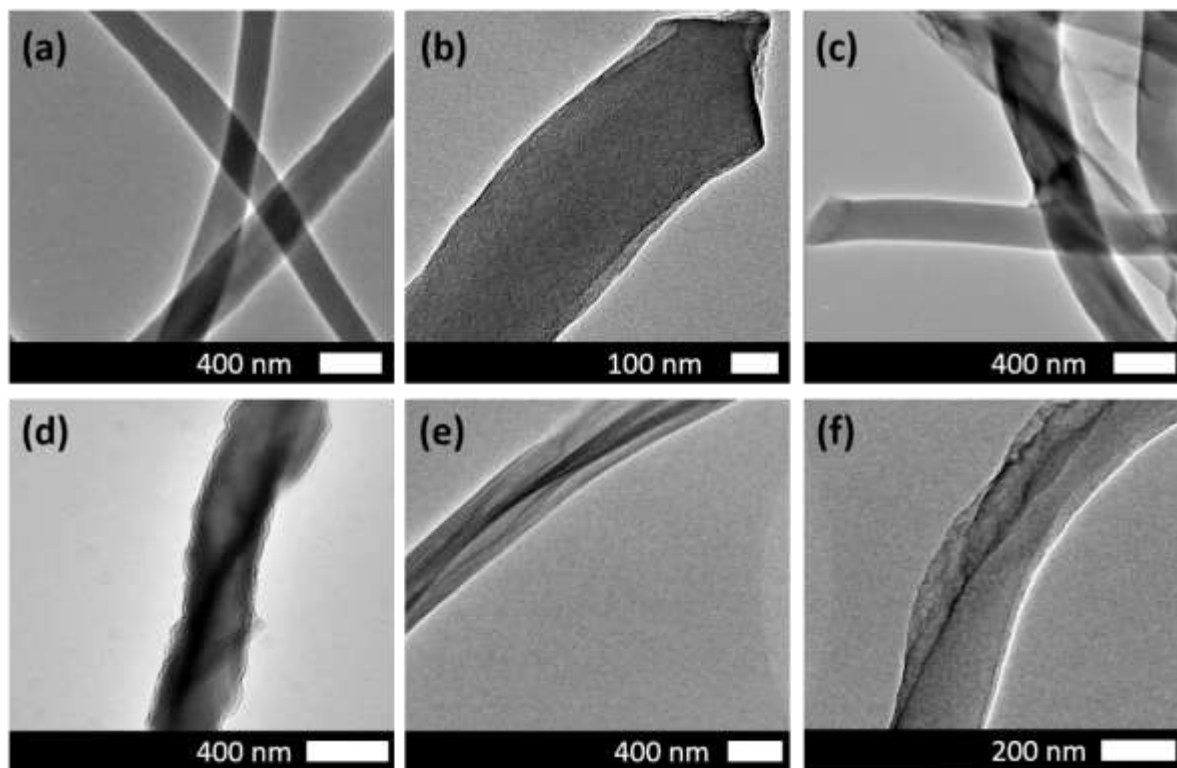


**Figure 3.5.** TEM images of (a, b) CNFs and (c,d) 5, (e) 10 and, (f) 20 wt% TRGO/CNFs.

In addition to the TRGO/CNFs physical features characterized above, we investigated the chemical structure of the composite fibers, which also plays a critical role in electrochemical performance. The low heat-treatment temperature (HTT, 650°C) of GO/PAN fibers produced a disordered (non-graphitic) carbon structure, as evidenced by the broad (002)

peak from XRD (**Figure 3.6a**). The chemical composition (comprising residual nitrogen and oxygen compounds inherent to stabilized PAN) of fibers carbonized at low HTT and the subsequent amorphous state effect low electronic conductivity. The incorporation of GO, which is reduced during the thermal treatments of the fibers, increase the conductivity of the mat (**Table 3.2**). The conductivity of the carbonized composite fibers increased from 0.28 to 1.22 S cm<sup>-1</sup> as the concentration increased from 0 to 20 wt% TRGO/CNFs due to the added sp<sup>2</sup> structure of TRGO. It has been proposed that the removal of oxygen functional groups of GO occurs at temperatures as low as 200°C<sup>39</sup>, producing a defective yet carbon-rich, sp<sup>2</sup> structure. Despite the defective TRGO structure, thermal reduction of GO generates many of the beneficial properties of pristine graphene such as mechanical flexibility and a high conductivity<sup>40</sup>. We further employed Raman spectroscopy to study the effects of TRGO addition on low-HTT PAN fibers.

The two peaks of interest in Raman spectra for disordered carbons are the D peak at ~1350 cm<sup>-1</sup> and the G peak at ~1580 cm<sup>-1</sup>, which originate from the defective and graphitic nature of carbon<sup>41</sup>, respectively. The intensity of the D peak relative to the G peak ( $R = I_D/I_G$ ) decreased with increasing GO concentration, with pure TRGO (pre-exfoliated GO that underwent heat treatment identical to the fibers) having the largest  $R$ -value (**Figure 3.6b**). Thus, TRGO has a less defective structure than the PAN-derived CNFs carbonized at 650°C and contributes to a more ordered composite CNF mat. The ratio of D to the G peak intensities may also be used to estimate the sp<sup>2</sup> boundary size ( $L_a$ ) of a carbon species *via* the empirical relation  $L_a$  [nm] = 4.4/ $R$ <sup>42,43</sup>. The Raman spectra were fit using a Gaussian-Lorentzian function

(OriginLab software) with the results for  $L_a$  plotted in **Figure 3.6b**. The  $sp^2$  regions range from 1.45 nm in CNFs to 1.63 nm in 20 wt% TRGO/CNFs, while a sample of pure TRGO was estimated to have an  $L_a$  of 2.3 nm. The higher concentrations of GO increase the crystallite size of composite fibers, which correlates to the enhanced conductivity at high GO loadings.

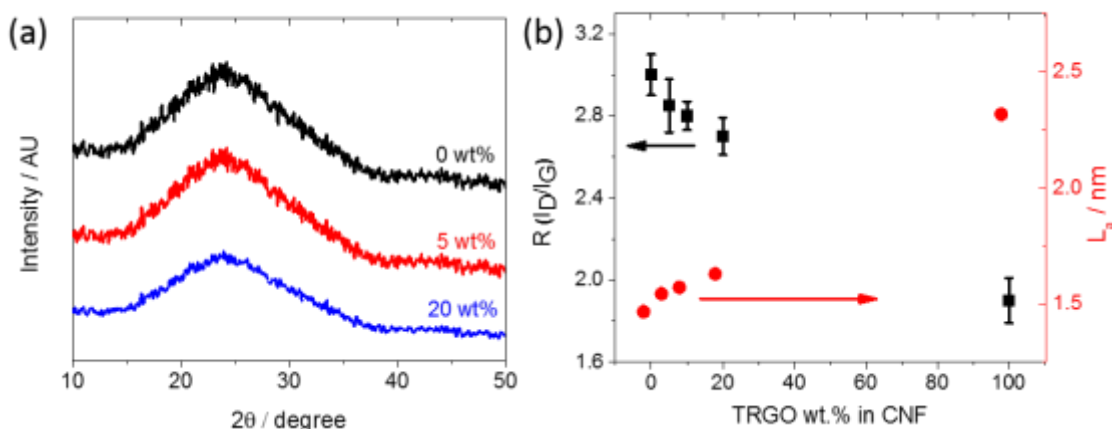


**Figure 3.6.** (a) XRD spectra of CNFs and TRGO/CNFs with 5 and 20 wt% GO; (b) The ratio (R) of D to G absorption peak intensity measured by Raman spectroscopy and estimated crystallite size ( $L_a$ ) for CNFs, TRGO/CNFs, and heat-treated GO.

### 3.3.3. TRGO/CNF electrochemical characterization

The electrochemical performance of TRGO/CNFs was investigated by symmetrical charge/discharge cycling in 2032 coin cells within a voltage range of 2.5 and 0.025 V vs. Li/Li<sup>+</sup>, where charge and discharge refer to Li insertion and extraction into the composite fibers, respectively. Unless stated otherwise, each cell underwent two formation cycles at C/24 (15.6 mA g<sup>-1</sup>) to form the solid-electrolyte interphase (SEI). The initial galvanostatic charge and discharge profiles of CNFs and TRGO/CNFs (**Figure 3.7a**) show hysteresis characteristic of a nano-structured carbon species such as graphene<sup>17</sup> and CNTs<sup>44</sup>. The shape of the charge and discharge profile is unaffected by TRGO addition. The first plateau observed in the initial

cycle ( $\sim 0.8$  V vs Li/Li<sup>+</sup>) is attributed to formation of the SEI, or irreversible electrolyte decomposition<sup>45</sup>. Due to the structural advantages and favorable Li-binding stoichiometry of carbons, coulombic efficiencies (CEs)  $\sim 70$ - $80\%$  are observed on the first cycle. The irreversible capacity loss during SEI formation is attributed to the large surface area of CNFs and TRGO/CNFs ( $\sim 200$  m<sup>2</sup> g<sup>-1</sup> irrespective of TRGO concentration).

The addition of TRGO was found to enhance the capacity of CNFs (**Figure 3.7a**). Fibers with 5 wt% GO demonstrated the highest capacity on the first cycle with a discharge capacity of 830 mAh g<sup>-1</sup>, while CNFs in the absence of TRGO produced an initial discharge capacity of 595 mAh g<sup>-1</sup>. The enhanced cycling performance, coupled with the rheological data and the SEM images, suggest that GO optimally exfoliated (either during sonication or the electrospinning process) at 5 wt% GO and formed aggregates at higher GO concentrations. The TRGO aggregates formed at  $> 5$  wt% GO led to a decrease in the discharge capacities relative to 5 wt% GO but nevertheless greater capacities than CNFs. The enhanced capacity is attributed to the 2-dimensional structure of graphene, which is thought to yield a theoretical charge capacity twice that of graphite<sup>46</sup> (744 mAh g<sup>-1</sup>) and provides locations for Li to bind within the composite fibers. Additionally, the carbon-rich TRGO composition hinders side reactions between Li-ions/electrolyte with residual oxygen and nitrogen<sup>47</sup> compounds inherent to carbonized PAN, which otherwise increases the irreversible capacity loss. Other interesting phenomenon, such as a maximum in tensile strength, have been reported with 5 wt% CNTs in PAN NFs<sup>48</sup>.

Differentials of the charge capacity with respect to voltage were examined (**Figure 3.7b**) to study SEI formation and lithium intercalation into the composite carbon structure. The peaks observed in **Figure 3.7b** correspond to the onset of an electrochemical reaction. The first peak at  $\sim 0.75$  V represents SEI formation, or reduction of the electrolyte. Although the CNFs produced in this study were amorphous, the voltage at which the SEI forms is similar to that of graphite. With TRGO addition to the CNFs, we observed SEI formation at more positive potentials due to increased electrical conductivity, which provides a larger driving force for electrolyte reduction. A second, broader peak located at  $\sim 0.07$  V is attributed to Li intercalation. The gradually declining slope at low potentials in the charge/discharge curves (**Figure 3.7a**) does not produce a minimum in the  $dQ/dV$  curves, which suggests that the composite carbon electrodes are not fully lithiated (due to the tortuous and amorphous carbon structure) or that non-carbonaceous species are reducing. Both of the aforementioned phenomena are independent of GO concentration. It should be noted no peaks were observed at  $\sim 0.75$  V in the 2<sup>nd</sup> charge cycle, which indicates stable SEI formation on the first cycle and low irreversible capacity loss on successive cycles.

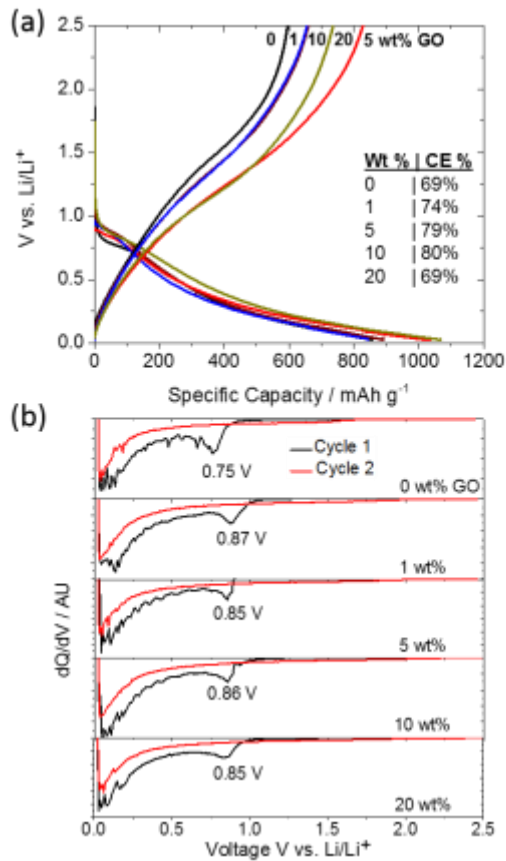


**Figure 3.7.** (a) The formation charge/discharge profiles for CNFs and TRGO/CNFs. The discharge of 1 and 10 wt% TRGO/CNFs coincide; (b) the derivatives ( $dQ/dV$ ) during charge.

To gain insight on the irreversible capacity losses of 5 wt% TRGO/CNF half-cells, results of 20 cycles at  $C/5$  were compared to CNFs in the absence of TRGO (**Figure 3.8**). The discharge capacity of the CNFs decreased 16% from 595 to 500  $\text{mAh g}^{-1}$  after the first cycle as a result of SEI formation. The discharge capacity further decreased 2% from the 5<sup>th</sup> to the 20<sup>th</sup> cycle as capacity stabilized. When compared to CNFs in the absence of TRGO, the TRGO/CNF composites exhibited a larger irreversible capacity loss after the first cycle (23.5%). Nevertheless, the TRGO/CNFs exhibited a capacity 125% higher than CNF electrodes. We attribute the larger irreversible capacity loss of the TRGO/CNFs to SEI

formation on cycle-induced TRGO exfoliation. Similar to the CNFs in the absence of TRGO, a decrease in charge capacity of 2% was observed as the capacity stabilized from the 5<sup>th</sup> to the 20<sup>th</sup> cycle. The capacity fade after 20 cycles for TRGO/CNFs and CNFs suggest a similar microstructure of the two materials.

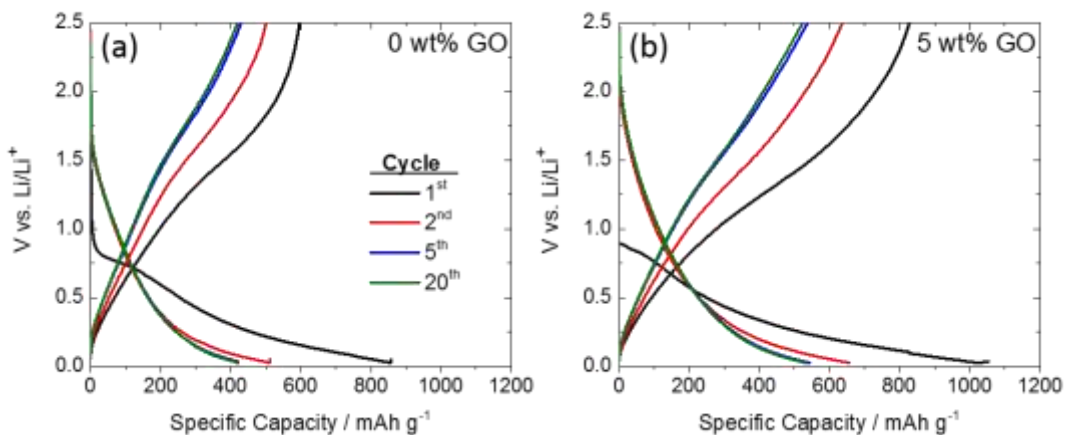


**Figure 3.8.** The charge/discharge profiles for the first 20 cycles of (a) CNFs and (b) 5 wt% TRGO/CNFs at  $75 \text{ mA g}^{-1}$  (C/5).

**Figure 3.9** shows the discharge capacity averaged over 10 cycles of CNFs and the composite fibers at various current densities. Consistent with previous cycling data, 5 wt% TRGO/CNFs displayed the highest capacities. We did not observe as large of a capacity enhancement in the composite fibers when cycled at slow charge rates, presumably due to minimal mass transport effects. However, we observed capacity-enhancing effects of TRGO at high current densities; electrodes with 5 wt% TRGO experienced increases in discharge capacity of 25% at  $15.6 \text{ mA g}^{-1}$  and >400% at  $750 \text{ mA g}^{-1}$ , compared to CNFs. The 2-dimensional TRGO structure offers a smaller size-scale and a more ordered structure than the amorphous and tortuous diffusion pathways in CNFs. The addition of TRGO shortened Li-diffusion pathways and facilitated Li-transport for rapid charge transfer at fast charging rates.

It has also been proposed that the basal plane defects in reduced GO facilitate Li diffusion<sup>49</sup>, which may further increase the rate performance in TRGO/CNFs. While the incorporation of TRGO encapsulated in the fiber may add to the capacity, we propose that the TRGO interwoven in the mat mimics a conductive connector (**Figure 3.4c**) by bridging fibers and further enhancing electron transport in the nonwoven mat.

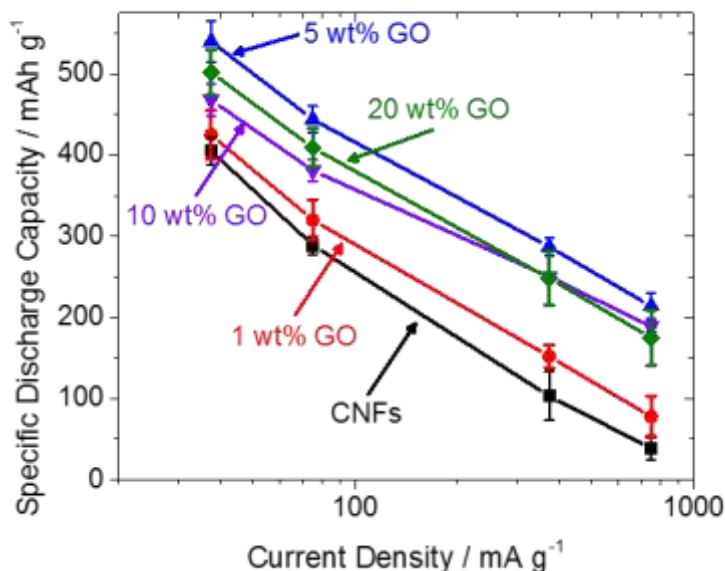


**Figure 3.9.** Rate dependence on discharge capacities of CNF and TRGO/CNF electrodes, averaged over first 10 cycles.

Extended cycling of electrodes provided insight on possible cell-failure mechanisms such as the resilience of the nonwoven fibrous structure and side reactions that occurred on the electrode surface. Composite CNFs were cycled at 750 mA g<sup>-1</sup> (2C) for 200 cycles (**Figure 3.10a**). As noted by other researchers using nano-scale carbonaceous materials<sup>50</sup>, the discharge capacity of the nanofibers increased with cycle number. A 600% increase in discharge capacity was measured for CNFs while ~ 40% increase was observed for 1, 5, 10, and 20 wt %

TRGO/CNFs. Although a mechanism to describe the increase in capacity has not been proven, it has been proposed to be a result of graphene layer exfoliation<sup>50</sup> or delayed electrolyte wetting. Coulombic efficiencies (CE) greater than 100% were observed in CNFs and composite CNFs with 1 wt% GO (**Figure 3.10b**). High CEs are not expected in cycle-induced, exfoliated carbon due to continual SEI formation. While some structural rearrangement is possible, our data also suggests that an oxidation reaction may occur at higher potentials (> 1V vs Li/Li<sup>+</sup>) to increase the capacity. Coulombic efficiencies below 99% observed in 10 and 20 wt% TRGO/CNFs suggests graphene exfoliation in TRGO aggregates, and the formation of an SEI on newly exposed carbon. The cycle-induced, exfoliated TRGO provides access to carbon that was previously inaccessible.

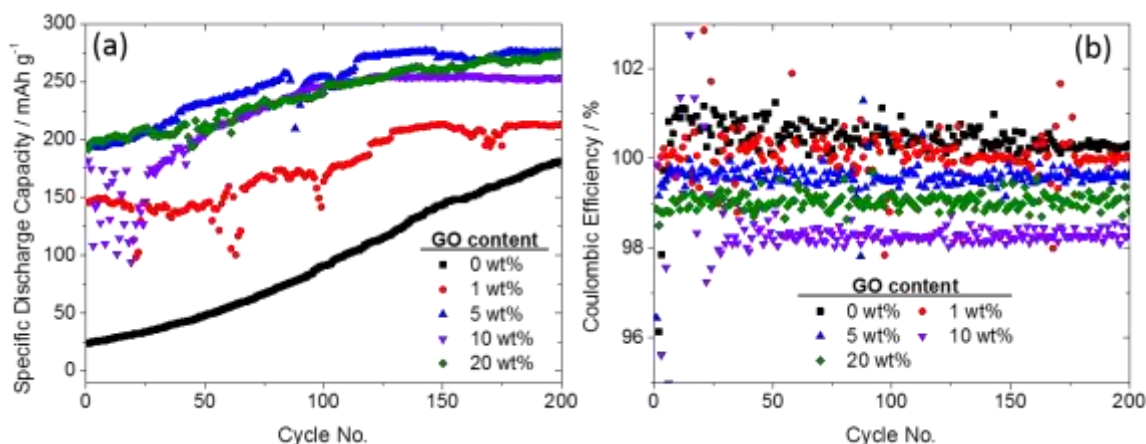


**Figure 3.10.** (a) Discharge capacities of CNF and TRGO/CNF electrodes over 200 cycles at 750 mA g<sup>-1</sup> (2-C) and (b) corresponding Coulombic efficiencies.

After 200 cycles at 750 mA g<sup>-1</sup>, the half-cells were disassembled and the anodes washed in acetonitrile and dried for SEM imaging. Exposure to air was kept at a minimum. The CNFs in the absence of TRGO (**Figure 3.11a**) maintained their nonwoven structure. The addition of GO to the CNFs did not alter the architecture of composite CNF electrodes. The TRGO/CNFs

maintained their nonwoven structure (**Figure 3.11b-c**) after the 200 cycles. A porous SEI (**Figure 3.11d**) with pore size of  $\sim 2$  nm (measured *via* the SEM image) formed on the surface of the fibers, allowing for fast Li transport at high currents.

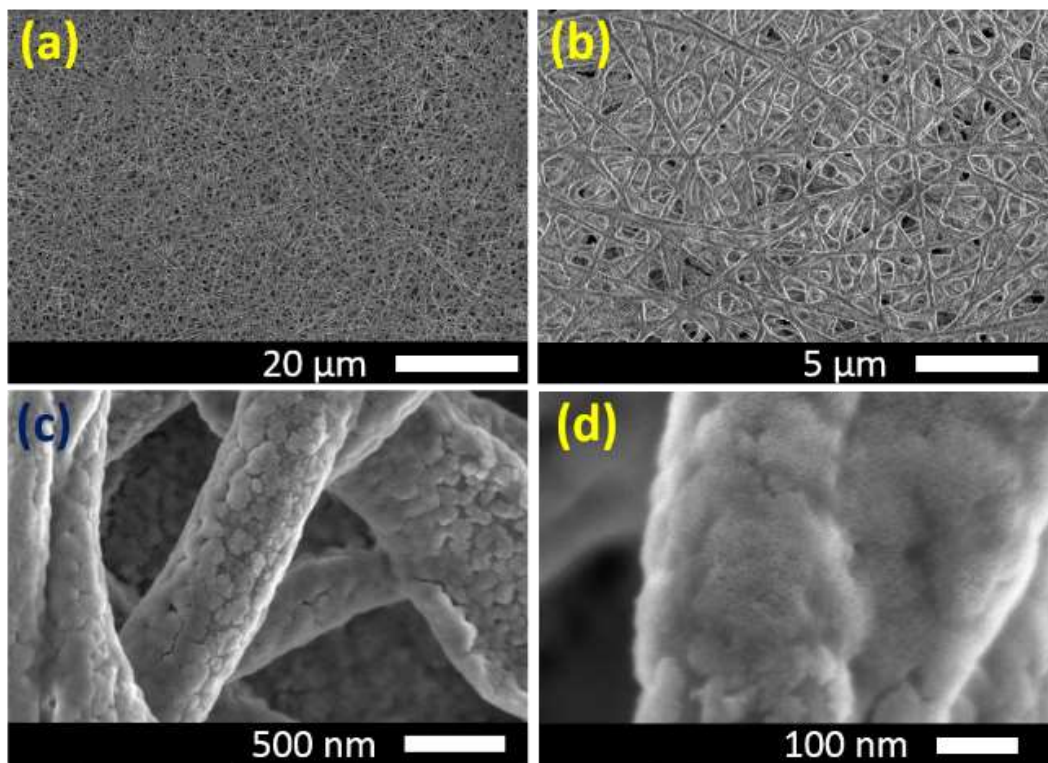


**Figure 3.11.** Post-mortem SEM images of working electrodes after 200 cycles at  $750 \text{ mA g}^{-1}$  ( $2C$ ) of (a) CNFs and (b) 20 wt% GO shows the nonwoven fiber structure is retained. High-resolution images of TRGO/CNFS shows a (c) stable and (d) porous SEI film on the fiber surface.

Electrochemical impedance spectroscopy (EIS) provided internal resistance values as a function of cycle number on delithiated electrodes. Between each EIS measurement, the half-cells were charged/discharged at  $75 \text{ mA g}^{-1}$  ( $C/5$ ). Formation cycles were not conducted on half-cells analyzed using EIS, resulting in an incomplete SEI after the first cycle. The incomplete SEI increased the impedance of each CNF and TRGO/CNF electrode after the first cycle. Between the 2<sup>nd</sup> and 5<sup>th</sup> cycles, a complete SEI formed on the electrode surface, which

reduced the half-cell impedance. The impedance data were fit to an equivalent circuit (**inset, Figure 3.12**) to deconvolute and quantify the change in resistances with cycle number. The circuit comprised a high-frequency solution resistance,  $R_s$ , a medium-frequency film resistance,  $R_{SEI}$ , and a low-frequency charge-transfer resistance,  $R_{CT}$ . A constant-phase element was used to model Li diffusion at low frequencies. A solution resistance of  $4.7 \Omega$  (not shown in Figure 12) irrespective of sample and cycle number indicated similar electrode/electrolyte interactions. The TRGO/CNF electrode with 5 wt% GO displayed the largest film resistance (**Figure 3.12a**), possibly due to optimal GO exfoliation during electrospinning and sonication. After 5 cycles, a stable SEI formed and the film resistance remained relatively constant. The  $R_{CT}$  (**Figure 3.12b**) of uncycled cells correlated positively with added GO; that is, a higher TRGO concentration decreased the charge-transfer resistance. After the SEI formed, the  $R_{CT}$  of the delithiated electrodes decreased to a value equal to or less than the  $R_{CT}$  of fully discharged electrodes before cycling. Although 5 wt% TRGO/CNFs displayed the highest capacity, the electrodes also displayed the largest resistances. This trend is under further investigation. Moreover, further examination is needed to discern if a decrease in  $R_{CT}$  is observed at higher charging rates over prolonged cycling.

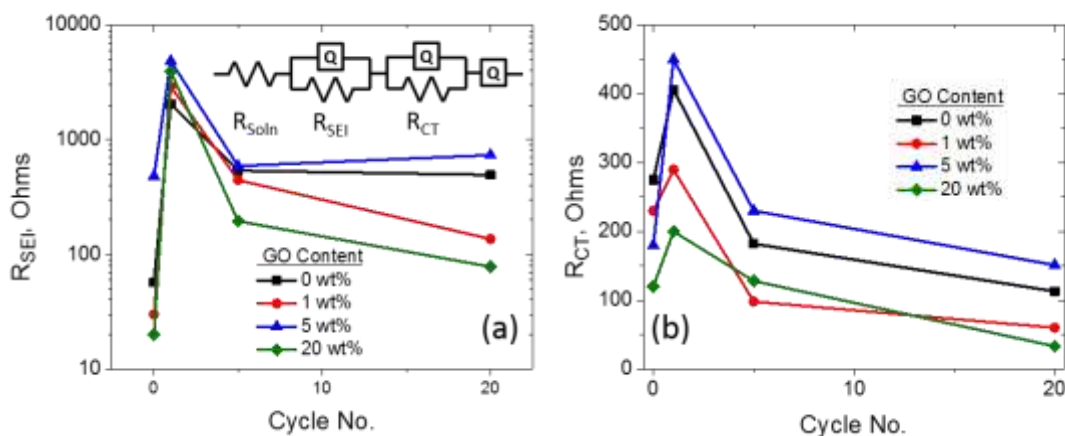


**Figure 3.12.** The (a) film resistance and (b) charge-transfer resistance over 20 cycles for delithiated CNF and TRGO/CNF electrodes cycled at  $75 \text{ mA g}^{-1}$ . The inset in Figure 3.11a shows the equivalent circuit used to model the system.

### 3.4. Summary

We report enhanced capacity and electrical conductivity of graphene-containing CNFs, compared to CNFs, in Li-ion anodes. Concentrations ranging from 0 - 20 wt% GO were dispersed in PAN solutions and electrospun to produce GO/PAN nanofibers. Rheological data of the nanofiber precursor solutions revealed that the induced shears from electrospinning cleave GO networks formed at GO loadings  $>5 \text{ wt\%}$ . The GO/PAN nanofibers were heat-treated to produce TRGO/CNFs. The low carbonization temperature ( $650^\circ\text{C}$ ) resulted in fibers with disordered carbon structures, as measured via Raman spectroscopy. The addition of GO to the fibers reduced disorder in carbon structure (producing larger graphitic domains), and thus, enhanced the electrical conductivity of the mats, compared to CNFs. The enhancement in conductivity may also be attributed to TRGO sheets conductively connecting the CNFs, as apparent in SEM images. Half-cell cycling of the TRGO/CNFs showed that CNFs benefitted from GO addition by increasing the charge capacity; composite fibers with 5 wt% TRGO

performed the best (40% increase in capacity at C/10 and 400% increase in capacity at 2-C compared to CNFs). Further, no capacity fade and CEs >99% were observed after 200 charge/discharge cycles for the 5 wt% TRGO/CNF electrodes. Capacity increases may reach a maximum at 5 wt% GO loading due to optimal exfoliation, which resulted in a composite mat with fragmented fibers. Despite fragmentations, the TRGO/CNF mats maintained their fiber structure after 200 cycles. The TRGO/CNF mats provide a material with conductivity, composition, and nano-architecture favorable for LIB anodes without the use of a binder or a conductive additive. The results reported in this work contribute to improving the capacity of carbon electrode materials, and provide a positive outlook on a new class of composite carbon materials for Li-ion battery anodes.

### 3.5. References

- (1) Chen, J.; Xu, L.; Li, W.; Gou, X.  $\alpha$ -Fe<sub>2</sub>O<sub>3</sub> Nanotubes in Gas Sensor and Lithium-Ion Battery Applications *Adv. Mater* 2005, 17, 582–586.
- (2) Wang, B.; Chen, J. S.; Wu, H. B.; Wang, Z.; Lou, X. W. Quasiemulsion-Templated Formation Of  $\alpha$ -Fe<sub>2</sub>O<sub>3</sub> Hollow Spheres With Enhanced Lithium Storage Properties *J. Am. Chem. Soc* 2011, 133, 17146–17148.
- (3) Idota, Y.; Kubota, T.; Matsufuji, A. Tin-Based Amorphous Oxide : A High-Capacity Lithium-Ion-Storage Material *Science* 1997, 276, 1395–1397.
- (4) Winter, M.; Besenhard, È. O. Electrochemical Lithiation of Tin and Tin-Based Intermetallics and Composites *Electrochim. Acta* 1999, 45, 31–50.
- (5) Wang, Y.; Lee, J. Y.; Deivaraj, T. C. Tin Nanoparticle Loaded Graphite Anodes for Li-Ion Battery Applications *J. Electrochem. Soc* 2004, 151, A1804- A1809.
- (6) Xu, Y.; Qing, L.; Zhu, Y.; Liu, Y.; Langrock, A.; Zachariah, M. R.; Wang, C. Uniform Nano-Sn/C Composite Anodes for Lithium Ion Batteries *Nano Lett* 2013, 13, 470–474.

- (7) Green, M.; Fielder, E.; Scrosati, B.; Wachtler, M.; Moreno, J. S. Structured Silicon Anodes for Lithium Battery Applications *Electrochem. Solid-State Lett* 2003, 6, A75-A79.
- (8) Chan, C. K.; Peng, H.; Liu, G.; McIlwrath, K.; Zhang, X. F.; Huggins, R. A.; Cui, Y. High-Performance Lithium Battery Anodes Using Silicon Nanowires *Nat. Nanotechnol* 2008, 3, 31–35.
- (9) Magasinski, A.; Dixon, P.; Hertzberg, B.; Kvit, A.; Ayala J.; Yushin, G. High-Performance Lithium-Ion Anodes Using a Hierarchical Bottom-Up Approach *Nat. Mater* 2010, 9, 353–358.
- (10) Dufficy, M. K.; Khan, S. A.; Fedkiw, P. S. Galactomannan Binding Agents for Silicon Anodes in Li-Ion Batteries *J. Mater. Chem. A* 2015, 3, 12023–12030.
- (11) Obrovac, M. N.; Christensen, L. Structural Changes in Silicon Anodes During Lithium Insertion/Extraction *Electrochem. Solid-State Lett* 2004, 7, A93-A96.
- (12) Winter, B. M.; Besenhard, J. O.; Spahr, M. E.; Novák, P. Insertion Electrode Materials for Rechargeable Lithium Batteries *Adv. Mater* 1998, 10, 725–763.
- (13) Goodenough, J. B.; Kim, Y. Challenges for Rechargeable Li Batteries *Chem. Mater* 2010, 22, 587–603.
- (14) Zhang, S. S.; Xu, K.; Jow, T. R.; Electrochemical Impedance Study on the Low Temperature of Li-Ion Batteries *Electrochim. Acta* 2004, 49, 1057–1061.
- (15) Liu, Y.; Xue, J. S.; Zheng, T.; Dahn, J. R. Mechanism of Lithium Insertion in Hard Carbons *Carbon* 1996, 34, 193–200.
- (16) Lee, K. T.; Lytle, J. C.; Ergang, N. S.; Oh, S. M.; Stein, A. Synthesis and Rate Performance of Monolithic Macroporous Carbon Electrodes for Lithium-Ion Secondary Batteries *Adv. Funct. Mater* 2005, 15, 547–556.
- (17) Guo, P.; Song, H.; Chen, X. Electrochemical Performance of Graphene Nanosheets as Anode Material for Lithium-Ion Batteries *Electrochem. Commun* 2009, 11, 1320–1324.
- (18) Yoo, E.; Kim, J.; Hosono, E.; Zhou, H. S.; Kudo, T.; Honma, I. Large Reversible Li Storage of Graphene Nanosheet Families for Use in Rechargeable Lithium Ion Batteries *Nano Lett* 2008, 8, 2277–2282.
- (19) Liang, M.; Zhi, L. Graphene-Based Electrode Materials for Rechargeable Lithium Batteries *J. Mater. Chem* 2009, 19, 5871-5878.

- (20) Li, D.; Xia, Y. Electrospinning of Nanofibers: Reinventing the Wheel? *Adv. Mater* 2004, 16, 1151–1170.
- (21) Chien, A. T.; Liu, H. C.; Newcomb, B. A.; Xiang, C.; Tour, J. M.; Kumar, S. Polyacrylonitrile Fibers Containing Graphene Oxide Nanoribbons *ACS Appl. Mater. Interfaces* 2015, 7, 5281–5288.
- (22) Matsumoto, H.; Imaizumi, S.; Konosu, Y.; Ashizawa, M.; Minagawa, M.; Tanioka, A.; Lu, W.; Tour, J. M. Electrospun Composite Nanofiber Yarns Containing Oriented Graphene Nanoribbons *ACS Appl. Mater. Interfaces* 2013, 5, 6225–6231.
- (23) Tai, Z.; Yan, X.; Lang, J.; Xue, Q. Enhancement Of Capacitance Performance of Flexible Carbon Nanofiber Paper by Adding Graphene Nanosheets *J. Power Sources* 2012, 199, 373–378.
- (24) Stankovich, S.; Dikin, D. A.; Piner, R. D.; Kohlhaas, K. A.; Kleinhammes, A.; Jia, Y.; Wu, Y.; Nguyen, S. T.; Ruoff, R. S. Synthesis Of Graphene-Based Nanosheets Via Chemical Reduction Of Exfoliated Graphite Oxide *Carbon* 2007, 45, 1558–1565.
- (25) Loebl, A. J.; Oldham, C. J.; Devine, C. K.; Gong, B.; Atanasov, S. E.; Parsons, G. N.; Fedkiw, P. S. Solid Electrolyte Interphase on Lithium-Ion Carbon Nanofiber Electrodes by Atomic and Molecular Layer Deposition *J. Electrochem. Soc* 2013, 160, A1971– A1978.
- (26) Fitzer, E.; Frohs, W.; Heine, M. Optimization of Stabilization and Carbonization Treatment of PAN Fibres and Structural Characterization of the Resulting Carbon Fibres *Carbon* 1986, 24, 387–395.
- (27) Jur, J. S.; Sweet, W. J.; Oldham, C. J.; Parsons, G. N. Atomic Layer Deposition of Conductive Coatings on Cotton, Paper, and Synthetic Fibers: Conductivity Analysis and Functional Chemical Sensing Using ‘All-Fiber’ Capacitors *Adv. Funct. Mater* 2011, 21, 1993–2002.
- (28) Kim, C.; Yang, K.S.; Kojima, M.; Yoshida, K.; Kim, Y. J.; Kim, Y. A.; Endo, M. Fabrication of Electrospinning-Derived Carbon Nanofiber Webs for the Anode Material of Lithium-Ion Secondary Batteries *Adv. Funct. Mater* 2006, 16, 2393-2397.
- (29) Kim, H.; Abdala, A. A.; Macosko, C. W. Graphene/Polymer Nanocomposites *Macromolecules* 2010, 43, 6515–6530.
- (30) Fong, H.; Chun, I.; Reneker, D. H. Beaded Nanofibers Formed During Electrospinning *Polymer* 1999, 40, 4585–4592.

- (31) Walls, H.J.; Fedkiw, P. S.; Zawodzinski, T. A.; Khan, S. A. Ion Transport in Silica Nanocomposite Electrolytes *J. Electrochem. Soc* 2003, 150, E165- E174.
- (32) Burns, N. A.; Naclerio, M. A.; Shojaei, A.; Raghavan, S. R.; Khan, S. A. Nanodiamond Gels In Nonpolar Media: Colloidal And Rheological Properties *J. Rheol* 2014, 58, 1599-1614.
- (33) Walls, H. J.; Caines, S.B.; Sanchez, A. M.; Khan, S. A. Yield Stress and Wall Slip Phenomena in Colloidal Silica Gels *J. Rheol* 2003, 47, 847-868.
- (34) Stankovich, S.; Piner, R. D.; Nguyen, S. T.; Ruoff, R. S. Synthesis and Exfoliation of Isocyanate-Treated Graphene Oxide Nanoplatelets *Carbon* 2006, 44, 3342–3347.
- (35) Kakida, H.; Tashiro, K.; Kobayashi, M. Mechanism and Kinetics of Stabilization Reaction of Polyacrylonitrile and Related Copolymers I. Relationship Between Isothermal DSC Thermograms and FT/IR Spectral Change of an Acrylonitrile/Methacrylic Acid Copolymer *Polym. J* 1996, 28, 30–34.
- (36) Dreyer, D. R.; Park, S.; Bielawski, C. W.; Ruoff, R. S. The Chemistry of Graphene Oxide *Chem. Soc. Rev* 2010, 39, 228–240.
- (37) Dikin, D. A.; Stankovich, S.; Zimney, E. J.; Piner, R. D.; Dommett, G. H. B.; Evmenenko G.; Nguyen S. T.; Ruoff, R. S. Preparation and Characterization of Graphene Oxide Paper *Nature* 2007, 448, 457–460.
- (38) Allen, R. A.; Ward, I. M.; Bashir, Z. The Variation of the d-Spacings with Stress in the Hexagonal Polymorph of Polyacrylonitrile Polymer 1994, 35, 4035–4040.
- (39) Mcallister, M. J.; Li, J. L.; Adamson, D.H.; Schniepp, H. C.; Abdala, A. A.; Liu, J.; Herrera-Alonso, M; Milius, D. L.; Car, R.; Prud'homme, R. K.; Aksay, I. A.. Single Sheet Functionalized Graphene by Oxidation and Thermal Expansion of Graphite *Chem. Mater* 2007, 19, 4396–4404.
- (40) Jung, I.; Dikin, D. A.; Piner, R. D.; Ruoff, R. S. Tunable Electrical Conductivity of Individual Graphene Oxide Sheets Reduced at 'Low' Temperatures *Nano Lett* 2008, 8, 4283–4287.
- (41) Ferrari, A. C.; Robertson, J. Resonant Raman Spectroscopy of Disordered, Amorphous, And Diamondlike Carbon *Phys. Rev. B* 2001, 64, 075414.
- (42) Knight, D. S.; White, W. B. Characterization of Diamond Films by Raman Spectroscopy *J. Mater. Res* 1989, 4, 385–393.

- (43) Tuinstra, F.; Koenig, J. L. Raman Spectrum of Graphite *J. Chem. Phys* 1970, 53, 1126–1130.
- (44) Landi, B. J.; Ganter, M. J.; Cress, C. D.; DiLeo, R. A.; Raffaele, R. P. Carbon Nanotubes for Lithium Ion Batteries *Energy Environ. Sci* 2009, 2, 638-654.
- (45) Zhang, S.; Ding, M. S.; Xu, K.; Allen, J.; Jow, T. R. Understanding Solid Electrolyte Interface Film Formation on Graphite Electrodes *Electrochem. Solid-State Lett* 2001, 4, A206- A208.
- (46) Wang, G.; Wang, B.; Wang, X.; Park, J.; Dou, S.; Ahn, H.; Kim, K.. Sn/Graphene Nanocomposite with 3D Architecture for Enhanced Reversible Lithium Storage in Lithium Ion Batteries *J. Mater. Chem* 2009, 19, 8378-8384.
- (47) Bulusheva, L. G.; Okotrub, A. V.; Kurennya, A. G.; Zhang, H.; Zhang, H.; Chen, X.; Song, H. Electrochemical Properties of Nitrogen-Doped Carbon Nanotube Anode in Li-Ion Batteries *Carbon* 2011, 49, 4013–4023.
- (48) Hou, H.; Ge, J. J.; Zeng, J.; Li, Q.; Reneker, D. H.; Greiner, A.; Cheng, S. Z. D. Electrospun Polyacrylonitrile Nanofibers Containing a High Concentration of Well-Aligned Multiwall Carbon Nanotubes. *Chem. Mater.* 2005, 17, 967–973.
- (49) Zhao, X.; Hayner, C. M.; Kung, M. C.; Kung, H. H. In-Plane Vacancy-Enabled High-Power Si-Graphene Composite Electrode for Lithium-Ion Batteries *Adv. Energy Mater* 2011, 1, 1079–1084.
- (50) Wu, Y.; Reddy, M. V.; Chowdari, B. V. R.; Ramakrishna, S. Long-Term Cycling Studies on Electrospun Carbon Nanofibers as Anode Material for Lithium Ion Batteries *ACS Appl. Mater. Interfaces* 2013, 5, 12175–12184.

## **Chapter 4. Effects of Composition and Structure on Performance of Tin/Graphene-Containing Carbon Nanofibers for Li-ion Anodes**

Chapter 4 is essentially a manuscript by Martin K. Dufficy, Sheng-Yang Huang, Saad A. Khan, and Peter S. Fedkiw that was submitted to *The Journal of Physical Chemistry C*

**Abstract:**

Tin is a promising replacement for graphite anodes in Li-ion batteries (994 mAh g<sup>-1</sup> for Sn vs. 372 mAh g<sup>-1</sup> for graphite), but suffers from particle pulverization upon lithiation that causes capacity fade. Herein, thermally reduced graphene oxide-containing carbon nanofibers (TRGO/CNFs) are used as scaffolds to house Sn/SnO<sub>2</sub> particles, enhance anode capacity beyond graphite, and prolong cycle life of Sn-based electrodes. This study attempts to elucidate structure-composition relationships of tin-TRGO/CNF electrodes that lead to increased capacity retention. Composition and morphology of tin-TRGO/CNFs are assessed as a function of heat-treatment temperature and Sn loading as a means to understand and correlate electrochemical performance with physical features. We find: (1) the oxidation state of tin in TRGO/CNFs is determined by temperature-dependent, thermal-decomposition products of polyacrylonitrile-derived CNFs, and (2) precursor Sn(IV) loadings ≤ 10 wt% in the tin-TRGO/CNFs lead to Sn(0) or SnO<sub>2</sub> particles embedded within the fiber + TRGO matrix. Electrodes with precursor Sn(IV) loading ≤ 10 wt% have smaller tin particles than electrodes with Sn(IV) loadings >10 wt%, and have longer cycle-lives; reversible capacities of ~ 600 mAh g<sup>-1</sup> are observed at 0.2-C rates, while capacities of ~ 400 mAh g<sup>-1</sup> are observed after hundreds of cycles at 2-C rates. The durable graphene-containing nanofiber matrix, coupled with the high-capacity of tin, provides a promising anode material for Li-ion cells.

#### 4.1. Introduction

Advancements in mobile technology require electrochemical energy storage devices with an energy and power density beyond that of current Li-ion batteries. Enhanced Li-ion battery performance may be achieved with new active materials that exhibit charge capacities beyond carbon.<sup>1-3</sup> Tin is an attractive anode material with a large theoretical charge capacity (994 mAh g<sup>-1</sup>, 1990 mAh cm<sup>-3</sup>), but suffers from particle pulverization due to catastrophic mechanical strains at full lithiation.<sup>4</sup> Pulverization results in electronic isolation—caused by recurrent solid-electrolyte interphase (SEI) formation—and a short cycle life. One proposed method to cope with strains of Li-insertion is to form composite tin materials, such as tin alloys or Sn/C materials. A battery using tin alloy anodes, introduced by Sony under the name Nexelion,<sup>5,6</sup> saw limited success due to capacity fade and short cycle life. Another common method to cope with the frail Sn-Li complex is to use the oxide of tin. Fuji introduced batteries with tin-composite oxide anodes under the name Stalion,<sup>7</sup> which never reached commercialization due to its large capacity fade. Thus, new methods to extend the cycle-life of tin-based anodes are a worthy research thrust. Herein, we report upon tin/carbon composites as a means to enhance Sn-based anode cycle life.

Carbon composites have long been a common method to enhance electrode cycle life.<sup>8</sup> Moreover, carbon nanofibers (CNFs) provide a favorably-sized support for composite electrodes for fast Li-diffusion and high-rate capabilities.<sup>9</sup> CNFs are also durable materials, and thus composite materials (e.g., Sn particles) may impart strains to the CNF matrix during volume expansions to inhibit pulverization; volume expansions in the LiC<sub>x</sub> complex are small

(~10% graphene layer expansion) relative to the  $\text{Li}_x\text{Sn}$  complex (~300% volume expansion).<sup>10</sup> The CNF electrode is well characterized,<sup>11,12</sup> and long cycle lives have been reported<sup>13</sup> with use of CNF anodes produced via electrospinning. The nonwoven carbon architecture from electrospinning negates the need for binder and conductive additive,<sup>14,15</sup> which enhances electrode gravimetric energy density.

We recently demonstrated that thermally reduced graphene oxide-containing carbon nanofibers (TRGO/CNFs) increase charge capacity and electronic conductivity compared to CNFs.<sup>16</sup> As a continuation of our investigation of TRGO/CNFs anodes for LIBs, we study composite CNFs as a matrix for embedding Sn or  $\text{SnO}_2$  particles to produce Sn- or  $\text{SnO}_2$ -containing TRGO/CNF electrodes. While Sn-containing CNFs have been applied to LIB anodes,<sup>12,14-16</sup> such studies frequently highlight the electrochemical cycling behavior and minimize importance of structure evolution. Studies on production of Sn or  $\text{SnO}_2/\text{C}$  composites from precursors such as  $\text{SnCl}_4$  and polyacrylonitrile (PAN, a common CNF precursor) do not discuss simultaneous Sn(II) or (IV) reduction and the carbonization process. Additionally, to our knowledge, the influence of tin loading on fiber morphology has not been reported. Herein, we report the formation and evolution of Sn-TRGO/CNFs electrodes; we explore the influence of heat-treatment temperature (HTT) on Sn oxidation state, and the influence of Sn-precursor concentration on particle size after heat treatment. We relate physical parameters favorable for LIB electrodes (composition, morphology, Sn-particle size, etc.) to electrochemical half-cell cycling performance. The  $\text{SnO}_2$ -based electrodes produced in this work revealed capacities ~ 400 mAh  $\text{g}^{-1}$  after 900 cycles at 2-C rates, and Sn-based electrodes revealed similar capacities

~ 400 mAh g<sup>-1</sup> after 500 cycles at 2-C rates. Long-cycle lives are ascribed to preservation of TRGO/CNF structure, which withstands structural rearrangement of Sn during Li-insertion. This study shows Sn and SnO<sub>2</sub>-TRGO/CNF is promising electrode material for Li-ion cells.

## 4.2. Experimental

### 4.2.1 Preparation of electrospinning solution

Appropriate amounts of SnCl<sub>4</sub> (Sigma Aldrich, 99.995%) were added to anhydrous dimethylformamide (DMF, Sigma Aldrich, 99.8%) in an argon-filled glove box, such that Sn(IV) content in dry polymer fibers comprised 0, 5, 10, 15, or 30 wt%. Anhydrous ethylene glycol (Sigma Aldrich, 99.8%) was added to the SnCl<sub>4</sub>/DMF mixture in a ratio of 4:1 mol ethylene glycol:SnCl<sub>4</sub>. Graphite oxide<sup>16</sup> was then added to the solution, resulting in a loading of 5 wt% relative to dry polymer-fiber content. The mixture was sealed, taken out of the glove box, and sonicated for 1 hour to exfoliate graphite oxide into single-to-multilayer graphene oxide (GO) sheets. After sonication, polyacrylonitrile (PAN, Scientific Polymer Products, 150 kDa) was added to the dispersion in ambient conditions, resulting in an 8 wt% polymer solution, and stirred overnight at 60°C.

### 4.2.2 Preparation of Sn-containing fibers

The electrospinning precursor solution was cooled to room temperature and then electrospun using a needle-and-plate collector system, as described elsewhere.<sup>17</sup> Typical process parameters include flow rate, voltage, tip-to-collector plate distance, and relative humidity of 1 mL h<sup>-1</sup>, 5-7 kV, 17 cm, and 50-60%, respectively. Composite polymer fibers amassed in a nonwoven mat on an Al-foil collector to create Sn-GO/PAN fibers. The mats

were thermally treated in a quartz tube furnace using a two-step process. The first thermal treatment, stabilization, was conducted under dry air at 275°C for 2 hours, using a heating ramp rate of 5°C min<sup>-1</sup> followed by uncontrolled cooling to room temperature. The second heat treatment, carbonization, was conducted under nitrogen at 650 or 850°C using a heating rate of 2°C min<sup>-1</sup>, a dwell time of 1 hour at maximum temperature, and uncontrolled cooling to room temperature (typically 3 hours). The quartz furnace was purged with nitrogen for 3 hours prior to carbonization. The notation used to represent the electrodes produced in this study denotes precursor Sn(IV) wt% in the polymer fibers, followed by the carbonization temperature (in °C). For example, a tin-GO/PAN solution electrospun with 10 wt% Sn(IV) and carbonized at 650°C is denoted 10Sn650.

#### *4.2.3 Characterization of Sn-containing fibers*

Solution rheology was measured using an AR2000 (TA Instruments) stress-controlled rheometer with 40-mm diameter, parallel-plate geometry and a gap size of 100 µm. Ionic conductivity of the electrospinning precursor solution was measured using a Mettler Toledo S47-K conductivity meter. Scanning electron microscope (SEM) images were captured on a FEI Verios 460L XHR equipped with an energy-dispersive X-ray spectroscopy (EDS) detector. Polymer fibers were sputter coated with 4 nm of Au/Pd alloy to increase conductivity before imaging. Fiber-diameter distributions were obtained by measuring diameters from SEM images of 100 fibers from three locations on a nonwoven mat. Transmission electron microscope (TEM) images were taken on a JEOL 2010F, which was also equipped with an EDS detector. To prepare samples on TEM grids, we first dispersed fiber mats in acetone

followed by sonication for 1 hour. Thermogravimetric analysis (TGA) of composite-polymer fibers was conducted on a Discovery Series thermogravimetric analyzer (TA Instruments). Bulk structure analysis was measured on a Rigaku SmartLab X-ray diffractometer (Cu K $\alpha$ ,  $\lambda = 1.5406 \text{ \AA}$ ). Surface analysis of fibers was conducted on a SPECS X-ray photoelectron spectroscopy (XPS) unit equipped with a dual Al/Mg anode monochromator source. The carbon transition (C 1s, 285 eV) was used to normalize the spectra. Samples were dried in a vacuum oven overnight at 100°C prior to XPS analysis.

#### *4.2.4 Electrochemical characterization*

Carbonized mat working electrodes were punched into 1.11-cm diameter discs from the electrospun mat and dried in a vacuum oven overnight at 100°C. The discs were transferred to an argon-filled glove box. Carbonized mats (areal loading: 1-1.3 mg cm<sup>-2</sup>) were placed on a Cu foil current collector and cycled against metallic Li (Sigma Aldrich, 99%) in 2032 half-cells. The electrolyte, 1 M LiPF<sub>6</sub> (>99% purity, BASF) dissolved in ethylene carbonate (EC, 99% purity, Sigma Aldrich) and ethyl methyl carbonate (EMC, 99% purity, Sigma Aldrich) comprising a 1:1 wt% EC:EMC solution, was added by pipette onto the working electrode (~50  $\mu\text{L}$ ) and Celgard separator (~50  $\mu\text{L}$ ). Prior to use, the electrolyte was dried in 4  $\text{\AA}$  molecular sieves (Sigma Aldrich) to a water content < 10 ppm. All half-cells underwent a formation cycle at C/24 prior to further cycling. Charge/discharge cycling and cyclic voltammetry (CV) was conducted on a Bio-Logic VMP3 between 2.5 and 0.01 V vs. Li/Li<sup>+</sup>. Electrochemical measurements were conducted on at least 3 half-cells to assure reproducibility, typically within 10%.

### 4.3. Results and Discussion

#### 4.3.1 Characterization of Sn-fibers

Prior to thermal treatment, tin-polymer fibers were analyzed via SEM to observe fiber morphology (**Figure 4.1a-e**). Images in **Figure 4.1** show (1) a continuous network of fibers with fiber beading at Sn(IV) concentrations  $> 5$  wt%, and (2) fiber diameter increases with Sn-loading. As noted in our previous study,<sup>16</sup> the appearance of beads may be caused by encapsulated GO in the mats, which was added at 5 wt% to the fibers to increase the charge capacity and conductivity of CNFs. However, the beading observed at  $> 5$  wt% Sn(IV) loading (**Figure 4.1c-e**) is not due to GO sheets, as evidenced by a different morphology than reported in our previous study on TRGO/CNFs in the absence no Sn(IV),<sup>16</sup> and may be attributed to decreased “effective” polymer concentration as filler content increased. We measured electrospinning precursor solution properties that govern the electrospinning process, such as solution rheology and ionic conductivity, in attempt to correlate fiber diameter and beading in the fibers with Sn(IV) loading. Steady-shear rheology (**Appendix Figure A1**) of the electrospinning solution revealed viscosity (1) to be independent of SnCl<sub>4</sub> concentration at high-shear stresses (or shear rates), and (2) to marginally increase with EG addition (added 4:1 mol ratio EG:SnCl<sub>4</sub>). However, the increased viscosity we measured from EG addition ( $< 1$  Pa-s at high-shear stresses) is not significant to increase the fiber diameter. Interestingly, increasing SnCl<sub>4</sub> concentration, and thus ionic conductivity (**Figure 4.1f**), did not lead to smaller fiber diameters; it is generally accepted that increasing solution conductivity increases whipping instabilities of the polymer jet during electrospinning that reduces fiber diameter.<sup>18</sup>

Thus, we attribute the increase in fiber diameter to EG swelling in PAN; a larger EG content is associated with higher SnCl<sub>4</sub> concentration. Insets of **Figure 4.1a-e** show high-resolution images of a typical fiber extruded during the electrospinning process. The fibers produced are porous, which may be the result of volatilized solvent.

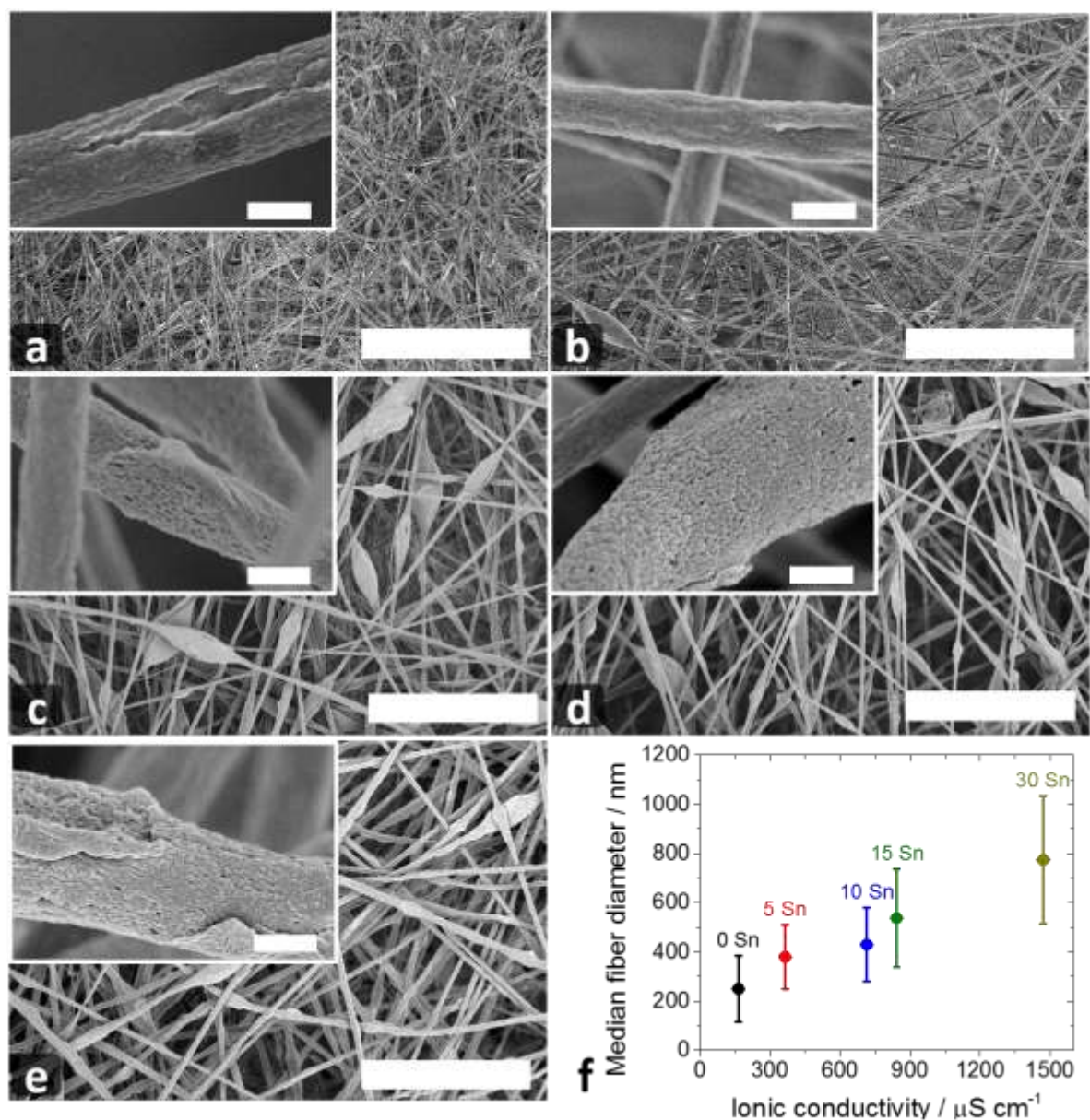


**Figure 4.1.** SEM images of nonwoven GO/PAN mats with (a) 0, (b) 5, (c) 10, (d) 15, and (e) 30 wt% Sn(IV). The scale bars represent 20  $\mu\text{m}$ . The insets show high-resolution SEM images of a typical fiber. Scale bars of insets represent 500 nm; (f) Fiber diameter plotted against ionic conductivity of electrospinning solution, with Sn(IV) loading [wt%] labeled on the plot.

Thermally treating (stabilization and carbonization) tin-GO/PAN fibers (to produce Sn- or SnO<sub>2</sub>-TRGO/CNFs) decreased diameters to values independent of Sn(IV) loading (**Appendix Figure A2**); the average fiber diameter ranged from 340 to 470 nm at 650°C and

280 to 330 at 850°C, but fiber diameter did not systematically increase with Sn(IV) loading. The diameter distributions (**Appendix Figure A2**) suggest EG swelled PAN to increase fiber size, as unevaporated EG generated larger resistances to whipping instabilities during electrospinning. Heat treatments also collapsed large pores (**Figure 4.1a-e** inset), although it is possible that heat-treated fibers retain a porous structure too small to discern in the SEM images.

As apparent by SEM, tin-TRGO/CNFs carbonized at 650°C produced similar morphologies, irrespective of Sn(IV) loading (**Appendix Figure A3**); we did not observe sintering or agglomeration of tin despite carbonization temperatures above the melting point of Sn (232°C). Increasing carbonization temperature from 650 to 850°C and Sn(IV) loadings > 5 wt% produced Sn particles on the fiber surface (**Figure 4.2**). Loadings of 5 wt% Sn(IV) (**Figure 4.2a, b**) produced fibers with a morphology similar to fibers in the absence of tin (**Appendix Figure A4**), suggesting that small Sn particles, not discernable at the magnifications employed, are present. An increased loading of 10 wt% Sn(IV) effected sparsely-decorated Sn particles on fibers (**Figure 4.2c, d**), however the majority of Sn appeared to be within the TRGO/CNF scaffolding. Sn(IV) loadings > 10 wt% produced fibers with abundant, large particles on the fiber surface. Mean Sn particle diameters of 830 and 330 nm were observed with 15 (**Figure 4.2e, f**) and 30 wt% Sn(IV) (**Figure 4.2g, h**), respectively. Similar Sn-aggregation has recently been reported with Sn(IV) heat treated at 700°C.<sup>19</sup>

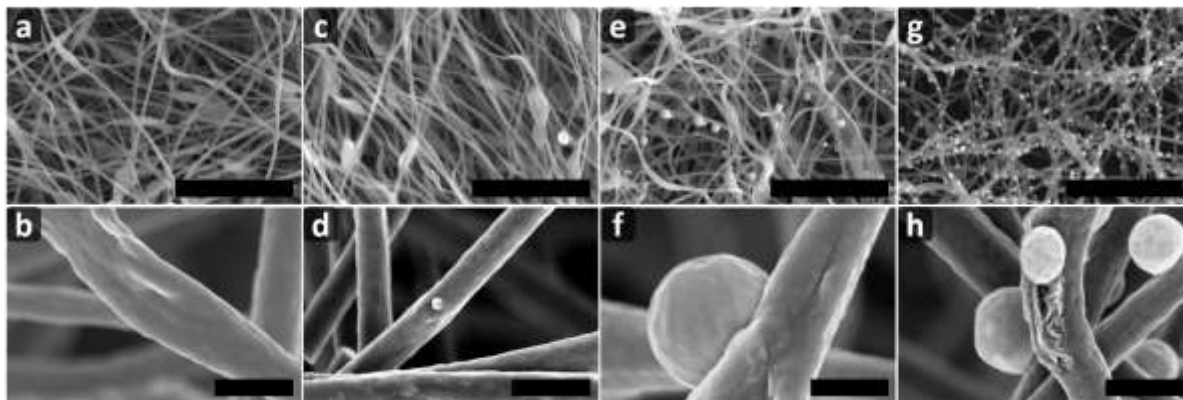


**Figure 4.2.** SEM images of TRGO/CNFs carbonized at 850°C with (a, b) 5, (c, d) 10, (e, f) 15, and (g, h) 30 wt% Sn(IV). Scale bars represent (a, c, e, and g) 10  $\mu$ m and (b, d, f, and h) 500 nm.

Heat treatments of tin-GO/PAN fibers likely produced temperature-dependent gaseous atmospheres, leading to unique fiber morphologies (previously seen in SEM images) and tin oxidation states. Carbonization of PAN releases gases such as  $H_2$ , HCN,  $NH_3$ , and  $CH_4$ ,<sup>20,21</sup> and evolution of particular gases during carbonization is temperature dependent.<sup>21</sup> It has been proposed that  $H_2$  off-gasses (producing a reducing atmosphere) at  $\sim 900^\circ C$ <sup>21</sup> as a product of reactions between hydrogenated carbons and nitrogen molecules in cyclic compounds, whereas  $N_2$  off-gasses at  $600^\circ C$  as a product of reactions between cyclic nitrogen compounds. We observed evidence of these two reactions (releasing  $H_2$  and  $N_2$ ) via derivative thermogravimetric analysis (DTG) of PAN fibers (**Appendix Figure A5**). DTG plots produced a broad peak at  $\sim 650^\circ C$  with a shoulder appearing at  $850^\circ C$ , which likely corresponded to thermal decomposition of PAN releasing  $N_2$  and  $H_2$ , respectively. We propose that  $H_2$  is a major PAN-decomposition product at  $850^\circ C$ , resulting in reduction and agglomeration of Sn(IV) to metallic Sn (as seen in **Figure 4.2c, d**). Such a mechanism is likely, as researchers<sup>22</sup> have shown that  $SnO_2$  reduces to Sn(0) at temperatures as low as  $450^\circ C$  in a  $H_2$  atmosphere. In contrast,  $N_2$  comprised the majority of decomposition gases released at  $650^\circ C$ , resulting in

SnO<sub>2</sub> particles in TRGO/CNFs. Sn-O bonds form *via* condensation reaction between SnCl<sub>4</sub> and EG, releasing HCl.<sup>23</sup> Thermal treatment then decomposed Sn-EG entities to SnO<sub>2</sub>.

We employed XPS on tin-GO/PAN fibers and tin-TRGO/CNFs carbonized at 650 and 850°C in an attempt to detect the presence of contaminants such as Cl, observe polymer degradation through the nitrogen signal, and identify tin oxidation state. Fibers with 10 wt% Sn(IV) loading were analyzed. Chlorine (4:1 mol Cl:Sn in precursor) was not detected on survey scans (**Figure 4.3a**), and produced weak signals on the Cl 2p transition (**Appendix Figure A6a**). Absence of Cl from the survey of as-spun fibers suggests a surface (< 10 nm) relatively free of Cl or HCl (product from condensation of SnCl<sub>4</sub> and EG). The XPS survey also shows decreasing N-content in the fibers, from 22 to 15 to 8 wt% N in as-spun fibers, and fibers heat-treated at 650 and 850°C, respectively, as PAN thermally degrades into a carbon-rich structure. We observed slightly lower binding energies than expected in the N 1s transition (**Appendix Figure A6b**) of tin-TRGO/CNFs, which may be due to metal-nitride (Sn-N) formation, as reported elsewhere.<sup>24</sup> Nonetheless, nitrogen-containing compounds in large quantities are undesired,<sup>25</sup> as they may result in the irreversible formation of LiN during LIB charge cycles and decrease capacity retention. Interestingly, Sn 3d<sub>5/2</sub> (**Figure 4.3b**) peaks in as-spun mats shifted positive ~1 eV upon carbonization, which suggests formation of the oxide (SnO<sub>2</sub> ~486.5-486.7 eV). As previously stated, Sn-O bonds initially formed in as-spun mats via a reaction between SnCl<sub>4</sub> and EG. Lower binding energies in as-spun fibers may be due, in part, to remaining Sn-Cl linkages. Broad Sn 3d peaks from fibers carbonized at 650 and 850°C are similar, and we were unable to distinguish if the open-air environment prior to XPS analysis

resulted in 1) formation of a native-surface oxide layer on large Sn(0) particles, or 2) complete oxidation of small Sn(0) particles near the fiber surface to create SnO<sub>2</sub> particles. We employed XRD in attempt to make this distinction.

Composite tin fibers carbonized at 650°C displayed amorphous structures, with diffraction patterns independent of tin loading (**Figure 4.3c**). Crystalline SnO<sub>2</sub> may be present in the form of small particles that do not generate diffraction patterns. Likewise, TRGO/CNFs carbonized at 850°C with  $\leq 10$  wt% Sn(IV) did not produce diffraction patterns (**Figure 4.3d**). Although large (and sparsely dispersed) particulates were observed in SEM images of 10Sn850 (**Figure 2d**), the sensitivity of XRD was insufficient to register a diffraction signal. The diffractions pattern of fibers with loadings  $\leq 10$  wt% Sn(IV) displayed the amorphous (002) phase of TRGO/CNFs ( $2\theta \approx 25^\circ$ , not shown), as we described elsewhere.<sup>16</sup> Greater than 10 wt% Sn(IV) loading formed crystalline structures of metallic Sn (**Figure 4.3d**); the peaks are associated with the large Sn particles that were observed via SEM. Thus, it is reasonable to infer that H<sub>2</sub> off-gassing occurred during the carbonization process to reduce Sn(IV) to Sn(0).

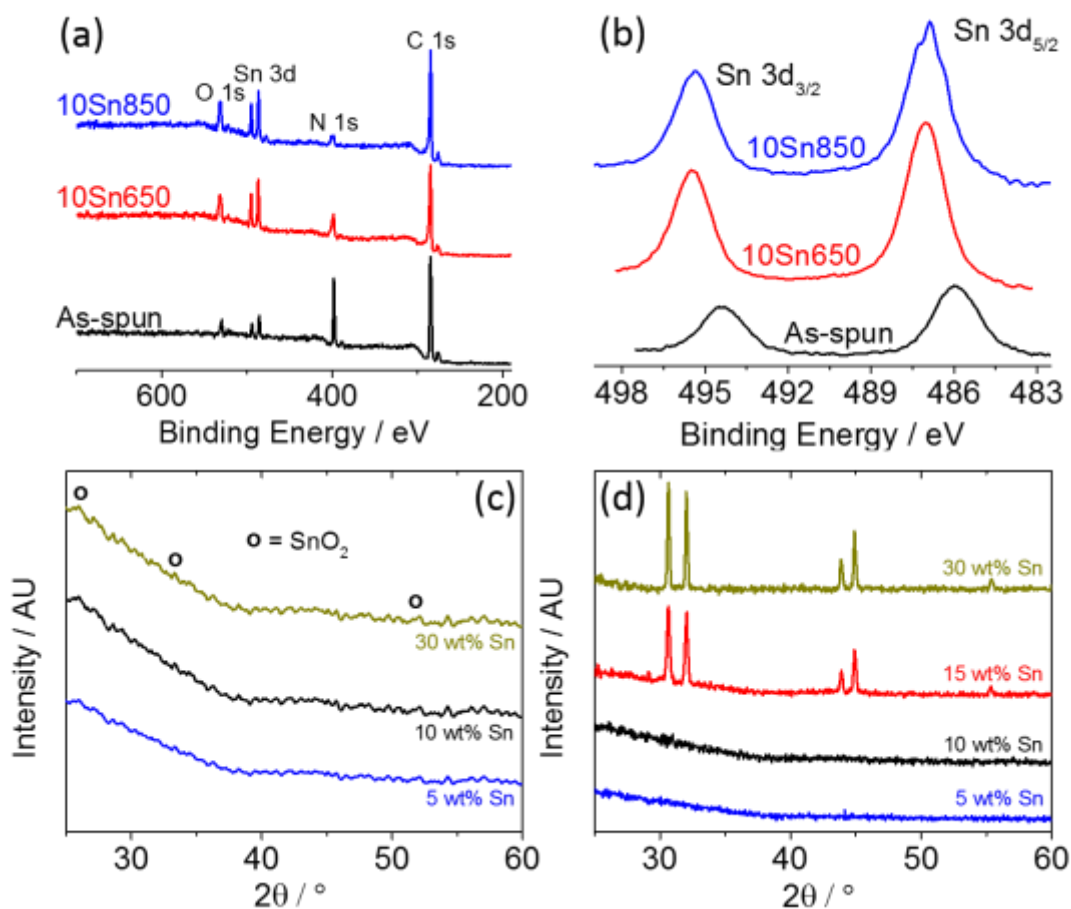


**Figure 4.3.** Surface and bulk characterization of Sn-containing fibers; XPS data of as-spun GO/PAN fibers containing 10 wt% Sn(IV), along with the ensuing spectra of fibers carbonized at 650 and 850°C showing (a) the survey and (b) high-resolution Sn 3d transition. XRD profiles for tin-TRGO/CNFs carbonized at (c) 650°C and (d) 850°C with Sn loadings labeled on the plot. The location of the strongest peaks associated with SnO<sub>2</sub>, if present, are labeled in (c)

In an attempt to detect Sn(0) or SnO<sub>2</sub> particles that were not found with XRD (e.g., fibers with low,  $\leq 10$  wt%, Sn(IV) loading), we examined heat-treated fibers under high-resolution TEM. As expected, tin-TRGO/CNFs heat-treated at 650°C did not contain crystalline particles; we merely observed the amorphous Sn/C structure (**Figure 4.4a**). On the other hand, tin-TRGO/CNFs carbonized at 850°C contained crystalline particles of SnO<sub>2</sub> that were visible near the fiber surface (**Figure 4.4b**). Particulates near the fiber surface may

originate from the mobility of low-molecular weight Sn-EG entities, which migrate to the air-fiber interface during heat treatments. Particles encapsulated within a fiber matrix are favorable for LIB cycling, as they may impart stresses onto the TRGO/CNF scaffolding during volume expansions of lithiation to minimize cracking. Measurements of lattice fringes confirmed presence of SnO<sub>2</sub> (JCPDS 41-1445) within TRGO/CNFs carbonized at 850°C, with a particle size < 15 nm. Particles of SnO<sub>2</sub> also appeared on TRGO that was protruding through the fiber surface (**Figure 4.4c**). Presence of tin particles on TRGO (or within few layers) may originate from hydrogen bonding interactions between terminal hydroxyl groups of EG-Sn entities and oxygen functional groups of GO in the electrospinning solution. Appearance of SnO<sub>2</sub> on TRGO/CNFs with 10 wt% Sn(IV) and carbonized at 850°C was not expected since we detected Sn(0) on TRGO/CNFs with >10 wt% Sn(IV) and carbonized at 850°C using XRD. However, we note that TEM sample preparation (exposure to air and sonication in acetone, which heats the sample to ~ 45°C) likely oxidized small Sn(0) particles on or near the TRGO/CNF surface to SnO<sub>2</sub>.

Well-dispersed tin-particulates in the anode presumably leads to uniform stress during lithiation and hinders regions of disproportionate stress that may lead to electrode cracking. Thus, a uniform Sn-particle dispersion is necessary to extend the cycle life of high-capacity anodes. We used EDS to determine the dispersion of tin within tin-TRGO/CNF fibers. **Figure 4.4d** shows typical EDS maps (acquired via STEM imaging) for 10Sn650. Regions of Sn appear dispersed throughout *many* fibers on the EDS image, however Sn-rich regions throughout *all* fibers could not be resolved (in a manner similar to element maps of carbon and

oxygen) due to curvature of the fibers, shadowing effects, and focal plane of the image. It should be noted that a small amount of Cl was observed via EDS, which produced a negligible peak ~2.6 keV in the EDS spectrum (**Appendix Figure A7b**). Coupling EDS and XPS data suggest a Cl content in tin-TRGO/CNFs < 0.2 wt%. Typical EDS maps of tin-TRGO/CNFs at 850°C are shown in **Appendix Figure A7-8**. Tin also appeared well-dispersed in TRGO/CNFs carbonized at 850°C and at low Sn(IV) loadings ( $\leq 10$  wt%), while larger tin loadings produced EDS maps with tin appearing both on large aggregated particles and dispersed throughout the fiber—not all tin aggregated into large Sn(0) particles. Interestingly, we found that EDS maps of Sn and N overlapped (**Appendix Figure A7a**). Overlapping Sn and N EDS maps, coupled with XPS data (**Appendix Figure A6b**) that show N 1s transitions at more negative binding energies than expected for Sn/C composites, may indicate formation of tin nitride upon thermal treatments. Tin nitride is produced via thermal treatment of Sn(IV) with NH<sub>3</sub> and N<sub>2</sub> gases<sup>26,27</sup> and may exist in small quantities in the fibers since NH<sub>3</sub> and N<sub>2</sub> are products of PAN carbonization. The lack of Sn<sub>x</sub>N<sub>y</sub> peaks on XRD suggests that small, amorphous regions of Sn<sub>x</sub>N<sub>y</sub> may exist. While reports suggest that nitrogen-doped carbons<sup>28,29</sup> (and perhaps doping Sn in the process) leads to enhanced cycling, to our knowledge the electrochemical performance of tin nitride has not been assessed.

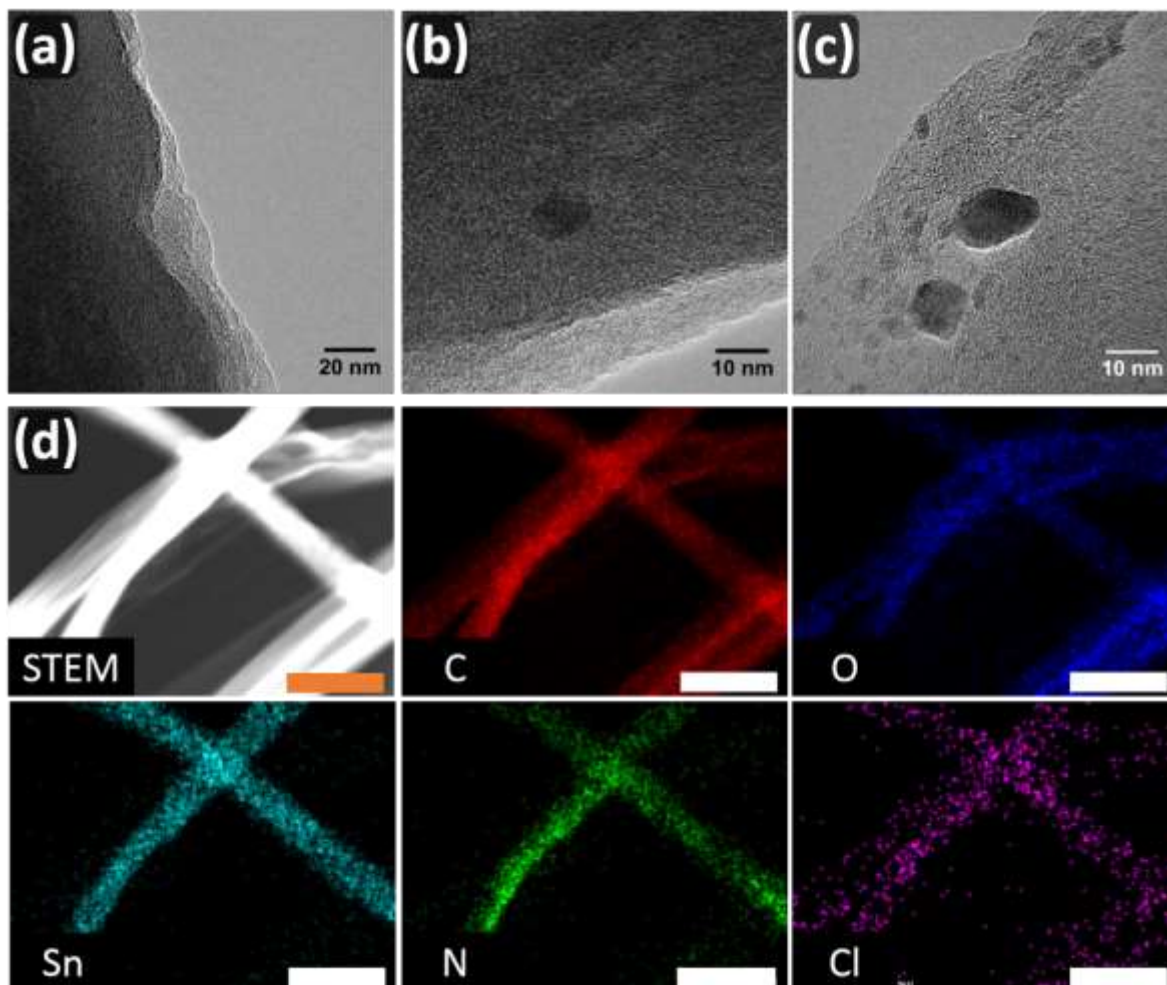
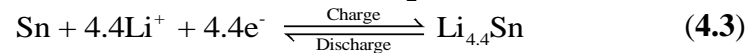
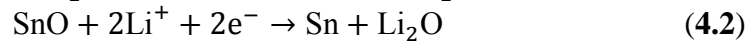
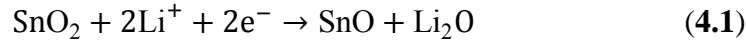


**Figure 4.4.** TEM images of (a) 10Sn650 (b,c) 10Sn850 (d) STEM image and corresponding EDS maps of 10Sn650. The element pertaining to each map is labeled in the lower left. Scale bars for EDS represent 1  $\mu\text{m}$ .

#### 4.3.2 Electrochemical characterization of Sn-containing fibers

Since we were unable to conclusively deduce the oxidation state of tin within fibers heat-treated at 650°C and Sn(IV) loadings <15 wt% in fibers heat-treated at 850°C using physical characterization methods, we employed CV as an electrochemical means to study composition of tin in the fibers. Working electrodes consisted of 10Sn650 and 10Sn850, identical to samples analyzed via XPS and TEM. Voltammograms of tin-TRGO/CNFs

carbonized at 650°C indicate presence of SnO<sub>2</sub> on the first cycle. The first cathodic polarization (**Figure 4.5a**) scan shows two peaks: (1) irreversible reduction of SnO<sub>2</sub> (**Reaction 4.1**) and electrolyte reduction causing SEI formation at ~0.7 V vs. Li/Li<sup>+</sup>, and (2) three overlapping peaks from SnO reduction (**Reaction 4.2**)<sup>30</sup>, Sn-Li complexation (**Reaction 4.3**), and Li-intercalation into carbon (until 0.01 mV). The irreversible nature of SnO<sub>2</sub> reduction is exemplified via CV, as the high-voltage reduction peak does not appear on the second cathodic cycle.



Unlike the voltammogram of 10Sn650, the first-cycle cathodic polarization of the 10Sn850 sample (**Figure 4.5b**) did not produce a broad peak at 0.7 V vs. Li/Li<sup>+</sup> related to SnO<sub>2</sub> reduction, which suggests the presence of Sn(0). Oxidized tin in TRGO/CNFs carbonized at 850°C (native surface oxide layers or SnO<sub>2</sub> particles near the electrode surface) did not contribute to appreciable reduction activity in the voltammograms. Thus, we infer the majority of tin in the fibers carbonized at 650°C and 850°C resides in the oxide and metallic state, respectively. Distinct phase transitions<sup>31</sup> in CV scans (labeled on **Figure 4.5b**) are present over 10 cycles. Reoccurrence of redox peaks over cycling suggest that the TRGO/CNF support provides stability for small Sn particles, and prevents catastrophic cracking of the frail Li-Sn complex. Broad peaks at ~1.2 V vs. Li/Li<sup>+</sup> during anodic polarization of Sn- and SnO<sub>2</sub>-based electrodes have been attributed to partial oxidation of Sn(0) particles with diameters on the order of 1 nm.<sup>32,33</sup> For comparison, voltammograms of TRGO/CNFs in the absence of tin

produced similar peaks at 1.2 V vs. Li/Li<sup>+</sup> with reduced magnitude (**Appendix Figure A9**). Thus, we attribute the low activity to the oxidation of small Sn(0) particles. The influence of tin oxidation state in TRGO/CNFs and fiber morphology on Li-ion half-cell cycling was subsequently evaluated.

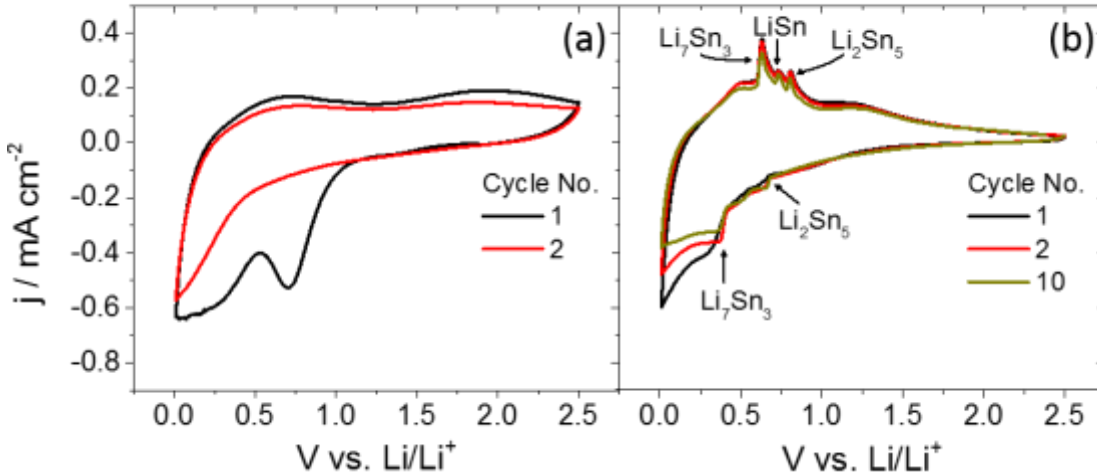


**Figure 4.5.** Typical CV profiles using scan rates of 0.1 mV s<sup>-1</sup> for (a) 10Sn650 and (b) 10Sn850 with phase transitions labeled.<sup>31</sup>

Prior to galvanostatic cycling, we approximated the specific theoretical (calculated) capacities. Theoretical capacities were approximated using Sn composition from EDS analysis (such that specific capacities accounted for entire mat weight) with the following equation:

$$\text{Capacity}_{\text{max}} \approx (1000 \text{ mAh/g})(x \text{ wt\% Sn}) + (375 \text{ mAh/g})(1 - x \text{ wt\% Sn})$$

Theoretical capacities, Sn concentration from EDS, and experimentally found, first-cycle lithiation capacities (using symmetrical constant current cycling at 0.05-C rates) are listed in **Table 4.1**. As a reminder, tin loadings in sample nomenclature are expressed in wt% of Sn(IV) in GO/PAN polymer fibers. Actual Sn content in heat treated fibers approximately doubles. For example, 10Sn650 and 10Sn850 contain ~ 20 and 21 wt% Sn, respectively.

On the first lithiation cycle at 0.05-C, working electrodes carbonized at 650°C exhibited capacities larger than calculated. For example, 5Sn650 electrodes displayed a capacity of 1465 mAh g<sup>-1</sup>, whereas 445 mAh g<sup>-1</sup> was calculated. The discrepancy is largely due to irreversible reduction of oxygen and nitrogen-containing entities (forming Li<sub>3</sub>N and Li<sub>2</sub>O) such as the electrochemical reduction of SnO<sub>2</sub>, as well as SEI formation. **Reaction 4.1-3** produce a theoretical charge capacity of 1494 mAh g<sup>-1</sup>, which is larger than the capacity from **Reaction 4.3** (~ 1000 mAh g<sup>-1</sup>) that we used to determine theoretical capacities for SnO<sub>2</sub>-TRGO/CNFs. In contrast, Sn-TRGO/CNF electrodes heat treated at 850°C exhibited first-cycle capacities closer to, but still greater than, calculated values (largely due to SEI formation). The thermal reduction of SnO<sub>2</sub> to Sn during carbonization of PAN at 850°C nullifies much of the irreversible capacity from **Reaction 4.1** and **2** on the first cycle. Increasing the carbonization temperature from 650 to 850°C produced higher coulombic efficiencies (**Table 4.1**), which we attribute to a more reduced electrode with less noncarbonaceous content; weight ratios of active (C + Sn) to inactive (N + O) material increased with carbonization temperature (**Appendix Figure A10**), which decreased irreversible capacity on the first cycle. Higher CEs observed in tin-TRGO/CNFs carbonized at 850°C, compared to those carbonized at 650°C, may also be due to less SEI formation, as specific surface area of carbonized PAN decreases with carbonization temperature.<sup>34</sup>

**Table 4.1:** List of calculated and experimentally found (actual) first-cycle lithiation capacities and coulombic efficiencies (CEs) in parentheses; calculated capacities were determined using Sn content from EDS. The table also shows the Sn(IV) content that was added to the fiber precursor solution and corresponding Sn content in the carbonized fibers.

[Sn(VI)] Wt%	[Sn] <sub>650</sub> (wt%)	Actual <sub>650</sub> [mAh g <sup>-1</sup> ] (CE %)	Calculated <sub>650</sub> [mAh g <sup>-1</sup> ]	[Sn] <sub>850</sub> (wt%)	Actual <sub>850</sub> [mAh g <sup>-1</sup> ] (CE %)	Calculated <sub>850</sub> [mAh g <sup>-1</sup> ]
0	0	1040 (75)	375	0	690 (79)	375
5	11	1465 (73)	445	15	780 (79)	473
10	20	1320 (72)	550	21	700 (80)	508
15	27	1200 (50)	542	23	643 (78)	523
30	42	1260 (24)	636	41	644 (76)	632

Rate capabilities of the carbonized electrodes (**Figure 4.6a, b**) were assessed using currents from the calculated capacities presented in **Table 4.1**. Discharge capacities from the fifth cycle (example of technique in **Appendix Figure A11a**) were used to represent the capacity at the respective rates. Rate studies on fibers carbonized at 650°C revealed high capacities at slower rates, which we attribute to incomplete reduction of non-carbonaceous groups on the formation cycle. For example, TRGO/CNFs with 5 and 10 wt% Sn(IV) both displayed capacities of  $\sim 600$  mAh g<sup>-1</sup> at 0.2-C rates. While PAN carbonized at low temperatures led to a disordered carbon structure and tortuous Li-transport pathways, the absence of mass/electron transport limitations at low currents enabled Li to diffuse through the TRGO/CNF structure, into encapsulated Sn particles, and produce large capacities. Capacities decreased as C-rates increased, in part due to ohmic and Li transport limitations. Electrodes comprising > 10 wt% Sn(IV) and carbonized at 650°C revealed large irreversible capacities (**Appendix Figure A11b** and **Table 4.1**) and typically failed after a few cycles. Large irreversible capacity loss was likely due to formation of Li<sub>2</sub>O during irreversible reduction of

SnO<sub>2</sub> to Sn. Thus, their cycling performance beyond the first cycle was not pursued in this study.

Increasing HTT to 850°C produced fibers with larger capacities at fast rates when compared to electrodes produced at 650°C (**Figure 4.6b**), which we attribute to a more ordered carbon scaffolding for Sn particles. For example, at 2-C rates, electrodes comprising 10 wt% Sn(IV) and heat-treated at 650°C produced capacities of ~ 50 mAh g<sup>-1</sup>, whereas electrodes heat-treated at 850°C produced capacities of ~ 500 mAh g<sup>-1</sup>. A more ordered carbon structure facilitates Li and electron transport in electrodes. The I<sub>D</sub>/I<sub>G</sub> ratios (a measure of defects in carbons) calculated from Raman spectroscopy decrease with HTT, which indicates larger graphitic domains and enhanced sp<sup>2</sup> ordering (**Appendix Figure A12a**). The enhanced sp<sup>2</sup> ordering corresponds to an increased electronic conductivity in the fibers (**Appendix Figure A12a**) and decreased internal cell resistances. Increasing HTT also created smaller fibers, which reduced Li diffusion pathway length. Nevertheless, electrodes with Sn(IV) loadings > 10 wt% did not produce large capacities at fast rates; large Sn particles on the fiber surface of electrodes carbonized at 850°C initially added capacity at cycles with slow C-rates, but cracked/deactivated after successive cycling with faster C-rates (**Figure 4.6b**). We subsequently investigated electrode cycle life over hundreds of cycles to evaluate the robustness of the tin-containing electrodes. Long cycle lives are required for electrodes to be considered for commercial applications.

Extended cycling was executed in half-cells via symmetrical cycling at fast ( $\geq 1$ -C) rates. As reported in our previous study,<sup>16</sup> capacities of TRGO/CNFs carbonized at 650°C

increase with cycle number, which suggests incomplete reduction of noncarbonaceous species or restructuring of Li-active material. We observed similar results in this study; after capacity increase and stabilization, TRGO/CNF electrodes registered capacities  $\sim 270 \text{ mAh g}^{-1}$ , while 5Sn650 electrodes registered capacities  $\sim 400 \text{ mAh g}^{-1}$  after 900 cycles at 2-C rates—the added capacity is attributed to tin (**Figure 4.6c**). High capacities were also observed at 1-C rates, however capacities faded after 200 cycles. We attribute capacity fade to pulverization and deactivation of Sn within the TRGO/CNF matrix; volume expansions (during lithiation) of encapsulated particles produced strains too great for the fiber matrix to endure.

Contrary to the capacity growth exhibited by fibers carbonized at  $650^\circ\text{C}$  at 2-C rates, fibers carbonized at  $850^\circ\text{C}$  exhibited monotonic capacity fade (**Figure 4.6d**). Fibers with Sn(IV) loadings  $> 10 \text{ wt}\%$  displayed the largest amount of capacity fade; after 500 cycles at 2-C rates, these electrodes revealed capacities similar to TRGO/CNFs in the absence of Sn. The similarity in capacities indicates that the Sn on the surface of the fibers (as seen in **Figure 4.2e, g**) cracked and inactivated. The cracked and inactive Sn particles may be seen in SEM images of 30Sn850 electrodes after 500 cycles in **Appendix Figure A13**. Compared to the aforementioned highly loaded Sn electrodes, electrodes with Sn(IV) loadings  $\leq 10 \text{ wt}\%$  exhibited greater capacity retention over 500 cycles at 2-C rates; the 10Sn850 electrodes displayed capacities  $\sim 400 \text{ mAh g}^{-1}$  ( $> 75\%$  capacity retention), nearly doubling the capacity of TRGO/CNFs in the absence of Sn.

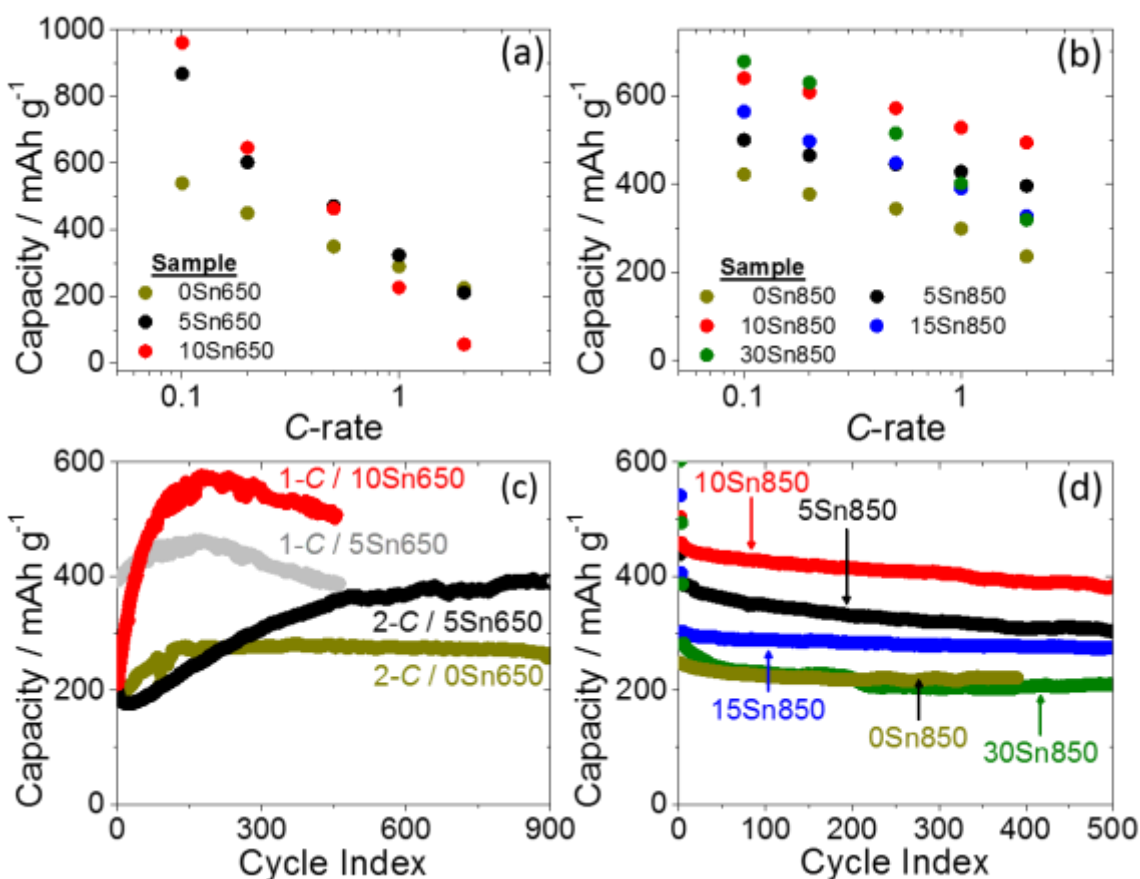


**Figure 4.6.** Rate capability measurements of tin-TRGO/CNFs carbonized at (a) 650°C and (b) 850°C; Symmetrical Li-extraction cycling data of tin-TRGO/CNFs carbonized at (c) 650°C and (d) 850°C cycled at 2-C rates.

Electrodes comprising  $\leq 10$  wt% Sn(IV) displayed the largest capacities and capacity retention. We attribute these performance enhancements to the favorable electrode morphology that was produced at low Sn(IV) loadings, which resulted in a mechanically durable electrode and limited catastrophic structure rearrangements during lithiation. Favorable electrode morphologies include: (1) encapsulated particles, yet wetted by electrolyte, in the carbon fiber matrix, which were able to impart stresses to the robust scaffolding; (2) small Li-host particle sizes ( $\leq 15$  nm), which resulted in small absolute

volume expansions upon Li-insertion; (3) uniform dispersions of tin in the fibers, which limited region of disproportionate stress and reduced fiber cracking. However, capacity fade exhibited by tin-containing electrodes at capacities greater than 400 mAh g<sup>-1</sup>, warrants the necessity for a tailored fiber morphology.

Researchers have proposed that SnO<sub>2</sub> electrodes display longer cycle lives and better capacity retention than Sn electrodes.<sup>35</sup> It is thought that the initial reduction of SnO<sub>2</sub> (**Reaction 4.1** and **2**) generates lithia-rich regions that hinder Sn aggregation to retain a small particle size during cycling. However, we did not observe better cycling performances in the SnO<sub>2</sub>-based electrodes produced at 650°C, compared to Sn-based electrodes produced at 850°C. Rather, we attribute differences in cycling performance to the TRGO/CNF scaffolding. After hundreds of cycles at 2-C rates, SnO<sub>2</sub>-TRGO/CNF electrodes produced at 650°C and Sn-TRGO/CNF electrodes produced at 850°C exhibited similar capacities. Additionally, electrode microstructure of both Sn and SnO<sub>2</sub>-TRGO/CNFs using Sn(IV) loadings of 5 wt% appeared similar after 500 cycles. SEM images of 5Sn650 (washed in EMC and dried in the glovebox) after 900 cycles at 2-C (**Figure 4.7a**) and 500 cycles at 2-C in 5Sn850 (**Figure 4.7b**) revealed a nonwoven structure similar to pre-cycled electrodes (picture in **Appendix Figure A3** and **Figure 4.2**).

The promising capacity retention of tin-TRGO/CNF electrodes is attributed, in part, to high CEs; fibers carbonized at 650°C displayed average CEs ≥ 99.8% for 1-C rates and ≥ 99.9 for 2-C rates (**Appendix Table C1**). Average CEs decreased to ≥ 99.2% for fibers carbonized at 850°C (**Appendix Table C2**), which may be associated with capacity fade.

Additionally, we did not observe Sn particle agglomeration upon cycling (other than previously observed upon thermal treatments), suggesting that loadings < 15 wt% Sn(IV) produced particle sizes within TRGO/CNF favorable for LIB anodes. In contrast to the uncycled electrode particles (**Figure 4.2f**), the Sn particles of 15Sn850 after 500 cycles at 2-C rate (**Figure 4.7c**) show a highly roughened surface, indicating significant fracturing. EDS map of the fractured Sn particle reveal SEI formation; concentrated regions of electrolyte salt decomposition products (fluorine and phosphorous maps) and electrolyte solvent reduction and polymerization (oxygen map) appear on the fractured Sn particle. It is likely that formation of the SEI on the Sn particles ohmically limited the electrodes, which decreased capacity at fast rates (as seen in **Figure 4.6b**). As previously mentioned, N-rich regions appear on the EDS maps of pulverized Sn-particle, which is not a decomposition product of the electrolyte. Introduction of nitrogen most likely occurred during electrode processing, and we are currently investigating the electrochemical performance of  $\text{Sn}_x\text{N}_y$ -based electrodes.

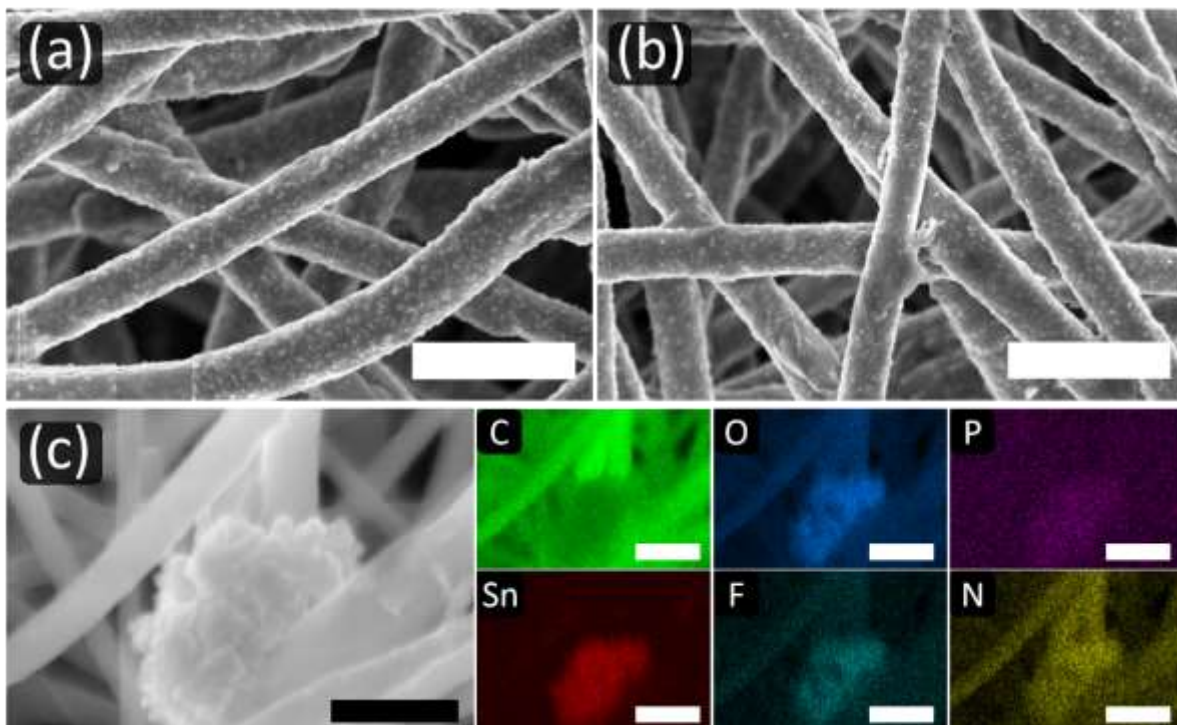


**Figure 4.7.** Post cycle SEM images of (a) 5Sn650 after 900 cycles at 2-C, (b) 5Sn850 after 500 cycles at 2-C, and (c) 15Sn850 after 500 cycles at 2-C with EDS mapping of the individual elements. The scale bars represent 1  $\mu\text{m}$ .

#### 4.4. Summary

In this study, we used thermally reduced graphene oxide-containing carbon nanofibers (TRGO/CNFs) as a matrix for tin particles to produce high-capacity and high-capacity retention anodes for Li-ion battery applications. The Sn-precursor,  $\text{SnCl}_4$ , was electrospun with ethylene glycol, polyacrylonitrile (PAN), and exfoliated graphene oxide, followed by heat treatments to produce Sn or  $\text{SnO}_2$ -TRGO/CNFs. The effects of heat-treatment temperature and Sn(IV) loading on fiber structure and morphology were assessed. Oxidation state of Sn within the fiber mat, inferred from cyclic voltammetry, varied with carbonization temperature;  $\text{SnO}_2$  and Sn(0) were produced at 650 and 850°C, respectively. Thermal decomposition of PAN released  $\text{H}_2$  at 850°C, resulting in the reduced Sn(0) oxidation state. Increased HTT also

volatilized Sn-EG entities, which brought Sn to the TRGO/CNF surface. Low Sn(IV) loadings,  $\leq 10$  wt%, produced small tin particles encapsulated within the TRGO/CNF matrix, whereas high Sn(IV) produced large tin particulates on the fibers. The ensuing fiber morphology was critical to electrochemical performance.

Fibers with  $\leq 10$  wt% Sn(IV) produced the smallest size particles ( $< 15$ -nm diameter), which reduced absolute volume expansions and led to higher capacities over hundreds of cycles than fibers with larger tin loadings. For example, TRGO/CNFs with 10 wt% Sn(IV) loading produced capacities  $\sim 400$  mAh  $g^{-1}$  after 900 cycles. Fibers with  $\leq 10$  wt% Sn(IV) also produced fibers with encapsulated particles within the TRGO/CNF matrix that were able to impart their stresses onto the carbon substrate to withstand the mechanical strains of lithiation. The aforementioned particle size and location within the fibers led to a longer cycling life for Sn and SnO<sub>2</sub>-TRGO/CNFs. We also attribute the long cycle life at low-Sn(IV) loadings to uniform dispersion of Sn(IV) throughout fiber mats, which created a uniform stress profile across the electrode during lithiation to reduce fiber fragmentation. On the other hand, Sn(IV) loadings  $> 15$  wt% produced fibers that were not conducive for LIB anodes; large irreversible capacities in SnO<sub>2</sub>-based fibers and large particles on the TRGO/CNF surface led to large initial capacities, but a short cycle life. Additional research is needed to take full advantage of the large-charge capacity inherent to Sn/SnO<sub>2</sub> anodes. However, this work provides a critical step in producing tin-based anodes that operate at fast rates with high-capacities that endure lithiation over hundreds of cycles.

#### 4.5. References

- 1 Nitta, N.; Yushin, G. High-Capacity Anode Materials for Lithium-Ion Batteries: Choice of Elements and Structures for Active Particles. *Particle & Particle Systems Characterization* **2014**, 31, 317-336.
- 2 Li, H.; Wang, Z.; Chen, L.; Huang, X. Research on Advanced Materials for Li-Ion Batteries. *Advanced Materials* **2009**, 21, 4593.
- 3 Park, C.-M.; Kim, J.-H.; Kim, H.; Sohn, H.-J. Li-Alloy Based Anode Materials for Li Secondary Batteries. *Chemical Society Reviews* **2010**, 39, 3115-3141.
- 4 Winter, M.; Besenhard, J. O. Electrochemical Lithiation of Tin and Tin-Based Intermetallics and Composites. *Electrochimica Acta* **1999**, 45, 31-50.
- 5 Inoue, H. in *International meeting on lithium batteries, Biarritz*.
- 6 Wolfenstine, J.; Allen, J. L.; Read, J.; Foster, D. Chemistry and Structure of Sony's Nexelion Li-Ion Electrode Materials. (DTIC Document, 2006).
- 7 Idota, Y.; Kubota, T.; Matsufuji, A.; Maekawa, Y.; Miyasaka, T. Tin-Based Amorphous Oxide: A High-Capacity Lithium-Ion-Storage Material. *Science* **1997**, 276, 1395-1397.
- 8 Etacheri, V.; Marom, R.; Elazari, R.; Salitra, G.; Aurbach, D. Challenges in the Development of Advanced Li-Ion Batteries: A Review. *Energy & Environmental Science* **2011**, 4, 3243-3262.
- 9 Kim, C. *et al.* Fabrication of Electrospinning-Derived Carbon Nanofiber Webs for the Anode Material of Lithium-Ion Secondary Batteries. *Advanced Functional Materials* **2006**, 16, 2393-2397.
- 10 Winter, M.; Besenhard, J. O.; Spahr, M. E.; Novak, P. Insertion Electrode Materials for Rechargeable Lithium Batteries. *Advanced Materials* **1998**, 10, 725-763.
- 11 Inagaki, M.; Yang, Y.; Kang, F. Carbon Nanofibers Prepared Via Electrospinning. *Advanced Materials* **2012**, 24, 2547-2566.
- 12 Zhang, B.; Kang, F.; Tarascon, J.-M.; Kim, J.-K. Recent Advances in Electrospun Carbon Nanofibers and Their Application in Electrochemical Energy Storage. *Progress in Materials Science* **2016**, 76, 319-380.

- 13 Wu, Y.; Reddy, M.; Chowdari, B.; Ramakrishna, S. Long-Term Cycling Studies on Electrospun Carbon Nanofibers as Anode Material for Lithium Ion Batteries. *ACS Applied Materials & Interfaces* **2013**, 5, 12175-12184.
- 14 Ji, L.; Zhang, X. Electrospun Carbon Nanofibers Containing Silicon Particles as an Energy-Storage Medium. *Carbon* **2009**, 47, 3219-3226.
- 15 Bonino, C. *et al.* Electrospun Carbon-Tin Oxide Composite Nanofibers for Use as Lithium Ion Battery Anodes. *ACS Applied Materials & Interfaces* **2011**, 3, 2534-2542.
- 16 Dufficy, M. K.; Khan, S. A.; Fedkiw, P. S. Hierarchical Graphene-Containing Carbon Nanofibers for Lithium-Ion Battery Anodes. *ACS Applied Materials & Interfaces* **2016**, 8, 1327-1336.
- 17 Tang, C.; Ozcam, A. E.; Stout, B.; Khan, S. A. Effect of Ph on Protein Distribution in Electrospun Pva/Bsa Composite Nanofibers. *Biomacromolecules* **2012**, 13, 1269-1278.
- 18 Fong, H.; Chun, I.; Reneker, D. Beaded Nanofibers Formed During Electrospinning. *Polymer* **1999**, 40, 4585-4592.
- 19 Wang, J.; Song, W.-L.; Wang, Z.; Fan, L.-Z.; Zhang, Y. Facile Fabrication of Binder-Free Metallic Tin Nanoparticle/Carbon Nanofiber Hybrid Electrodes for Lithium-Ion Batteries. *Electrochimica Acta* **2015**, 153, 468-475.
- 20 Rahaman, M.; Ismail, A. F.; Mustafa, A. A Review of Heat Treatment on Polyacrylonitrile Fiber. *Polymer Degradation and Stability* **2007**, 92, 1421-1432.
- 21 Saha, B.; Schatz, G. C. Carbonization in Polyacrylonitrile (Pan) Based Carbon Fibers Studied by Reaxff Molecular Dynamics Simulations. *The Journal of Physical Chemistry B* **2012**, 116, 4684-4692.
- 22 Yang, S.; Song, H.; Chen, X. Nanosized Tin and Tin Oxides Loaded Expanded Mesocarbon Microbeads as Negative Electrode Material for Lithium-Ion Batteries. *Journal of Power Sources* **2007**, 173, 487-494.
- 23 Zhang, G.; Liu, M. Preparation of Nanostructured Tin Oxide Using a Sol-Gel Process Based on Tin Tetrachloride and Ethylene Glycol. *Journal of Materials Science* **1999**, 34, 3213-3219.
- 24 Ye, S.; Vijh, A. K. A New Fuel Cell Electrocatalyst Based on Carbonized Polyacrylonitrile Foam the Nature of Platinum-Support Interactions. *Journal of the Electrochemical Society* **1997**, 144, 90-95.

- 25 Bulusheva, L. G. *et al.* Electrochemical Properties of Nitrogen-Doped Carbon Nanotube Anode in Li-Ion Batteries. *Carbon* **2011**, 49, 4013-4023.
- 26 Nand, S. V.; Ankur, K.; Brijesh, K.; Raj, M. B. Synthesis of Single Phase Cubic Tin Nitride Nanoparticles by Atmospheric Pressure–Halide Vapor Phase Epitaxy. *Solid State Sciences* **2008**, 10, 569-572.
- 27 Othonos, A.; Zervos, M. Carrier Relaxation Dynamics in Snxny Nanowires Grown by Chemical Vapor Deposition. *Journal of Applied Physics* **2009**, 106, 114303.
- 28 Zhou, X.; Wan, L. J.; Guo, Y. G. Binding SnO<sub>2</sub> Nanocrystals in Nitrogen-Doped Graphene Sheets as Anode Materials for Lithium-Ion Batteries. *Advanced Materials* **2013**, 25, 2152-2157.
- 29 Zhu, Z. *et al.* Ultrasmall Sn Nanoparticles Embedded in Nitrogen-Doped Porous Carbon as High-Performance Anode for Lithium-Ion Batteries. *Nano letters* **2013**, 14, 153-157.
- 30 Kim, Y.-J.; Lee, H.; Sohn, H.-J. Lithia Formation Mechanism in Tin Oxide Anodes for Lithium–Ion Rechargeable Batteries. *Electrochemistry Communications* **2009**, 11, 2125-2128.
- 31 Courtney, I.; Tse, J.; Mao, O.; Hafner, J.; Dahn, J. Ab Initio Calculation of the Lithium-Tin Voltage Profile. *Physical Review B* **1998**, 58, 15583.
- 32 Chen, Z. *et al.* In Situ Generation of Few-Layer Graphene Coatings on SnO<sub>2</sub>-SiC Core-Shell Nanoparticles for High-Performance Lithium-Ion Storage. *Advanced Energy Materials* **2012**, 2, 95-102.
- 33 Chen, Y.; Song, B.; Chen, R. M.; Lu, L.; Xue, J. A Study of the Superior Electrochemical Performance of 3 Nm SnO<sub>2</sub> Nanoparticles Supported by Graphene. *Journal of Materials Chemistry A* **2014**, 2, 5688-5695.
- 34 Kim, D.-K. *et al.* Electrospun Polyacrylonitrile-Based Carbon Nanofibers and Their Hydrogen Storages. *Macromolecular Research* **2005**, 13, 521-528.
- 35 Courtney, I. A.; Dahn, J. Electrochemical and in Situ X-Ray Diffraction Studies of the Reaction of Lithium with Tin Oxide Composites. *Journal of the Electrochemical Society* **1997**, 144, 2045-2052.

## **Chapter 5. Galactomannan binding agents for silicon anodes in Li-ion batteries**

Chapter 5 is essentially a manuscript by Martin K. Dufficy, Saad A. Khan, and Peter S. Fedkiw that was published in *The Journal of Materials Chemistry A*, 2015, **3**, 12023-12030

## **Abstract**

The challenge to incorporate Si into Li-ion battery anodes has attracted much attention. Binding agents are a critical component in a battery that may also be used to enhance electrode performance. Herein, we report the use of galactomannans—a low-cost, environmentally friendly, biorenewable polymer—as a novel binding agent for Si-containing electrodes. Silicon-containing electrodes with as low as 5 wt% binder show large reversible capacities with > 90% charge retention after 100 cycles without the use of electrolyte additives. Large capacities and low binder content when compared to carboxymethyl cellulose allows for greater energy densities and fast Li-extraction for high-power applications. The performance enhancement may be attributed to polymer-particle interactions between the hydroxyl groups of galactomannans and native-oxide layer of Si. These interactions, coupled with the inherent mechanical integrity of galactomannan thin films, allow for minimal cracking and delamination of the electrode upon lithiation. An undamaged electrode microstructure during large volume expansions allows for coulombic efficiencies > 99%. Galactomannans also experience ample polymer swelling in common electrolyte solvents, which leads to rapid Li transport and higher ionic conductivities than other biopolymer-bound electrodes. Galactomannan binders may thus provide a critical step forward in next-generation lithium-ion batteries.

### **5.1. Introduction.**

Lithium-ion batteries (LIBs) are a ubiquitous power source for portable electronic devices. The appeal for LIBs manifests in an energy and power density exceeding >200 Wh

$\text{kg}^{-1}$  and  $300 \text{ W kg}^{-1}$ , respectively<sup>1</sup>. However, improvements are imperative for electric vehicle applications<sup>2</sup>. A decrease in cost and an increase in energy density are needed before electric vehicles can compete competitively in the market with internal combustion engine vehicles. Research is looking into cheaper materials and facile production procedures to drive costs lower. Many methods to increase energy density focus on implementing high-capacity materials such as silicon in LIB anodes<sup>3,4</sup>. Silicon has a theoretical charge capacity of  $4.2 \text{ Ah g}^{-1}$  but suffers from pulverization and electronic isolation upon prolonged cycling. The pulverization stems from the large ( $>300\%$ ) volume expansions upon lithiation that lead to cell failure. Researchers have employed three disparate approaches to prolong the cycle life of Si-based electrodes: 1) varying electrode architecture<sup>5</sup>, 2) composite carbon/Si materials<sup>6-8</sup>, and 3) electrode binding agents<sup>9-13</sup>. The first two methods require rigorous multi-step processing conditions that increase cost, leading to increased attention in exploring novel binding materials. Some binders currently used in electrode materials pose a health risk, as the casting processes require harsh solvents, for example, N-methyl-2-pyrrolidone (NMP) is commonly used to prepare the binder polyvinylidene fluoride (PVDF). The need to implement environmentally benign and abundant binding materials that function at low loadings is an issue facing lithium-ion battery technology. One potential class of binding materials for LIBs are galactomannans.

Galactomannans are polysaccharides found in leguminous seed endosperm and account for the majority of seed content. The biopolymers have many commercial applications including usage in the food, textile, and petroleum industries<sup>14-16</sup>. Two galactomannan

biopolymers, guar gum (GG) and locust bean gum (LBG), are shown in **Figure 5.1**. The difference in molecular composition of galactomannans lies in the degree of substitution, or the amount of galactose side-chains distributed throughout the mannose backbone. Guar gum has a mannose (M) to galactose (G) concentration (M:G) of ~2:1, whereas LBG has that of ~4:1. The degree of substitution gives each galactomannan unique properties such as viscosity, strength, and biopolymer self-association<sup>17,18</sup>.

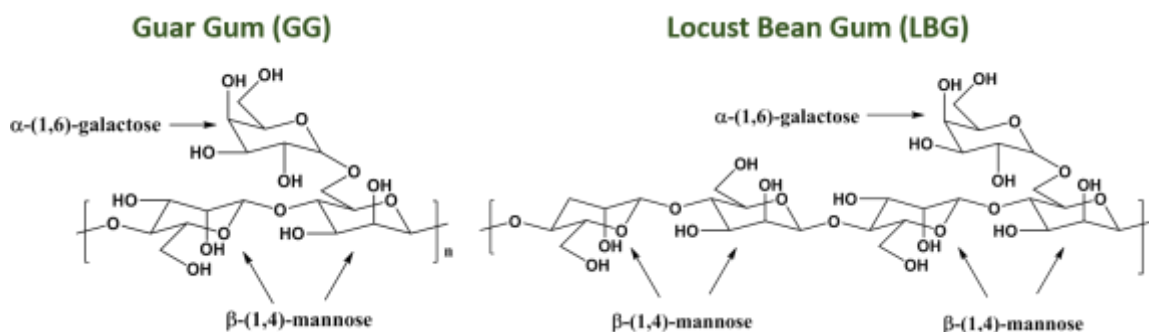


**Figure 5.1.** The chemical composition of guar gum (GG) and locust bean gum (LBG). Galactomannans are polysaccharides comprised of a mannose backbone and galactose side-chains, which can be distributed randomly or in blocks<sup>19</sup> throughout the molecule.

Herein, we report that galactomannans may be used as an environmentally friendly binding agent for Si electrodes. Galactomannan binders have recently been employed in Li-titanate electrodes<sup>20</sup>, here we report use of galactomannan binders in Si-containing electrodes of much lower potential and significant volume change upon Li insertion/extraction. The novelty of this work lies in the low-binder content of galactomannans used to obtain high charge capacities. Unlike other polysaccharide binders for Si anodes<sup>13,21</sup> that require up to 25 wt.% binder and an excess of conductive additives, we observe large capacities and prolonged electrode stability at much lower galactomannan-binder loadings (5 wt%), decreasing the amount of conductive carbon necessary and further increasing the electrode energy density.

Electrode slurries are film-cast in an aqueous medium using a process similar to commercial coating methods. Galactomannan binders provide high Si-binding strength at low-binder concentrations in Li-ion anodes. The favorable particle-binder interaction and inherent mechanical strength of galactomannans allows for stable Li-ion performances with 90% discharge capacity retention upon 100 charge/discharge cycles with coulombic efficiencies (CEs) in excess of 99% after 250 cycles at 1-C charge/discharge rates; solid-electrolyte interface (SEI) stability is observed in the absence of electrolyte additives such as fluoroethylene carbonate (FEC). The results reported in this study using galactomannans as binders provide a promising inexpensive alternative to carboxymethyl cellulose (Na-CMC) and PVDF binders.

## **5.2. Experimental**

### *5.2.1. Materials*

The binding materials used in the study are guar gum (GG, Sigma Aldrich), locust bean gum (LBG, Sigma Aldrich), carboxymethyl cellulose sodium salt (Na-CMC, Sigma Aldrich), and Kynar 500 polyvinylidene fluoride (PVDF, Arkema). The conductive carbon Super P Li (Timcal Graphite & Carbon) and silicon nanoparticles (SiNPs, Alfa Aesar, average particle size  $\leq 50$  nm) complete the balance of electrode materials. Guar gum, LBG, and Na-CMC were dissolved in DI water (18.2 M $\Omega$ -cm, Millipore) while PVDF was dissolved in anhydrous N-methyl-2-pyrrolidone (NMP, 99.5% purity, Sigma Aldrich). The slurries of SiNPs + carbon + binder were cast onto copper foil (9- $\mu$ m, MTI Corporation) and cycled against a Li counter/reference electrode (Sigma Aldrich) in a coin cell (2032, MTI Corporation). A

separator (Celgard, 25- $\mu\text{m}$  thick) prohibited physical contact between the electrodes. Electrodes were wetted with an ethylene carbonate (EC, 99% pure, Sigma Aldrich) + ethyl methyl carbonate (EMC, Ferro Corp.) mixture with lithium hexafluorophosphate salt ( $\text{LiPF}_6$ , BASF). The electrolyte solvents were dried in molecular sieves (4A, Sigma Aldrich) to a water content  $< 10$  ppm. Anhydrous acetonitrile (Acros Organic) was used to wash cycled electrodes.

### *5.2.2. Binder purification and dissolution*

The biopolymers Na-CMC, LBG, and GG were purified for 7 days in dialysis tubing (14 kDa MW cutoff) to remove low-molecular weight impurities. After dialysis, the biopolymers were dried in a vacuum oven at  $40^\circ\text{C}$ . A LBG solution in water was heated and stirred at  $80^\circ\text{C}$  for at least 24 hrs to fully dissolve the polymer. The solution was cooled to room temperature before casting a film. Guar gum and Na-CMC were dissolved in water while PVDF was dissolved in NMP, all at room temperature. This study addressed the effect of various binder loadings in SiNP electrodes. Polymer solution concentrations were varied to prevent the aggregation of hydrophobic carbon in the aqueous slurry and to adjust dispersion viscosity to enable coating, for example, casting SiNP electrodes using LBG binders (SiNP/LBG) required 0.7-1 wt%, while polymer with lower viscosities such as Na-CMC required concentrations of 2-3 wt%.

### *5.2.3. Half-cell fabrication*

Si-based electrodes comprising 75, 80, or 85 wt% SiNPs + 10 wt% C + balance binder solution, were placed into a mortar. A pestle was used to mix the materials for at least 20 minutes. Films cast onto Cu foil ( $0.75 \text{ mg cm}^2$  SiNP loading,  $\sim 11.3 \text{ mg}$  total disk weight) were

placed in a convection oven at 80°C for 30 mins to dry. Disks of 1.27-cm diameter were punched from the coated Cu foil and placed in a vacuum oven at 120°C for at least 18 hours. The dried disks were transferred to an argon-filled glove box and placed into button half-cells with polished lithium as the counter and reference electrode. The electrolyte, 1 M LiPF<sub>6</sub> in 1:1 wt EC: EMC, was added by pipette onto the working electrode (~50 μL) and the Celgard separator (~50 μL). The half-cell can was hermetically crimped with a stainless steel spacer and spring on top of the Li metal to guarantee good contact. Polymer-only films for cyclic voltammetry and impedance testing were made by casting a polymer solution on Cu foil with the doctor-blade gap height set to 1 μm. The drying and assembly process was identical to the aforementioned Si-based electrodes. A 24-hour rest period was given to all half-cells after fabrication to stabilize open-circuit potential.

#### 5.2.4. Electrochemical testing

A capacity of 3600 mAh g<sup>-1</sup> was used to calculate C-rates for electrochemical experiments. Unless otherwise stated, cells were cycled between 1 V and 10 mV vs. Li/Li<sup>+</sup> using an Arbin BT2000 battery cycler. Cyclic voltammetry was performed with a Princeton Analytical Research VersaSTAT 4 potentiostat between 3.4 V and -25 mV vs Li/Li<sup>+</sup> for polymer-only films, and between 1V and 10 mV Li/Li<sup>+</sup> for SiNP electrodes. Electrochemical impedance spectroscopy (EIS) was conducted on polymer films using a VersaSTAT 4 with frequencies between 100 MHz and 10 mHz and amplitude of 10 mV. Impedance was measured at 10 mV vs Li/Li<sup>+</sup>. Prior to EIS measurements, the cells were held at 10 mV for at least 6 hrs.

At least 4 half-cells were used for all electrochemical tests to assess reproducibility of the results. All measurements were performed at ambient conditions.

#### *5.2.5. Solvent Uptake*

Polymer films were produced by casting equal amounts of 2 wt% polymer solutions into Teflon molds and drying at ambient temperatures. Once dry, the films were removed from the molds and placed in a vacuum oven at 120°C overnight to remove solvent. The films were immediately transferred to a glove box, weighed, and placed into electrolyte (1 M LiPF<sub>6</sub> in 1:1 wt EC: EMC). After 24, 48, and 72 hours, the films were carefully blotted dry to remove excess surface electrolyte and weighed.

#### *5.2.6. Physical Characterization*

Infrared spectroscopy was used to determine the presence of functional groups on SiNPs, the binder, and the electrodes using a Thermo Scientific Nicolet 6700 FT-IR. The crystallinity of the SiNPs was observed by X-Ray Diffraction (XRD) on a Rigaku SmartLab X-ray diffractometer (Cu K<sub>α</sub>,  $\lambda = 1.54060 \text{ \AA}$ ). The size of the crystallites was calculated using the Scherrer equation and averaging the particle size for the (111), (220), and (311) peaks. All SEM images were captured on an FEI XHR Verios 460L. Low operating voltages ( $\leq 1 \text{ kV}$ ) and a stage bias (700 V) were used to prevent sample charging. Conductive coatings were not applied to better observe surface structure and morphology. To image the electrodes post-mortem, the button cells were first deprimed and washed in acetonitrile to remove the electrolyte. This process was conducted in a glove box. The electrodes were removed and transferred to a vacuum oven and dried at 120°C overnight. Steady shear viscosity of polymeric

binder solutions were measured using a stress-controlled rheometer (Discovery Hybrid Rheometer-2, TA Instruments). A 4-cm cone with a 2° geometry was used for all experiments.

### 5.3. Results and Discussion

This study examines two types of galactomannans for their use as binding agents for Si-based electrodes in LIB anodes, guar gum (GG) and locust bean gum (LBG). Many researchers have observed interactions between SiNPs and other polymers used for binders such as alginate<sup>11</sup>, carboxymethyl cellulose<sup>22</sup> (Na-CMC), and polyacrylic acid<sup>23</sup> (PAA). All are polyelectrolytes that contain carboxylic groups capable of H-bonding or undergoing a condensation reaction with the native-oxide layer of SiNPs<sup>17</sup>. The strong Si-binder interactions are thought to play a major role in electrode stability<sup>11,22,23</sup>. Galactomannans do not contain carboxylic groups, and we hypothesize that H-bonding interactions occur between the less polar –OH groups (mainly from galactose) and the oxide layer of SiNPs to promote electrode stability during charge/discharge cycling. The FT-IR spectra (**Figure 5.2a**) of SiNPs, GG, and cast SiNPs electrodes using a GG binder (SiNP/GG) provide evidence for H-bonding interactions. Many peaks in the GG spectrum arise from the polymer backbone, including sp<sup>3</sup> stretching and bending at ~2920 and ~1390 cm<sup>-1</sup>, respectively, and C-O-C antisymmetric vibrations at ~1150 cm<sup>-1</sup>. However, of importance for H-bonding is the peak at ~3420 cm<sup>-1</sup> corresponding to –OH stretching, which is present in all three sample spectra, and the peaks between 1150 and 1000 cm<sup>-1</sup> corresponding to secondary alcohols in GG<sup>14</sup>. The SiNP spectrum displays peaks between 900-1200 cm<sup>-1</sup> that correspond to Si-O-Si bonding and confirm the presence of a native-oxide layer. Additional peaks corresponding to Si-OH<sup>24</sup> and Si-H<sup>25</sup>

stretching at  $\sim 3650$  and  $2110\text{-}2140\text{ cm}^{-1}$ , respectively, suggest a functionalized surface capable of H-bonding with galactomannans. We present further commentary on potential bonding between GG and SiNPs in **Appendix B**, with X-ray photoelectron spectroscopy in **Appendix Figure B1 and Table B1**.

Studies<sup>26</sup> suggest that galactomannans with a low degree of substitution (high M:G) undergo self-association; the mannan regions preferentially bind with other mannan regions<sup>27,28</sup> giving LBG a higher solution viscosity (**Appendix Figure B2**) and lower solubility in water than more-substituted galactomannans. Although the solution viscosities of galactomannans are high (30 Pa·s at 2 wt% LBG) and the solutions cannot be cast using a doctor-blade method, the galactomannans undergo syneresis as a result of the milling process. The solvent extraction that occurs allows for slippage in the casting method, and uniform films are produced. Regardless of mannose concentration, the high viscosity of galactomannan solutions arises from the hydrogen bonding (H-bonding) of the  $\text{-OH}$  groups and facilitates production of homogenous electrode materials without particle settling. Harding's group proposed<sup>29</sup> that the mannose and galactose monomer contribute to the hydrophobic and hydrophilic nature of the galactomannan, respectively. Thus, the more hydrophilic galactose regions would preferentially bind to the native-oxide layer of SiNPs. A cartoon of the proposed SiNP-galactomannan interactions (**Figure 5.2b**) depicts: 1) H-bonding, preferentially between the galactose side groups and the oxide layer of SiNPs, and 2) self-association between the mannan backbone, which may reduce the amount of mobile galactose sites.

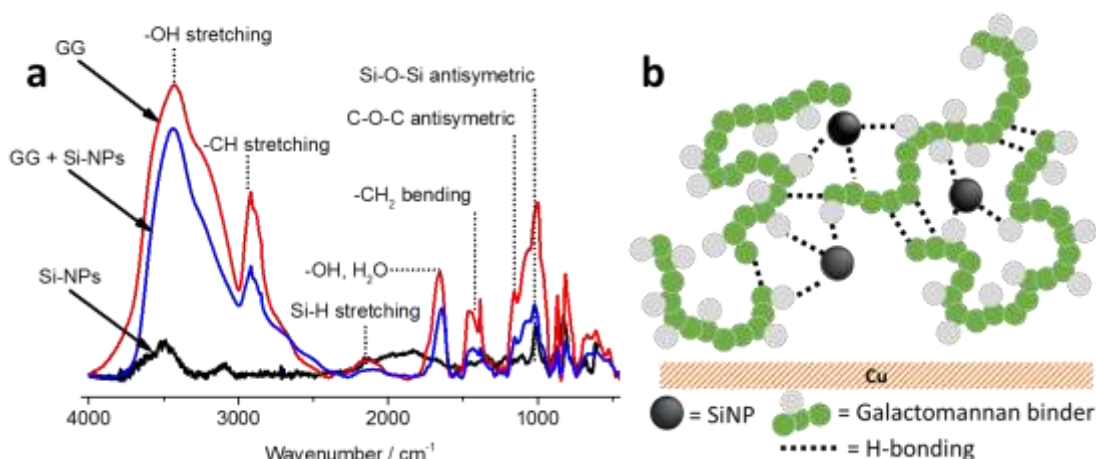


**Figure 5.2.** a) FT-IR spectra of GG, SiNPs, and the composite electrodes. Hydroxyl groups are observed on the surface of both GG and SiNPs; b) Depiction of H-bonding that may contribute to the good cyclability of electrodes using GG binders. The grey circles correspond to the galactose side-groups on the GG backbone.

Prior to electrochemical cycling, the electrodes contain crystalline SiNPs, as determined via XRD (**Appendix Figure B3**) with an average crystallite size of 42 nm, which is different than the average particle size of 58 nm observed via HR-SEM imaging. A bimodal particle-size distribution, an artifact of SiNP processing<sup>30</sup>, is observed from the HR-SEM images and is one potential cause for the size disagreement between XRD and SEM measurements (**Appendix Figure B3**). Composite SiNP electrodes with 5 wt% GG + 10 wt% C + 85 wt% SiNP (**Figure 5.3a, b**) result in a void volume of ~30%, as determined via ImageJ software (National Institutes of Health). Images with binder loadings of 10 and 15 wt% for both GG and LBG (**Appendix Figure B4**) reveal a nanostructure and porosity similar to the electrodes cast with 5 wt% binder; a higher-binder content did not fill voids in the electrode structure. The porosity of the film allows for electrolyte infusion, rapid Li-ion transport and accommodates electrode expansion during lithiation.

After 50 charge/discharge cycles in a half-cell at a 1-C rate ( $3.6 \text{ A g}^{-1}$ ) between 1 V and 10 mV vs. Li/Li<sup>+</sup>, SEM images of the SiNP/GG electrodes (**Figure 5.3c, d**) reveal a resilient porous nanostructure after deep-lithiation cycling. The SiNP/GG electrodes retain the pre-cycling microstructure and the active materials remain in electronic contact to allow for rapid (de)lithiation. The presumed thinness of the GG coating, consequence of the low-binder loading, leads to a mechanically durable electrode that limits pulverization during volume expansions exceeding 300%. Macro-scale electrode cracking, a common feature found in SEM post-mortem analysis of Si-based electrodes, is attributed to a loss in electrode activity<sup>31</sup>. Significantly, we did not observe micro-scale cracking in the images of SiNP electrodes using galactomannan binder. In contrast, images of SiNP electrodes using Na-CMC (SiNP/CMC) and PVDF (SiNP/PVDF) binders (**Appendix Figure B5**) cycled through identical conditions do not retain their pre-cycling nanostructure, as much of the initial porosity is lost. Electrode cracking is a common observation in SiNP/CMC electrodes.

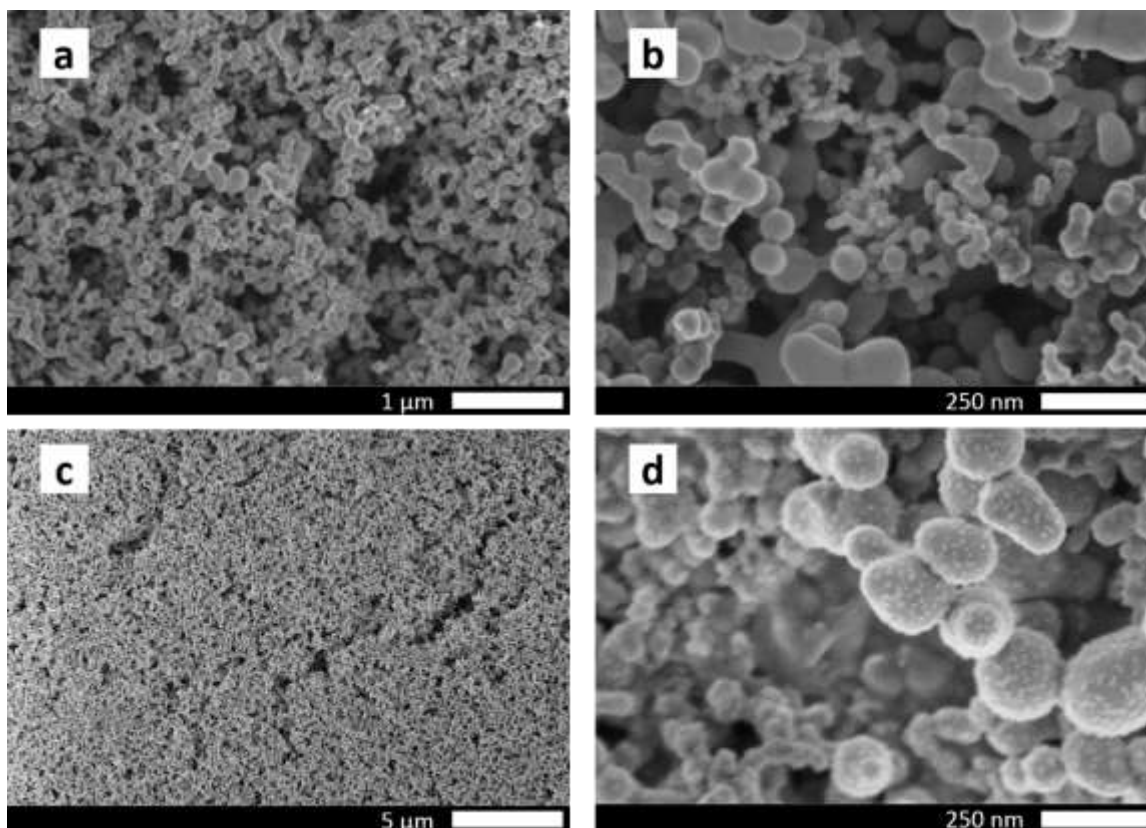


**Figure 5.3.** SEM images of (a, b) pre-cycled SiNP/GG electrodes and (c, d) post-cycled delithiated SiNP/GG electrodes. The porous structure is maintained after 50 cycles. The size of the SiNPs increase after cycling. Electrode composition is 85:10:5, SiNPs:C:Binder wt%.

Electrolyte uptake in the polymers provides insight on polymer-solvent interactions. Some degree of swelling is necessary in the binder to facilitate Li-transport through the polymer. The polymers investigated achieved a steady-state electrolyte uptake after 24 hours. Polymer-only films comprised of PVDF, LBG, GG, and Na-CMC submerged in electrolyte increase 39, 20, 14, and 6% in mass, respectively (**Figure 5.4a**). The greater electrolyte uptake of galactomannan binders compared to Na-CMC may improve the rate performance of Si electrodes, as more Li-ions are able to insert/extract. The swelling of the films may also reduce brittleness in the polymer, reducing fractures upon lithiation. The small amount of electrolyte

uptake in Na-CMC films and ensuing brittleness is postulated to be one reason for the electrode cracks observed in SiNP/CMC post-mortem analysis.

Li-ions travel through absorbed electrolyte in the polymer binder to reach Li-active host materials, and electrolyte uptake may consequently correlate with Li-ion conductivity. The ionic resistivity of a material may be gauged by fitting the high-frequency impedance data to an equivalent circuit and extrapolating the data to the x-intercept of a Nyquist plot. The impedance spectra (**Figure 5.4b**) of electrolyte-swelled LBG, GG, Na-CMC, and PVDF polymer-only films were fit to a Randles circuit. Resistances associated with the high-frequency resistor in the Randles circuit, including the solution and electronic contact, are considered constant; the variation in high-frequency resistor values stems from the ionic conductivity through the polymer film. A fit of the data reveals high-frequency resistor values of 12.7, 13.1, 16, and 9.1 ohms for GG, LBG, Na-CMC and PVDF films, respectively (**Figure 5.4b inset**). As expected, PVDF films with the most electrolyte solvent uptake yield the lowest high-frequency resistor values (least ionic resistance) while Na-CMC films with the least electrolyte solvent uptake have the highest high-frequency resistor values (most ionic resistance). There is an insignificant difference in the ionic resistance of galactomannan films based on the high-frequency impedance data. The galactomannan films have lower ionic resistances than Na-CMC films, which may facilitate the transfer of Li-ions through SiNP electrodes using galactomannans as binders. Because the films are not electrochemically active, the resistances remain constant between 0.01-3.5 V vs. Li/Li<sup>+</sup>. Voltammograms on GG, LBG, Na-CMC, and PVDF (**Appendix Figure B6**) also reveal the polymer-only films to be

electrochemically inert over the same potential range, which suggests galactomannans may also be used as binders for cathode materials, although not explained in the present study.

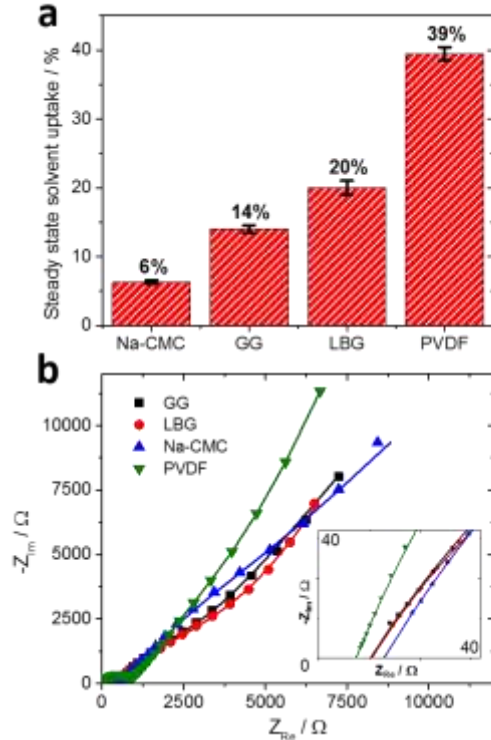


**Figure 5.4.** (a) Steady-state swelling of polymer-only films in 1 M LiPF<sub>6</sub> salt with EC:EMC (1:1 wt) solvents shows PVDF and galactomannans uptake more electrolyte than Na-CMC; (b) The EIS spectra of electrolyte-swelled PVDF, Na-CMC, LBG, and GG films deposited on Cu foil in the absence of Si and C show resistances that can be attributed to the binder material. The symbols represent the measured data and the lines correspond to an equivalent-circuit model. The inset shows the high-frequency data. EIS measurements were conducted at 10 mV vs Li/Li<sup>+</sup>.

The lithiation of SiNPs at a 10 mV cutoff voltage may be used to gauge material properties of the polymer binders including the mechanical integrity of the binder during volume changes and at full lithiation, as well as the ability of the binder to adhere to the SiNPs via particle-polymer interactions. The SiNP electrodes using GG and LBG binders exhibited a delithiation capacity of 2150 and 1850 mAh g<sup>-1</sup>, respectively, after 20 cycles at 0.05-C (**Figure 5.5**) while retaining 75% of the initial delithiation capacity. The higher capacity observed in

SiNPs/GG electrodes when compared to SiNP/LBG may be attributed to an increase in the hydrophilic galactose groups bonding to the native-oxide layer of the SiNPs, which results in a more robust composite electrode. Because LBG films take in more electrolyte than GG films, we also hypothesize that electrolyte uptake may diminish particle-polymer interactions—galactose interactions in particular. Additionally, constant-current, constant-voltage cycling<sup>32</sup> of SiNP/GG and SiNP/LBG electrodes using a 100 mV cutoff voltage produce stable delithiation capacities (**Appendix Figure B7**); galactomannan binders permit the SiNPs to reach steady capacities of  $\sim 2000 \text{ mAh g}^{-1}$ .

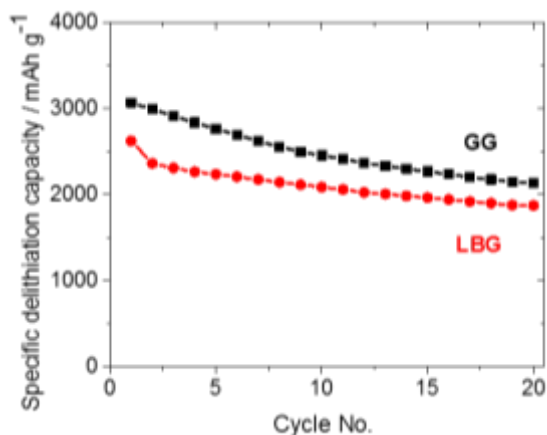


**Figure 5.5.** The delithiation capacities of SiNP/GG and SiNP/LBG electrodes using a symmetric charge/discharge rate of 0.05-C and electrode composition of 85:10:5, SiNPs:C:Binder wt%.

Electrodes using galactomannans as the binding agent retain a large amount of the initial lithiation capacity under deep-lithiation conditions (1 V to 10 mV vs Li/Li<sup>+</sup>). On the formation cycle, a single cycle at 0.05-C (180 mA g<sup>-1</sup>), typical lithiation capacities > 3600 mAh g<sup>-1</sup> and coulombic efficiencies exceeding 85% are observed in SiNP/galactomannan electrodes (**Appendix Figure B8**). While such high coulombic efficiencies were observed in SiNP/CMC electrodes, SiNP/PVDF displayed coulombic efficiencies of  $\sim 20\%$ . The poor performance of

SiNP/PVDF electrodes has been reported elsewhere<sup>10,33</sup>. The irreversible capacity loss on the formation cycle is attributed to SEI formation on the large surface area electrodes (SiNPs have an as-received surface area of 70-100 m<sup>2</sup> g<sup>-1</sup>) and the presence of Si surface oxide groups. The overpotential in the initial lithiation cycle may be attributed to the native-oxide film decelerating the already sluggish redox kinetics of SiNPs<sup>24</sup>.

Cyclic voltammetry of the SiNP/galactomannan electrodes provides further assessment on the reduction of the native-oxide layer. The current continues to increase after 9 cycles at a slow scan rate (0.2 mV s<sup>-1</sup>) as more SiO<sub>x</sub> reduces to active Si<sup>0</sup> and becomes available for lithiation (**Figure 5.6**). An increase in current with cycle number may also be attributed to crystalline Si morphing into the amorphous phase. A stable current is typically achieved after thirteen cycles (**Appendix Figure B9**). The CVs of the SiNP/GG electrodes also provide evidence suggesting why GG performs better than LBG as a binder in a Li-ion half-cell. The reason stems from a difference in conjugate redox peaks, where lithiation/extraction peaks in SiNP/GG electrodes are observed in a smaller potential range than the redox peak of SiNP/LBG electrodes. The voltammogram of SiNP/GG electrodes exhibits a cathodic peak (i) related to high-voltage lithiation at 190 mV and the conjugate anodic peak (iii) at 525 mV. The difference in voltage between the pair is 335 mV. SiNP/LBG electrodes display a larger separation of 360 mV between peaks (i) and (iii). Furthermore, an additional peak (ii) in the anodic polarization of SiNP/GG electrodes relating to a low-voltage delithiation was not distinctly observed in SiNP/LBG electrodes. The results suggest either slower kinetics or greater irreversibility of lithiation/extraction in the SiNP/LBG electrodes.

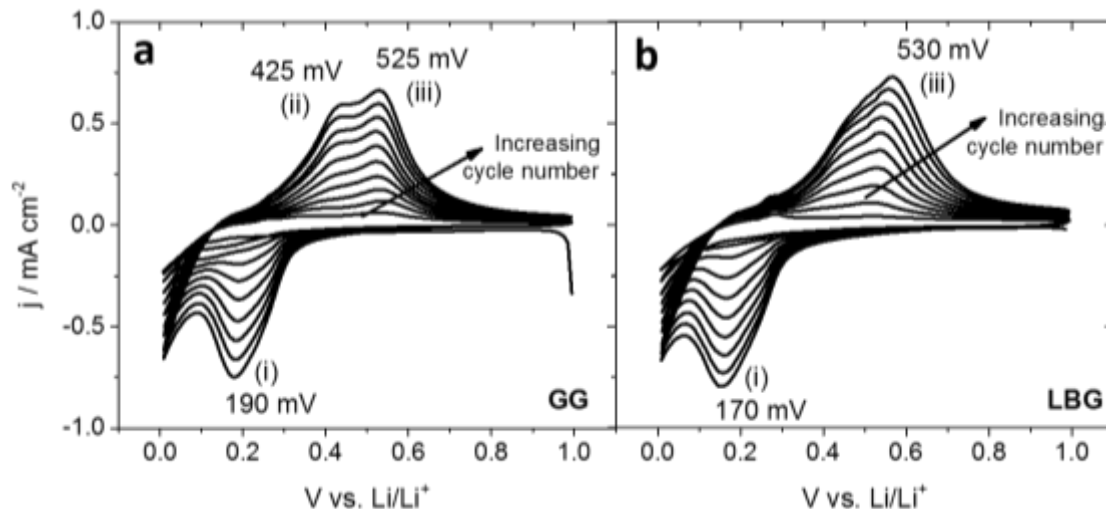


**Figure 5.6.** Cyclic voltammograms of (a) SiNP/GG and (b) SiNP/LBG electrodes. The half-cells were scanned between 1 V and 0.01 V vs Li/Li<sup>+</sup> using a scan rate of 0.2 mV s<sup>-1</sup>. Electrode composition is 85:10:5, SiNPs:C:Binder wt%.

The SiNP electrodes were subject to 250 symmetric charge/discharge cycles at 1-C (3.6 A g<sup>-1</sup>) to provide insight on the cycling life of galactomannan binders (**Figure 5.7a**). All electrodes with biopolymer binders exhibit ~90% capacity retention over the first 100 cycles as sufficient polymer-SiNP interactions in the biopolymers allow for electrode stability. The PVDF binder does not hydrogen bond to the SiNP oxide surface, but rather forms weak van der Waals interactions resulting in poor LIB performance. The PVDF binder cannot withstand the large volume expansion of lithiation, and the electronically resistive SEI forms between SiNPs leading to premature cell failure. After 100 cycles, SiNP/GG, LBG, and CMC electrodes retain delithiation capacities of 1000, 860, and 700 mAh g<sup>-1</sup>, respectively. It should be noted that the SiNP electrodes using biopolymer binders exhibited stable discharge capacities over the initial 100 cycles in the absence of fluoroethylene carbonate (FEC), an electrolyte additive known to enhance the stability and cycling life of Si-based electrodes<sup>34</sup>. While the capacities begin to fade after 100 cycles, coulombic efficiencies remain ~99% indicating a highly

reversible system with the formation of a stable SEI. We show the enhanced capacity and capacity retention from using 10, 20, and 30 wt% FEC as an additive in SiNP/GG electrodes in **Appendix Figure B10**. We attribute the enhanced electrochemical performance to decreased internal half-cell resistances, as we measured using EIS and show via Nyquist plots in **Appendix Figure B11**.

Electrodes using GG as a binding agent also outperform SiNP/CMC electrodes in symmetric charge/discharge rate capability studies (**Figure 5.7b**). SiNP/GG electrodes exhibit capacities of 1900 mAh g<sup>-1</sup> at a 0.5-C rate (1.8 A g<sup>-1</sup>). The larger extent of swelling coupled with the preservation of the pre-cycled SiNP microstructure apparently allows for enhanced Li transport and electronic contact in SiNP/GG electrodes when compared to SiNP/CMC electrodes. Interestingly, SiNP/LBG electrodes perform poorly at 2-C rates. An understanding of the phenomenon is under further investigation, however, we speculate the low capacity stems from self-association of the mannan-rich regions; more mannose-mannose interactions decreases the amount of free galactose sites that can form favorable interactions with the SiNP native-oxide layer, which yields large areas of insoluble/unswelled polymer.

In addition to the high capacity observed in SiNP/GG electrodes, the GG binder also permits fast Li-extraction for high-rate performances (**Figure 5.7c**). The initial cycle, identical to a conditioning cycle, allows for large amounts of lithium insertion. Although not typical, SiNP electrodes exhibited lithiation capacities > 3.6 Ah g<sup>-1</sup>—the capacity of Li<sub>3.75</sub>Si and proposed maximum capacity of silicon at ambient temperatures. The additional capacity beyond 3.6 Ah g<sup>-1</sup> may be attributed to electrolyte reduction (> 200 mAh g<sup>-1</sup>) and the formation

of  $\text{Li}_2\text{Si}_2\text{O}_5$  and  $\text{Li}_4\text{SiO}_4$  from  $\text{SiO}_x$  reduction<sup>24</sup>. The reduction of  $\text{SiO}_x$  is a kinetically slow reaction and is one reason for an overpotential on the first lithiation cycle. After lithiation at 0.05-C, SiNP/GG electrodes outperform SiNP/CMC electrodes and exhibit delithiation capacities of 3368, 3049, 2875, and 2311  $\text{mAh g}^{-1}$  at 0.25-C, 1-C, 2-C, and 5-C, respectively. The discharge capacity observed at 5-C ( $18 \text{ A g}^{-1}$ ) amounts to a 68% capacity retention when compared to the initial delithiation at 0.05-C. Similar to a CV, differential delithiation-capacity curves (**Appendix Figure B12**) provide Li-extraction potentials, which offer insight into the kinetics of the Li-extraction process. A peak potential increase of 80 mV is observed in high-potential  $\text{Li}_x\text{Si}$  phase delithiation when current increased from 0.05-C to 1-C. When the delithiation rate increases by two orders of magnitude, from 0.05-C to 5-C, a 180 mV peak potential increase is observed. To compare, SiNP/CMC electrodes exhibit a 280 mV increase in delithiation peak potential when current density increases from 0.05-C to 5-C. The high-discharge capacities and low potential at which Li-extraction occurs in SiNP/GG electrodes may lead to a more energy dense anode. High Li-extraction capacities stem from thinness of the GG coating at low-binder concentrations in the electrodes, which undergoes less mechanical stress during expansion and facilitates the transfer of Li-ions through the binding material. The low-binder content also allows for excellent capacity retention, with a delithiation capacity of 3405  $\text{mAh g}^{-1}$  during a subsequent 0.05-C cycle (**Appendix Figure B12**). Similarly, high-delithiation capacities are observed in SiNP/LBG electrodes.

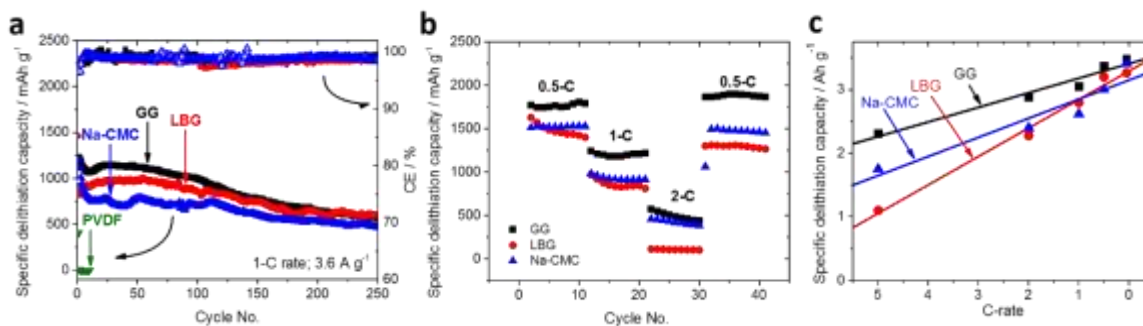


**Figure 5.7.** a) The symmetrical cycling performance of SiNPs with GG, LBG, Na-CMC and PVDF binders. After 250 cycles at 3.6 A g<sup>-1</sup>, both SiNP/LBG and GG show superior capacity to SiNP/CMC and PVDF. The coulombic efficiency (CE) of all SiNP electrodes using biopolymer binders remains >99% throughout cycling; b) Rate capability of the SiNPs electrodes using biopolymer binders at symmetric 0.5, 1 and 2-C rates; c) Delithiation capacities of SiNP electrodes from asymmetric charge-discharge using various binders. All Li-insertion was performed at 0.05-C to ensure full electrode lithiation while Li-extraction was performed at an increasing C-rate. The GG binder is capable of allowing Li to extract at high rates, i.e. 2300 mAh g<sup>-1</sup> at 18 A g<sup>-1</sup>. Electrode composition is 85:10:5, SiNPs:C:Binder wt%.

Capacities further increase in SiNP/GG electrodes when the binder content rises from 5 to 15 wt% (**Figure 5.8**), with these electrodes still outperforming SiNP/CMC electrodes. For example, symmetrical 0.5-C charge/discharge rates of SiNP electrodes with 15 wt% GG result in a capacity of 2500 mAh g<sup>-1</sup> as compared with a 1750 mAh g<sup>-1</sup> capacity in SiNP electrodes with 5 wt% GG content. Typical values for initial capacity upon half-cell conditioning further increased with binder loading while maintaining high coulombic efficiencies of ~88% (**Supplemental Figures B8 and B13**). The larger galactomannan concentration provides more electrolyte in the electrode, increasing the capacity at higher charge/discharge rates. However, capacity retention in all 15 wt% biopolymer binders began to fade after ~40 cycles. The origin of the capacity fade is under further investigation, but we speculate the increased thickness of the binder film encapsulating the SiNPs may not cope with the large mechanical stresses during lithiation. While capacity retention may be improved by electrolyte additives such as FEC,

these studies are beyond the scope of the current work. Again, we see the capacity fade in SiNP electrodes using 15 wt% binder upon prolonged cycling (**Appendix Figure B14**); after 100 cycles at 1-C ( $3.6 \text{ A g}^{-1}$ ), SiNPs with 15 wt% GG retain only 47% of their original capacity compared to an 80% capacity retention observed in electrodes using 5 wt% GG. Unlike the galactomannan binders, SiNP/CMC electrodes experience no further improvements in rate capability when binder content increased from 5 to 15 wt%. The unchanged capacity when Na-CMC content is increased may originate from the particle-binder interactions; the highly polar carboxyl groups of Na-CMC provides a stronger H-bond with SiNPs than does the hydroxyl moiety with galactomannans.

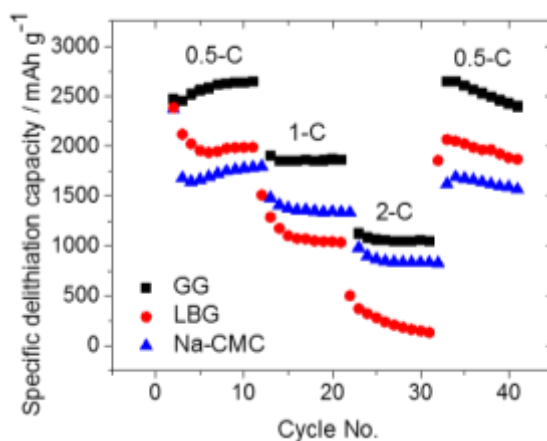


**Figure 5.8.** Rate performance for biopolymer binders reveal that SiNP/GG electrodes are capable of the highest capacities while SiNP/LBG electrodes suffer large capacity losses at elevated currents. Electrodes composition is 75:10:15, SiNP:C:binder.

The role of any binder is to 1) protect the active material from mechanical and chemical degradations while 2) maintaining a homogenous mixture of components and 3) permitting the passage of Li-ions and electrons through the binding matrix. The > 90% capacity retention after 100 cycles and the undisrupted nano/ microstructure of the SiNPs after cycling are

evidence that galactomannans may be used as a binder for SiNP electrodes. A common thread among many Si binding agents, be it glucose derivatives such as alginate, Na-CMC, and galactomannans or polymers such as polyacrylic acid, is that they are all thickening agents that utilize H-bonding to both increase the viscosity of an aqueous solution and interact with the surface oxide layer of SiNPs. High capacities and good rate capabilities have been attributed to such interactions<sup>35</sup>. However, one key difference is the functional group present in the H-bonding mechanism. PAA, Na-CMC, and alginate are all polyelectrolytes that bind through the stronger, more polar carboxyl moiety. The polyelectrolytic nature of the polymers may also influence Si interactions. Galactomannans are neither charged nor have carboxyl moieties, suggesting that the polarity of hydroxyl groups is sufficient for Si-particle binding and mechanical strength during lithiation.

#### **5.4. Summary**

The main goal of this study was to integrate novel and environmentally friendly binder components into lithium-ion batteries with an emphasis on low-cost materials that allow Si-based electrodes to operate with high energy densities. We successfully showed that galactomannans, more specifically guar gum, may be used as a binding agent for SiNP electrodes at low loadings and outperform SiNP electrodes using Na-CMC binders. The interactions between the native-oxide layer of SiNPs and the polar hydroxyl groups (more specifically the galactose side chains) inherent to galactomannans provide for excellent cyclability and capacity retention in Li-ion half-cells. Capacity retention in SiNP/GG electrodes may be attributed to the mechanical integrity of galactomannans; electrode

microstructure and porosity are retained even after deep lithiation cycles. The superior electrolyte uptake capabilities of galactomannans when compared to Na-CMC correlates to lower ionic resistances, which allows for enhanced-rate performances. Due to the electrochemical stability of these biopolymers, the use of galactomannans may also be extended beyond Si-based electrodes to other anode or cathode materials.

## 5.5. References

- (1) C.-X. Zu and H. Li, *Energy Environ. Sci.*, 2011, **4**, 2614.
- (2) R. Van Noorden, *Nature*, 2014, **507**, 26.
- (3) J.R. Szczech and S. Jin, *Energy Environ. Sci.*, 2011, **4**, 56.
- (4) U. Kasavajjula, C. Wang, A. J. Appleby, *J. Power Sources*, 2007, **163**, 1003.
- (5) H. Wu and Y. Cui, *Nano Today*, 2012, **7**, 414.
- (6) A. Magasinski, P. Dixon, B. Hertzberg, A. Kvit, J. Ayala, G. Yushin, *Nat. Mater.*, 2010, **9**, 353.
- (7) H. Lin, W. Weng, J. Ren, L. Qiu, Z. Zhang, P. Chen, X. Chen, J. Deng, Y. Wang, H. Peng, *Adv. Mater.*, 2014, **26**, 1217.
- (8) H. Wu, G. Zheng, N. Liu, T. J. Carney, Y. Yang, Y. Cui, *Nano Lett.*, 2012, **12**, 904.
- (9) M. Wu, X. Xiao, N. Vukmirovic, S. Xun, P. K. Das, X. Song, P. Olalde-Velasco, D. Wang, A. Z. Weber, L.-W. Wang, V. S. Battaglia, W. Yang, G. Liu, *J. Am. Chem. Soc.*, 2013, **135**, 12048.
- (10) B. Koo, H. Kim, Y. Cho, K. T. Lee, N.-S. Choi, J. Cho, *Angew. Chem.*, 2012, **51**, 8762.
- (11) I. Kovalenko, B. Zdyrko, A. Magasinski, B. Hertzberg, Z. Milicev, R. Burtovyy, I. Luzinov, G. Yushin, *Science*, 2011, **334**, 75.
- (12) C. Erk, T. Brezesinski, H. Sommer, R. Schneider, J. Janek, *ACS Appl. Mater. Interfaces*, 2013, **5**, 7299.

- (13) M. Murase, N. Yabuuchi, Z.-J. Han, J.-Y. Son, Y.-T. Cui, H. Oji, S. Komaba, *ChemSusChem*, 2012, **5**, 2307.
- (14) S. Mahammad, R. K. Prud'homme, G. W. Roberts, S. A. Khan, *Biomacromolecules*, 2006, **7**, 2583.
- (15) V. B. Pai and S. A. Khan, *Carbohydr Polym*, 2002, **49**, 207.
- (16) A. Tayal, V. B. Pai, S. A. Khan, *Macromolecules*, 1999, **32**, 5567.
- (17) I. C. M. Dea, E. R. Morris, D. A. Rees, J. Welsh, H. A. Barnes, J. Price, *Carbohydr. Polym.*, 1977, **57**, 249.
- (18) M. A. Cerqueira, B. W.S. Souza, J. Simões, J. A. Teixeira, M. R. M. Domingues, M. A. Coimbra, A. A. Vicente, *Carbohydr. Polym.*, 2011, **83**, 179.
- (19) Y. Wu, W. Li, W. Cui, N. a. M, Eskin, H. D. Goff, *Food Hydrocoll.*, 2012, **26**, 359.
- (20) B.-R. Lee, S. Kim, E.-S. Oh, *J. Electrochem. Soc.*, 2014, **161**, A2128.
- (21) Y. K. Jeong, T. Kwon, I. Lee, T.-S. Kim, A. Coskun, J. W. Choi, *Energy Environ. Sci.*, 2015, **DOI**: 10.1039/C5EE00239G.
- (22) N. S. Hochgatterer, M. R. Schweiger, S. Koller, P. R. Raimann, T. Wöhrle, C. Wurm, M. Winter, *Electrochem. Solid-State Lett.*, 2008, **11**, A76.
- (23) Z.-J. Han, N. Yabuuchi, K. Shimomura, M. Murase, H. Yui, S. Komaba, *Energy Environ. Sci.*, 2012, **5**, 9014.
- (24) S. Xun, X. Song, L. Wang, M. E. Grass, Z. Liu, V. S. Battaglia, G. Liu, *J. Electrochem. Soc.*, 2011, **158**, A1260.
- (25) D. C. Marra, E. Z. Edelberg, R. L. Naone, E. S. Aydil, *J. Vac. Sci. Technol. A*, 1998, **16**, 3199.
- (26) R. O. Mannion, C. D. Melia, B. Launay, G. Cuvelier, S. E. Hill, S. E. Harding, J. R. Mitchelp, *Carbohydr. Polym.*, 1992, **19**, 91.
- (27) M. D. Burke, J. O. Park, M. Srinivasarao, S. A. Khan, *Journal of controlled release*, 2005, **104**, 141.
- (28) K.S Mikkonen, H. Rita, H. Hele, R. A. Talja, L. Hyvo, *Biomacromolecules*, 2007, **8**, 3198.

- (29) D. R. Picout, S. B. Ross-Murphy, K. Jumel, and S. E. Harding, *Biomacromolecules*, 2002, **3**, 761.
- (30) Y.-M. Lin, K. C. Klavetter, P. R. Abel, N. C. Davy, J. L. Snider, A. Heller, C. B. Mullins, *Chem. Commun.*, 2012, **48**, 7268.
- (31) J. Li, A. K. Dozier, Y. Li, F. Yang, Y.-T. Cheng, *J. Electrochem. Soc.*, 2011, **158**, A689.
- (32) M. N. Obrovac, and L. J. Krause, *J. Electrochem. Soc.*, 2007, **154**, A103.
- (33) G. Liu, S. Xun, N. Vukmirovic, X. Song, P. Olalde-Velasco, H. Zheng, V. S. Battaglia, L. Wang, W. Yang, *Adv. Mater.*, 2011, **23**, 4679.
- (34) V. Etacheri, O. Haik, Y. Go, G. A. Roberts, I. C. Stefan, R. Fasching, D. Aurbach, *Langmuir*, 2012, **28**, 965.
- (35) M.-H. Ryou, J. Kim, I. Lee, S. Kim, Y. K. Jeong, S. Hong, J. H. Ryu, T.-S. Kim, J.-K. Park, H. Lee, J. W. Choi, *Adv. Mater.* 2013, **25**, 1571.

## **Chapter 6. Guar hydrogel binders for silicon nanoparticle anodes: a case study of binder rheology on electrode performance**

*Chapter 6 is essentially a manuscript by Martin K. Dufficy, Kimberly A. Dennis, Peter S. Fedkiw, and Saad. A. Khan to be submitted to the Journal of Materials Chemistry A*

## Abstract

Binding agents are a critical component of Si-based electrodes. Herein, we introduce a composite hydrogel binder consisting of guar and carbon black (CB), which is chemically crosslinked with glutaraldehyde as a means to reinforce electrode structure during lithiation and improve electronic conductivity. Dynamic rheological experiments are used to monitor the crosslinking reaction and show that rheology plays a significant role in binder performance. The crosslinking reaction occurs at a faster rate and produces stronger networks in the presence of CB, as evidenced from higher gel elastic modulus in guar + CB gels than guar gels alone. Silicon nanoparticle (SiNP) electrodes that use binders with low-crosslink densities ( $t_{\text{rxn}} < 2$  days) demonstrate discharge capacities  $\sim 1200 \text{ mAh g}^{-1}$  and coulombic efficiencies  $> 99.8\%$  after 300 cycles at 1-C. Low-crosslink densities likely increase the capacity of SiNP anodes due to binder-Si hydrogen-bonding interactions that accommodate volume expansions. In addition, the crosslinked binder demonstrates self-healing capabilities, as evidenced by an increased elastic modulus after the gel was mechanically fragmented, which may preserve electrode microstructure during lithiation and increase capacity retention. The composite hydrogel with integrated conductive additive gives promise to a new type of binder for next-generation lithium-ion batteries.

## 6.1. Introduction

Silicon is a promising alternative to conventional graphite anodes for Li-ion batteries (LIBs), as Si has a specific capacity ( $\text{Li}_{3.75}\text{Si}$ ,  $3579 \text{ mAh g}^{-1}$ ) approximately ten-times that of graphite ( $\text{LiC}_6$ ,  $372 \text{ mAh g}^{-1}$ ). However, structural rearrangements upon charge-discharge cycling limit the use of Si in commercial cells. Silicon particles undergo volume expansions  $> 300\%$  at full lithiation, and mechanical stresses at such large volume expansions cause cracks and formation of a solid-electrolyte interphase (SEI) on the newly exposed Si surface, which irreversibly consumes lithium. The SEI is an electronic insulator, and recurrent cracking results in electronic isolation of Si particles and untimely cell failure. Low-electronic conductivity in Si electrodes also limits their use in commercial cells. Compared to the electronic conductivity of graphite, electron transport through semi-conductor Si is lower. To decrease ohmic resistances, researchers have investigated various architectures<sup>1-5</sup> on the nano-scale, which shortens electron and Li-diffusion pathway lengths and minimizes overpotential and charge-transfer resistance during charge/discharge cycles.<sup>6</sup> Research also focuses on combining Si nano-structures with carbon material, such as amorphous carbon<sup>7</sup>, graphene,<sup>8</sup> and carbon coatings,<sup>9</sup> to increase conductivity and cycle life. While Si/C composites result in improved electrode materials, the entire capacity of Si is not realized and carbon addition involves another processing step. Thus, research has turned to studying binding agents to enhance capacity and cycle life, and the conductivity of Si electrodes.

Binding agents have multiple roles in LIB electrodes. In addition to adhering materials to a current collector, the binding agent must allow sufficient ionic and electronic conductivity

within the porous electrode structure and promote formation of a stable SEI. Researchers observed that Si anodes using carboxyl methylcellulose (CMC) as a binding agent enhanced the capacity and cycle life beyond the (then) conventional binding material, polyvinylidene fluoride (PVDF), which was attributed to bonding between the Si oxide layer and binding agent.<sup>10</sup> The enhanced electrochemical performance of Si/CMC electrodes led to the discovery of novel binding agents, many with carboxyl moieties.<sup>11-13</sup> However, the aforementioned binders failed to preserve electrode microstructure over many cycles and required electrolyte additives such as fluoroethylene carbonate to achieve good cyclability.<sup>14</sup> Additionally, these Si electrodes required a high-binder content and a conductive additive to achieve high capacities and charge retention, which increased the amount of Li-inactive material (or “dead weight”) in electrodes. Preservation of Si nanoparticle (SiNP) electrode microstructure using minimal binder loading continues to draw significant research interest. Recently, attempts to add functionality, such as an improved electronic conductivity,<sup>3,15,16</sup> have attracted a great deal of attention.

Taking into account the roles of the binder and drawbacks of previously studied binders, we tailored binder properties to create a novel hydrogel binding agent for Si anodes. The binder presented in this study incorporates a conductive additive (carbon black, CB) within a crosslinked polymeric framework (guar gum, referred to as guar) to form a composite hydrogel. This work builds upon our initial study on galactomannan binding agents,<sup>17</sup> to introduce novel facets: To the best of our knowledge, this is the first study to incorporate CB in a guar crosslinking reaction. The composite guar + CB binders studied are chemically

crosslinked with glutaraldehyde to produce a mechanically reinforced electrode microstructure to preserve Li and electron pathways and enhance cycling performance. We correlate the extent of crosslinking to the electrochemical performance of Si anodes using gel binders; we monitor gelation using dynamic rheology to observe an “extent” of reaction and relate viscoelastic properties of these gels to capacity and cycle life in Li-ion half-cells. We find that low degrees of crosslinking increase the capacity of SiNP anodes. For example, SiNPs anodes are found to exhibit  $\sim 1200 \text{ mAh g}^{-1}$  at 1-C rate after 300 cycles. We attribute these high capacities to well-dispersed active materials, which lead to favorable H-bonding between the oxide layer of SiNPs and the binder. The binders may form crosslink- or H-bonds, which act to preserve electrode microstructure during stress of lithiation. This self-healing effect is one possible reason why SiNP electrodes using crosslinked guar binders had increased half-cell capacity retention compared to electrodes using non-crosslinked binders. Taken together, this study shows that tailoring viscoelastic properties of polysaccharide gels may be used as a means to improve the performance of Si anodes.

## **6.2. Materials and Methods**

### *6.2.1. Guar purification*

Commercial-grade guar typically contains 10-17 wt% insoluble content,<sup>18,19</sup> rendering the need for further purification. To purify the sample, guar (MP Biomedical, molecular weight  $\sim 250 \text{ kDa}$ ) was dissolved for 4 hours in 30°C deionized water ( $18.2 \text{ M}\Omega\text{-cm}$  at 25°C) at a concentration of 1 wt%, which was then centrifuged at 5,000 RPM for 30 minutes. The soluble portion was separated from the insoluble and less hydrophilic guar via decantation. Acetone

was added to the supernatant to precipitate guar. The precipitate was placed in a convection oven overnight at 45°C to dry. Dried guar was cryomilled to a fine powder in a mortar containing liquid nitrogen.

### 6.2.2. Hydrogel preparation

A typical batch of guar hydrogels was formed by first dissolving 0.7 g purified guar in 69.3 g DI water at room temperature. Appropriate amounts of carbon black (CB, Super P-Li, Imerys Graphite & Carbon, 40-nm average particle size) were added to the guar solution (to obtain volume fractions of  $\phi = 0.01, 0.025, 0.04, 0.05,$  and  $0.1$ ) and high-shear mixed (Silverson L5M-A) at 7500 RPM for 15 minutes. Next, glutaraldehyde (GA, Alfa Aesar, 25 wt% in water) was added to the guar + CB mixture in amounts equal to 1 mol hydroxyl from GA ( $\text{OH}_{\text{GA}}$ ) per repeat unit guar, assuming galactose:mannose unit composition of 1:2 in guar. Typical molecular structures of GA and guar are illustrated in **Figure 6.1a**. Sulfuric acid (98% purity, BDH Chemical) was added to the mixture to produce a 75 mM acid solution, which kept GA from self-polymerizing.<sup>20</sup> To our knowledge, the crosslinking mechanism has not been definitively identified, however a cartoon of the proposed reaction is given in **Figure 6.1b**. It was assumed that primary hydroxyls on the galactose side-chain are less sterically hindered and more reactive than secondary hydroxyls and hydroxyls on the mannan backbone; hydrogen bonding between mannan-rich chains (referred to as hyper-entanglements)<sup>21</sup> is preferred, which restricts backbone movement and renders side chains more accessible to crosslink with GA, as shown in **Figure 6.1c**. The final mixture was high-shear mixed for 5 minutes at 7500 RPM. The solution was left in a water bath at 40°C for various lengths of time ( $t_{\text{rxn}} = 0, 1, 2,$

3, 5 days) to allow the reaction to progress. After the specified reactions time, gels were transferred to dialysis tubing (cutoff molecular weight ~ 14 kDa) for 3 days to stop the crosslinking reaction and leach out acid and unreacted crosslinker.

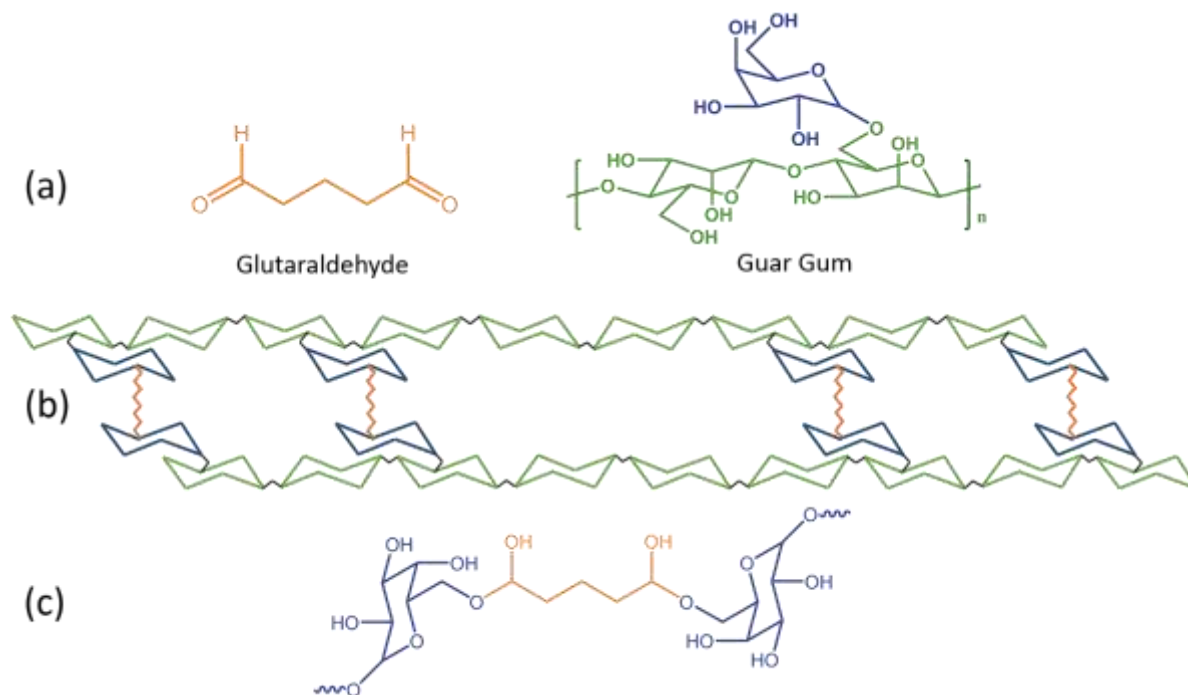


**Figure 6.1.** a) Molecular structure of glutaraldehyde (GA) and typical representation of guar gum; b) cartoon of crosslinked guar showing GA (orange) attacking the galactose side chain (blue). The mannose backbone is pictured in green; c) proposed crosslink, where GA reacts with the primary hydroxyl on two separate galactose side-chains (in acidic conditions) to form a hemiacetal linkage. Other hydroxyl sites are capable of crosslinking, including those on the mannan backbone. Acetal linkage (not shown) is also possible with the remaining hydroxyl on the GA and galactose hydroxyl.

It should be noted that high-shear mixing did not permanently degrade the guar networks; microstructure quickly rebuilt after mixing, as evidenced from dynamic rheology measurements of the elastic ( $G'$ ) and viscous ( $G''$ ) moduli conducted over a range of frequencies before and after high-shear mixing guar solutions at 7500 RPM for 15 mins. The data for the two sets of experiments overlap (**Appendix Figure C1**) indicating that the microstructure remains intact or reverts back to its original state following shear.

### 6.2.3. Hydrogel characterization

Dynamic rheological experiments were conducted at room temperature on a stress-controlled rheometer (DHR-2, TA Instruments) using a gap size of  $2 \pm 0.2$  mm. Sandpaper (3M, Pro Grade Precision, 60 grit) was glued to 25-mm diameter parallel-plates to prevent wall slip. Loaded samples were given a 10-minute rest period prior to rheological characterization. In these experiments, the samples were subjected to an oscillatory shear and the corresponding elastic ( $G'$ ) and viscous ( $G''$ ) moduli measured as a function of increasing strain amplitude (at a fixed frequency of oscillation) or frequency (keeping strain small in the linear viscoelastic regime).<sup>22</sup> Hydrated gels were imaged using a JEOL JSM-7600F scanning electron microscope (SEM) outfitted with a cryogenic transfer system and stage. Samples were frozen in liquid nitrogen prior to imaging. Dehydrated gels and electrode material were imaged using an FEI 460L field emission SEM equipped with energy-dispersive x-ray spectroscopy (EDS). Solids content in dehydrated gels, after dialysis, was measured in a thermogravimetric analyzer (TGA, Discovery Series, TA Instruments). Fourier transform infrared spectroscopy (FTIR) of dehydrated films was conducted on a Thermo Scientific Nicolet 6700. Electrolyte uptake measurements were conducted in an argon-filled glovebox.

The uptake of electrolyte in guar and crosslinked guar films was determined by submerging vacuum-dried films (overnight at 100°C) with dry-weight  $w_d$  in electrolyte for 24 hours. The allotted time was deemed sufficient to reach a steady-state mass uptake. After 24 hours, the films were removed from solution, surface-blotted dry, and weighed to get the wetted weight ( $w_w$ ), which was measured ~ 15 seconds after removal of the films from solution.

Mass uptake was calculated as:  $\text{Uptake [mass\%]} = 100 * (w_w - w_d) / w_d$ . Values reported in this study represent the mean of measurements from six films.

#### 6.2.4. Electrochemical characterization

Half-cells comprising Si nanoparticles (SiNPs, Alfa Aesar, average particle size ~ 50 nm) and crosslinked guar + CB hydrogels were milled in mortar and pestle, expelling the water to form homogenous slurries. The slurry (80:10:10 wt% SiNP:CB:guar) was doctor-bladed onto a Cu foil current collector and punched into 1-cm<sup>2</sup> discs with dry areal silicon loadings of 0.5-0.6 mg cm<sup>-2</sup>. The discs were dried at 100°C under vacuum overnight. The SiNP discs were used as working electrodes in 2032 coin cells (MTI Corp) with Li metal (99%, 0.75 mm thick, Sigma Aldrich) as counter and reference electrode. Half-cells were assembled in an argon-filled glove box. Approximately 50 µl of electrolyte (< 10 ppm water), was added on working electrodes and Celgard separators. Electrolyte comprised 1 M LiPF<sub>6</sub> (> 99.8% purity, BASF) in fluoroethylene carbonate (Solvay): ethylene carbonate (Sigma Aldrich): ethyl methyl carbonate (Ferro Corp), FEC:EC:EMC = 2:9:9 wt. Electrochemical formation cycles, 1 charge-discharge cycle at 180 mA g<sup>-1</sup> within a potential window of 1 - 0.01 V vs Li/Li<sup>+</sup>, preceded half-cell measurements. Charge-discharge cycling and electrochemical impedance spectroscopy (EIS) were conducted using a Biologic VMP3 with at least three samples, results were typically reproducible within 10%. EIS measurements were conducted on half-cells at 10 mV vs. Li/Li<sup>+</sup> using a sinusoidal voltage amplitude of 10 mV from 200 kHz to 100 mHz. Prior to EIS experiments, half-cells were lithiated using a constant current of 3600 mA g<sup>-1</sup> (cutoff voltage:

10 mV vs. Li/Li<sup>+</sup>) followed by a constant-voltage step at 10 mV vs. Li/Li<sup>+</sup> (cutoff current: 36 mA g<sup>-1</sup>). Half-cells were delithiated at a constant current of 3600 mA g<sup>-1</sup> to 1 V vs. Li/Li<sup>+</sup>.

### 6.3. Results

#### 6.3.1. Gelation rheology

Dynamic rheological measurements of elastic ( $G'$ ) and viscous ( $G''$ ) moduli, provide a powerful means to examine gelation behavior of hydrogel networks without disrupting microstructure.<sup>23</sup> Here, we examine the behavior and magnitude of gel moduli as a function of frequency or strain to 1) obtain details on a possible crosslinking mechanism, and 2) distinguish differences in gelation of filled and unfilled hydrogel systems. We begin by assessing the evolution of  $G'$  and  $G''$  over time for unfilled systems. We note that modifications to polymer and crosslinker concentration, as well as pH, produce different gelation kinetics. For example, kinetics of the crosslinking reaction may be slowed by limiting concentration of crosslinker, glutaraldehyde (GA), and reducing the temperature.<sup>24</sup> Herein, we purposefully slowed crosslinking kinetics (e.g., room-temperature reaction with stoichiometric amounts of crosslinker); the aim of this study was to determine viscoelastic responses of guar gels with varying crosslinking density, and to use the gels as binders for Si nanoparticle electrodes. Herein, reaction time is used as proxy for crosslinking density, with increased reaction time corresponding to increased crosslinking density.

**Figure 6.2** shows  $G'$  and  $G''$  as a function of frequency and strain, as well as the loss tangent,  $\tan \delta$ , defined as the ratio  $G''/G'$  for unreacted guar and guar crosslinked for 1-5 days. Samples comprised 1 wt% guar, 1 mol OH<sub>GA</sub> per repeat unit guar, in 75 mM H<sub>2</sub>SO<sub>4</sub> aqueous

solution. Frequency spectra of  $G'$  and  $G''$  in **Figure 6.2a** reveal a transition from solution to gel with time. Frequency spectra of the guar solution immediately after being mixed with acid and GA (day 0) shows viscous modulus  $G''$  dominates at low frequencies and both moduli to be frequency-dependent, which is behavior characteristic of viscoelastic solutions.<sup>22,25</sup> After 1 day, the moduli decrease, yet interestingly  $G'$  and  $G''$  are approximately equal over all frequencies examined, akin to a system at a 'critical gel point.'<sup>23,26</sup> With increasing reaction time (day 2 and beyond), we find the moduli to increase,  $G'$  becomes greater than  $G''$ , and moduli become less frequency-dependent, which suggests formation of a crosslinked network structure.<sup>23,25</sup>

We surmise that there are two phenomena occurring in the system. During the initial stage (day 1), guar undergoes acid hydrolysis because of the instability of guar in acid, as reported by Prud'homme and coworkers.<sup>27</sup> Acid hydrolysis occurs through random chain scissions leading to a decrease in the moduli, as is observed in both frequency and strain sweep experiments (**Figure 6.2a, b**). To the best of our knowledge, such molecular breakdown in guar has not been reported while simultaneous crosslinking with GA. Acid treatments also decrease mannan-mannan interactions on the polymer backbone, as evidenced by a decrease in Huggins coefficient upon acid treatment.<sup>27</sup> Although the guar backbone undergoes hydrolysis, there are physical association/interactions taking place in the system. As a result, the system crosslinked for 1 day shows critical gel-like features (**Figure 6.2a**): the loss tangent is lower than un-crosslinked guar at low frequencies and remains constant as a function of frequency (**Figure 6.2c**). Non-linearity in strain sweeps, as evidenced by a decrease in  $G'$  with

strain, suggests that associations within the guar + GA gel are predominantly physical in nature; the microstructure after crosslinking for 1 day is fragile and breaks down with increasing strain (**Figure 6.2b**). Following breakdown of guar after 1 day,  $G'$  and  $G''$  increase systematically with reaction time, while loss tangent decreases and remains lower than unity (**Figure 6.2a, c**) via chemical crosslinking with GA. The increased moduli observed after the first day of crosslinking from frequency-sweep data is consistent with strain-sweep data (**Figure 6.2b**), which also shows strain-hardening with increasing strain. Similar strain hardening behavior has been observed in other chemically crosslinked system.<sup>28</sup> Thus, addition of acid to the guar + GA crosslinking reaction has a role supplementary to that previously proposed, which was to protonate GA;<sup>29</sup> we posit that acid helps maintain monomeric GA, breaks down the mannan-rich backbone to improve molecule mobility, and facilitate the crosslinking reaction.

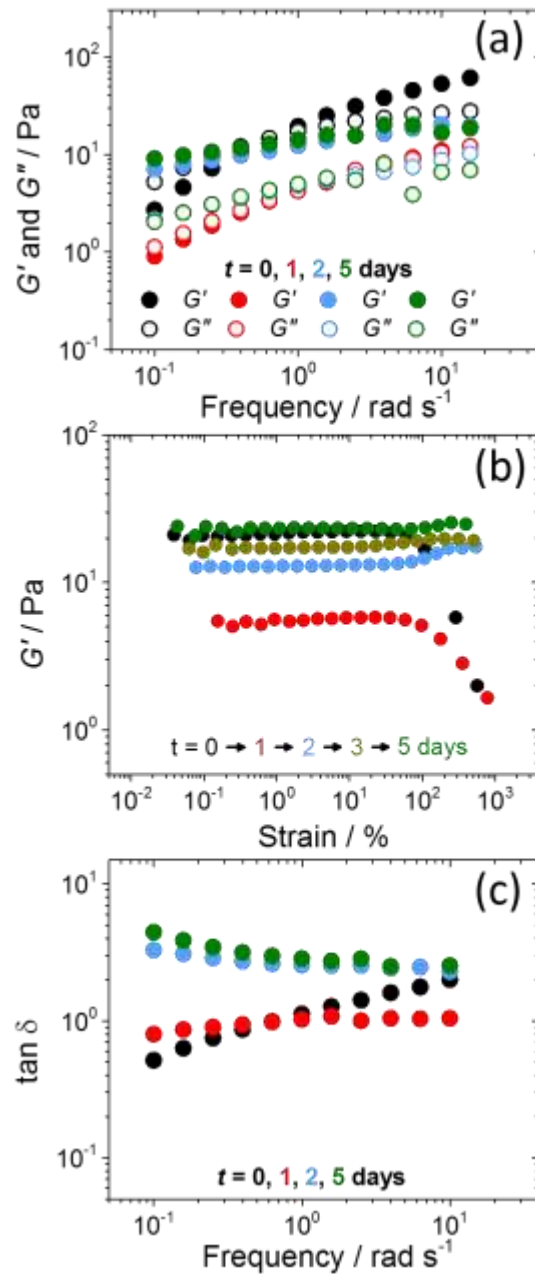


**Figure 6.2.** Dynamic rheology of 1 wt% guar solutions at different crosslinking reaction times; a) frequency sweeps show that the guar structure breaks down within the first day, but begins to build after 24 hours; b) strain sweeps show that guar gels crosslinked for > 1 day did not enter the nonlinear viscoelastic regime at high (> 100%) strains; c) loss tangent for guar samples that were used to assess the extent of the crosslinking reaction (gelation).

To decouple the contributions of each constituent in the crosslinking reaction, we ran rheological experiments on aqueous solutions of guar + GA and guar + acid. We found that viscosities and moduli (**Appendix Figure C2**) of crosslinking solutions in the absence of GA significantly decreased with time. Note that the viscosity of guar alone decreases with time due to bacterial digestion of guar, and GA is commonly added to guar to slow bacterial digestion and increase shelf life. However, the sample with acid decreases considerably more than samples without acid. In contrast, no significant change in viscosity was observed in crosslinking solutions (guar + GA) in the absence of acid. Deconvolution of components in the systems supports the claim that acid is responsible for breaking down the structure of guar, and plays a critical step in the crosslinking reaction by GA.

We then analyzed the viscoelastic behavior of guar gels containing carbon black (CB) (**Figure 6.3**) to compare gelation parameters (moduli as a function of frequency and strain and loss tangent) with unfilled gels. Several features are evident from the data. First, stronger networks are created with the addition of CB. For example,  $G'$  of the guar + CB sample is at least twice as large as that of the sample without CB after 2 days of crosslinking reaction and almost an order of magnitude higher after 5 days (**Figures 6.2, 3 a, b**). A lower loss tangent is also observed in the guar + CB samples (**Figure 6.3c**). Second, frequency sweeps before crosslinking of guar + CB systems (**Figure 6.3a, c**) reveal that  $G' > G''$ . We do not observe a cross-over in  $G'$  and  $G''$ , as displayed in unfilled systems for day 0 (**Figure 6.2a**). This may suggest that CB is creating physical associations within the system and extending the relaxation time. Third, even though acid hydrolysis of guar occurs, we see little decrease in modulus

(**Figure 6.3a**) unlike its analog in the non-CB containing sample (**Figure 6.2a**). In fact,  $\tan \delta$  is approximately less than or equal to 1 over all frequencies (**Figure 6.3c**). The decrease in modulus due to hydrolysis is thus compensated by formation of physical associations/aggregation due to the presence of CB. Finally, strain-sweep data (**Figure 6.3b**) shows evolution from a physically to chemically crosslinked systems; for days 0 and 1, the system is dominated by physical associations as there is microstructure breakdown ( $G'$  decrease) with increasing strain. At day 2, the system shows strain hardening followed by a decrease in  $G'$ ; both physical and chemical crosslinks play a role here. For longer reaction times ( $> 2$  days), we observe strain hardening only. These results taken together indicate a system initially dominated by physical associations of CB, transforming into to a chemical crosslinked system with a transition time wherein both physical and chemical crosslinks are playing a role. Such a behavior has been observed for fumed silica in a UV curable system by Chiou et al.<sup>30</sup> The higher  $G'$  of the CB-containing sample at longer crosslinking times also suggests that CB is playing a role in increasing the effective crosslink density of the sample either through physical associations or chemical crosslinking of oxygenated moieties on the surface of CB particles with the hydroxyls of guar.

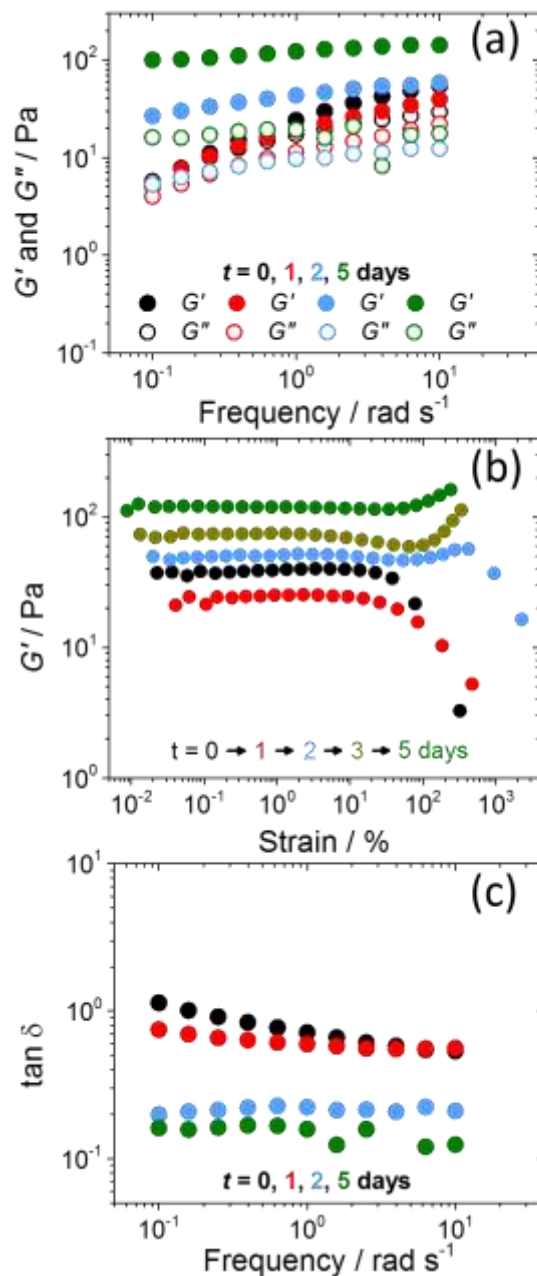


**Figure 6.3.** Dynamic rheology of guar + CB ( $\varphi = 0.05$ ) solutions at different crosslinking reaction times; a) frequency sweeps show that the guar structure breaks down within the first day, but begins to build after 24 hours to a gel with near frequency-independent moduli; b) strain sweeps show that guar + CB deviate from the linear viscoelastic regime at high (> 40%) strains; c) loss tangent for guar + CB samples that were used to assess the crosslinking reaction (gelation).

To further observe the effect of CB addition, we measured viscoelastic properties of guar + CB gels crosslinked for two days and comprising various amounts of CB.<sup>31</sup> Here, we observed that addition of CB increased network strength of the gels, as evidenced by a systematic increase in  $G'$  with  $\varphi$ , (**Figure 6.4**). We calculated  $G'$  by averaging values measured within the first decade of frequency sweeps (angular frequency from  $10^{-1}$  to  $10^0$  s $^{-1}$ ). Detailed  $G'$  and  $G''$  versus frequency of guar + CB gels is shown as supplementary material (**Appendix Figure C3**). Added network strength may be caused by CB interactions with the polymer to form physical crosslinks, aggregation of CB, or chemical crosslinks. For colloidal particles, scaling of  $G' \sim \varphi^n$  has been reported, where is  $n \sim 3.6$  for diffusion-limited aggregation.<sup>32,33</sup> Additional models have been developed to account for attractive particles in a viscous medium.<sup>34</sup> However, our data does not fit such scaling with  $\varphi < 0.01$  in guar gels. We obtain a power value of  $n \sim 1.0$ , which likely indicates that elastic contributions are dominated by chemical crosslinks in the guar network<sup>35</sup> and that CB plays a minor role in crosslinking. We also measured the elastic modulus of un-crosslinked guar solutions (1 wt% in water) with various CB loadings ( $\varphi = 0.025, 0.05, 0.01$ ) and determined an exponential value of  $n \sim 0.50$  (**Appendix Figure C4**), which is again much smaller than 3.6. The significance of the slope is beyond the scope of the current paper. However, we infer that the influence of  $\varphi$  on  $G'$  suggests that inter-polymer interactions, or hyper-entanglements, are more dominant than particle-particle interactions.

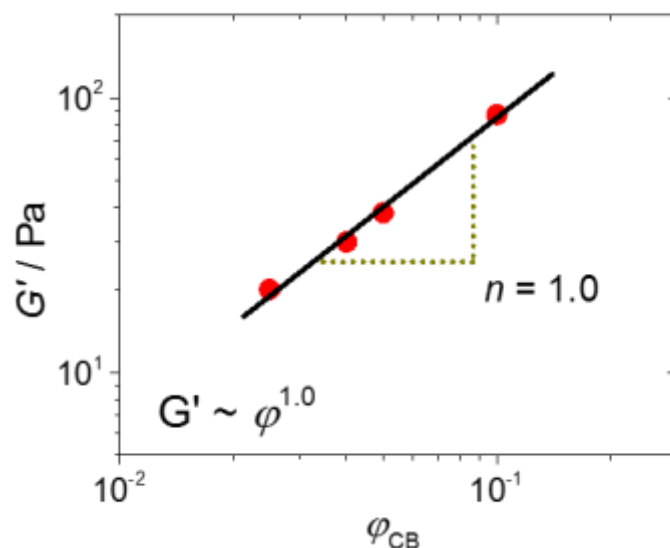


**Figure 6.4.** Elastic modulus as a function of CB loadings using of 1 wt% guar gels crosslinked for 2 days and dialyzed for 3 days with various loadings of CB. The addition of CB enhances the strength of the gels.

### 6.3.2. Materials characterization

Cross section cryo-SEM images of hydrated guar + CB gels ( $\phi = 0.05$ ) revealed interesting characteristics about gel structure. We obtained cross sections by cryo-fracturing gels prior to SEM analysis. **Figure 6.5a** shows a low-magnification image of guar + CB gels that had been crosslinked for 2 days. Crosslinked guar + CB gels formed honeycomb-like structures. Irregularities in gel microstructure, or deviation from honeycomb-like structure, may be attributed to artifacts from sample preparation, such as ice formation in the cryo-freezing process, or large CB aggregates. High-resolution cryo-SEM images of the filled gels (**Figure 6.5b, c**) show individual-to-slightly aggregated CB particles in the gel. Particles, with average diameter  $\sim 45$  nm (that of CB), are well dispersed within the gel. The appearance of un-aggregated, hydrophobic CB particles in the hydrogel network was not expected, and

understanding the CB particle dispersion is a topic of future work. However, we speculate that high-shear mixing, coupled with the large viscosity of the guar solutions, may have minimized agglomeration of CB particles prior to gelation. Because CB did not form gel-like structures or highly percolated networks, guar + CB hydrogel electronic conductivities ( $\varphi < 0.1$ ) are low (**Appendix Figure C5**). Percolated CB structures may be formed by decreasing the shear used to mix CB in guar or by increasing CB loading ( $\varphi > 0.1$ ). Compared to the structure of guar + CB gels, cryo-SEM images of guar gels in the absence of CB revealed a similar honeycomb-like macrostructure (**Appendix Figure C6a**), but a different, more complex microstructure (**Appendix Figure C6b**). These cryo-SEM images reveal the influence of CB in the crosslinking reaction, and suggest that dispersed CB particles may impart interfacial contributions<sup>36</sup> to the guar + CB gel that act to increase  $G'$  beyond that of guar gels, as seen in **Figure 6.2a** and **6.3a**.

Although hydrated guar + CB gels exhibited high-electronic resistances, the presence of CB did not hinder ionic conductivity. Impedance measurements of hydrated guar + CB gels using various volume fractions of CB ( $\varphi = 0.01 - 0.1$ ) in 0.1 M H<sub>2</sub>SO<sub>4</sub> revealed high-frequency responses similar to H<sub>2</sub>SO<sub>4</sub> in the absence of the gel (**Appendix Figure C7**), suggestive of favorable ion transport.

Field emission SEM images of dehydrated CB + guar networks (vacuum dried at 100°C overnight) showed aggregated CB particles (**Figure 6.5d, e**). It appears that the top surface of the dehydrated gels is relatively CB-free, as compared to the cross section (**Figure 6.5f**). These images suggest that guar migrates to the sample perimeter during the drying process. Cross-

sectioned images of dehydrated gels reveal CB aggregation, which is significantly different than the dispersed particles seen in hydrated gels. A thin polymer layer is likely coating the surface of the carbon black particles, which was evidenced by charging in the SEM; the non-conducting, guar-coated, CB film required a DC bias of 1 kV to suppress charging in the SEM. During the drying process, the hydrated guar collapsed to encapsulate CB aggregates, as illustrated in the cartoon in **Figure 6.5g**. The collapsed film creates a coating that is reinforced by crosslinked guar. With the addition of SiNP to guar + CB gels, it is reasonable to infer that SiNPs will also become encapsulated within the dehydrated structure to create durable electrodes that are capable of preserving (to an extent) electrode microstructure upon volume expansions of lithiation.

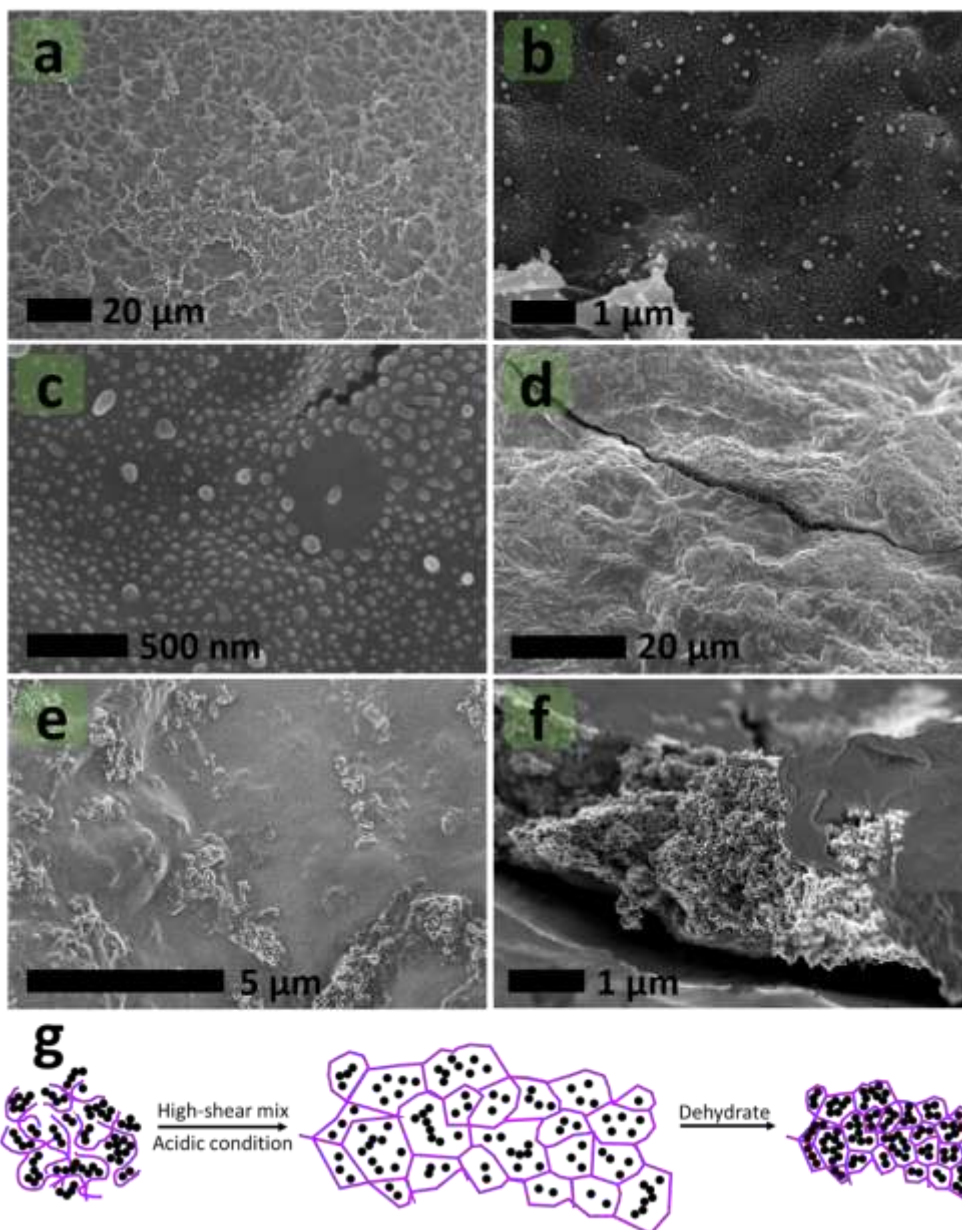


**Figure 6.5.** (a-c) Cross-sectional, cryo-SEM images of hydrated guar + CB gels (crosslinked for 2 days and  $\phi_{CB} = 0.05$ ); Field emission SEM images of the same dehydrated guar + CB gels showing (d, e) the surface and (f) cross section; (g) cartoon of: the guar + CB mixture before high-shear mixing and crosslinking; the structure of guar + CB gel after high-shear mixing and crosslinking; the dehydrated guar + CB gel structure. The aggregation of CB after dehydration coats the CB surface with crosslinked guar to create a durable binding material.

Prior to charge-transfer at the surface of Si, Li-ions transport through the binder swelled with electrolyte. Binders that uptake more electrolyte have larger quantities of Li-ions present about Si, which facilitates Li-ion transport. We assessed steady-state swelling, or mass uptake of electrolyte, in vacuum-dried films (overnight at 100°C) in the absence of CB. Mass uptake initially increased after 1 day of crosslinking, then decreased with crosslinking beyond 1 day (**Figure 6.6a**). Guar gels crosslinked for 0, 1, 2, and 3 days revealed electrolyte mass uptakes of ~ 14, 16, 13, 10%, respectively. The increased swelling in films reacted for 1 day may be attributed in a decrease in elastic properties ( $G'$ ), as seen in **Figure 6.2b**, where moduli of crosslinked systems decrease over the first day. It is possible that mobility of crosslinked guar networks at 1 day increase sol-like properties (from acid hydrolysis), which facilitates interactions with electrolyte solvents to enhance swelling beyond non-crosslinked guar.<sup>37</sup> Decreased swelling with increased crosslinking time (increased crosslinking density,  $t_{\text{rxn}} > 1$  day) may be attributed to a decrease in mobile guar chains that interact with solvent. Since electrolyte uptake provides a means for Li-transport through the binder, binder swelling may be correlated to ionic conductivity. However, we saw no such correlation. High-frequency resistances of dehydrated guar gels (4- $\mu\text{m}$  polymer film coated on Cu foil) were measured in Li-ion half-cells via electrochemical impedance spectroscopy (EIS) at 10 mV vs. Li/Li<sup>+</sup> (**Figure 6.6b**). Assuming all else in half-cells is constant, the high-frequency contributions are dominated by binder ionic conductivity. High-frequency resistances of crosslinked samples decreased compared to non-crosslinked samples, however, we did not observe a significant difference in high-frequency resistances of the crosslinked samples. Other researchers have

reported that increased crosslinking density decreases Li-ion conductivity,<sup>38</sup> contrary to our findings. Further investigation is required to determine if and how the crosslinked guar structure affects ionic transport. Nonetheless, the decreased cell resistance in crosslinked guar films that we measured is favorable, since it facilitates Li-transport.

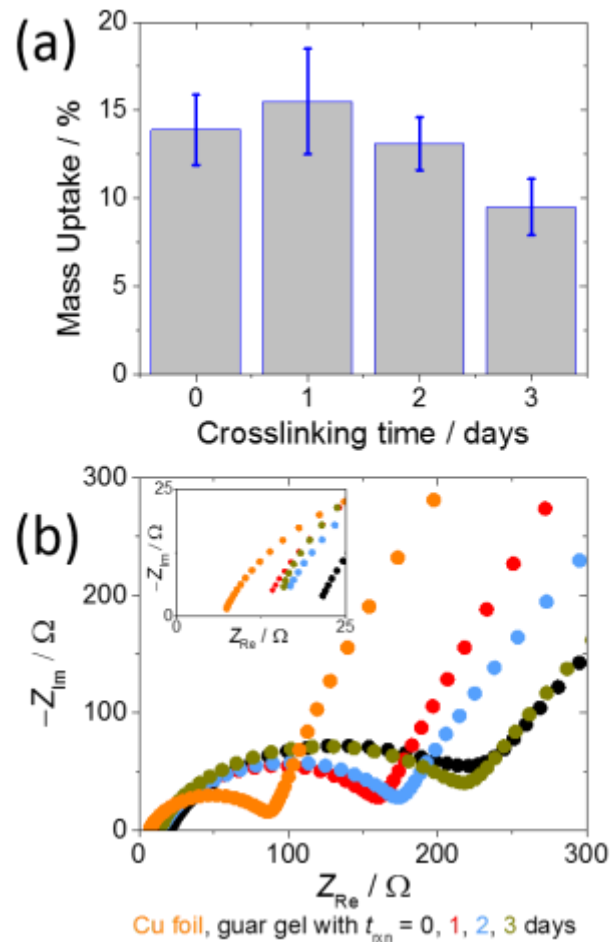


**Figure 6.6.** (a) Mass uptake as a function of crosslinking time (b) Nyquist plot of Cu foil, and guar films crosslinked for 0-3 days on Cu foil at 10 mV vs Li/Li<sup>+</sup>. The inset in (b) shows high-frequency impedance data

We characterized crosslinking of the guar networks via FTIR in an attempt to elucidate guar-GA bonding locations. Spectra of dehydrated guar gels crosslinked for 0, 1, and 3 days

were normalized to the –OH stretching peaks at  $3400\text{ cm}^{-1}$  (**Appendix Figure C8**). As crosslinking progressed, hydroxyl stretching shifted to higher frequencies, which may be attributed to decreased H-bonding interactions<sup>39</sup> in the guar + CB gels from 1) mannan-mannan de-association in acidic conditions and 2) conversion of hydroxy groups to (hemi)acetal groups during the crosslinking reaction. Researchers using GA crosslinker on polyvinyl alcohol systems observed an increase in –CH peak intensity with crosslinking density,<sup>40</sup> which was attributed to the carbon backbone of GA. Similarly, we observed a systematic increase in –CH stretching ( $\sim 1450\text{ cm}^{-1}$ ) peak intensity with crosslinking reaction time. We also observed maximum peak intensity after 3 days of crosslinking at  $\sim 880\text{ cm}^{-1}$ , which may be attributed to O-C-O bending from hemiacetal formation.<sup>41</sup> A reduction in hydroxyls on the binder reduces potential H-bonding associations between the binder and the native-oxide surface layer of SiNPs, which may lead to deleterious electrochemical performances. Thus, a fully crosslinked binder is not desirable for SiNP electrodes. To corroborate this claim, we assessed the electrochemical properties (charge capacity and cycle life) of SiNP electrodes using crosslinked guar binders with various crosslinking densities.

### *6.3.3 Electrochemical characterization*

We studied the electrochemical performance of SiNP electrodes using guar + CB binders in Li-ion half-cells within a potential window of 1 and 0.01 V vs. Li/Li<sup>+</sup>. The electrodes were dried in a vacuum oven at  $100^{\circ}\text{C}$  prior to cell assembly. These binders did not thermally degrade at  $100^{\circ}\text{C}$ , as assessed by thermal gravimetric analysis (**Appendix Figure C9**). Thermal stability is needed in binders to preserve electrode microstructure; guar gels degraded

in a  $N_2$  atmosphere at  $\sim 300^\circ C$ , which is beyond the flash point of many electrolyte solvents. First-cycle charge-discharge plots at  $180 \text{ mA g}^{-1}$  ( $0.05\text{-C}$ ) for SiNP electrodes containing guar + CB gel binders ( $t_{\text{rxn}} = 0, 1, 2,$  and  $3$  days) are shown in **Figure 6.7**. We observed high-discharge capacities ( $> 2500 \text{ mAh g}^{-1}$ ) and coulombic efficiencies (CEs) of  $\sim 80\%$  in SiNP electrodes using guar + CB binders with low-crosslink densities (e.g.  $t_{\text{rxn}} = 0 - 2$  days). As crosslinking density increased ( $t_{\text{rxn}} > 2$  days), we observed a decrease in first-cycle capacity and CE.

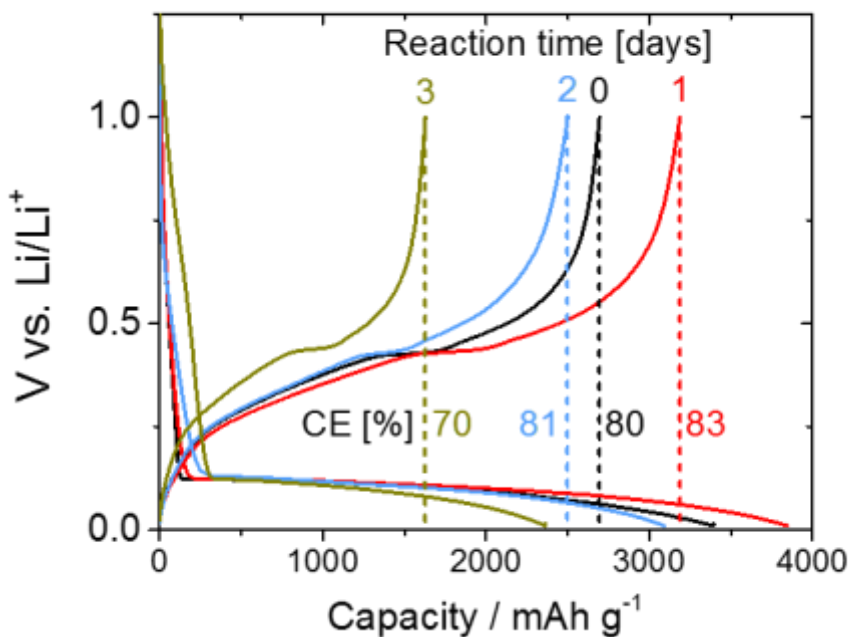


**Figure 6.7.** Typical first-cycle capacities at  $180 \text{ mA g}^{-1}$  ( $0.05\text{-C}$ ) for SiNP electrodes using crosslinked guar + CB binders; first-cycle coulombic efficiencies (CEs) are reported on the plot

To further assess the electrochemical performance of SiNP electrodes using crosslinked guar + CB binders, we probed the rate capability and capacity over hundreds of cycles. Rate-capability experiments consisted of 10 symmetrical charge-discharge cycles at

0.2-C, 0.5-C, 1-C, and 2-C, using a basis capacity of 3600 mAh g<sup>-1</sup> (**Figure 6.8a**). We observed decreases in discharge capacity with rate/cycle number with low-crosslinked binders ( $t_{\text{rxn}} = 0$ -2 days). SiNP electrodes using guar + CB binders with higher crosslinking densities ( $t_{\text{rxn}} = 2$  and 3 days) exhibited the highest capacities at fast (2-C) rates. For example, these electrodes produced capacities of  $\sim 800$  mAh g<sup>-1</sup> at current densities of 7.2 A g<sup>-1</sup>. Significant capacities at fast charge-discharge rates may be due to a binder framework that is capable of withstanding the still relatively small volume expansions at 800 mAh g<sup>-1</sup> (compared to expansions at, say, 2000 mAh g<sup>-1</sup>), which preserves electronic conduction pathways during lithiation.

After 300 cycles at 1-C rates, SiNP electrodes using crosslinked guar + CB binders exhibited higher capacities than non-crosslinked binders (**Figure 6.8b**); electrodes using guar + CB binders crosslinked for 1-2 days displayed capacities of  $\sim 1200$  mAh g<sup>-1</sup> after 300 cycles, whereas electrodes using un-crosslinked binders displayed  $\sim 500$  mAh g<sup>-1</sup>. We note all SiNP electrodes displayed average coulombic efficiencies  $> 99.8\%$  over the 300 cycles (**Appendix Figure C10a**). SiNP electrodes using low- and un-crosslinked binders all displayed similar capacities after the first 100 cycles, however, SiNP electrodes using un-crosslinked guar + CB binders experienced considerable capacity fade after 100 cycles. As crosslinking density increased, capacity retention systematically increased (**Figure C10b**). For example, SiNP electrodes using guar + CB binders crosslinked for 0, 1, 2, and 3 days exhibited capacity retention of  $\sim 15, 40, 60,$  and  $75\%$ , respectively, after 300 cycles at 1-C rates. We attribute the superior capacities and capacity retention over hundreds of cycles, in part, to the favorable viscoelastic properties in low-crosslinked systems ( $t_{\text{rxn}} > 2$  days), as discussed below.

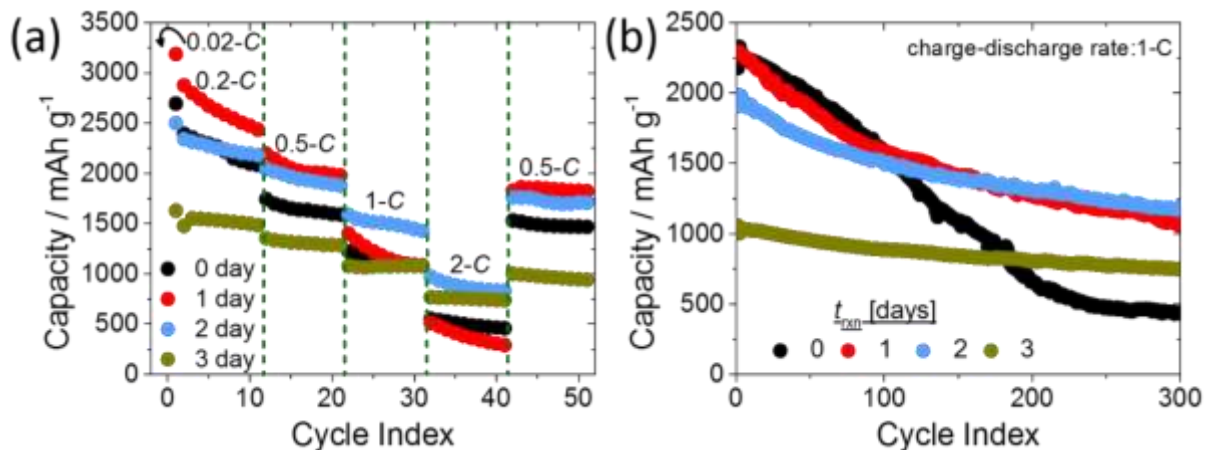


**Figure 6.8.** Effect of crosslinking density on electrochemical cycling performance of SiNP electrodes using guar + CB binders with various crosslinking time; typical symmetrical cycling of a) rate capability performances and 2) performances over 300 cycles

Coupling rheological data with electrochemical performance provides insight on binder-viscoelastic properties that increase capacity retention in SiNP electrodes. For example, guar + CB gels with low-crosslinking densities ( $t_{\text{rxn}} = 0\text{-}2$  days) exhibited a decrease in elastic modulus at high strains (**Figure 6.3b**), where physical crosslinks likely dominate. The decrease in  $G'$  at high strains from oscillatory strain-sweep data suggests that low-crosslinked guar chains extend during slurry-cast preparation to encapsulate SiNPs and create a conformal coating about SiNPs. The binder coating may then H-bond with SiNPs (between the surface oxide layer of SiNPs and the hydroxyls of guar). Hydrogen bonding between the binder and SiNPs, coupled with the durable crosslinked network, acts to maintain the pre-cycled electrode structure during lithiation and increases the performance of SiNP electrodes.<sup>42</sup> We used EDS to assess the dispersion of the guar + CB gel binder ( $t_{\text{rxn}} = 2$  days) throughout the electrode (**Appendix Figure C11**), assuming that concentrated regions of carbon on EDS maps signified

gelled networks that did not break upon milling. Carbon-rich regions appeared sparsely decorated throughout the electrodes, suggesting the gel conformally coat the SiNP surface.

Contrary to the decrease in  $G'$  at high strains in guar + CB gels crosslinked for 0-2 days, guar + CB gels crosslinked for 3 days experience strain-hardening, where  $G'$  increases with strain (**Figure 6.3b**). Strain hardening is commonly attributed to extensional limitations of entangled polymer structures,<sup>43,44</sup> and may deter either SiNP incorporation and/or H-bonding interactions between SiNPs and guar. High-crosslinking densities, inferred from the large  $G'$  in frequency sweeps (**Figure 6.3a**), increase the rigidity of both hydrated and dehydrated gels and preclude SiNPs-binder interactions. Highly crosslinked gels also fold upon themselves as the polymer de-swells and networks collapse, which limits adhesion between the current collector and electrode materials. **Appendix Figure C12** shows photographs of the collapse of guar hydrogels crosslinked for 1, 2, and 3 days from heating at 35°C in a convection oven. As apparent from images of dehydrated guar gels, gels crosslinked for 1 and 2 days revealed little film folding when dehydrated. The lack of film folding observed in these gels also suggests limited electrode delamination from the current collector, which minimizes ohmic resistances in cells. In contrast, images of dehydrated guar gels crosslinked for 3 days revealed more folding after the gel network collapsed than guar gels crosslinked for 1 and 2 days. We also attribute superior capacity retention seen in **Figure 6.8b**, in part, to the self-healing capabilities in the crosslinked binder.

Self-healing is quite common in hydrogels, and has been observed in many polysaccharide systems for applications such as drug delivery.<sup>45</sup> While self-healing guar gels

have been reported using ionic liquids as crosslinking agents,<sup>46</sup> to the best of our knowledge self-healing capabilities of guar gels crosslinked in a GA + CB mixture have not been reported. To undergo self-healing, we speculate that bonds form in gel networks that fractured during volume expansion of lithiation. Mobility of binder networks to reform bonds is possible, since partially crosslinked guar swells in electrolyte. Self-healing may occur via hydrogen bonding between hydroxyl groups of crosslinked guar, or self-healing may occur via a continuation in the crosslinking reaction (e.g., addition reaction between partially reacted hydroxyls of guar with GA reacted with one –OH from guar). The acidic conditions necessary to initiate self-healing occur in the electrolyte via hydrolysis of the salt (LiPF<sub>6</sub>) and additive (FEC) to form HF.

To test the self-healing ability of guar + CB hydrogels, we ran rheological experiments on gels crosslinked for 2 days (**Figure 6.9a**), and the same gel that had been fragmented with a razorblade (**Figure 6.9b**), placed in a scintillation vial (**Figure 6.9c**), and swelled with 75 mM H<sub>2</sub>SO<sub>4</sub> for 24 hours. The gel revealed an increase in elastic modulus after swelling with acid, as apparent from dynamic rheology (**Figure 6.9 d, e**). The elastic modulus (as measured from low-frequency data) increased from ~ 30 to 60 Pa upon acid treatment, which is likely due to hydrogen bonding within the guar + CB gel and increased crosslinked density from covalent bonding (crosslinking of partially reacted GA-guar with unreacted guar). Self-healing may thus preserve electrode microstructure by restoring mechanical integrity and shortening inter-particle distances between SiNPs and CB.

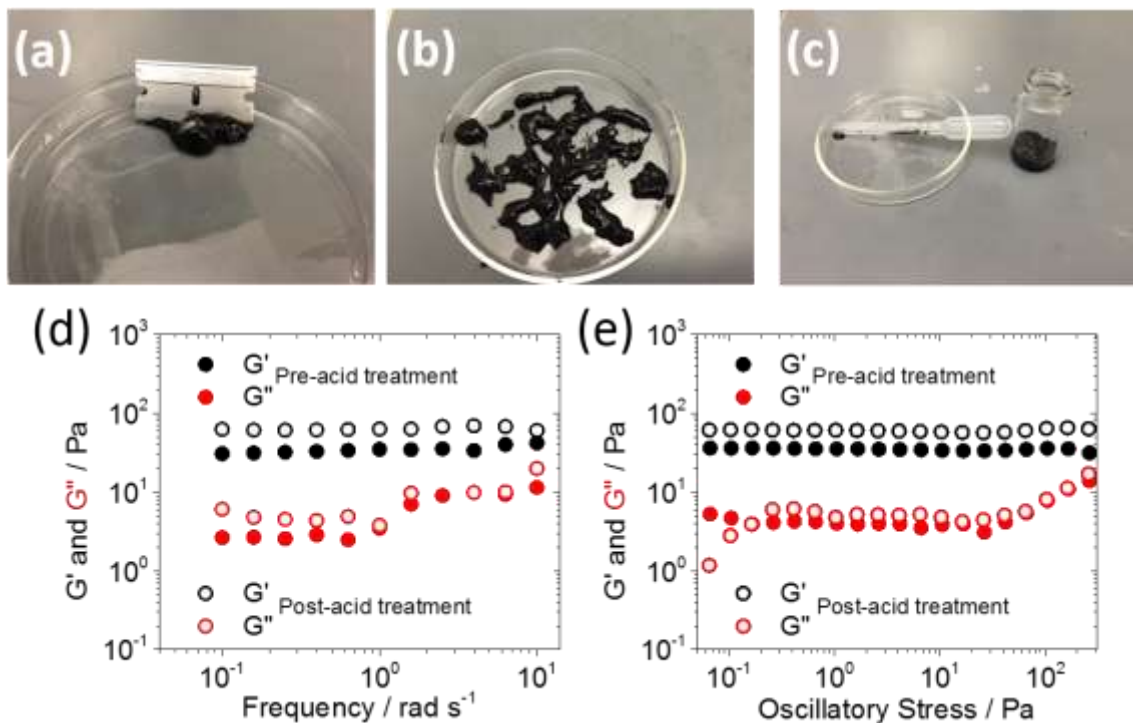


**Figure 6.9.** (a-c) Images of (a) guar + CB gel with the razor blade used to produce (b) a fragmented gel. The gel was (c) placed in a scintillation vial and  $\text{H}_2\text{SO}_4$  was added to yield a concentration of 75 mM. The gel was given 24 hours to swell; Changes in network structure before and after acid treatment were assessed via (d) frequency and (e) stress sweeps.

We examined internal cell resistance of SiNP electrodes using crosslinked guar + CB binders over 300 cycles, and compared the values to SiNP electrodes using non-crosslinked guar +CB binders. Cell resistances were measured on lithiated electrodes via electrochemical impedance spectroscopy (EIS) at 10 mV vs.  $\text{Li}/\text{Li}^+$ . Electrodes were lithiated using a constant-current, constant-voltage technique. Using this technique, SiNP electrodes with crosslinked guar + CB binders displayed higher capacities than SiNP electrodes with non-crosslinked guar binders (**Figure 6.10a**). Addition of the constant-voltage step increased capacities beyond those observed in constant-current cycling measurements shown in **Figure 6.8b**. For example, SiNP electrodes using guar + CB binders crosslinked for 1 day displayed a capacity of  $\sim 2000$

mAh g<sup>-1</sup> after 300 cycles under constant-current, constant-voltage cycling, which is ~ 67% larger than capacities measured using constant current cycling. The large volume expansions during constant-current, constant-voltage lithiation strained the electrodes, and likely increased impedance values. We fit impedance data (as represented in Nyquist plots in **Figure 6.10b**) to the equivalent circuit pictured in **Figure 6.10c**. The circuit comprises: a high-frequency resistance dominated by electronic contact of electrode to current collector ( $R_{CC}$ ); two parallel  $RQ$  elements in series corresponding to film resistance through the SEI and charge-transfer resistance, respectively; a constant phase element ( $Q_3$ ) to model diffusion at low frequencies. Fitting the Nyquist plots to the equivalent circuit revealed an increased high-frequency resistance in SiNP electrodes using non-crosslinked guar binders after 300 cycles (**Figure 6.11d**), as compared to SiNP electrodes using crosslinked binders, which may be attributed to electrode delamination or electrolyte degradations. Relatively unchanged high-frequency resistance values suggest that electrode adhesion to the current collector did not worsen with crosslinking density. Fitting the impedance data to the equivalent circuit after 300 cycles also revealed an increased film resistance (not shown) and slightly lower charge-transfer resistance in SiNP electrodes using crosslinked binders (**Figure 6.10e**), when compared to un-crosslinked systems. Low charge-transfer resistances after 300 cycles may be attributed to the self-healing effect of the binder, which preserved conduction pathways during cycling and allowed SiNP to retain capacity over hundreds of cycles.

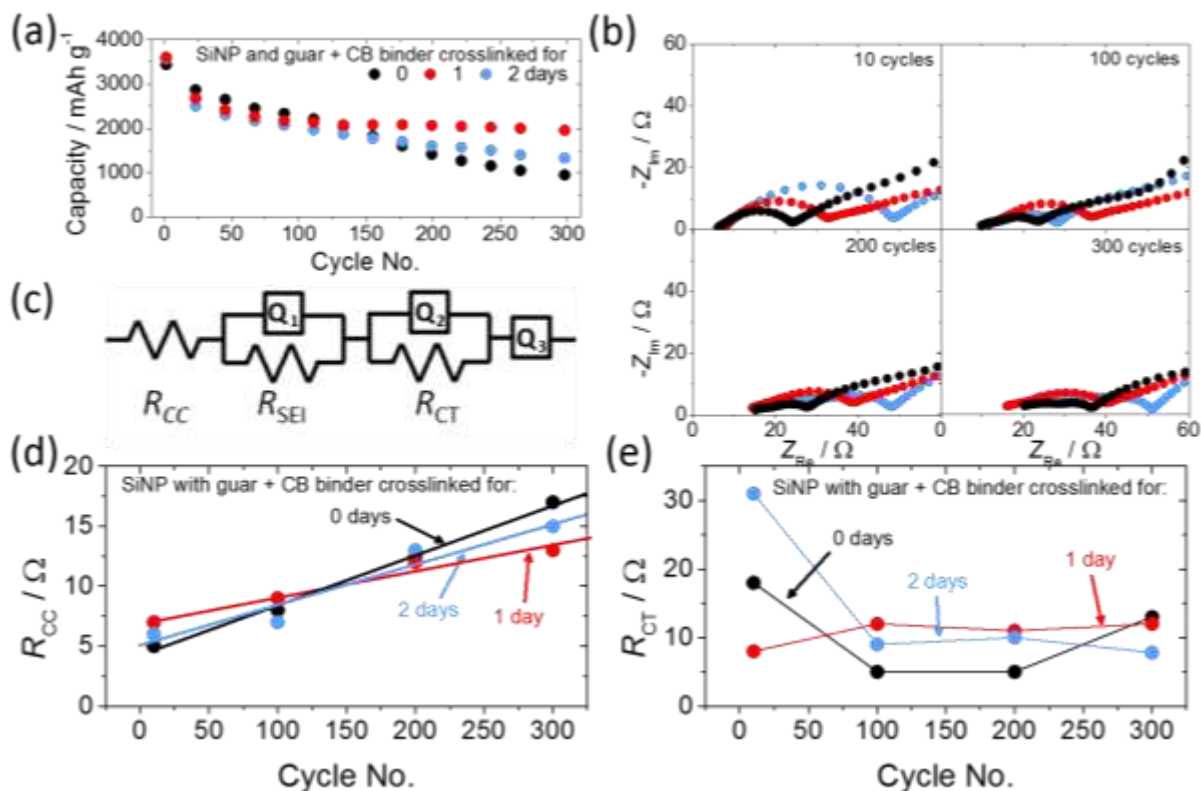


**Figure 6.10.** (a) Capacity over 300 cycles for SiNP electrodes using guar + CB binders that have been crosslinked for 0, 1, and 2 days. Electrodes were lithiated using a constant-current, constant-voltage technique and delithiated at 3.6 A g<sup>-1</sup>; (b) Nyquist plots at select cycles for lithiated electrodes at 10 mV vs. Li/Li<sup>+</sup>; (c) equivalent circuit used to fit impedance data; (d) the high-frequency solution resistance and (e) the charge-transfer resistance, determined by fitting impedance data to the equivalent circuit

#### 6.4. Summary

This study describes a potential next-generation binding agent for SiNP with integrated conductive additive and shows how the viscoelastic properties of the novel binder correlate with electrochemical performance of Li-ion anodes. To achieve this, we chemically crosslinked guar with glutaraldehyde (GA) and carbon black (CB) to produce a binder that reinforced electrode microstructure during the large stresses of lithiation. The crosslinking reaction was monitored using small-amplitude oscillatory rheology, in which we observed a

faster crosslinking reaction and production of stronger networks when guar was crosslinked with carbon black, as compared to unfilled samples. Rheology data suggest that CB may form associations with constituents of the crosslinking mixture (partially crosslinked guar) to enhance network strength. Fourier transform infrared spectroscopy provided a means to assess the crosslinking reaction. We observed increased  $\text{-CH}$  and  $\text{O-C-O}$  peak intensities from the carbon backbone of glutaraldehyde and hemiacetal linkages, respectively, with crosslinking time. We used cryo-SEM to observe relatively dispersed CB particles in the hydrogel binders.

A decrease in elastic modulus for low-crosslink density gels (e.g.  $t_{\text{rxn}} = 1, 2$  days) at strains  $> 40\%$  rendered conformally coated SiNPs, as measured via energy-dispersive x-ray spectroscopy. These SiNP electrodes using low-crosslink density binders exhibited discharge specific capacities  $\sim 1200 \text{ mAh g}^{-1}$  and coulombic efficiencies of  $\sim 99.9\%$  after 300 cycles at 1-C; the crosslinked binders did not hinder volume expansion during lithiation. High capacities in SiNP electrodes after hundreds of cycles using low-crosslink density gel binders may be attributed to favorable electrolyte uptake and lower higher-frequency resistances than un-crosslinked gels and highly crosslinked gels ( $t_{\text{rxn}} > 2$  days). In contrast, gel binders with high-crosslinking density ( $t_{\text{rxn}} > 2$  days) resulted in rigid gel structures that were difficult to deform for slurry casting, and hindered interactions with SiNPs and the electrolyte. First-cycle delithiation capacities decreased by 40% in SiNP electrodes using high-crosslink density binders compared to un-crosslinked binders, which may be due to the lack of binder-Si interactions, or the rigidity of the polymer prohibiting volume expansion.

We observed a systematic increase in capacity retention with crosslinking time using crosslinked guar + CB binders in SiNP electrodes after hundreds of symmetrical charge-discharge cycles at 1-C rates. We attribute the increased retention, in part, to a self-healing phenomenon in the electrodes. Self-healing was evidenced by an increase in elastic modulus after crosslinked guar + CB gels were fragmented and swelled in dilute acid solutions using small-amplitude oscillatory rheology experiments. Self-healing in crosslinked guar binders may arise from hydrogen-bonding or a continuation of the crosslinking reaction in partially crosslinked guar. Thus, the binder has the ability to form bonds in the system to reinforce the electrode and preserve the microstructure. Such preservation of microstructure preserves electron pathways for rapid charge-transfer and a decreased internal cell resistance.

## 6.5. References

- 1 C. K. Chan, H. Peng, G. Liu, K. McIlwrath, X. F. Zhang, R. A. Huggins, Y. Cui. High-performance lithium battery anodes using silicon nanowires, *Nature nanotechnology* (2008), **3**, 31-35.
- 2 K. Peng, J. Jie, W. Zhang, S.-T. Lee. Silicon nanowires for rechargeable lithium-ion battery anodes, *Applied Physics Letters* (2008), **93**, 033105.
- 3 H. Wu, G. Yu, L. Pan, N. Liu, M. T. McDowell, Z. Bao, Y. Cui. Stable Li-ion battery anodes by in-situ polymerization of conducting hydrogel to conformally coat silicon nanoparticles, *Nature communications* (2013), **4**.
- 4 X. H. Liu, L. Zhong, S. Huang, S. X. Mao, T. Zhu, J. Y. Huang. Size-dependent fracture of silicon nanoparticles during lithiation, *ACS nano* (2012), **6**, 1522-1531.
- 5 Y. Yao, M. T. McDowell, I. Ryu, H. Wu, N. Liu, L. Hu, W. D. Nix, Y. Cui. Interconnected silicon hollow nanospheres for lithium-ion battery anodes with long cycle life, *Nano letters* (2011), **11**, 2949-2954.

- 6 T. Swamy, Y.-M. Chiang. Electrochemical Charge Transfer Reaction Kinetics at the Silicon-Liquid Electrolyte Interface, *Journal of the Electrochemical Society* (2015), **162**, A7129-A7134.
- 7 H. Li, X. Huang, L. Chen, Z. Wu, Y. Liang. A high capacity nano Si composite anode material for lithium rechargeable batteries, *Electrochemical and Solid-State Letters* (1999), **2**, 547-549.
- 8 J. K. Lee, K. B. Smith, C. M. Hayner, H. H. Kung. Silicon nanoparticles–graphene paper composites for Li ion battery anodes, *Chemical communications* (2010), **46**, 2025-2027.
- 9 H. Kim, J. Cho. Superior lithium electroactive mesoporous Si@ Carbon core– shell nanowires for lithium battery anode material, *Nano letters* (2008), **8**, 3688-3691.
- 10 J. Li, R. Lewis, J. Dahn. Sodium carboxymethyl cellulose a potential binder for Si negative electrodes for Li-ion batteries, *Electrochemical and Solid-State Letters* (2007), **10**, A17-A20.
- 11 A. Magasinski, B. Zdyrko, I. Kovalenko, B. Hertzberg, R. Burtovyy, C. F. Huebner, T. F. Fuller, I. Luzinov, G. Yushin. Toward efficient binders for Li-ion battery Si-based anodes: polyacrylic acid, *ACS Applied Materials & Interfaces* (2010), **2**, 3004-3010.
- 12 B. Koo, H. Kim, Y. Cho, K. T. Lee, N. S. Choi, J. Cho. A Highly Cross-Linked Polymeric Binder for High-Performance Silicon Negative Electrodes in Lithium Ion Batteries, *Angewandte Chemie International Edition* (2012), **51**, 8762-8767.
- 13 I. Kovalenko, B. Zdyrko, A. Magasinski, B. Hertzberg, Z. Milicev, R. Burtovyy, I. Luzinov, G. Yushin. A major constituent of brown algae for use in high-capacity Li-ion batteries, *Science* (2011), **334**, 75-79.
- 14 M. H. Ryou, J. Kim, I. Lee, S. Kim, Y. K. Jeong, S. Hong, J. H. Ryu, T. S. Kim, J. K. Park, H. Lee. Mussel-Inspired Adhesive Binders for High-Performance Silicon Nanoparticle Anodes in Lithium-Ion Batteries, *Advanced Materials* (2013), **25**, 1571-1576.
- 15 M. Wu, X. Xiao, N. Vukmirovic, S. Xun, P. K. Das, X. Song, P. Olalde-Velasco, D. Wang, A. Z. Weber, L.-W. Wang. Toward an ideal polymer binder design for high-capacity battery anodes, *Journal of the American Chemical Society* (2013), **135**, 12048-12056.

- 16 G. Liu, S. Xun, N. Vukmirovic, X. Song, P. Olalde-Velasco, H. Zheng, V. S. Battaglia, L. Wang, W. Yang. Polymers with tailored electronic structure for high capacity lithium battery electrodes, *Advanced Materials* (2011), **23**, 4679-4683.
- 17 M. K. Dufficy, S. A. Khan, P. S. Fedkiw. Galactomannan binding agents for silicon anodes in Li-ion batteries, *Journal of Materials Chemistry A* (2015), **3**, 12023-12030.
- 18 Y. Cheng, K. M. Brown, R. K. Prud'homme. Characterization and intermolecular interactions of hydroxypropyl guar solutions, *Biomacromolecules* (2002), **3**, 456-461.
- 19 J. Chatterji, J. Borchardt. Applications of water-soluble polymers in the oil field, *Journal of Petroleum Technology* (1981), **33**, 2,042-042,056.
- 20 D. R. Walt, V. I. Agayn. The chemistry of enzyme and protein immobilization with glutaraldehyde, *TrAC Trends in Analytical Chemistry* (1994), **13**, 425-430.
- 21 M. D. Burke, J. O. Park, M. Srinivasarao, S. A. Khan. A novel enzymatic technique for limiting drug mobility in a hydrogel matrix, *Journal of controlled release* (2005), **104**, 141-153.
- 22 S. R. Raghavan, J. Hou, G. L. Baker, S. A. Khan. Colloidal interactions between particles with tethered nonpolar chains dispersed in polar media: direct correlation between dynamic rheology and interaction parameters, *Langmuir* (2000), **16**, 1066-1077.
- 23 A. K. Higham, L. A. Garber, D. C. Latshaw, C. K. Hall, J. A. Pojman, S. A. Khan. Gelation and cross-linking in multifunctional thiol and multifunctional acrylate systems involving an in situ comonomer catalyst, *Macromolecules* (2014), **47**, 821-829.
- 24 C. Sandolo, P. Matricardi, F. Alhaique, T. Coviello. Effect of temperature and cross-linking density on rheology of chemical cross-linked guar gum at the gel point, *Food Hydrocolloids* (2009), **23**, 210-220.
- 25 N. A. Burns, M. A. Naclerio, S. A. Khan, A. Shojaei, S. R. Raghavan. Nanodiamond gels in nonpolar media: Colloidal and rheological properties, *Journal of Rheology (1978-present)* (2014), **58**, 1599-1614.
- 26 H. Winter. Transient Networks: Evolution of rheology during chemical gelation, *Progress in Colloid & Polymer Science* (1987), **75**, 104-110.

- 27 Y. Cheng, K. M. Brown, R. K. Prud'homme. Preparation and characterization of molecular weight fractions of guar galactomannans using acid and enzymatic hydrolysis, *International Journal of Biological Macromolecules* (2002), **31**, 29-35.
- 28 S. Khan. Effect of shear on the gelation of UV-curable polymers, *Journal of Rheology (1978-present)* (1992), **36**, 573-587.
- 29 I. Gliko-Kabir, B. Yagen, A. Penhasi, A. Rubinstein. Low swelling, crosslinked guar and its potential use as colon-specific drug carrier, *Pharmaceutical research* (1998), **15**, 1019-1025.
- 30 B.-S. Chiou, S. R. Raghavan, S. A. Khan. Effect of colloidal fillers on the cross-linking of a UV-curable polymer: gel point rheology and the Winter-Chambon criterion, *Macromolecules* (2001), **34**, 4526-4533.
- 31 T. Van Vliet. Rheological properties of filled gels. Influence of filler matrix interaction, *Colloid and Polymer Science* (1988), **266**, 518-524.
- 32 R. Buscall, P. D. Mills, J. W. Goodwin, D. Lawson. Scaling behaviour of the rheology of aggregate networks formed from colloidal particles, *Journal of the Chemical Society, Faraday Transactions 1: Physical Chemistry in Condensed Phases* (1988), **84**, 4249-4260.
- 33 M. Chen, W. Russel. Characteristics of flocculated silica dispersions, *Journal of colloid and interface science* (1991), **141**, 564-577.
- 34 V. Trappe, D. Weitz. Scaling of the viscoelasticity of weakly attractive particles, *Physical review letters* (2000), **85**, 449.
- 35 W.-H. Shih, W. Y. Shih, S.-I. Kim, J. Liu, I. A. Aksay. Scaling behavior of the elastic properties of colloidal gels, *Physical Review A* (1990), **42**, 4772.
- 36 N. Jouault, P. Vallat, F. Dalmas, S. Said, J. Jestin, F. Boué. Well-Dispersed Fractal Aggregates as Filler in Polymer– Silica Nanocomposites: Long-Range Effects in Rheology, *Macromolecules* (2009), **42**, 2031-2040.
- 37 S. Nandi, H. H. Winter. Swelling behavior of partially cross-linked polymers: a ternary system, *Macromolecules* (2005), **38**, 4447-4455.
- 38 J. Lopez, Z. Chen, C. Wang, S. C. Andrews, Y. Cui, Z. Bao. The effects of crosslinking in a supramolecular binder on cycle life in silicon microparticle anodes, *ACS Applied Materials & Interfaces* (2015).

- 39 B. Auer, R. Kumar, J. Schmidt, J. Skinner. Hydrogen bonding and Raman, IR, and 2D-IR spectroscopy of dilute HOD in liquid D<sub>2</sub>O, *Proceedings of the National Academy of Sciences* (2007), **104**, 14215-14220.
- 40 K.-J. Kim, S.-B. Lee, N. W. Han. Effects of the degree of crosslinking on properties of poly (vinyl alcohol) membranes, *Polymer Journal* (1993), **25**, 1295-1302.
- 41 P. Calvini, A. Gorassini, G. Luciano, E. Franceschi. FTIR and WAXS analysis of periodate oxycellulose: evidence for a cluster mechanism of oxidation, *Vibrational Spectroscopy* (2006), **40**, 177-183.
- 42 C. Wang, H. Wu, Z. Chen, M. T. McDowell, Y. Cui, Z. Bao. Self-healing chemistry enables the stable operation of silicon microparticle anodes for high-energy lithium-ion batteries, *Nature chemistry* (2013), **5**, 1042-1048.
- 43 H. Van Melick, L. Govaert, H. Meijer. On the origin of strain hardening in glassy polymers, *Polymer* (2003), **44**, 2493-2502.
- 44 E. J. Kramer. Open questions in the physics of deformation of polymer glasses, *Journal of Polymer Science Part B: Polymer Physics* (2005), **43**, 3369-3371.
- 45 T. R. Hoare, D. S. Kohane. Hydrogels in drug delivery: progress and challenges, *Polymer* (2008), **49**, 1993-2007.
- 46 M. Sharma, D. Mondal, C. Mukesh, K. Prasad. Self-healing guar gum and guar gum-multiwalled carbon nanotubes nanocomposite gels prepared in an ionic liquid, *Carbohydrate Polymers* (2013), **98**, 1025-1030.

## **Chapter 7. Vacancy-Induced Manganese Vanadates and Their Potential Application to Li-ion Batteries**

Chapter 7 is essentially a manuscript by Martin K. Dufficy, Lan Luo, Peter S. Fedkiw, and Paul A. Maggard that was published in *Chemical Communication*, 2016, **52**, 7509-7512

## Abstract

We report on the synthesis and characterization of a novel manganese vanadate,  $\text{Mn}_{1.5}(\text{H}_2\text{O})(\text{NH}_4)\text{V}_4\text{O}_{12}$ , with rare in-situ disorder of  $\text{Mn}(\text{H}_2\text{O})_2^{2+}/2\text{NH}_4^+$ . We show that vacancies created by ammonium ions and coordinating water molecules in the manganese vanadate crystal structure yield high-charge capacity, favorable rate capability, and long cycle life in Li-ion half-cells.

## 7.1. Introduction

Lithium-ion batteries are ubiquitous electrochemical energy storage devices used in mobile appliances due to high-energy density and power output.<sup>1</sup> Aspirations to enhance performance beyond current commercial batteries spurred exploration of new, inexpensive electrode materials that host large quantities of Li to increase charge capacity.<sup>2</sup> This study focuses on a new manganese vanadate composed of coordinating water and ammonia ions,  $\text{Mn}_{1.5}(\text{H}_2\text{O})(\text{NH}_4)\text{V}_4\text{O}_{12}$  (**I**), as an active anode material. Previous attempts to utilize manganese vanadates as active anode materials were marred by a short cycle life<sup>3</sup> and poor electronic conductivity, which hinders rate capabilities at fast charging rates.<sup>4</sup> To combat the aforementioned issues with manganese vanadates, we introduce Mn-ion deficiencies and coordinating  $\text{H}_2\text{O}/\text{NH}_4^+$  into the crystal structure to create channels that facilitate Li-transport. In this chapter, we report the development and characterization of a manganese vanadate with a rare *in-situ* disorder of  $\text{Mn}(\text{H}_2\text{O})_2^{2+}/2\text{NH}_4^+$  and demonstrate impressive charge-carrying capability as electrode materials in Li-ion half-cells. The vacancy-induced structure allows for capacities beyond that of the standard graphite ( $372 \text{ mAh g}^{-1}$ ) and alternate lithium titanate

(LTO ~ 175 mAh g<sup>-1</sup>); we observe initial charge capacities of ~1600 mAh g<sup>-1</sup>, with stable capacities at fast rates (500 mAh g<sup>-1</sup> at 500 mA g<sup>-1</sup>) over hundreds of cycles.

## 7.2. Experimental Section

### 7.2.1. Materials and Instrumentation

All reagents were used as supplied by the manufacturer without further purification, including: Mn(NO<sub>3</sub>)<sub>2</sub>·nH<sub>2</sub>O (99.98%, Alfa Aesar), Co(NO<sub>3</sub>)<sub>2</sub>·6H<sub>2</sub>O (98.0%, Alfa Aesar), and NH<sub>4</sub>VO<sub>3</sub> (99.99%, Aldrich). Deionized water was used as a reagent in each hydrothermal reaction. The inactive electrode materials consisted of Super P Li (Timcal Graphite & Carbon) and carboxymethyl cellulose (Sigma Aldrich). The electrolyte comprised 1 M lithium hexafluorophosphate salt (LiPF<sub>6</sub>, BASF) dissolved in ethylene carbonate (EC, 99% pure, Sigma Aldrich) and ethyl methyl carbonate (EMC, Ferro Corp.) 1:1 wt% mixture. Electrolyte solvents were dried in molecular sieves (4Å, Sigma Aldrich) to a water content < 10 ppm. A 25-μm thick separator (Celgard) was used to prevent contact between the working electrode and the Li counter/reference electrode (Sigma Aldrich).

High-resolution Powder XRD data were collected on a RIGAKU R-Axis Spider Powder X-ray diffractometer (graphite monochromatized Cu Kα radiation) at room temperature. Powder X-ray diffraction patterns were scanned with a step size of 0.02° over the 2θ angular range from 4° to 100° and dwell times of 4 s for each step. Thermogravimetric analyses were taken on a TA Instruments TGA Q50 by loading ~5.0 mg onto a platinum pan. The pan was equilibrated and tared at room temperature and heated to 600 °C at a rate of 5 °C/min in air. The post-heated TGA residues were characterized by powder XRD, as described

above. Specific surface areas of **I** was measured on a Quantachrome ChemBET Pulsar TPR/TPD. Samples were preheated to 140 °C under flowing N<sub>2</sub> to degas for 3 h, and then cooled with liquid nitrogen and analyzed using a 30% He/N<sub>2</sub> gas mixture. Both pre-cycled and post-cycled electrodes were imaged on an FEI Verios 460L field-emission scanning electron microscope (FESEM). In a glovebox, post-cycled cells were decrimped, and the working electrode was washed with EMC and dried; exposure to air was limited to the FESEM sample loading. Half-cell cycling experiments were performed on an Arbin BT-2000 while cyclic voltammetry (CV) and electrochemical impedance spectroscopy (EIS) experiments were performed on a Bio-Logic VMP3.

#### 7.2.2. Synthetic Procedures.

Mn<sub>1.5</sub>(H<sub>2</sub>O)(NH<sub>4</sub>)V<sub>4</sub>O<sub>12</sub> (**I**) was synthesized by mixing of 0.0367 g Mn(NO<sub>3</sub>)<sub>2</sub>·nH<sub>2</sub>O, 0.0400 g NH<sub>4</sub>VO<sub>3</sub>, and ~1mL H<sub>2</sub>O in a molar ratio of 1:2:~300 into a polytetrafluoroethylene Teflon pouch (3'' × 3'') that was then heat sealed in air. The pouch was placed into a 125 mL polytetrafluoroethylene-lined stainless-steel autoclave that was backfilled with ~40 mL deionized water before closing. The reaction vessel was heated to 130°C for 72 h in a convection oven, then subsequently slowly cooled to room temperature at a rate of 6°C/h. The products were washed with deionized water, collected, and dried at 60°C overnight. Small brown needlelike crystals were obtained in a yield of ~70.0% (based on vanadium). **I** was obtained in high phase purity (> 95%) according to powder X-ray diffraction data. Crystallographic data on **I** with CCDC No. 1477963.

### 7.2.3. *Electrode Fabrication and Characterization.*

A slurry comprising 70 wt% **I**, 20 wt% carbon black, and 10 wt% binder was cast on Cu foil. Slurries were cast using the doctor-blade method to a desired thickness (25 or 50  $\mu\text{m}$ , corresponding to 1 or 2  $\text{mg cm}^{-2}$  of **I**, respectively). The resulting electrode film was dried in a convection oven at 40°C, punched into 1  $\text{cm}^2$  disks, and dried in a vacuum oven at 110°C overnight. The disks were placed as the working electrode vs Li metal in 2032 coin-cells. The electrolyte was added via pipette onto the working electrode ( $\sim 50 \mu\text{L}$ ) and the separator ( $\sim 50 \mu\text{L}$ ). A spacer and spring were placed on top of Li metal and the coin-cell was hermetically crimped. Half-cells were given a 24 hour rest period at open circuit prior to electrochemical characterization. We defined the capacity of the half-cells such that a 1-C rate corresponds to 1.2  $\text{A g}^{-1}$ . All half-cells were cycled between 10 mV and 3 V vs. Li/Li<sup>+</sup>. A formation cycle (one cycle at C/24) was applied to all half-cells prior to electrochemical performance assessments. The capacity for **I** electrodes at various rates was determined using the 10<sup>th</sup> cycle in an experiment. Potentiostatic impedance experiments were performed between 100 kHz and 100 mHz using an amplitude of 10 mV. Prior to running EIS, half-cells were (dis)charged using a current density of 10  $\text{mA g}^{-1}$  to a specified voltage followed by constant voltage until a current of C/100.

### 7.2.4. *Ex-Situ Electrode Characterization.*

Half-cells were charged/discharged using a constant current-constant voltage technique; constant currents of 10  $\text{mA g}^{-1}$  were applied to **I** electrodes to reach specific voltages, followed by constant voltage until a current of C/100. The cell was transferred into

the glovebox where it was decrimped, washed with EMC, and vacuum dried overnight at room temperature. Still in the glovebox, the electrode material was scraped off the copper foil current collector, milled in a mortar and pestle, and sealed in a capillary to prevent contact with air. Powder XRD was run on the samples. The electrode material from *ex-situ* PXRD analysis, described above, was heated to 600°C in air at a heat rate of 5°C min<sup>-1</sup>.

### 7.3. Results

#### 7.3.1. Crystallographic characterization

**I** was prepared hydrothermally from Mn(NO<sub>3</sub>)<sub>2</sub>•nH<sub>2</sub>O and NH<sub>4</sub>VO<sub>3</sub> via a procedure presented in the Supplementary Information. The crystalline structure of **I** consists of edge-sharing VO<sub>5</sub> chains linked through vertical oxygen atoms of MnO<sub>6</sub> octahedra (**Figure 7.1a**). There are two symmetry inequivalent vanadium (V1, V2) and manganese (Mn1, Mn2) atoms in square pyramidal and octahedral geometries, respectively. The VO<sub>5</sub> square pyramids share basal oxygen atoms and form zigzag chains along the *b*-axis (**Figure 7.1b** and **7.1c**). The two parallel vanadate chains bridge two parallel MnO<sub>6</sub> octahedral chains and form a channel along the *b*-axis. To form the three-dimensional network shown in Figures 1a and 1b, adjacent polyhedral layers bridge through Mn1 in the Mn(H<sub>2</sub>O)<sub>2</sub>O<sub>4</sub> octahedra via apical oxygen atoms of the square pyramidal environment of V2. However, the crystallographic site for Mn1 is statistically only 50% occupied (described below), resulting in weakened bonding interactions between the layers.

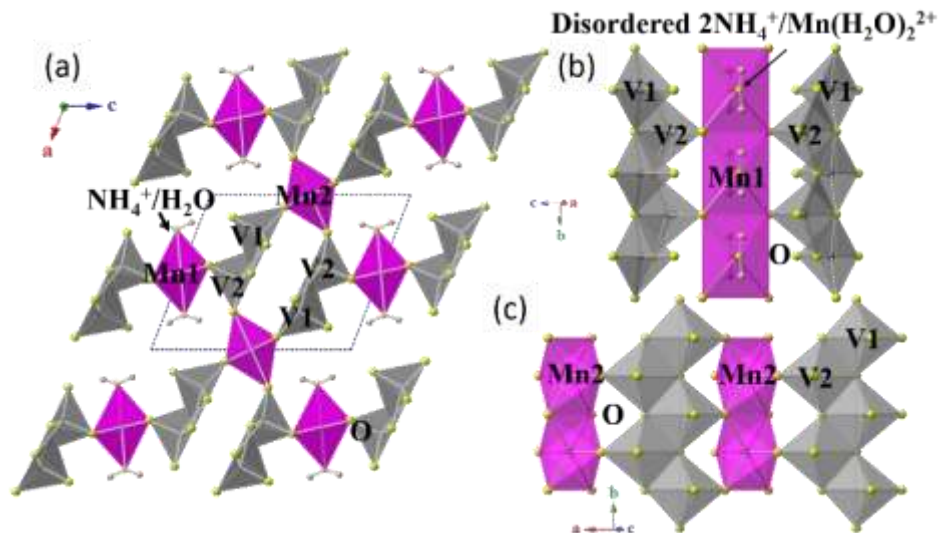


**Figure 7.1.** Polyhedral view of **I** showing (a) the unit cell down the  $b$ -axis; Edge-sharing  $\text{VO}_5$  square pyramidal chains along the  $b$ -axis, bridged through corner oxygen atoms by (b)  $\text{MnO}_6$  octahedral chains and (c) disordered  $\text{MnO}_4(\text{H}_2\text{O})_2^{2+}/2\text{NH}_4^+$ .

Two water molecules coordinate to Mn1 in a *trans* fashion, and thus disrupt the connectivity of the metal-oxygen networks. This results in two adjacent Mn1 atoms bridged through four additional  $\text{VO}_5$  pyramids, forming a larger channel along the  $b$ -axis as compared to that formed by Mn2. Interestingly, Mn1 is only half occupied. In the absence of Mn1, two  $\text{NH}_4^+$  ions occupy the same position as  $\text{H}_2\text{O}$ . Notably, the bond length between Mn and  $\text{H}_2\text{O}$  is 2.122(3) Å, which is shorter than a typical Mn-OH<sub>2</sub> bond at 2.21(1) Å.<sup>5</sup> The list of bond lengths and angles for the Mn and V atoms (**Appendix Table D1**), thermogravimetric analysis (**Appendix Figure D1**) and infrared spectra (**Appendix Figure D2**) of **I** are provided in the Supplementary Information, as evidence of two symmetry inequivalent Mn and V atoms, coordinating water, and ammonia ions. To the best of our knowledge, this type of disorder has not previously been reported. The strong bonding interaction between  $\text{H}_2\text{O}$  and  $\text{Mn}^{2+}$  of **I** yields neither  $\text{H}_2\text{O}$  dissolution nor electrochemical reduction/oxidation during Li-ion half-cell

cycling. The coordinating H<sub>2</sub>O molecules help expand channels in the structure, and NH<sub>4</sub><sup>+</sup> ions aid in creating Mn<sup>2+</sup> vacancies while maintaining charge balance and stabilizing the structure. The Mn<sup>2+</sup> deficiency serves to increase the porosity of the structure. Therefore, **I** is less condensed than other anhydrous manganese vanadates, e.g. MnV<sub>2</sub>O<sub>6</sub>, Mn<sub>2</sub>V<sub>2</sub>O<sub>7</sub> etc., creating probable active sites for Li-insertion and channels for facilitated Li-diffusion.

### 7.3.2. Electrochemical characterization

We first probed the electrochemical performance in Li-ion half-cells by studying full insertion and extraction capacities at slow (10 mA g<sup>-1</sup>) rates. Electrode films of **I** were slurry-cast in aqueous media (procedure in Supplementary Information). **I** electrodes exhibited an initial intercalation capacity of ~1600 mAh g<sup>-1</sup> and de-intercalation capacity of ~1400 mAh g<sup>-1</sup>, resulting in ~88% capacity retention on the first cycle (**Figure 7.2a**). Initial Li-insertion and subsequent Li-extraction capacities are the highest reported for manganese vanadates to our knowledge.<sup>6</sup> While vanadates have been investigated as cathode materials in Li-ion batteries, (reviewed by Whittingham et al.<sup>7</sup>) incorporation of Mn in **I** decreased the Li-insertion potential vs Li/Li<sup>+</sup> and increased the Li-insertion capacity beyond vanadates. We acknowledge that the Li-extraction potential is high, making **I** a possible candidate for anodes with appropriate pairing of high-voltage cathodes. Potentials at which Li-ions (de)intercalate into the host structure are labeled on Figure 2a and exemplified by peaks in the capacity differential (dQ/dV) profiles (**Appendix Figure D3**).

We estimated a total of ~18 mols Li intercalate per mol **I** (calculations detailed in Supplementary Information). While large quantities of Li in the electrode structure give **I** a

large capacity, they may also contribute to stress within the crystal structure and promote structure rearrangement. The obtrusive nature of Li-insertion has been observed in elemental Li-host electrodes such as Si.<sup>8</sup> We employed ex-situ powder XRD (PXRD, procedure in Supplementary Information) to observe impending structural rearrangement. Powder x-ray diffractograms provided insight on likely Li-binding sites in novel **I** electrodes, structure rearrangements caused by Li-insertion, and possible dissolution of Mn-ions (**Figure 7.2b**). We analyzed the crystal structure at potentials —lettered **A-G** in Figure 2a—corresponding peaks in dQ/dV plots (**Appendix Figure D3**). The diffractogram of as-synthesized **I** (**A**) revealed a pattern similar to the calculated structure (**Appendix Figure D4**)—evidence of a pure, single-phase product. Upon full-lithiation, diffraction patterns revealed a structural change, from an as-synthesized crystalline to amorphous. PXRD data upon intercalation at **B** (1.5 V) and **C** (270 mV) indicated structures maintained crystallinity, and Li-insertion positions at **B** and **C** were estimated and simulated (**Appendix Figure D5**).

Upon insertion at **B**, a slight *d*-spacing expansion ( $\sim 1.3$  Å) was observed along the *a*-axis as the peak shifted to a smaller angle. The change is consistent with one Li<sup>+</sup> inserted into the (0, 0, 0) sites per unit cell, with a calculated volume increase of 15.1% ( $43.4$  Å<sup>3</sup>). The simulated PXRD pattern of **I** electrodes charged to **B** agrees with the experimental pattern; Li<sup>+</sup> binds in the vacancy created by water and ammonia ions, surrounded by four oxygen atoms from VO<sub>5</sub> (Li-O at  $2.431$  Å) and four H<sub>2</sub>O/NH<sub>4</sub><sup>+</sup> (Li-N(O) at  $3.178$  Å). The Li-O/N distances are significantly longer than the average Li-O/N distances ( $1.7$  Å), which allow further intercalation in this vacant site. At **C**, two additional Li<sup>+</sup> are inserted in the same site as in **B**

(approximate fractional coordination is (0.95, 0, 0.22)) and expanding the (0 0 1) interplanar spacing ( $\sim 1.1$  Å). The latter is found from the XRD peak shifting to lower angles, with an additional volume increase of 13.4% ( $38.3$  Å<sup>3</sup>). Similar to the first lithiation step at **B**, Li-ions are surrounded by five oxygen atoms (Li-O at 2.599-2.814 Å) and two nitrogen atoms (Li-N at 2.453 Å). This is expected as Li<sup>+</sup> binds along the *c*-direction. While lattice expansion along the *c*-axis increases the M-O (M = Mn and V) distances, compression along the *a*-axis may strengthen the M-O bonds and stabilize the structure. Reversibility of Li-O and Li-N bonds is under further investigation. Proposed structures of lithiated-**I** at **B** and **C** are shown in Figure 2c, d.

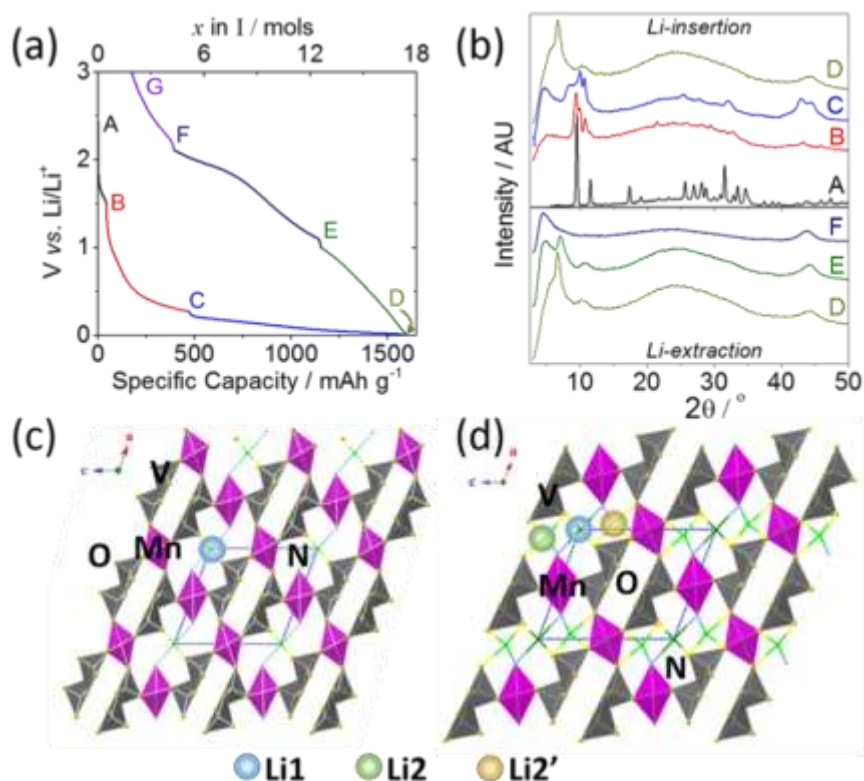


**Figure 7.2.** (a) Initial charge/discharge profile for **I** electrodes at  $10 \text{ mA g}^{-1}$ ; the lettering refers to potentials where Li-ion (de)intercalate; (b) PXRD patterns of **I** electrodes at (de)intercalation voltages lettered in (a); Proposed crystal structures of **I** after (c) 1 mol per formula Li-ion intercalate at **B** and (d) 3 mol per formula Li-ion intercalate at **C**.

At full-lithiation, **D** (10 mV), the interplanar spacing of (0 0 1) further increases. This continuous peak shifting suggests that Li intercalates into the same sites as **B** and **C**. The majority of Li-intercalation occurs between **C** and **D**, which results in a large lattice expansion. Based on the aforementioned PXRD data, a probable Li-insertion mechanism is proposed; Li-ions intercalate in the structure of **I** facilitated by the Mn-induced vacancies, diffusing along the MnO<sub>6</sub>/VO<sub>5</sub> channels down the *b*-axis, and binding in vacancies created by displaced water and/or ammonia ions.

Upon deintercalation at **E** (1 V), the (1 0 0) diffraction peak returns to a larger angle as Li-ions are extracted from the structure. An increased low-angle ( $2\theta \approx 4.5^\circ$ ) peak intensity was also observed, which may originate from Mn dissolution. Irreversible dissolution of Mn-ions in LiPF<sub>6</sub>-based electrolytes and consequential structural instabilities has plagued Mn-oxide cathodes.<sup>9</sup> The low-angle ( $2\theta \approx 4.5^\circ$ ) peak observed at **F** (2 V) suggests that the structure is generally maintained, albeit significantly more amorphous. The morphological changes in **I** are attributed to the irreversible Mn dissolution and the obtrusive nature of Li-insertion. The dissolution of Mn-ions was further probed via thermal decomposition of powder obtained at each voltage, as followed by PXRD (**Appendix Figure D6**). As the potential decreased, manganese contributed less to decomposition products. Major decomposition products of **I** electrodes included LiVO<sub>3</sub> and LiMnVO<sub>4</sub> at **B**, and Li<sub>3</sub>VO<sub>4</sub> from **C** to **F** (**Appendix Figure D6**). We observed strong diffraction peaks of LiMnVO<sub>4</sub> at **B** and weak peaks of Li<sub>2</sub>MnO<sub>3</sub> at **D**. Weak Li<sub>2</sub>MnO<sub>3</sub> peaks are attributed to disproportionation and dissolution of the Mn<sup>2+</sup> ions in electrolyte,<sup>10</sup> and may be the origin of the low-angle ( $2\theta \approx 4.5$ ) PXRD peak observed at **C**

in **Figure 7.2**. Manganese was nominally observed in decomposition products of **I** during Li-extraction (from **E** and **F**). We are currently attempting means to stabilize the disproportionation and resulting dissolution of Mn-ions.

Beyond the first charge/discharge cycle in half-cell tests, **I** electrodes performed much better than manganese vanadate electrodes reported in literature,<sup>11</sup> which may be attributed, in part, to the abundant Mn-site vacancies. After initial capacity loss, attributed to the restructuring and solid-electrolyte interphase (SEI) formation, we observed a stable discharge capacity of 500 mAh g<sup>-1</sup> (1 mAh cm<sup>-2</sup>) at a symmetrical current density of 500 mA g<sup>-1</sup> over 300 cycles (**Figure 7.3a**). The capacity reached a steady value after ~8 cycles, which is analogous to the cyclic voltammogram (**Appendix Figure D7**), where we observed no fluctuation in current densities and peak voltages stabilized after the eighth cycle. The coulombic efficiency averaged to > 99.9% following the restructuring of **I**. High-CEs indicate compatibility between the electrode, binder, and electrolyte and gives promise to the use of **I** as a stable electrode over many more cycles. Voltage profiles and corresponding capacity derivatives (**Appendix Figure D8**) revealed no (de)intercalation voltage fade in **I** electrodes once capacity stabilized. Unchanged voltage profiles with cycle index signify sustained full cell energy density. Although the energy density is low, we are pursuing efforts to reduce charge/discharge polarization. Efforts include coating **I** with carbon, which increases conductivity and extends cycle of electrode materials,<sup>12</sup> or substituting Mn with other transition metals.

Rate-capability tests (**Figure 7.3b**) revealed that **I** electrodes achieve capacities greater than graphite and LTO at charge/discharge rates commonly used in commercial batteries; at 0.4-C (0.5 A g<sup>-1</sup>), at measured capacities of ~500 mAh g<sup>-1</sup>. Discharge capacities in Figure 3b represent values on the tenth consecutive, symmetrical cycle. Capacity decrease (with current density) in **I** electrodes suggests ohmic limitations, most likely due to relatively poor electronic conductivity. Capacity decreases may be alleviated by using thinner electrodes; capacity increased in electrodes from 75 mAh g<sup>-1</sup> to 300 mAh g<sup>-1</sup> at 1200 mA g<sup>-1</sup> when areal loading decreased from 2 to 1 mg cm<sup>-2</sup>, respectively, giving promise to **I** electrodes for high-power applications (noting the low-cost and facile synthesis of **I**). Similarly, Wakihara and coworkers<sup>13</sup> discovered Mn vacancies introduced by Mo doping in MnV<sub>2</sub>O<sub>6</sub> improved Li-diffusion rates to enhance the rate performance. The large vacancies in **I**, created by water and ammonia-ions, produce channels and allow this materials to exhibit larger capacities with a longer cycle life than similar manganese-vanadates reported in literature.<sup>11-13</sup> While charge capacities between 450-500 mAh g<sup>-1</sup> are reported in literature, these electrodes were subject to higher cutoff voltages (increasing operating voltages), slower rates, and exhibited deleterious capacity fading. A literature survey (**Appendix Table D2**) reporting electrochemical performances of Mn-V-based anodes accentuates the superior performance of **I** anodes produced in this study.

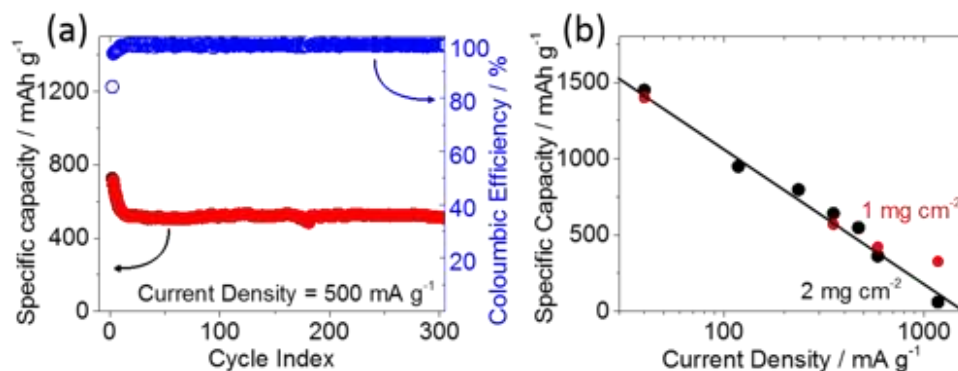


**Figure 7.3.** Electrochemical characterization of **I** electrodes in Li-ion half-cells showing (a) capacities for 300 cycles cycled at  $0.5 \text{ A g}^{-1}$  along with the corresponding coulombic efficiencies (CEs) with an areal loading =  $2 \text{ mg cm}^{-2}$ ; (b) capacities as a function of current density with varied areal loading.

The SEM images of **I** electrodes before cycling (**Figure 7.4 a, b**) show large particles with a relatively smooth, un-textured surface. The low-specific surface area particles ( $\sim 3 \text{ m}^2 \text{ g}^{-1}$  as measured via BET), particularly in relation to the conductive additive ( $62 \text{ m}^2 \text{ g}^{-1}$ ), contributed to less SEI formation than nanostructures with high-specific surface areas such as porous hard carbons.<sup>14</sup> Large amounts of SEI formation are undesired, as they produce an electronically resistive surface layer and induce irreversible capacity loss. In this study, we see stable capacities and CEs  $> 99.9\%$  throughout the duration of electrochemical testing, and low film resistances on the first cycle from electrochemical impedance spectroscopy (**Appendix Figure D9**), suggesting stable SEI formation on the initial cycle. Post-mortem SEM analysis was conducted to obtain more information on **I** electrode structure and ensuing SEI.

Post-mortem SEM analysis after 300 cycles (**Figure 7.4 c-f**) revealed many significant features related to cycling stability: (1) preservation of electrode morphology after cycling; (2) formation of SEI on **I** surface; and (3) lack of particle pulverizations. There is little difference in pre-cycled (**Figure 7.4a**) and post-cycled (**Figure 7.4c**) electrode microstructure, evidence that carboxymethyl cellulose (CMC) is a good binder for **I**; CMC may interact favorably with

complexed-surface water molecules via hydrogen bonding<sup>15</sup> to enhance electrochemical performance. Preservation of electrode microstructure is necessary to maintain electronic contact throughout the thick electrode (50  $\mu\text{m}$ ). It is also important to note that delamination of electrode from the Cu current collector was not observed (**Figure 7.4e**), which is also important to decrease electronic resistance within the half-cell. Higher-resolution images of post-cycled **I** electrode surface in contact with separator (**Figure 7.4d**) and cross-section (**Figure 7.4f**, inset) revealed a definitive change in surface texture from the un-cycled electrodes (**Figure 7.4b**). The newly developed surface texture depicts the SEI, which gives **I** great cycling ability over hundreds of cycles. Finally, we see no particle pulverization despite the large particle size. Pulverization and subsequent SEI formation on freshly exposed active surface leads to electronic isolation and short cycle life. The large particle sizes, and subsequent volume expansion (evidenced by ex-situ PXRD) due to the large amount of Li-ions present ( $\sim 18$  mol Li / mol **I**) in the material upon intercalation, are indicative of the strong, bonding interactions of the framework within the crystal structure.

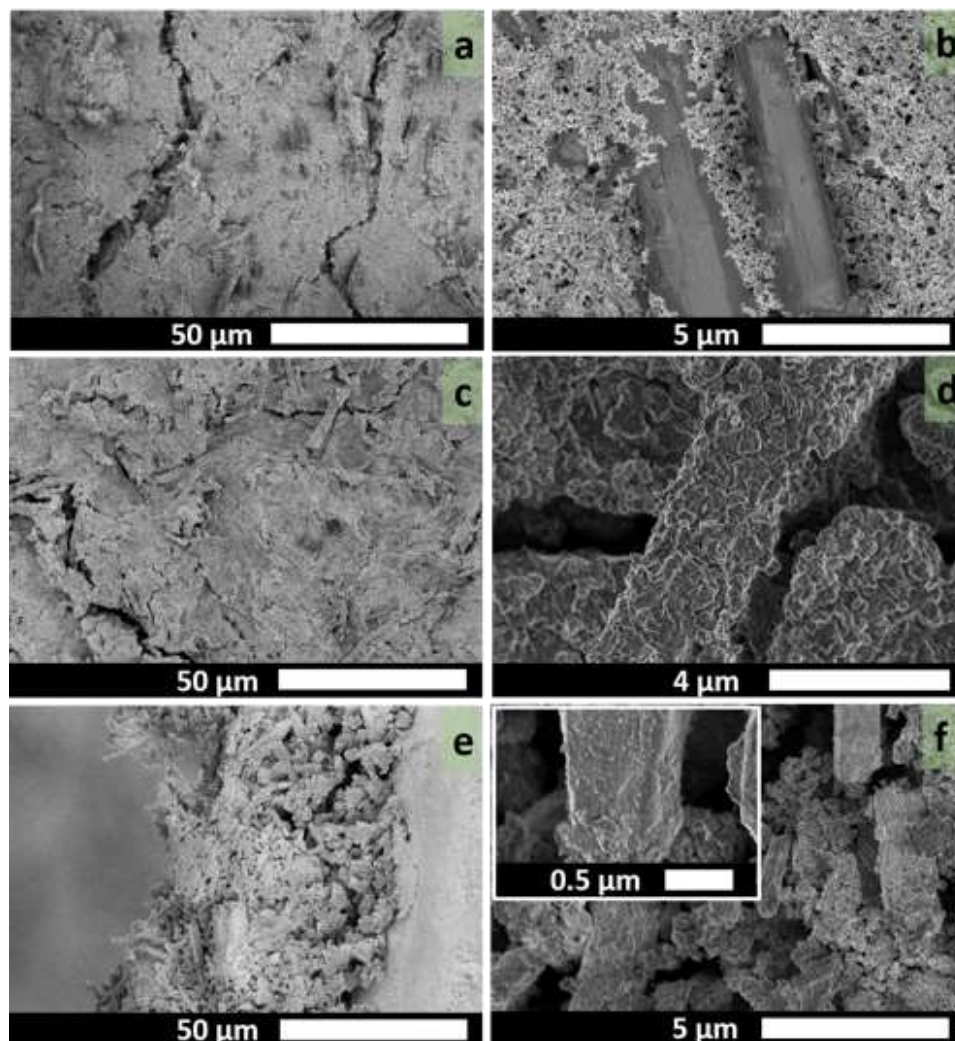


**Figure 7.4.** SEM images showing the top surface of **I** electrodes (a, b) before cycling and (c, d) after 300 cycles; (e,f) cross-section of electrodes after 300 cycles; inset of (f) reveals high-magnification image of a cycled **I** particle.

#### 7.4. Summary

To summarize, a new manganese vanadate,  $\text{Mn}_{1.5}(\text{H}_2\text{O})(\text{NH}_4)\text{V}_4\text{O}_{12}$  (**I**), was prepared with rare Mn-ion vacancies. When cycled against metallic Li in half-cells, these vacancies provided channels for Li-ions to transport and bind in **I**, thus giving way to a large initial charge capacity. After the first cycle, and amorphization, **I** electrodes decreased in capacity, yet led to a structure capable of generating capacities beyond commercial graphite for hundreds of cycles.

Reversible cycling was also attributed, in part, to compatibility between the electrode and electrolyte, which consisted of commercial salt and solvents. We envision **I** to be a prototypical vacancy-induced material with high Li-binding stoichiometries, as we strive to develop and assess vacancy-induced materials that further increase capacity and decrease Li-extraction potential for high-energy dense, next-generation Li-ion batteries.

## 7.5. References

- (1) a) C. K. Chan, H. Peng, G. Liu, K. McIlwrath, X. F. Zhang, R. A. Huggins, Y. Cui. *Nat Nano*, **3**, 2008, 31-35; b) B. A. Johnson, R. E. White. *Journal of Power Sources*, **70**, 1998, 48-54; c) K. T. Nam, D.-W. Kim, P. J. Yoo, C.-Y. Chiang, N. Meethong, P. T. Hammond, Y.-M. Chiang, A. M. Belcher. *Science*, **312**, 2006, 885-888.
- (2) a) B. Scrosati. *Electrochimica Acta*, **45**, 2000, 2461-2466; b) Z.-S. Wu, W. Ren, L. Xu, F. Li, H.-M. Cheng. *ACS nano*, **5**, 2011, 5463-5471; c) H. Li, Z. Wang, L. Chen, X. Huang. *Advanced Materials*, **21**, 2009, 4593.
- (3) F. Cheng, J. Chen. *Journal of Materials Chemistry*, **21**, 2011, 9841-9848.
- (4) E. Andrukaitis, J. P. Cooper, J. H. Smit. *Journal of Power Sources*, **54**, 1995, 465-469.
- (5) H. Reardon, J. M. Hanlon, M. Grant, I. Fullbrook, D. H. Gregory. *Crystals*, **2**, 2012, 193-212.
- (6) a) T. Morishita, K. Nomura, T. Inamasu, M. Inagaki. *Solid State Ionics*, **176**, 2005, 2235-2241; b) S.-S. Kim, H. Ikuta, M. Wakihara. *Solid State Ionics*, **139**, 2001, 57-65.
- (7) N. A. Chernova, M. Roppolo, A. C. Dillon, M. S. Whittingham. *Journal of Materials Chemistry*, **19**, 2009, 2526-2552.
- (8) M. Obrovac, L. Christensen. *Electrochemical and Solid-State Letters*, **7**, 2004, A93-A96.
- (9) a) N. P. W. Pieczonka, Z. Liu, P. Lu, K. L. Olson, J. Moote, B. R. Powell, J.-H. Kim. *The Journal of Physical Chemistry C*, **117**, 2013, 15947-15957; b) M. M. Thackeray, S.-H. Kang, C. S. Johnson, J. T. Vaughey, R. Benedek, S. Hackney. *Journal of Materials Chemistry*, **17**, 2007, 3112-3125.

- (10) J. B. Goodenough, K.-S. Park. *Journal of the American Chemical Society*, **4**, 2013, 1167-1176.
- (11) a) S. Zhang, R. Hu, L. Liu, D. Wang. *Materials Letters*, **124**, 2014, 57-60; b) L. Shuijin, T. Kaibin, J. Yi, C. Chunhua. *Nanotechnology*, **18**, 2007, 175605; c) Y. Piffard, F. Leroux, D. Guyomard, J. L. Mansot, M. Tournoux. *Journal of Power Sources*, **68**, 1997, 698-703; d) Y. S. Mario Simoes, Songhak Yoon, Corsin Battaglia, Simone Pokrant, Anke Weidenkaff. *Journal of Power Sources*, **291**, 2015, 66-74.
- (12) H. Li, H. Zhou. *Chemical Communications*, **48**, 2012, 1201.
- (13) D. Hara, H. Ikuta, Y. Uchimoto, M. Wakihara. *Journal of Materials Chemistry*, **12**, 2002, 2507-2512.
- (14) J. Dahn, T. Zheng, Y. Liu, J. Xue. *Science*, **270**, 1995, 590-593.
- (15) B. Lestriez, S. Bahri, I. Sandu, L. Roué, D. Guyomard. *Electrochemistry Communications*, **9**, 2007, 2801-2806.

## **Chapter 8. Conclusions and Recommendations for Future Work**

Hitherto, we reported a number of anode materials for Li-ion batteries (LIBs) and correlated physical properties with electrochemical performance. Each study investigated a multifaceted approach to enhance the electrochemical performance of high-capacity anodes for next-generation LIBs: from composite carbon nanofiber electrodes, to silicon electrode binders, to newly structured manganese vanadate electrodes. We begin this chapter with a summary of major findings from each study. The exciting discoveries reported in this thesis opens doors to many questions and opportunities, which we detail following the chapter summaries. We provide an outlook on the many encouraging LIB materials examined in this document, and suggest prospective directions to fundamentally understand and engineer next-generation LIBs. We challenge future researchers to build upon our work and to extrapolate use beyond Li-ion systems to next-generation electrochemical energy storage platforms for high-power and high-energy storage devices.

### **8.1. Chapter Summaries**

*Chapter 3:* We report enhanced capacity and electrical conductivity of thermally reduced graphene oxide-containing carbon nanofibers (TRGO/CNFs) in Li-ion anodes, compared to CNFs. Increasing concentration of graphene oxide (GO) in CNFs systematically reduced disorder in the carbon structure (producing larger graphitic domains), which enhanced electrical conductivity of the mats. We observed maximum GO exfoliation in CNFs containing ~ 5 wt% GO (evidenced by insignificant network formation from GO in electrospinning solution and highest active surface area), and half-cells using these anodes were 40% greater in capacity at C/10 and 400% at 2-C in comparison to CNFs. Further, no capacity fade and

CEs > 98% were observed in TRGO/CNF electrodes. The results reported in this work contribute to improving capacity and stability of carbon electrodes for Li-ion battery anodes.

*Chapter 4:* We used TRGO/CNFs as scaffolding for tin particles to produce high-capacity and high-capacity retention anodes for Li-ion battery applications. The oxidation state of Sn within fiber mats varied with carbonization temperature; fibers comprised SnO<sub>2</sub> and Sn(0) at 650 and 850°C, respectively. Thermal decomposition of PAN released H<sub>2</sub> at 850°C, resulting in the reduced Sn(0) oxidation state. Morphology of Sn particles was also temperature dependent; an increased heat-treatment temperature volatilized Sn-complexes, which brought more Sn to the TRGO/CNF surface. Tin loadings ≤ 20 wt% produced small tin particles, predominantly encapsulated within the TRGO/CNF matrix. The ensuing fiber morphology was critical to electrochemical performance. Fibers with tin loadings ≤ 20 wt% produced the smallest size particles (< 15 nm diameter), which reduced strains during lithiation and led to higher capacities over hundreds of cycles, as compared to CNFs and fibers with larger tin loadings; TRGO/CNFs with 20 wt% Sn produced capacities ~ 400 mAh g<sup>-1</sup> after 900 cycles at 2-C.

*Chapter 5:* We integrated a novel, inexpensive, and environmentally friendly binder into lithium-ion batteries that allow Si-based electrodes to operate with high-energy densities. We successfully showed that galactomannans, more specifically guar, may be used as a binding agent for Si nanoparticle (SiNP) electrodes at low binder loadings and outperform SiNP electrodes using carboxymethyl cellulose binders. Superior electrolyte uptake capabilities of galactomannans, compared to Na-CMC, correlates to lower cell resistances, which allowed for

enhanced rate performances. Interactions between the native-oxide layer of SiNPs and the polar hydroxyl groups (more specifically the galactose side chains) of galactomannans allowed for excellent cyclability and capacity retention in Li-ion half-cells over 100 cycles at 1-C.

*Chapter 6:* We chemically crosslinked guar with carbon black (CB) and glutaraldehyde to produce a binder that reinforced electrode microstructure during large stresses of lithiation. Gelation was monitored with dynamic rheology in which we observed faster kinetics and stronger networks when guar was crosslinked with carbon black, as compared to unfilled, crosslinked guar systems. We observed a systematic increase in capacity retention with crosslinking time in SiNP electrodes using crosslinked guar + CB binders after hundreds of symmetrical charge-discharge cycles at 1-C rates. We attribute increased retention to a self-healing phenomenon in the electrodes; the binder (re)forms inter-polymer bonds, which reinforced the electrode and preserved microstructure. Not only does this study report upon a next-generation binding agent for SiNP with integrated conductive additive, we also correlate viscoelastic properties of a novel binding agent to its electrochemical performance.

*Chapter 7:* We produced a disordered manganese vanadate,  $\text{Mn}_{1.5}(\text{H}_2\text{O})(\text{NH}_4)\text{V}_4\text{O}_{12}$  (**I**), which we explored for use as anode material in Li-ion batteries. The disorder in **I**, from combinations of metal-site vacancies and different molecules/ions (e.g.  $\text{H}_2\text{O}$  and  $\text{NH}_4^+$ ), is uncommon. To the best of our knowledge, this is the first observation of this disorder type. We measured stable Li-ion extraction capacities of  $\sim 500 \text{ mAh g}^{-1}$  in **I** electrodes over hundreds of cycles at currents up to  $500 \text{ mA g}^{-1}$ . The novel concept of introducing manganese vacancies by substituting coordinating water molecules and ammonium ions led to high Li-binding

stoichiometries and produced a stable electrode framework. However, **I** electrodes display a large-voltage hysteresis in charge-discharge cycling that decreases cell energy density. Prospective studies on **I** should aim to stabilize the pre-cycled framework and decrease charge-discharge voltage hysteresis for enhanced LIB performance.

## **8.2. Recommendations**

The following section suggests directions for future studies. Suggestions stem from conclusions drawn from our work and promising opportunities from the literature.

### *8.2.1. Electrospun carbon nanofiber anodes*

As we have shown in **Chapters 3** and **4**, CNF anodes are potential alternatives to graphite. CNF anodes display first-cycle gravimetric discharge capacities ( $\sim 600 \text{ mAh g}^{-1}$ ) roughly twice that of graphite anodes ( $325 \text{ mAh g}^{-1}$ ). The additional gravimetric capacity in CNF anodes is attributed to the amorphous structure, which is capable of storing more lithium than graphite. Other beneficial properties of amorphous CNF anodes include ease of fiber formation via the electrospinning process. Perhaps the most advantageous attribute of carbon-based electrodes is the long cycle life. However, there are shortcomings in the nanofiber-based anode system, and thus opportunity for future work: the porous macrostructure of nonwoven fibers produces excessive void volume, which decreases volumetric capacity; large first-cycle charge capacities are typically accompanied by large irreversible capacities, rendering the need for a thorough understanding of interfacial reactions between newly discovered carbons and electrolyte systems; and carbon should be sourced from sustainable precursors. Implementation of CNF-based anodes in commercial LIBs is contingent upon addressing these

shortcomings in the nanofiber-based anode system. In this section, we propose methods to: 1) increase volumetric capacity, 2) decrease irreversible capacity loss and voltage hysteresis in charge-discharge, and 3) produce carbon from inexpensive, environmentally benign sources.

The volumetric energy density of nonwoven CNF electrodes is not sufficient for mobile applications. The volumetric capacity of CNFs produced in this document ( $\sim 400 \text{ mAh cm}^{-3}$ ) is less than the volumetric capacity of graphite ( $\sim 660 \text{ mAh cm}^{-3}$ ),<sup>[1]</sup> and Li-extraction in CNF anodes occurs at potentials slightly more positive (vs. Li/Li<sup>+</sup>) than graphite. To produce an energy-dense anode material for mobile applications, fibers should be closely packed. Fiber packing may be increased via formation of aligned fibers. Researchers have reported on formation of aligned electrospun fibers by substituting a collector plate with a mandrel.<sup>[2]</sup> Mandrels have the added benefit of continuous operation, which streamlines fiber production. Large capacities, and resulting volume expansions, of amorphous carbons may induce restructuring in the aligned electrode macrostructure. Whereas the nonwoven architecture restricts fiber movement and negates requirement of a binding agent, the aligned conformation provides no such structural reinforcements. Thus, binders may be needed to retain the aligned conformation to preserve electron conduction pathways in electrodes. However, sufficient void volume should be available within the CNF microstructure such that electrodes are able to expand during lithiation. Should fibers comprise composite components (e.g. Si or Sn), more void volume will be necessary to accommodate large volume expansions.

Many studies report large first-cycle capacities using amorphous carbon anodes ( $> 1000 \text{ mAh g}^{-1}$ ) with large irreversible capacity losses ( $\sim 600 \text{ mAh g}^{-1}$ ). After the first cycle, the

reversible capacity of CNF anodes is similar to that of graphite (as we observed in **Chapter 3**), which gives industry no significant benefit to switch anode components. The irreversible capacity loss is attributed, in part, to restructuring of carbon and significant solid-electrolyte interface (SEI) formation. As with all high-capacity anode materials, restructuring occurs during volume expansion of lithiation and is difficult to prevent unless capacity (by depth of charge) is limited. To decrease irreversible capacity losses, future work should aim to better understand reactions at the electrode-electrolyte interface during lithiation that leads to SEI layer formation. Large amounts of SEI layer form on the surface (and within pores if accessible to electrolyte) of CNFs due to the high-specific surface area, which can be  $> 300 \text{ m}^2 \text{ g}^{-1}$ , i.e., two orders of magnitude larger than the specific surface area of graphite. Researchers have attempted to reduce the irreversible capacity loss by coating fibers with an artificial SEI via atomic layer deposition.<sup>[3]</sup> However, the artificial SEI hindered capacity of the material. Formation of an artificial SEI layer without compromising capacity is a possible research direction for promising anode materials. Additional irreversible capacity loss in PAN-derived CNF anodes may be attributed to Li binding with noncarbonaceous species such as oxygen- and nitrogen-containing compounds. Noncarbonaceous species may be chemical removal (with sulfuric acid and ammonium fluoride) or thermal removal (high-heat-treatment temperatures) prior to use in LIBs.<sup>[4]</sup>

Another possible method to decrease the irreversible capacity loss in CNF electrodes is the use of electrolyte additives. Researchers currently investigating amorphous carbon anodes for Na-ion batteries have found that electrolyte additive fluoroethylene carbon (FEC)

decreased capacity loss.<sup>[5]</sup> Interestingly, and to the best of our knowledge, only one study has been reported on electrochemical performance benefits of FEC in hard carbon anodes (films not fibers) for Li-ion battery applications.<sup>[6]</sup> Cycling enhancements in Na-ion batteries that use FEC have been attributed to a less resistive SEI on the carbon surface and suppression of side reactions between metallic Na and electrolyte solvents. As a preliminary experiment to observe the influence of FEC addition on electrochemical performance in composite CNF anodes, we added FEC to the electrolyte in Li-ion half-cells that comprised TRGO/CNF working electrodes containing 5 and 10 wt% Sn(IV) and carbonized at 650°C enhanced early-cycle capacities (**Figure 8.1**). Enhanced capacity within the first 100 cycles of half-cells containing FEC may be attributed to different SEI chemistries found on the carbon surface, as compared to half-cells in the absence of FEC. Electrolyte decomposition of half-cells containing FEC may alter electrode surface chemistries (which may be analyzed via X-ray photoelectron spectroscopy) to enhance cell performance. Little work has been conducted on FEC decomposition products for carbon-tin composites,<sup>[7]</sup> and future studies, including electrochemical performance beyond 300 cycles, would be fruitful..

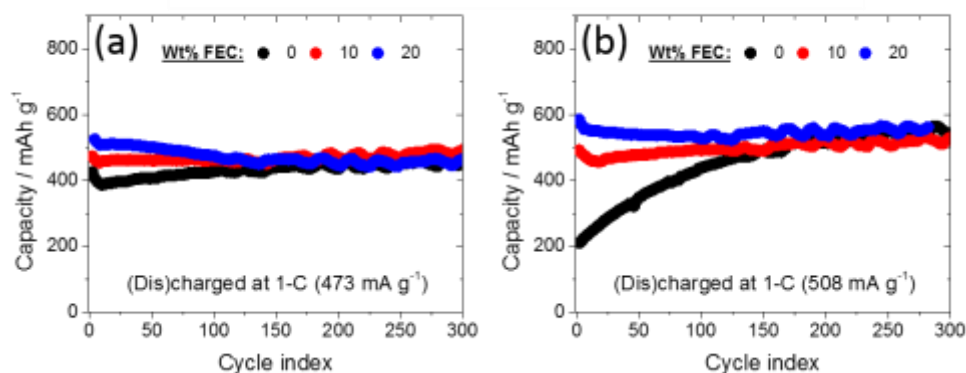


**Figure 8.1.** Discharge capacities of Li-ion half-cells using SnO<sub>2</sub>-TRGO/CNF working electrodes with Sn(IV) loadings of (a) 5 and (b) 10 wt%. The electrolyte comprises 1 M LiPF<sub>6</sub> in 1:1 wt ethylene carbonate: ethylmethyl carbonate with FEC concentration labeled on the plots.

In this document, PAN-derived CNF electrodes (with and without tin) that exhibited capacities > 400 mAh g<sup>-1</sup> were accompanied by capacity fade over hundreds of cycles. It is possible that limitations in CNF mechanical strength facilitated capacity fade through strains during lithiation producing structural rearrangements. While mechanical properties (i.e., strain at break) of a single nanofiber are difficult to measure, lithiation of amorphous carbons may be simulated using computer models to corroborate if the destructive nature of Li-insertion cracks fibers. Enhanced mechanical strength from GO addition to CNFs may also be assessed using such methods. Post-cycling CNF structure should be spectroscopically analyzed via techniques such as Raman. Carbon derived from PAN alternatives (as described below) may also mitigate lithiation-induced alterations to morphology or surface chemistry.

Lastly, future work on CNFs anodes should derive carbon from an inexpensive and environmentally benign source, replacing PAN. The electrospinning process uses large amounts of solvent to produce fibers. Dimethylformamide, the solvent used to dissolve PAN, is toxic and expensive. There is currently little work that investigates the pyrolysis of water-

soluble materials, such as table sugar or use of biopolymers,<sup>[8]</sup> to produce carbon fibers. This work should emphasize a low-cost, high-throughput fiber formation technique. Newly sourced carbons should be less expensive than high-purity graphite, which costs ~ \$500, \$1,000, and \$7,000-20,000 ton<sup>-1</sup> for amorphous, natural crystalline flake, and synthetic, respectively.<sup>[9]</sup> The search for novel, biopolymer sources of amorphous carbon is a worthy research thrust, as companies such as EnerG2<sup>[10]</sup> currently investigate inexpensive carbons that enhance capacities 30% beyond graphite anodes. One potential cost-reducing method involves decreasing the energy needed for production by decreasing pyrolysis temperature. However, low-pyrolysis temperatures decrease electronic conductivity and energy density. For example, charge-discharge profiles of PAN-derived carbon fibers using pyrolysis temperatures of 650 and 1050°C display voltage hystereses of 1.25 V and 75 mV, respectively, when cycled symmetrically at 15 mA g<sup>-1</sup>; the former is unacceptable for commercial use. Additionally, PAN should be replaced with an alternate carbon source because PAN-derived CNFs do not display flat voltage profiles. Batteries for energy-dense applications, such as mobile storage, require Li-insertion and extractions potentials that display a voltage plateau (vs. capacity) near the reduction of Li. It is possible that bio-based carbon derivatives exhibit large voltage hystereses (similar to low-temperature, PAN-derived CNFs) in which case blends, composites, and potential alterations to molecular structure will be needed to improve electrochemical performance.

### 8.2.2. Tin anodes

Tin is an attractive anode material with a large theoretical charge capacity (994 mAh g<sup>-1</sup>, 1990 mAh cm<sup>-3</sup>), but suffers from particle pulverization due to catastrophic mechanical strains at full lithiation <sup>[11]</sup> and short cycle life. One proposed method to cope with strains of Li-insertion is to form tin-composite anodes; a battery using tin-cobalt alloy anodes, introduced by Sony under the name Nexelion, <sup>[12]</sup> saw limited success due to capacity fade and short cycle life. Another common method to extend the cycle life of Sn anodes is to use tin oxides. Fujifilm introduced batteries with tin-composite oxide anodes under the name Stalion, <sup>[13]</sup> which never reached commercialization due to deleterious capacity fade. New methods to extend the cycle life of tin-based anodes present a challenging problem, however, the worth of pursuing these methods that enhance the Li-ion performance of Sn-based anodes is debatable. Researchers commonly overlook tin-based anodes, because Si anodes because have a charge capacity approximately three times larger than tin (~ 3600 mAh g<sup>-1</sup>). Both Sn and Si systems experience untimely cell failure due to electronic isolation of active particles, thus one hypothetical approach to extend cycle life (i.e., modification of particle surface, formation of carbon composites, application of coatings, usage of novel binders, etc.) may be applied to either electrode system. Thus, we focus on Si-based anodes, as presented in the following section.

### 8.2.3. Coating nano-Si anodes

There seems to be a consensus in the battery community that Si is the future anode material of LIBs. To make Si anodes a reality, research should focus on increasing the cycle life of Si-based composites. Many approaches to extend cycle life have been proposed in the

literature. Some approaches include investigating various nano-architectures or forming Si-carbon composites. For example: nanoparticles, nanorods and nanowires have all been considered as potential anode material, <sup>[14]</sup> yet a short-cycle life persists; researchers have grown carbon on SiNPs for long-cycle lives, <sup>[15]</sup> but carbon growth typically involves introducing complex material processing steps. Combining the two aforementioned approaches (nano + carbon coatings), future investigations of Si anodes may study effects of carbon precursor material (i.e., for different carbon coatings) on capacity and cycle life. Silicon is a semiconductor, and carbon coatings are advantageous because they provide electronic conductivity to the electrode. One potential method to produce carbon coatings is chemical vapor deposition. Attention should be focused on coatings that enable use of *thick electrodes* and large areal loadings. The electrodes used in **Chapter 5** and **6** were thin with low-areal loadings relative to conventional graphite electrodes (areal loadings were approximately 8 times less than industrial graphitic anodes). Thick, conductive electrodes comprising Si would provide a high-power and energy-dense anode for next-generation LIBs.

#### 8.2.4. Binders for Si anodes

Binders are currently studied as a means to enhance cycling performances in Si anodes, as binders are known to greatly impact electrochemical performance. The ideal binder should be conductive (both electronically and ionically), protect electrode microstructure, and interact with half-cell components (such as hydrogen bonding with the surface of Si, swelling in the electrolyte, and adhering to current collector and itself). However, such a material has proven difficult to create or discover. Efforts to find the quintessential binder (or improve upon

established binder systems) may use either naturally occurring polymers, synthetic polymers, or perhaps a combination of the two. By focusing on the aforementioned properties of ideal binding agents, we propose methods to study and improve Si anodes for enhanced cycle life.

Since naturally occurring polymers and biopolymers are typically not electronically conductive, researchers have examined synthetic polymers to enhance electrode conductivity. Conductive polymer binders are attractive because they act as both binder and conductivity additive, nullifying the need for carbon black and increasing energy density, and may facilitate use of thick Si anodes. However, many common conductive polymers, such as polyaniline,<sup>[16]</sup> do not remain in their conductive state (emeraldine salt configuration) at potentials needed for lithiation. Thus, researchers aspire to produce synthetic conductive polymers. The Liu group out of Lawrence Berkeley National Lab, developed a polymer that cathodically dopes (n-type) in reducing conditions (lithiation) to become electronically conductive.<sup>[17]</sup> The group modified the polymer poly(9,9-dioctylfluorene-co-fluorenone) via (1) addition of carbonyl moieties to tailor the LUMO so electrons dope the polymer and (2) addition of methylbenzoic ester moieties to enhance adhesion to current collectors. While such a feat involves complex synthetic chemistries, it demonstrates one possible approach to enhance electronic conductivity in a binding agent. Another possible method to enhance the electronic conductivity is to blend biopolymer-derived materials (guar, polylactic acid, alginate, cellulose acetate, etc.) with conductive polymers (polyactelyene, polypyrrole, polythiophene, etc). Conductive polymers are not currently used as binders for Si anodes because they are rigid (cause the electrode to crack during lithiation) and do not bond with Si (which is undesired for

reasons described later in this section). Blends of biopolymers and conducting polymers may be of interest for a wide range of applications, including biomedical applications. <sup>[18]</sup> For example, researchers blended polypyrrole with polylactic acid <sup>[19]</sup> and alginate <sup>[20]</sup> to form conductive bio-composites for tissue engineering applications. Using derivatives of guar may alter solubility and miscibility, such as hydroxypropyl guar. Literature reporting electronically conductive-aqueous polymer blends for Si anode binders is limited, <sup>[21]</sup> and presents an interesting research direction. It is possible that SiNP electrodes using guar-based blends as binders will exhibit encouraging electrochemical cycling performances. Guar and CB solutions did not produce percolating networks and, perhaps, limited electronic conductivity in dried SiNP electrodes (as presented in **Chapter 6**). We indirectly assessed ohmic limitations by increasing areal loadings of SiNP electrodes using guar binders and measuring discharge capacity. As areal loading increased, capacity decreased, as seen in **Figure 8.2**. Since thicker electrodes are desirable to improve cell energy density, studies that increase conductivity (reducing ohmic limitations) are worthy of further investigation.

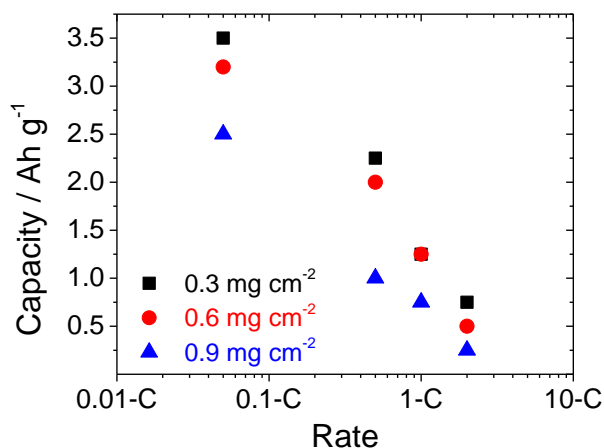


**Figure 8.2.** Discharge capacities as a function of symmetrical charge-discharge rate with various areal loadings of SiNP electrodes using guar binders. Capacities on the plot represent the 10<sup>th</sup> symmetric cycle at a specific rate. Basis rate: 1-C = 3.6 A g<sup>-1</sup>; Electrode composition: SiNP:CB:GG = 8:1:1 wt%; Electrolyte composition: 1 M LiPF<sub>6</sub> in 1:1 wt ethylene carbonate: ethylmethyl carbonate.

In addition to providing electronic pathways, binders should mechanically reinforce electrode microstructure so that electronic and ionic pathways are preserved despite stresses of lithiation. The elasticity of a binder is an important aspect to consider. For example, a binder that is too rigid may limit volume expansions, and thus capacity (as we observed in **Chapter 6**). The current binder of choice, carboxymethyl cellulose (CMC), is not elastic; dried films of CMC (not swelled in electrolyte) exhibited a Young's modulus > 200 MPa<sup>[22]</sup> and strain ~ 6% before breaking<sup>[23]</sup> (values are molecular weight-dependent). Since lithiation in Si is accompanied by large volume expansions (~ 100 and 300% at 1200 and 3600 mAh g<sup>-1</sup>, respectively), changes in microstructure likely occur in SiNP/CMC electrodes. Yet these binders result in good electrochemical performances when used in Si anodes. Good performance was also observed in SiNP/guar systems (Young's modulus of guar is approximately twice that of CMC). The mechanical integrity that binders impart on electrodes

is important, however, little is known on binder elasticity-electrochemical performance relationships. Studies have shown that crosslinking brittle polymers with elastic polymers (to an extent) <sup>[24]</sup> enhances flexibility and electrochemical performance of LIB anodes, while highly elastic binders produced poor cycling performances. <sup>[25]</sup> However, more research is needed to elucidate the influence of binder elasticity on cycling performance. Since both rigid biopolymers and elastic crosslinked polymers have displayed encouraging cycling performance as binders in Si anodes, we speculate that interactions between binders and surrounding half-cell components (such as the electrolyte and active/inactive materials in the anode) may be the critical factor in prolonging the cycle life of Si-based anodes. The remainder of this section offers future opportunities and methods to study interactions between binders and surrounding half-cell components.

*Inter-polymer interactions* preserve electrode microstructure, which maintain short Li-ion and electron pathways. Silicon pulverization upon volume expansions is a common occurrence. Binder-binder bonds may (re)form (via hydrogen bonding or binder-binder reactions may form covalent bond in electrolyte, as proposed in guar + CB systems in **Chapter 6**), which mitigate deleterious delamination and SEI formation. Reformation of inter-polymer bonds is known as a self-healing effect, and is credited to cycling enhancements reported in many binder systems for Si anodes. <sup>[26]</sup> For example, Zhenan Bao's lab synthesized a flexible polymer binder for Si anodes that self-heals via hydrogen bonding between amine and carbonyl groups (we, however, question the electrochemical stability of amine groups). Future directions for binder research should focus on electrochemically inert functional groups that

self-heal and that are either conductive or flexible (the two are typically competing phenomenon in polymers),<sup>[27]</sup> however, we presently don't have candidates for this group of materials.

*Binder-current-collector (Cu) interactions* should be examined with aim to enhance adhesion of electrode to the current collector. The binding agent or Cu foil may be chemically or physically modified to enhance electrode adhesion. For example, researchers<sup>[28]</sup> have reported enhanced electrochemical performances using chemically modified copper, which improves adhesion of electrode films to current collectors. Similar to inter-polymer hydrogen bonding, it may be worthy to induce binder-Cu self-healing capabilities. Delamination of the electrode from the current collector greatly increases the internal resistance of the cell, and one reasons researchers grow Si-nanowires on current collectors. Thus, electrochemical impedance spectroscopy studies may be used to observe the influence of altering the surface of Cu (chemically or physically) or the polymer on internal cell resistance. Improving binder-Cu adherence is one step closer to production of high-power Si-based anodes.

*Si-binder bonding:* Many polymers, spanning a plethora of chemistries, have been studied for binding agents for Si anodes (reviewed in **Chapter 1**). All studies claim that favorable bonding between polymers and the Si surface oxide layer leads to long cycle lives. Binders may form covalent and/or hydrogen bonds, similar to what we reported in **Chapter 5** and **6**. In contrast, polymers such as polyvinylidene fluoride, which are gradually being phased-out by industry and replaced by aqueous-based binders,<sup>[29]</sup> do not bond with the surface of Si and cells typically fail after a few cycles. Interfacial studies may be conducted to study

common bonding phenomenon between polymers that interact with Si. Researchers have also proposed that Si-polymer bonds reform during cycling. <sup>[26c]</sup> This self-healing, however, seems unlikely since oxygenated moieties likely reduce irreversibly during charge, or are involved in SEI formation (rendering oxygenated moieties inactive). More studies are needed to conclusively comment on existence of polymer-particle self-healing. Additionally, companies such as Samsung, <sup>[15]</sup> LG Chem, <sup>[30]</sup> and 3M <sup>[31]</sup> have revealed interest in Si-C composite anodes to enhance cycle life and conductivity of Si anodes. Binders, especially aqueous-based systems, should favorably interact with carbon coatings (in addition to Si) to form stable electrode slurries.

The aforementioned interactions and reactions (inter-polymer and polymer-particle) may be studied using isothermal titration calorimetry (ITC). ITC detects bonding such as H-bonding and reactions that form covalent bonds. The technique is commonly used to study bonding of bio-molecules, such as proteins, by measuring enthalpy changes on the nano-watt scale. <sup>[32]</sup> However, application may be extended to polymer-particle systems to study interactions or reactions between:

- 1) guar, glutaraldehyde, and carbon black in acidic conditions (in continuation of work in **Chapter 6**), to study reactions kinetics with and without carbon black. ITC could be used to decouple roles of each constituent in the crosslinking reaction (i.e. possible CB physical crosslinks with unreacted guar)
- 2) novel binder and SiNPs, to assess changes in associations with various SiNP oxide layer thickness, and investigate the affinity of unique binder chemistries towards SiNPs.

Employing ITC to assess particle-polymer bonding in electrode slurries (prior to film-casting) will provide a seminal study on use of calorimetry to study Si-binder interactions. Employing ITC may also be used to devise an initial screen for novel polymers that may be used as binders in Si electrodes.

*Binder-electrolyte interactions* are perhaps the most overlooked interactions (of those listed) in literature. To our knowledge, few studies discuss changes to polymer structure and mechanical properties when swelled in electrolyte. Calorimetry and extensional rheology may be used to study the structure and mechanical properties of swelled polymer films. There is also little information regarding the effect of swelling on bonding with SiNPs and Cu foil. Such studies are difficult to pursue since low-water content ( $< 10$  ppm), closed systems are needed to replicate the environment of Li-ion cells. However, these investigations would provide an understanding of binder interfacial chemistries needed to prolong the life of Si anodes. Many questions arise, such as: Does too much swelling in binder systems limit binder-Si interactions, reduce binder-Cu adhesion, or produce a thicker SEI? What are the implications of using binding agents that exhibit low-swelling in electrolyte? The answer to such questions may provide fruitful information on how to design novel binding systems that are applicable to all electrode materials.

As a final recommendation for future work, raw material cost for both Si and binders should be considered. This thesis studied binders for SiNP electrodes. These SiNPs are relatively expensive and produced in small batches via laser ablation. Use of binders to extend

the cycle life of micron-sized Si anodes, which are relatively inexpensive to produce, is a worthy research direction <sup>[33]</sup> if charging voltage is limited.

#### 8.2.5. *Manganese vanadate anodes*

Metal oxide anodes are considered alternatives to graphite for high-power LIBs. One example of a metal oxide anode is lithium titanate, LTO, which is considered for possible electric vehicle applications due to its high-rate capability, low-voltage hysteresis, favorable capacity retention, and long calendar life. Metal oxides have higher operating potentials than graphite, which decreases their energy density but increases their safety (by decreasing the likelihood of Li-plating). Nominal operating voltages of LIBs with graphite and LTO anodes are 3.6 and 2.4 V, respectively. Thus, metal oxide anodes should be considered with pairing of next-generation (5 V vs Li/Li<sup>+</sup>) cathodes to increase operating potential. The worth pursuing novel metal oxide anode components with superior electrochemical performance to LTO anodes is contingent upon increasing capacity beyond LTO (> 175 mAh g<sup>-1</sup>), decreasing the operating voltage vs. Li/Li<sup>+</sup> (< 1.5 V), or reducing production cost. The vacancy-induced manganese vanadate electrodes investigated in this thesis are still in their infancy (yet have many parallels to current LIB electrode material), <sup>[34]</sup> and much work is needed to improve their cycling performance. Future work should consider decreasing 1) irreversible capacities and 2) voltage hystereses. However, before either of these studies can be accomplished, a firm understanding of the charging and discharging mechanism is needed.

Origins of the irreversible capacity loss in manganese vanadate anodes are uncorroborated, however, structural rearrangements are a likely culprit. As we observed in

**Chapter 7**, Mn-content in the vacancy-induced manganese vanadates electrodes decreased with state-of-charge. The decreased Mn-content may be related to Mn-ion dissolution, which collapsed the pre-cycled molecular framework and decreased capacity. Dissolution of Mn-ions in LiPF<sub>6</sub>-based electrolyte is a known problem, <sup>[35]</sup> and has slowed development of Mn-based cathode materials. Thus, means to stabilize manganese vanadate structure (enhancing cycling performances) may be borrowed from cathode literature. To reduce irreversible capacity loss and capacity fade in cathodes (reducing Mn dissolution), researchers have substituted Mn with transition metals such as Co and Ni, <sup>[35]</sup> and coated the surface with films of Al<sub>2</sub>O<sub>3</sub> and carbon. <sup>[36]</sup> Introducing transition metals (doping the cathode with Co, Ni, or Zn) reduces Mn-ion concentration, which helps stabilize the structure upon Mn dissolution and decreases irreversible capacity. Additionally, carbon coatings may be used to form a different SEI on the particle surface, which may act to suppress dissolution of Mn-ions and protect the structure from deleterious rearrangements. <sup>[37]</sup> Carbon coatings are also advantageous for enhancing electrode conductivity. For example, rate capabilities of LTO electrodes increased with carbon coating. <sup>[38]</sup> Similarly, the electrochemical performance of manganese vanadates may be enhanced via carbon coatings to decrease Mn-ion dissolution and increase rate capabilities. It would also be interesting to test these manganese vanadates against Mn-based cathodes in full cells. As a result, both Mn- and Li-ions may shuttle across the cell. Allowing Mn-ions to shuttle may increase capacity by re-crystalizing and reinforcing structures (upon re-insertion).

The vacancy-induced manganese vanadates (produced in **Chapter 7**) exhibited a voltage hysteresis > 1 V during formation cycles, even when cycled at slow (10 mA g<sup>-1</sup>) rates.

Such a large voltage gap at slow rates is unlikely due to overpotential from current density or impedance from charge-transfer; it is possible that the large voltage hysteresis originates from a different set of reaction pathways during charge and discharge,<sup>[39]</sup> which is not desirable for LIB applications. The voltage hysteresis may decrease with carbon coatings (as we presented earlier), or by decreasing the size of the manganese vanadate particles (to accelerate electrochemical kinetics). However, to understand causes for the voltage hysteresis, in situ studies and computer simulations are needed to discern specific Li-bonding locations of lithiated manganese vanadate electrodes. Changes in the structure during charge and discharge may be further characterized via high-resolution transmission electron microscopy. Since the structure gradually converts from crystalline to amorphous near full lithiation, X-ray techniques become less effective due to a lack of diffraction. Neutron diffraction has been used to suggest possible causes in the voltage hysteresis observed in Li-rich Mn oxide cathodes,<sup>[40]</sup> and to observe (a) if both Li and Mn-ions migrate during cycling, (b) where in the structure Li-binds, and (c) the ensuing lithiated structure as a function of states-of-charge.

### 8.3. References

- (1) N. Nitta, G. Yushin. *Particle & Particle Systems Characterization*, **31**, 2014, 317-336.
- (2) E. Smit, U. Büttner, R. D. Sanderson. *Polymer*, **46**, 2005, 2419-2423.
- (3) A. J. Loebl, C. J. Oldham, C. K. Devine, B. Gong, S. E. Atanasov, G. N. Parsons, P. S. Fedkiw. *Journal of the Electrochemical Society*, **160**, 2013, A1971-A1978.
- (4) K. Zaghib, X. Song, A. Guerfi, R. Rioux, K. Kinoshita. *Journal of Power Sources*, **119**, 2003, 8-15.
- (5) S. Komaba, T. Ishikawa, N. Yabuuchi, W. Murata, A. Ito, Y. Ohsawa. *ACS Applied Materials & Interfaces*, **3**, 2011, 4165-4168.

- (6) D. Hirshberg, O. Yariv, G. Gershinsky, E. Zinigrad, D. Aurbach. *Journal of the Electrochemical Society*, **162**, 2015, A7001-A7007.
- (7) Z. Yang, A. A. Gewirth, L. Trahey. *ACS Applied Materials & Interfaces*, **7**, 2015, 6557-6566.
- (8) a) J. Spender, A. L. Demers, X. Xie, A. E. Cline, M. A. Earle, L. D. Ellis, D. J. Neivandt. *Nano letters*, **12**, 2012, 3857-3860; b) S.-X. Wang, L. Yang, L. P. Stubbs, X. Li, C. He. *ACS Applied Materials & Interfaces*, **5**, 2013, 12275-12282.
- (9) D. W. Olson, R. L. Virta, M. Mahdavi, E. S. Sangine, S. M. Fortier. *Geological Society of America Special Papers*, **520**, 2016, SPE520-508.
- (10) A. M. Feaver, H. R. Costantino, W. D. Scott in *Ultrapure synthetic carbon materials*, Vol. Google Patents, **2015**.
- (11) M. Winter, J. O. Besenhard. *Electrochimica Acta*, **45**, 1999, 31-50.
- (12) a) H. Inoue, *International meeting on lithium batteries, Biarritz 2006*; b) J. Wolfenstine, J. L. Allen, J. Read, D. Foster in *Chemistry and Structure of Sony's Nexelion Li-ion Electrode Materials*, Vol. DTIC Document, **2006**.
- (13) Y. Idota, T. Kubota, A. Matsufuji, Y. Maekawa, T. Miyasaka. *Science*, **276**, 1997, 1395-1397.
- (14) H. Wu, Y. Cui. *Nano Today*, **7**, 2012, 414-429.
- (15) I. H. Son, J. H. Park, S. Kwon, S. Park, M. H. Rummeli, A. Bachmatiuk, H. J. Song, J. Ku, J. W. Choi, J.-m. Choi. *Nature communications*, **6**, 2015.
- (16) A. Ray, G. Asturias, D. Kershner, A. Richter, A. MacDiarmid, A. Epstein. *Synthetic Metals*, **29**, 1989, 141-150.
- (17) a) G. Liu, S. Xun, N. Vukmirovic, X. Song, P. Olalde-Velasco, H. Zheng, V. S. Battaglia, L. Wang, W. Yang. *Advanced Materials*, **23**, 2011, 4679-4683; b) M. Wu, X. Xiao, N. Vukmirovic, S. Xun, P. K. Das, X. Song, P. Olalde-Velasco, D. Wang, A. Z. Weber, L.-W. Wang. *Journal of the American Chemical Society*, **135**, 2013, 12048-12056.
- (18) N. K. Guimard, N. Gomez, C. E. Schmidt. *Progress in Polymer Science*, **32**, 2007, 876-921.
- (19) G. Shi, M. Rouabhia, Z. Wang, L. H. Dao, Z. Zhang. *Biomaterials*, **25**, 2004, 2477-2488.

- (20) D. H. Kim, M. Abidian, D. C. Martin. *Journal of Biomedical Materials Research Part A*, **71**, 2004, 577-585.
- (21) Y. Bie, J. Yang, X. Liu, J. Wang, Y. Nuli, W. Lu. *ACS Applied Materials & Interfaces*, **8**, 2016, 2899-2904.
- (22) S. M. M. Dadfar, G. Kavvoosi. *Polymer Composites*, **36**, 2015, 145-152.
- (23) J. Li, R. Lewis, J. Dahn. *Electrochemical and Solid-State Letters*, **10**, 2007, A17-A20.
- (24) T. w. Kwon, Y. K. Jeong, I. Lee, T. S. Kim, J. W. Choi, A. Coskun. *Advanced Materials*, **26**, 2014, 7979-7985.
- (25) N. Yuca, H. Zhao, X. Song, M. F. Dogdu, W. Yuan, Y. Fu, V. S. Battaglia, X. Xiao, G. Liu. *ACS Applied Materials & Interfaces*, **6**, 2014, 17111-17118.
- (26) a) C. Wang, H. Wu, Z. Chen, M. T. McDowell, Y. Cui, Z. Bao. *Nature chemistry*, **5**, 2013, 1042-1048; b) Y. K. Jeong, T.-w. Kwon, I. Lee, T.-S. Kim, A. Coskun, J. W. Choi. *Nano letters*, **14**, 2014, 864-870; c) J.-S. Bridel, T. Azais, M. Morcrette, J.-M. Tarascon, D. Larcher. *Chemistry of Materials*, **22**, 2009, 1229-1241.
- (27) Y. Sun, J. Lopez, H. W. Lee, N. Liu, G. Zheng, C. L. Wu, J. Sun, W. Liu, J. W. Chung, Z. Bao. *Advanced Materials*, 2016.
- (28) G. Liu, Z. Zheng, X. Song, V. S. Battaglia in *Nanostructured Surface Modified Cu Thin Film for Lithium Ion Negative Electrode Application*, Vol. Google Patents, **2011**.
- (29) S.-L. Chou, Y. Pan, J.-Z. Wang, H.-K. Liu, S.-X. Dou. *Physical Chemistry Chemical Physics*, **16**, 2014, 20347-20359.
- (30) H. W. Kim, K. T. Kim in *Carbon-silicon composite, method of preparing the same, and anode active material including the carbon-silicon composite*, Vol. Google Patents, **2013**.
- (31) L. Christensen, D. B. Le, J. Singh, M. Obrovac, *27th International Battery Seminar & Exhibit* **2010**.
- (32) a) N. A. Demarse, C. F. Quinn, D. L. Eggett, D. J. Russell, L. D. Hansen. *Analytical biochemistry*, **417**, 2011, 247-255; b) E. Freire, O. L. Mayorga, M. Straume. *Analytical chemistry*, **62**, 1990, 950A-959A.
- (33) J. Lopez, Z. Chen, C. Wang, S. C. Andrews, Y. Cui, Z. Bao. *ACS Applied Materials & Interfaces*, 2015.

- (34) V. Etacheri, R. Marom, R. Elazari, G. Salitra, D. Aurbach. *Energy & Environmental Science*, **4**, 2011, 3243-3262.
- (35) P. K.-S. Goodenough J. B. *Journal of the American Chemical Society*, **4**, 2013, 1167-1176.
- (36) D. Guan, J. A. Jeevarajan, Y. Wang. *Nanoscale*, **3**, 2011, 1465-1469.
- (37) L. Jaber-Ansari, K. P. Puntambekar, S. Kim, M. Aykol, L. Luo, J. Wu, B. D. Myers, H. Iddir, J. T. Russell, S. J. Saldaña. *Advanced Energy Materials*, **5**, 2015.
- (38) E. Kang, Y. S. Jung, G. H. Kim, J. Chun, U. Wiesner, A. C. Dillon, J. K. Kim, J. Lee. *Advanced Functional Materials*, **21**, 2011, 4349-4357.
- (39) W. Dreyer, J. Jamnik, C. Gohlke, R. Huth, J. Moškon, M. Gaberšček. *Nature materials*, **9**, 2010, 448-453.
- (40) D. Mohanty, J. Li, D. P. Abraham, A. Huq, E. A. Payzant, D. L. Wood, C. Daniel. *Chemistry of Materials*, **26**, 2014, 6272-6280.

## Appendices

## **Appendix A: Supporting Information for Chapter 4**

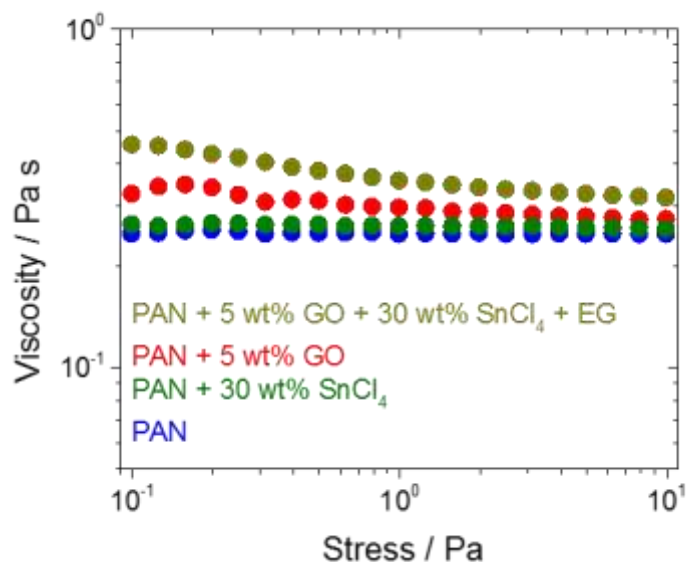


**Figure A1.** Steady-shear rheology of PAN systems; Experiments were performed to observe the influence of SnCl<sub>4</sub> and EG on the viscosity of electrospinning precursor solution. All experiments were conducted with 8 wt% polymer; EG concentration was 4:1 mol EG:SnCl<sub>4</sub>

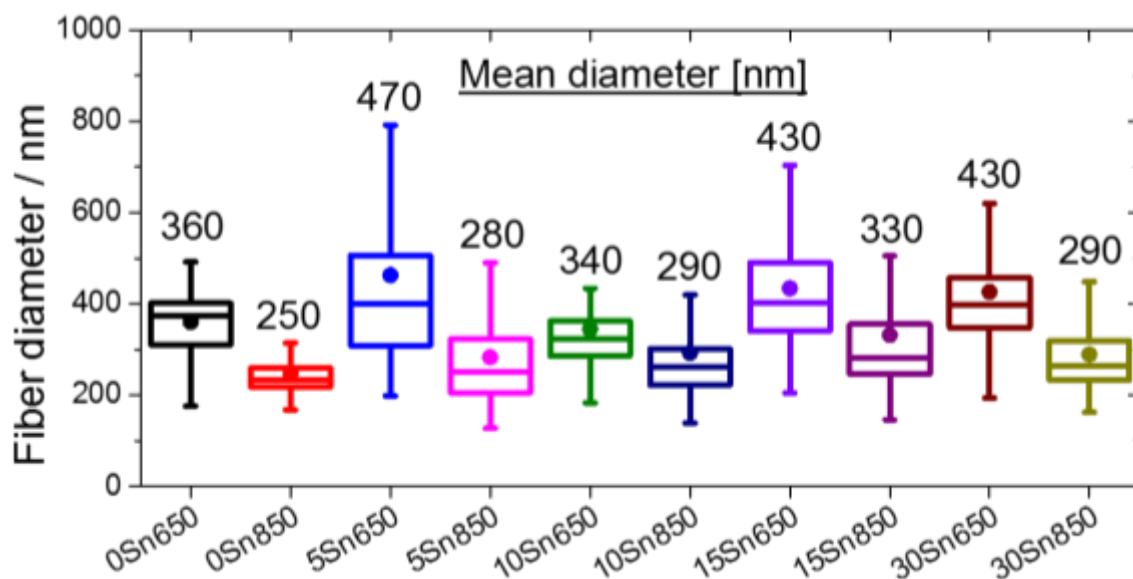


**Figure A2.** Box plots of fiber diameters for tin-TRGO/CNFs. The dot in each samples represents the mean diameter, which is also written above each individual box plot.

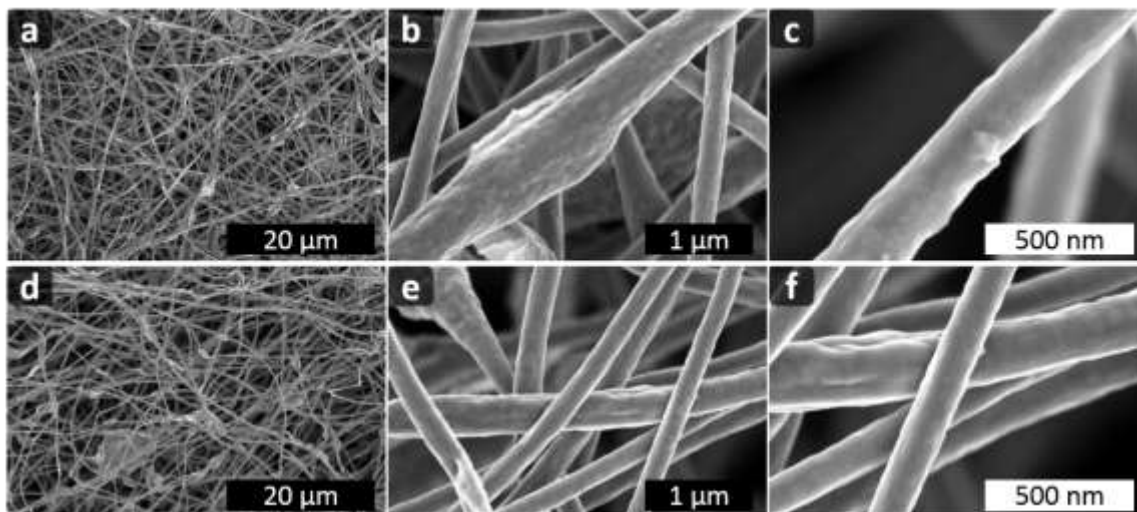


**Figure A3.** Images of SnO<sub>2</sub>-TRGO/CNFs carbonized at 650°C containing a Sn (IV) loadings of (a-c) 5 wt% and (d-f) 10 wt%

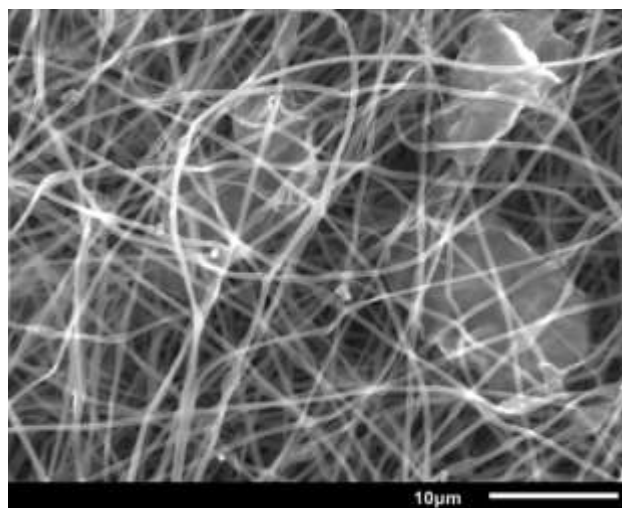


**Figure A4.** SEM image of TRGO/CNFs carbonized at 850°C

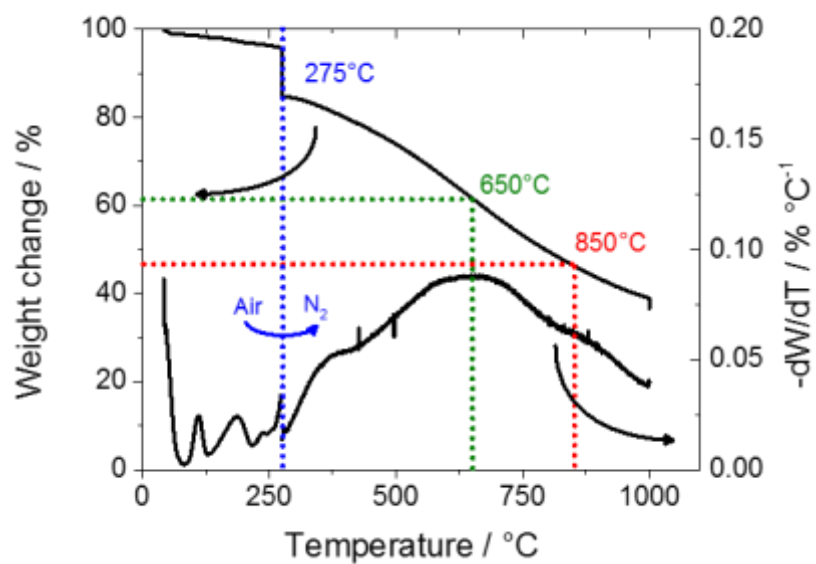


**Figure A5.** TGA and DTG of GO/PAN fibers. The technique (temperature, heating ramp-rate, and gaseous environment) used for TGA was analogous to stabilization and carbonization of PAN that was used in this study.

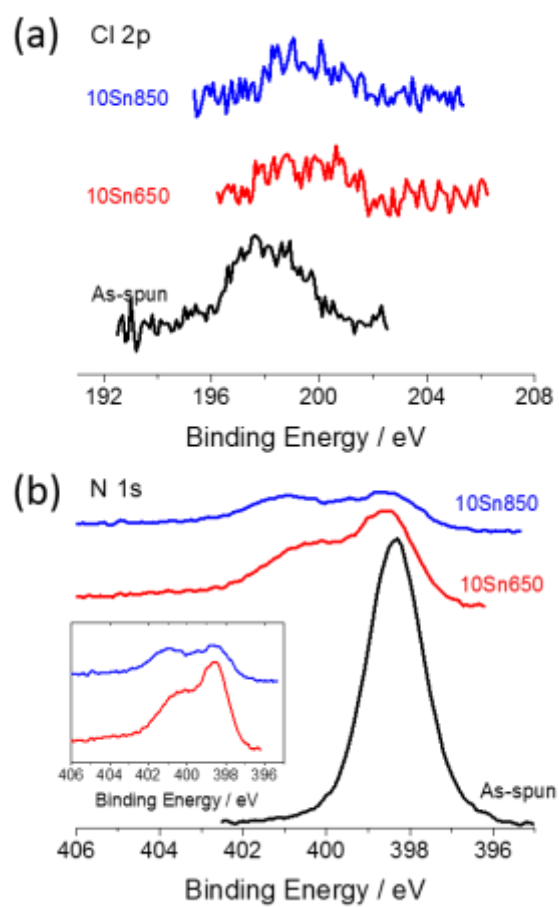


**Figure A6.** High-resolution XPS transitions of *as-spun* fibers with Sn (IV) loading of 10 wt%, 10Sn650, and 10Sn850 showing (a) Cl 2p and (b) N 1s; the inset of (b) magnifies the N 1s transition of heat treated samples

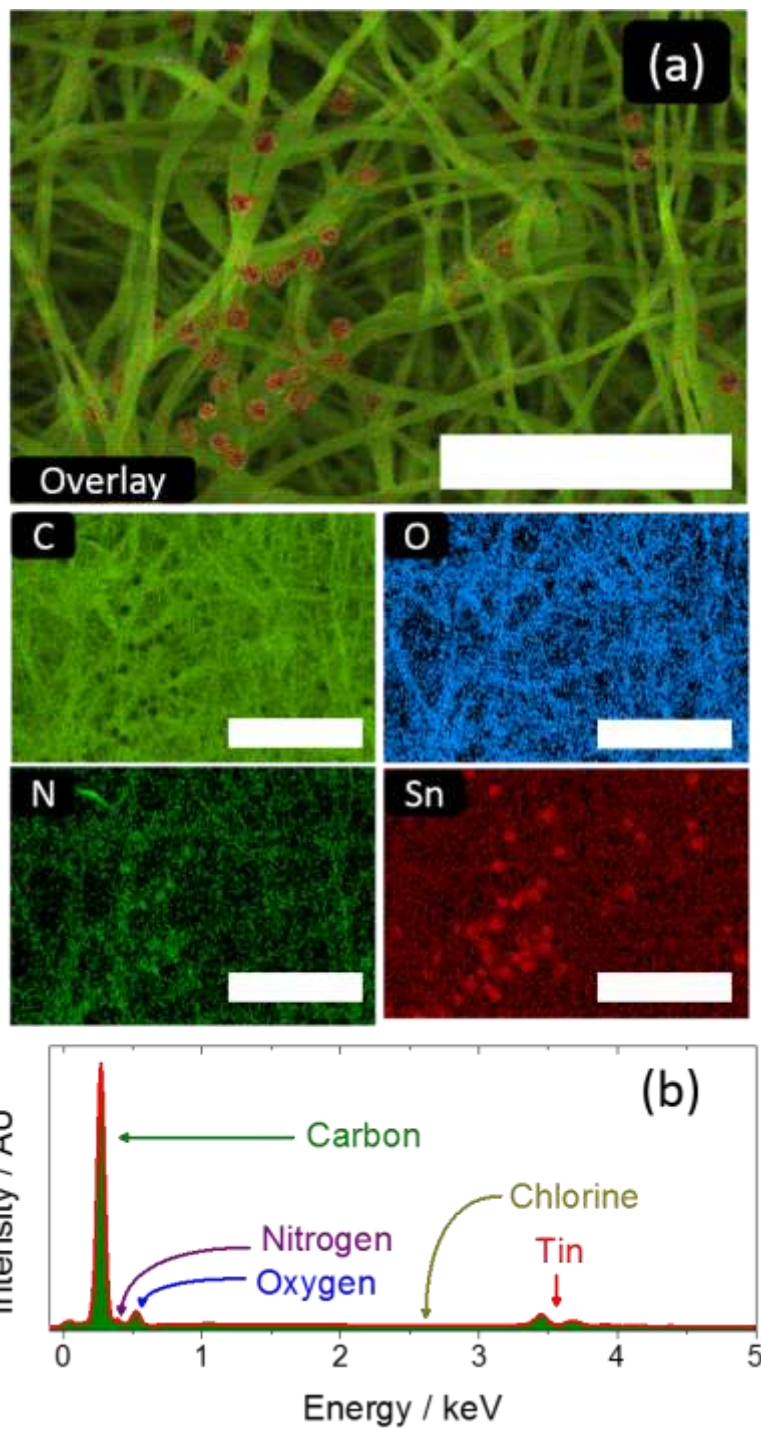


**Figure A7.** (a) EDS maps overlay on an SEM image of 15Sn850, with individual elemental maps below the overlay. The scale bar represents 10  $\mu\text{m}$ ; (b) EDS spectrum of the above sample.

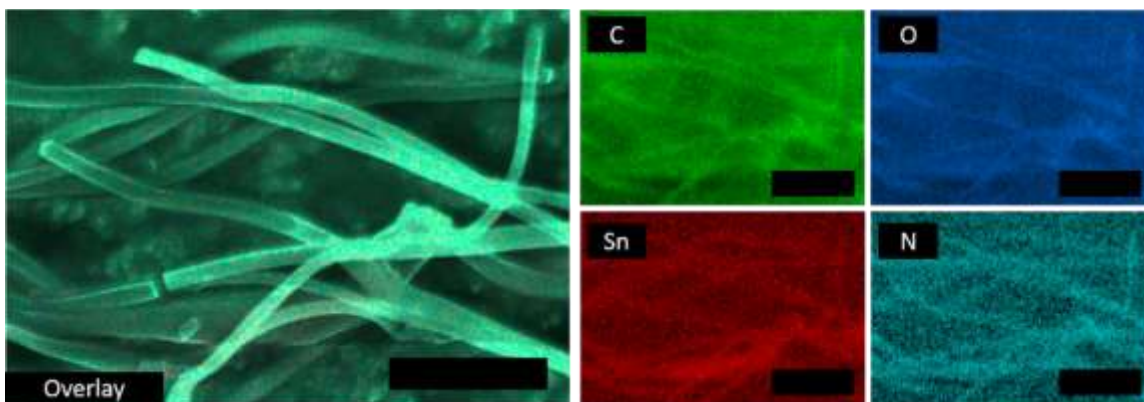


**Figure A8.** SEM image of 10Sn850 on carbon tape with EDS maps overlain, and the respective elemental maps; Scale bar represents 2.5  $\mu\text{m}$

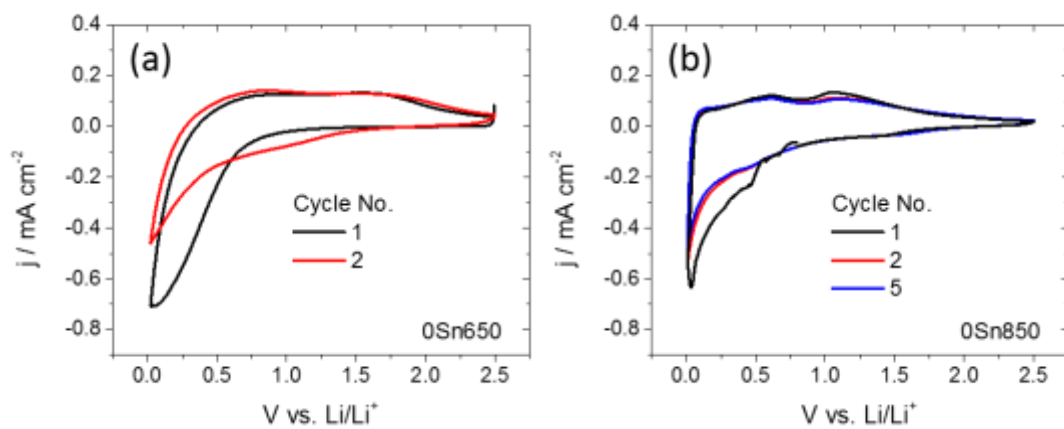


**Figure A9.** CV of TRGO/CNFs in the absence of tin that were carbonized at (a) 650°C and (b) 850°C

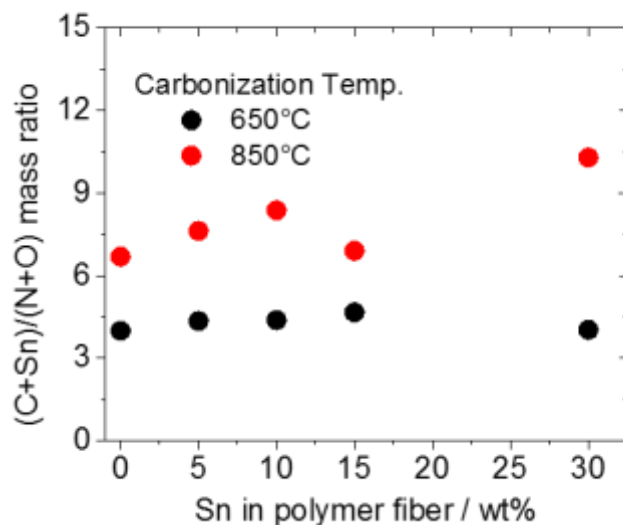


**Figure A10.** Ratios of Li-reversible to Li-irreversible host materials as measured via EDS.

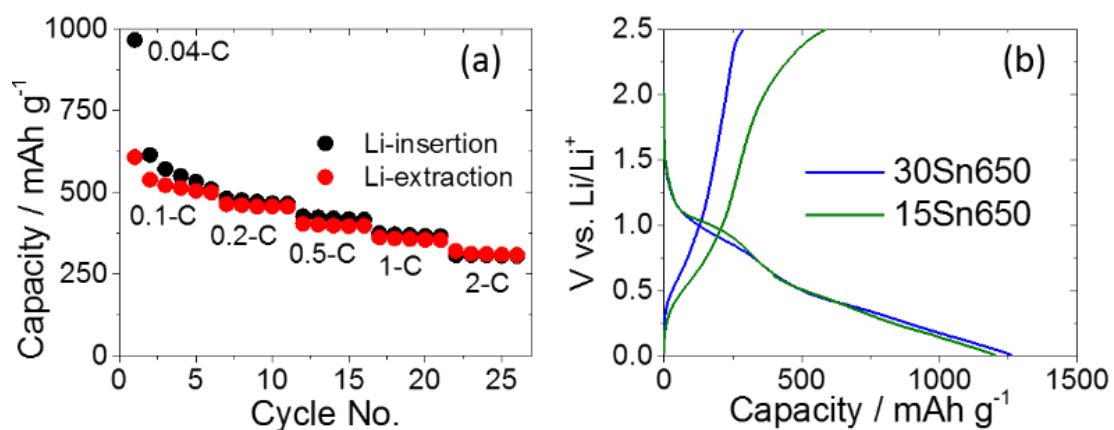


**Figure A11.** (a) Galvanostatic cycling with potential limitation technique used to calculate C-rates as a function of current density; (b) Charge/discharge curves of highly loaded tin electrodes that were carbonized at 650°C

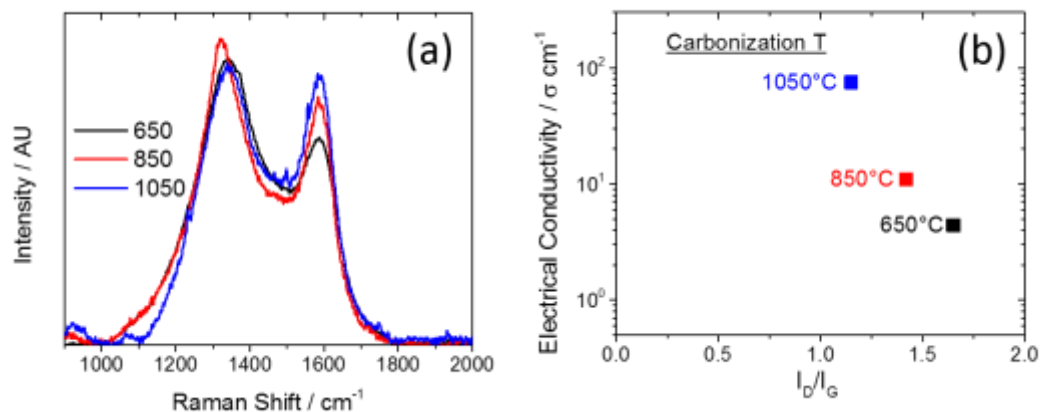


**Figure A12.** (a) Raman spectra for TRGO/CNFs carbonized at various HTTs; the two peaks in the spectrum above represent the defective (D peak  $\sim 1330\text{ cm}^{-1}$ ) and graphitic (G peak  $\sim 1580\text{ cm}^{-1}$ ) nature of TRGO/CNFs. An increased intensity ratio of the two peaks ( $I_D/I_G$ ) suggests increased disorder in the carbon structure. The  $I_D/I_G$  ratios for TRGO/CNFs carbonized at 650, 850, and 1050°C, are 1.65, 1.42, and 1.15, respectively; disorder decreases with HTT. (b) Electrical conductivity of TRGO/CNFs carbonized at different temperatures

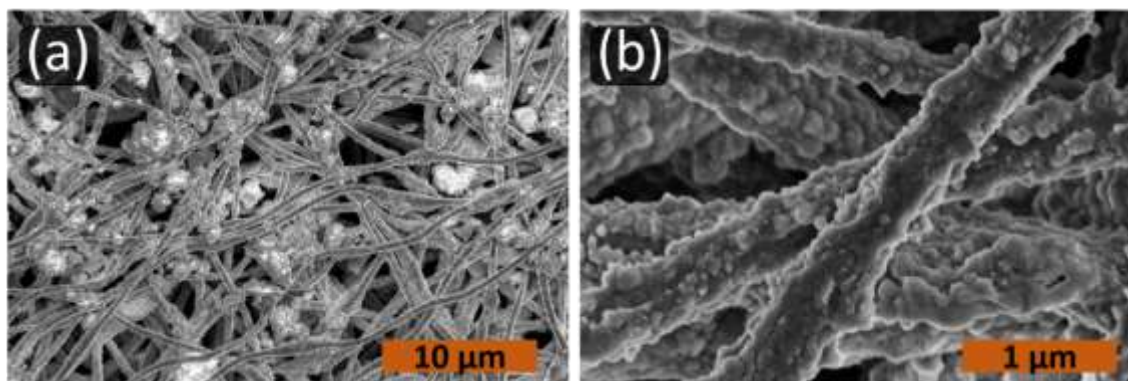


**Figure A13.** SEM image of 30Sn850 after 500 cycles at 2-C at (a) low and (b) high magnification. At low magnifications, we notice that Sn particles aggregate upon cycling, which likely occurred after recurrent pulverizations. After 500 cycles, capacities of TRGO/CNFs with high Sn loadings are equal to capacities in the absence of Sn, which suggests that the Sn deactivates and the fiber structure maintains electrochemical activity.

**Table A1.** Coulombic efficiencies, averaged per 100 cycles, corresponding to **Figure 4.6c**

Cycle Index	CE <sub>5Sn650</sub> 1-C [%]	CE <sub>10Sn650</sub> 1-C [%]	CE <sub>0Sn650</sub> 2-C [%]	CE <sub>5Sn650</sub> 2-C [%]
100	99.77	100.01	99.9	99.82
200	99.86	99.83	100.03	100.04
300	99.77	99.82	99.98	99.95
400	99.78	99.87	99.95	99.93
500	99.76	99.82	99.93	99.91
600	-	-	99.87	99.90
700	-	-	99.88	99.87
800	-	-	99.89	99.87
900	-	-	99.88	99.88

**Table A2.** Coulombic efficiencies, averaged per 100 cycles, corresponding to **Figure 4.6d**

Cycle Index	CE <sub>0Sn850</sub> 2-C [%]	CE <sub>Sn850</sub> 2-C [%]	CE <sub>10Sn850</sub> 2-C [%]	CE <sub>15Sn850</sub> 2-C [%]	CE <sub>30Sn850</sub> 2-C [%]
100	99.71	99.61	105.9	99.22	99.40
200	99.77	99.66	103.5	99.32	99.70
300	99.75	99.63	101.5	99.34	99.74
400	99.77	99.64	99.94	99.37	99.74
500	99.70	99.65	99.79	99.34	99.75

## **Appendix B: Supporting Information for Chapter 5**

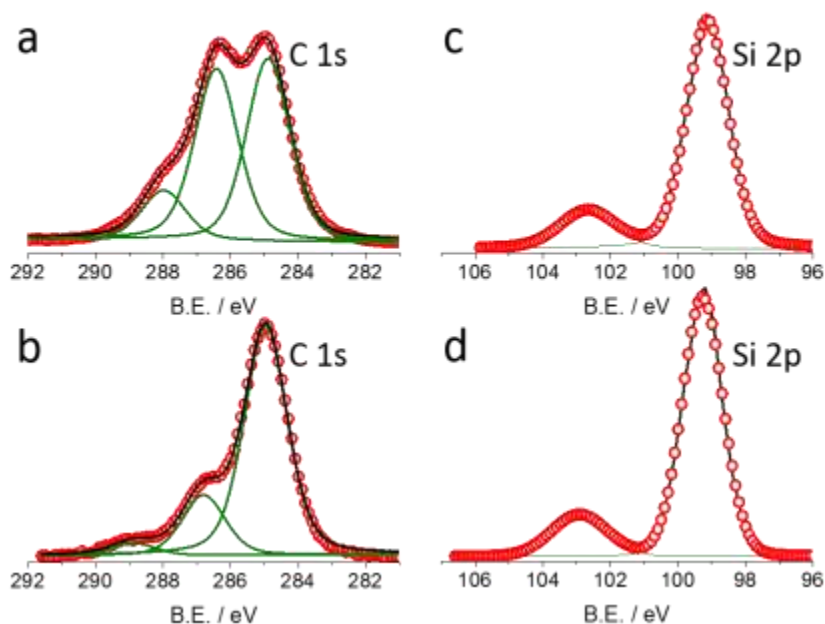


**Figure B1.** XPS data showing the C 1s transitions for (a) GG and (b) guar + SiNPs; the Si 2p transition for (c) SiNPs and (d) guar + SiNPs; The red circles are measured data, green peaks were fit using XPSEAK41 with a Shirley background, and the black line is the sum of calculated peaks. The guar used in this thesis was purified via centrifugation at 5000 RPM for 30 mins and decantation of the supernatant. A slight shift towards higher binding energies was observed in SiNP after they were coated with GG (0.1 eV shift), possibly due to oxidation.

**Table B1.** Carbon bond composition as determined via integrating the peaks of the spectra in **Figure B1**. The original atomic bond content of guar that we measured is close to the expected composition of guar gum. However, the mannose-to-galactose ratio was never determined, so exact composition remains unknown. Of importance in this table is the stark difference in the C 1s spectra when SiNPs are coated with GG, as compared to pure GG. Notably a decrease in C-O and O-C-O content and an increased C-C content. This change in composition may be caused by interactions or reactions between SiNPs and GG.

Bond	FWHM [eV]	B.E. GG [eV]	At % GG	B.E. GG+SiNP [eV]	At % GG+SiNP
C-C	1.5	284.90	45	284.96	76
C-O	1.5	286.45	43	286.80	20
O-C-O	1.5	288.00	12	288.86	4

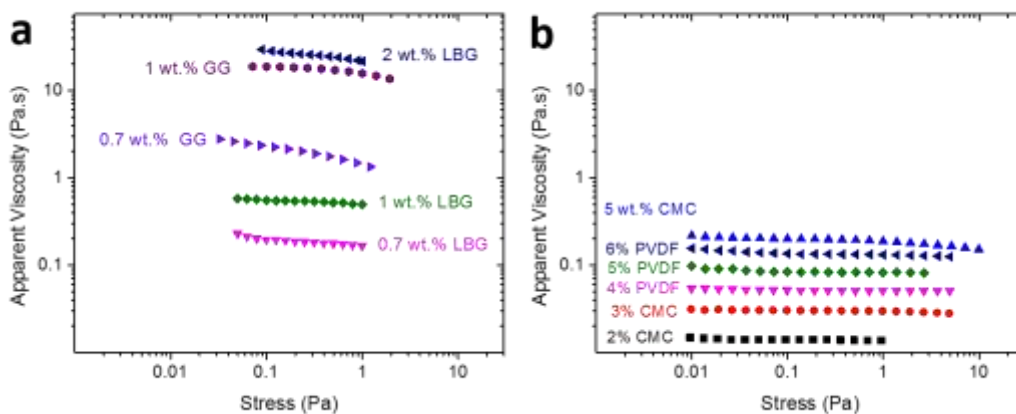


**Figure B2.** Steady-shear rheology of (a) galactomannan and (b) CMC and PVDF solutions; the concentration of each solution is labeled on the plots. As evident from comparison of the two graphs, galactomannans have a much higher viscosity than PVDF and CMC solutions.

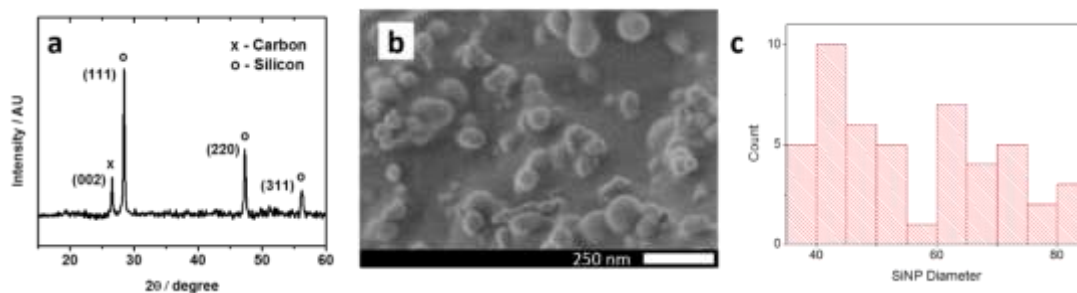


**Figure B3.** (a) XRD spectrum of the SiNP/GG electrodes used to determine the crystallite size of the SiNPs; (b) SEM image of the SiNPs on carbon tape and (c) the corresponding size distribution of the SiNPs as measured by HR-SEM images with average bi-modal particle size of 58 nm.

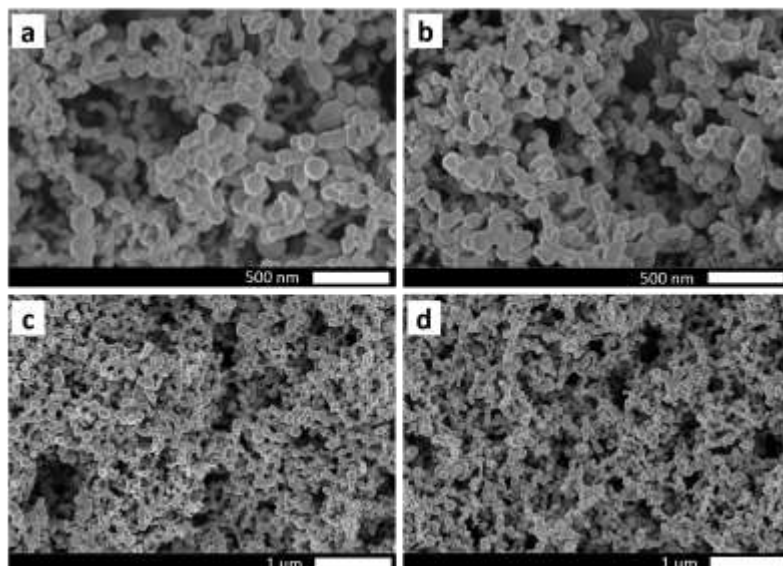


**Figure B4.** SEM images of SiNP/GG electrodes with (a) 10 wt% binder and (b) 15 wt% binder. As the concentration of binder increases, no dramatic decrease in film porosity is observed. Additionally, the size of the SiNPs encapsulated in the binder does not appear to increase as the binder loading increases. The same effect can be seen when the LBG concentration in the electrode increases from (c) 5 wt% to (d) 15 wt%.

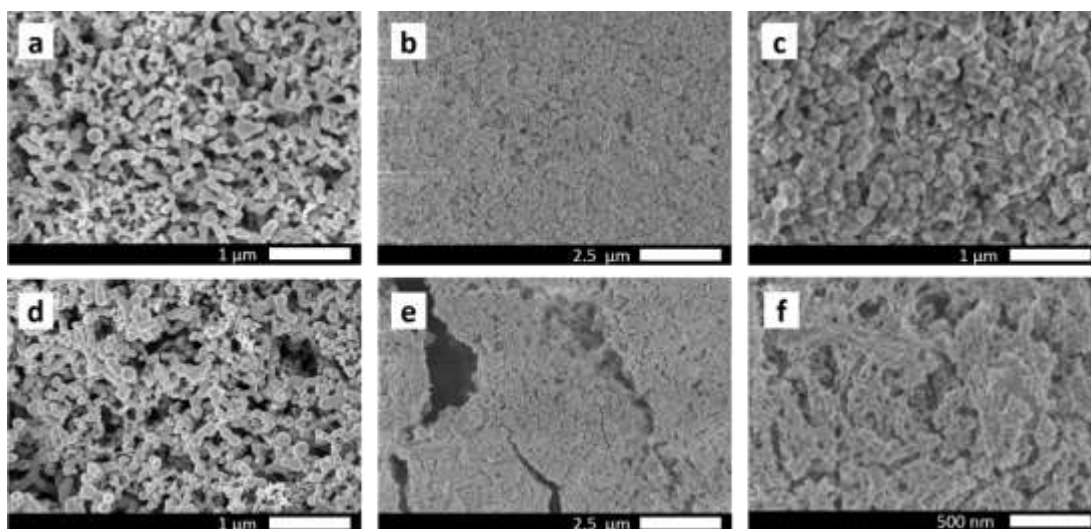


**Figure B5.** SEM images of pre-cycled (a) SiNP/PVDF and (d) SiNP/CMC electrodes. SiNP/PVDF electrodes appear to lose porosity and fuse together (b,c) upon cycling. A similar loss in pre-cycled electrode structure is observed in SiNP/CMC electrodes (e, f). Post-mortem images were captured after 50 charge/discharge cycles at  $3.6 \text{ A g}^{-1}$ .

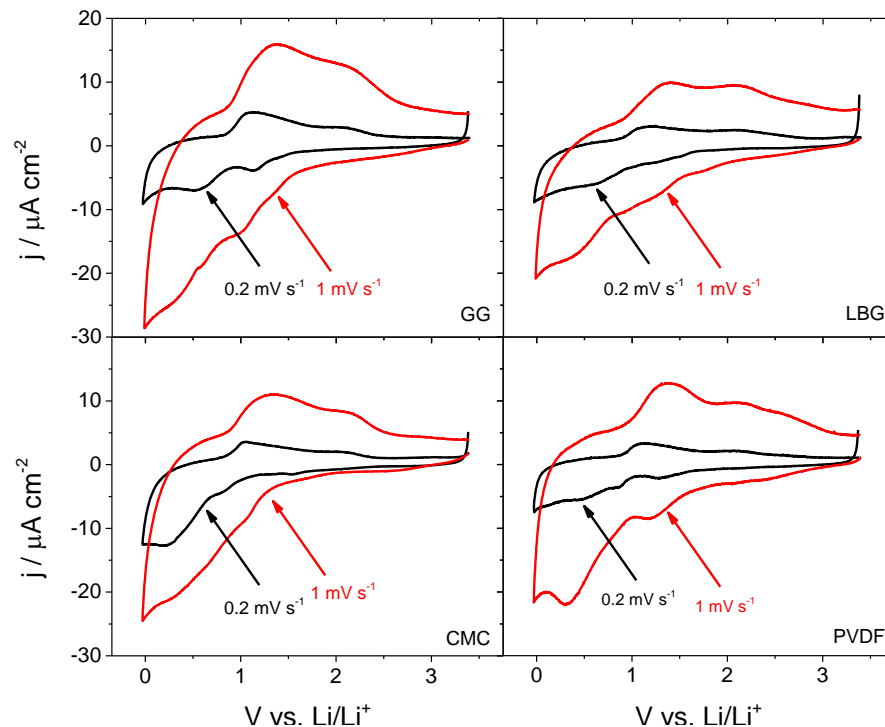


**Figure B6.** Cyclic voltammograms of (a) GG, (b) LBG, (c) CMC, and (d) PVDF polymer-only films on Cu foil indicate little current is produced with the binder materials. Additionally, given their electrochemical stability at potentials higher than 2 V vs Li/Li<sup>+</sup>, GG and LBG may be candidates for alternative cathode binding materials.

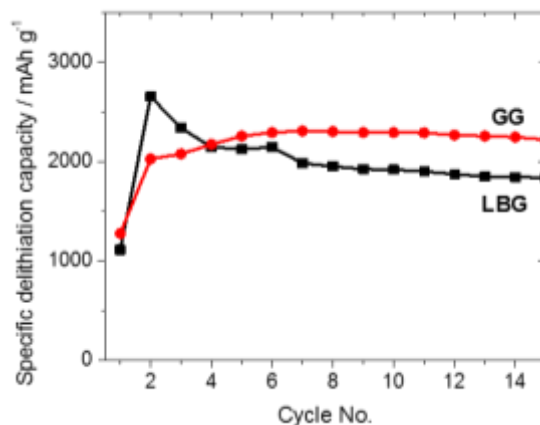


**Figure B7.** Cycling of SiNP electrodes in the absence of carbon with 100 mV cut-off voltage. The half-cells were lithiated to 1200 mAh g<sup>-1</sup> at 0.1-C (360 mA g<sup>-1</sup>) on the first cycle. On ensuing cycles the electrodes were lithiated under constant current to 100 mV at 0.1-C (360 mA g<sup>-1</sup>) and held under constant voltage conditions until 0.01-C (36 mA g<sup>-1</sup>). The binders allow for stable cycling at 0.1-C rates. The electrode contains 90 wt% SiNPs and 10 wt% binder.

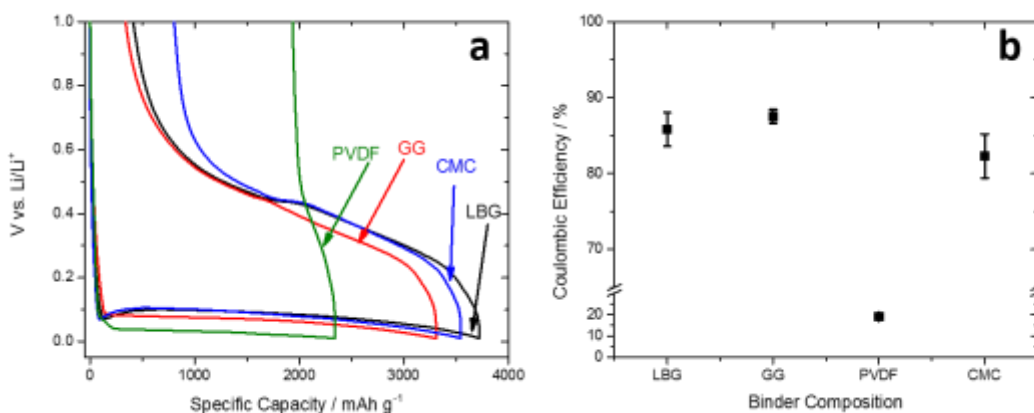


**Figure B8.** (a) Typical charge/discharge profiles of SiNP electrodes using various polymer binders. In the first lithiation the crystalline Si is converted to amorphous Si and the native-oxide layer is reduced to Si<sup>0</sup>; (b) Average coulombic efficiencies of SiNP electrodes on the formation cycle. The galactomannan binders operate with the highest initial CEs. The electrodes composition is 85:10:5, SiNPs:C:Binder wt%.

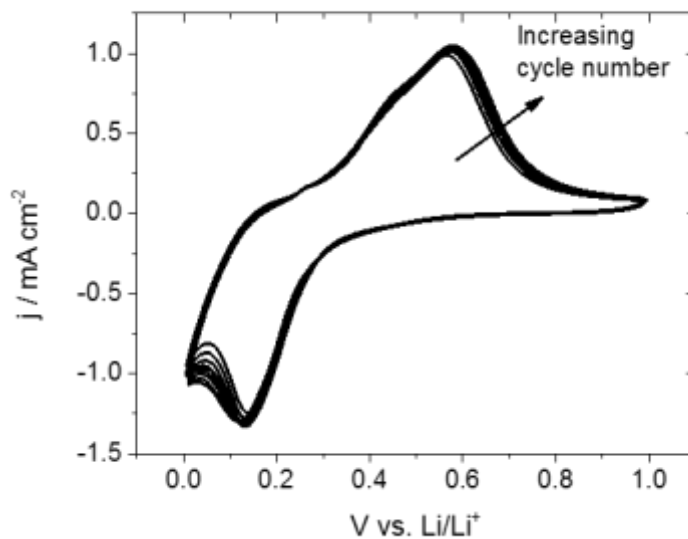


**Figure B9.** CV cycles 11-20 of a SiNP/LBG electrode. A maximum peak current density is attained after the 13<sup>th</sup> cycle. The half-cell was cycled between 1 V and 0.01 V vs Li/Li<sup>+</sup> using a scan rate of 0.2 mV s<sup>-1</sup>. Electrode composition is 85:10:5, SiNPs:C:LBG wt%.

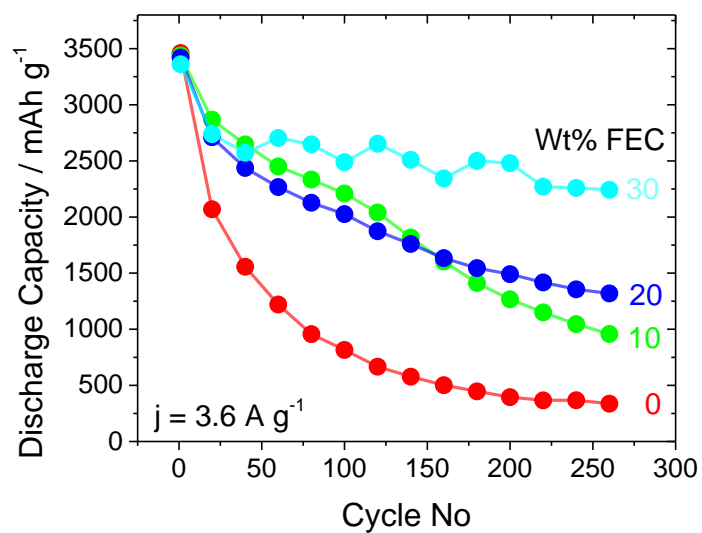


**Figure B10.** Discharge capacity as a function of cycle life using SiNP electrodes using guar binders. Each electrode contained various amounts of electrolyte additive fluoroethylene carbonate (FEC), and the amount of FEC is labeled on the figure. Half-cells were cycled symmetrically with electrode composition 80:10:10, SiNPs:C:Guar wt%.

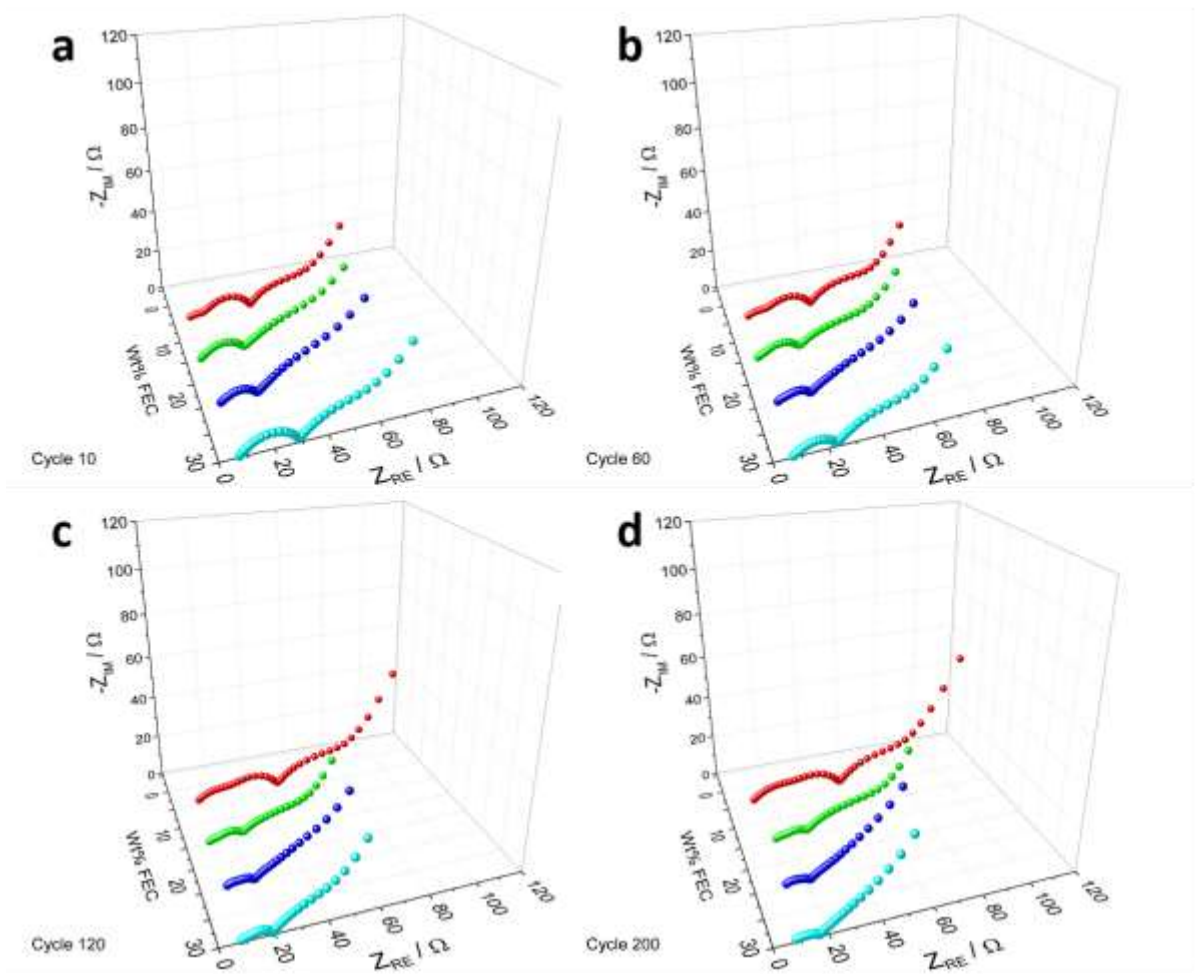


**Figure B11.** Nyquist plots from electrochemical impedance spectroscopy (EIS) from half-cells in Figure B9. Impedance values were measured on lithiated electrodes. The cells were charged at 1-C rates (corresponding to the values seen in Figure B9) to 10 mV vs. Li/Li<sup>+</sup> and let rest for 4 hours before EIS was run. Nyquist plots in this figure represent the impedance values after select cycle numbers: (a) 10 (b) 60 (c) 120, and (d) 200 cycles. From these plots, we can infer that electrodes in the absence of FEC have the largest resistance after 200 cycles, as Nyquist plots reveal largest high-frequency values and the largest semi-circles.

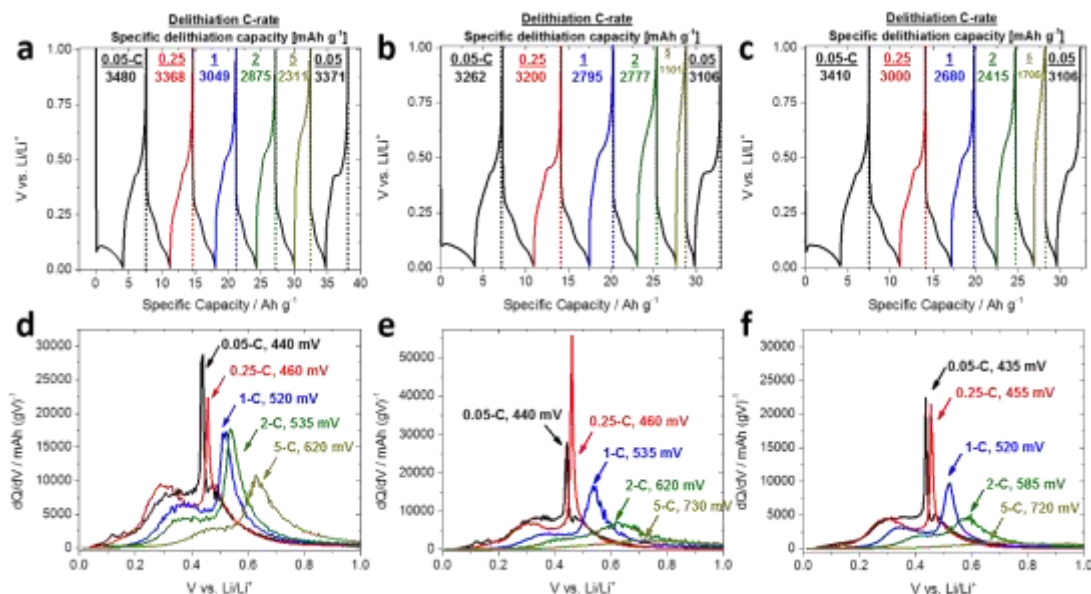


**Figure B12.** Asymmetric charge-discharge profile curves of SiNP electrodes using (a) GG (b) LBG and (c) CMC electrodes, as well as the corresponding differential capacities for the delithiation curve for the electrodes using (d) GG and (e) LBG and (f) CMC binders. All lithiation rates are 0.05-C to ensure full lithiation.

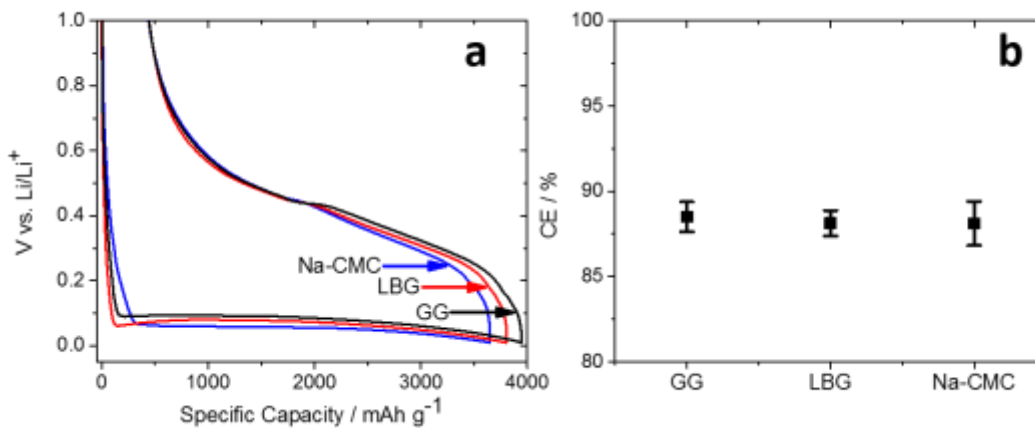


**Figure B13.** Typical (a) charge/discharge profiles of the formation cycle when binder loading is increased to 15 wt% and the (b) corresponding CEs reveal high CEs of ~88% (b). Electrode composition is 75:10:15, SiNPs:C:Binder wt%.

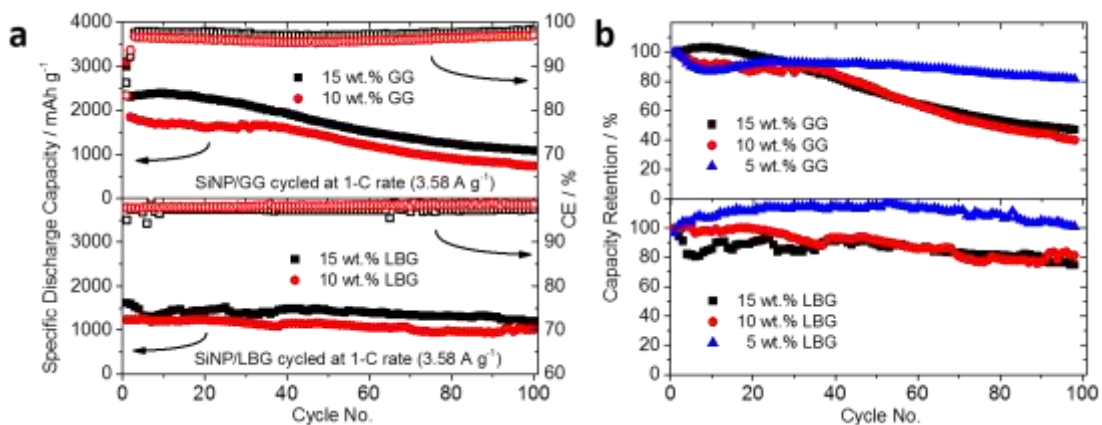


**Figure B14.** (a) Delithiation capacity and coulombic efficiency of SiNP electrodes using 10 and 15 wt% GG and LBG over 100 cycles at 1-C rate and (b) the capacity retention corresponding to (a). The capacity data from 5 wt% can be seen in Figure 7a in the text. As the amount of binder increases, so too does the irreversible capacity loss.

## **Appendix C. Supporting Information for Chapter 6**

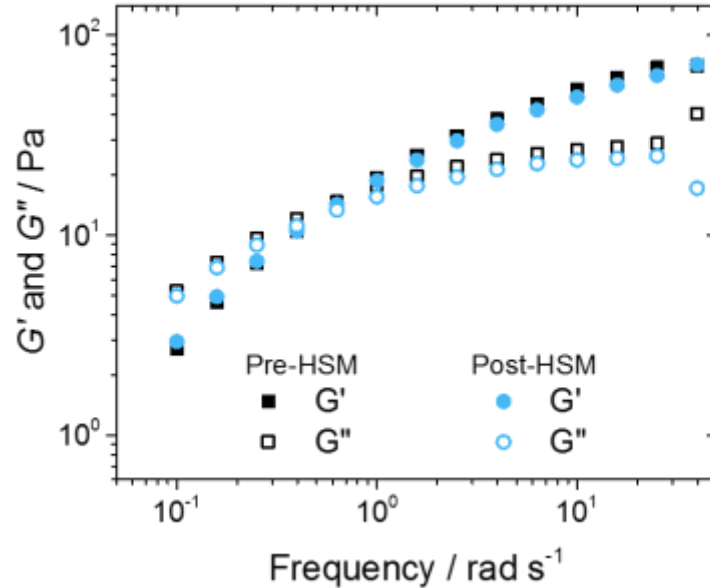


**Figure C1.** Dynamic rheology of 1 wt% guar in H<sub>2</sub>O before and after high-shear mixing (HSM) at 7500 RPM for 15 minutes; insignificant differences between pre- and post-sheared samples revealed that changes in microstructure occurred after high-shear mixing quickly rebuilt before sample loading.

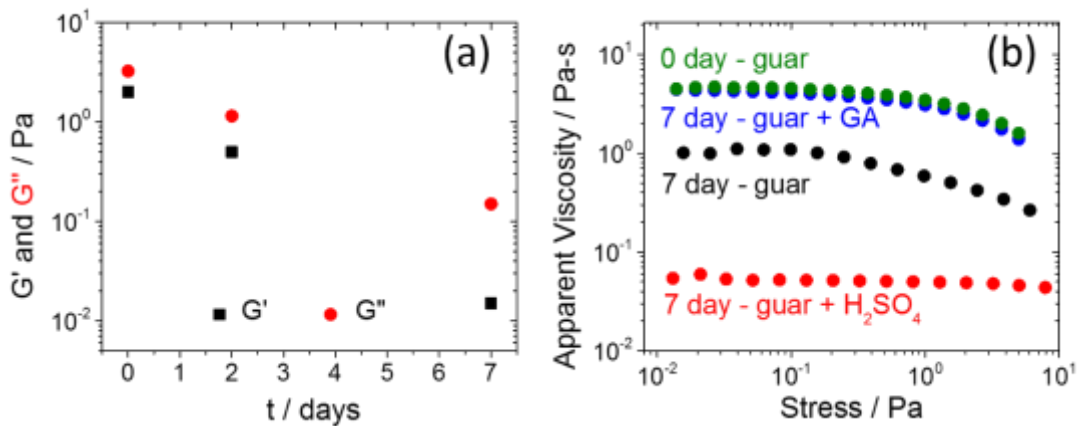


**Figure C2.** a) Decrease in the viscous and elastic moduli in a 0.70 wt% guar solution with 75 mM H<sub>2</sub>SO<sub>4</sub>. Values were obtained from the linear viscoelastic regime of a stress sweep with  $\omega = 1 \text{ rad s}^{-1}$ ; b) steady flow rheology values showing the decrease in viscosity of 0.70 wt% guar solutions with time. No significant decrease in viscosity was observed when glutaraldehyde (GA) was added to guar solutions (1 mol OH from GA to 1 repeat unit) because GA is a biocide and inhibits the breakdown of guar. A large decrease in viscosity of the guar + H<sub>2</sub>SO<sub>4</sub> (75 mM H<sub>2</sub>SO<sub>4</sub>) was observed.

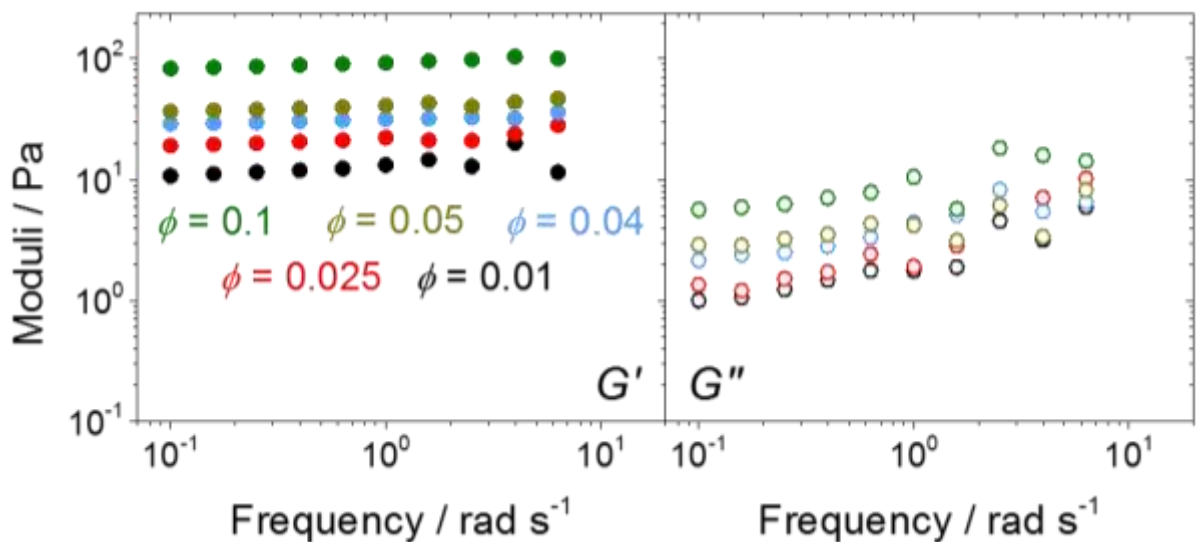


**Figure C3.** Frequency sweeps showing the elastic modulus (left) and viscous modulus (right) for guar solutions that have been crosslinked for 2 days with various volume fractions of CB.

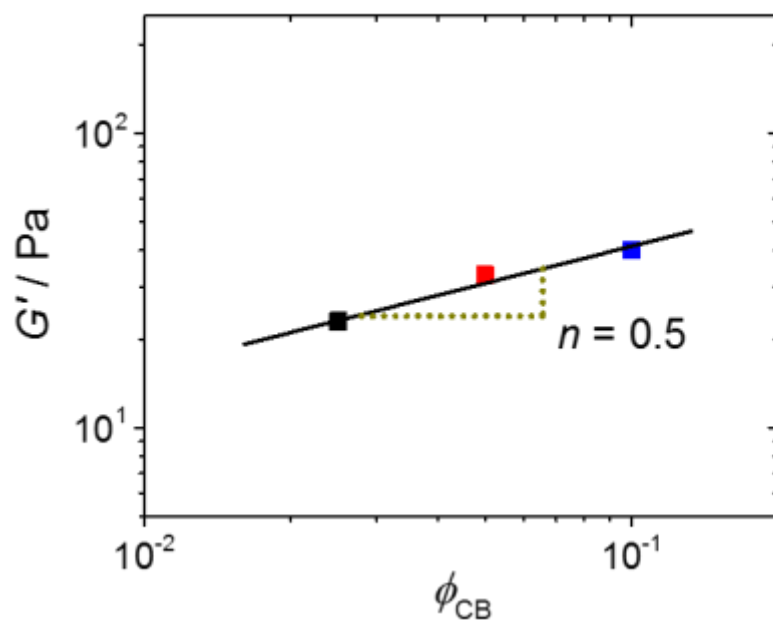


**Figure C4.** Elastic modulus for guar systems that were not crosslinked. Values represent those collected from frequency sweeps (within the linear viscoelastic regime) and at  $\omega = 1 \text{ rad s}^{-1}$ . The slope of the line is 0.5.

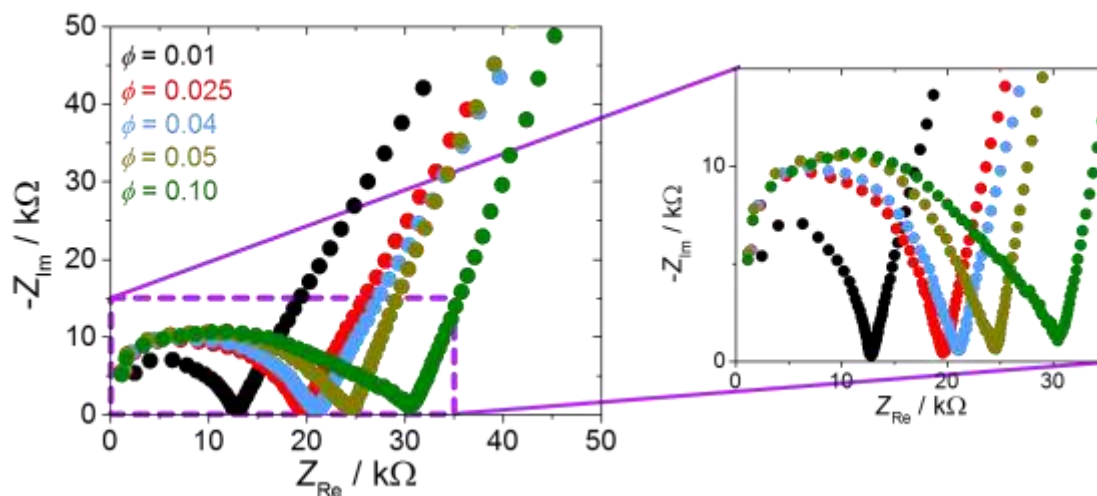


**Figure C5.** Nyquist plots of hydrated guar hydrogels crosslinked for 2 days and containing various amounts of CB (labeled on the plot). The gels were dialyzed for 3 days prior to measurements to leach out  $\text{H}_2\text{SO}_4$  and unreacted GA. Measurements were taken at open circuit from 1 GHz to 1 Hz with a voltage amplitude of 10 mV. The zoomed-in Nyquist plot (right) reveals that no difference in high-frequency resistance can be determined, which indicates no significant difference in electronic or ionic conductivities. Also, the high impedance values (values of plots on the kilo-ohm scale) indicate little conductivity, and thus percolation.

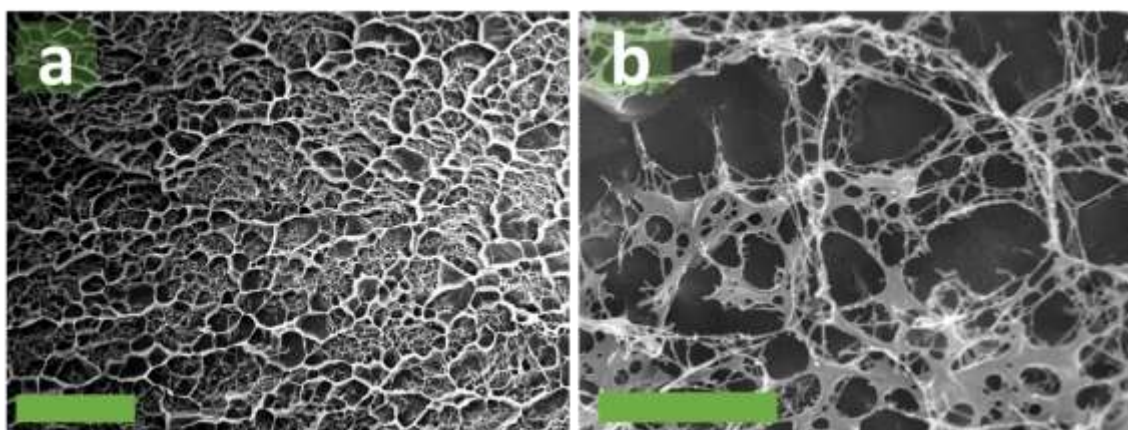


**Figure C6.** Cryo-SEM images of guar gel crosslinked for 2 days; (a) macrostructure at low-resolution, and (b) microstructure at high-resolution. The scale in (a) is 20  $\mu\text{m}$  and the scale in (b) is 1  $\mu\text{m}$ .

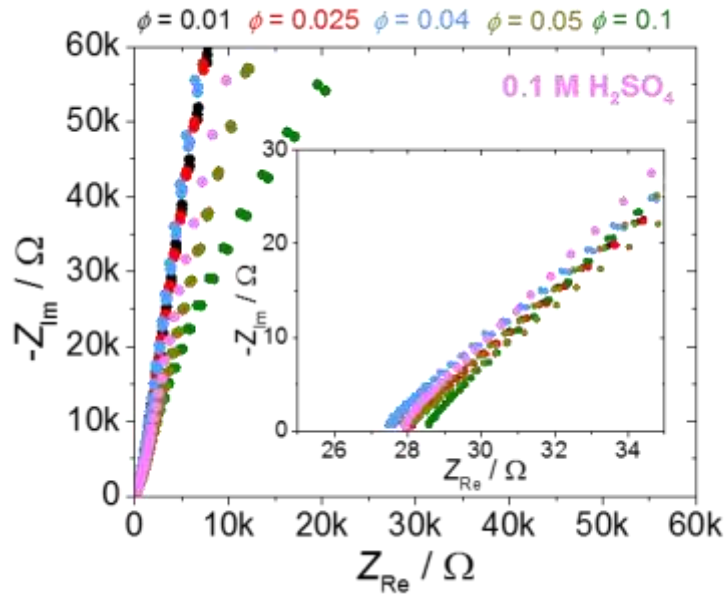


**Figure C7.** Nyquist plots of hydrated guar hydrogels crosslinked for 2 days and containing various amounts of CB (labeled on the plot). The gels were dialyzed for 3 days prior to measurements to leach out  $\text{H}_2\text{SO}_4$  and unreacted GA. The solids concentration of each sample was then determined by drying the contents overnight in a vacuum oven. Then,  $\text{H}_2\text{SO}_4$  was added to gels to make a 0.1 M sample and the gel was given 16 hours to swell. Measurements were taken at open circuit from 1 GHz to 1 Hz with a voltage amplitude of 10 mV. Cell constant =  $0.69 \text{ cm}^{-1}$ .

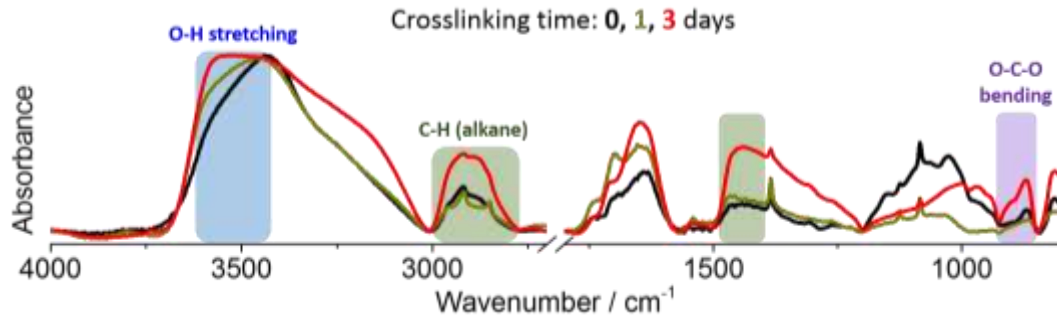


**Figure C8.** (a) FTIR spectra of guar and guar crosslinked for 1 and 3 days

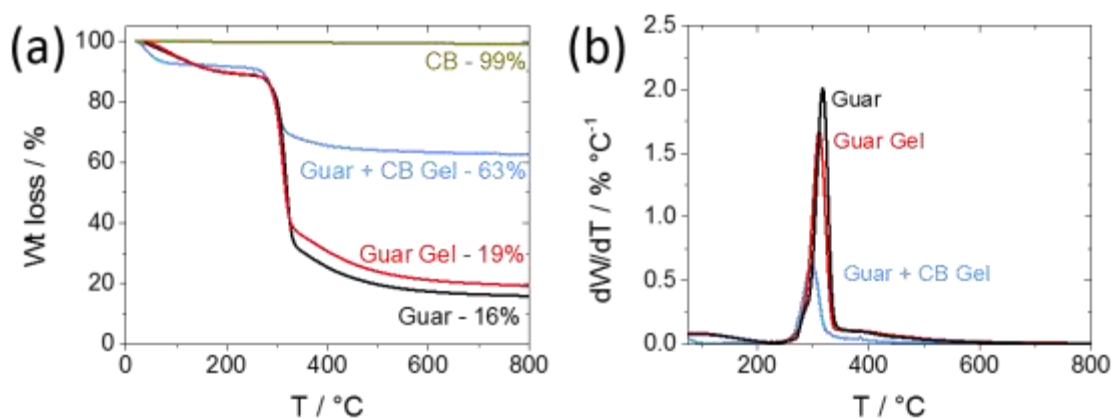


**Figure C9.** a) Thermal gravimetric analysis (TGA) of components in the guar + CB gels, as well as gels that had been crosslinked for 2 days. TGA was used to determine solids composition after dialysis; b) derivatives of (a), which show no significant difference in degradation temperature when crosslinked.

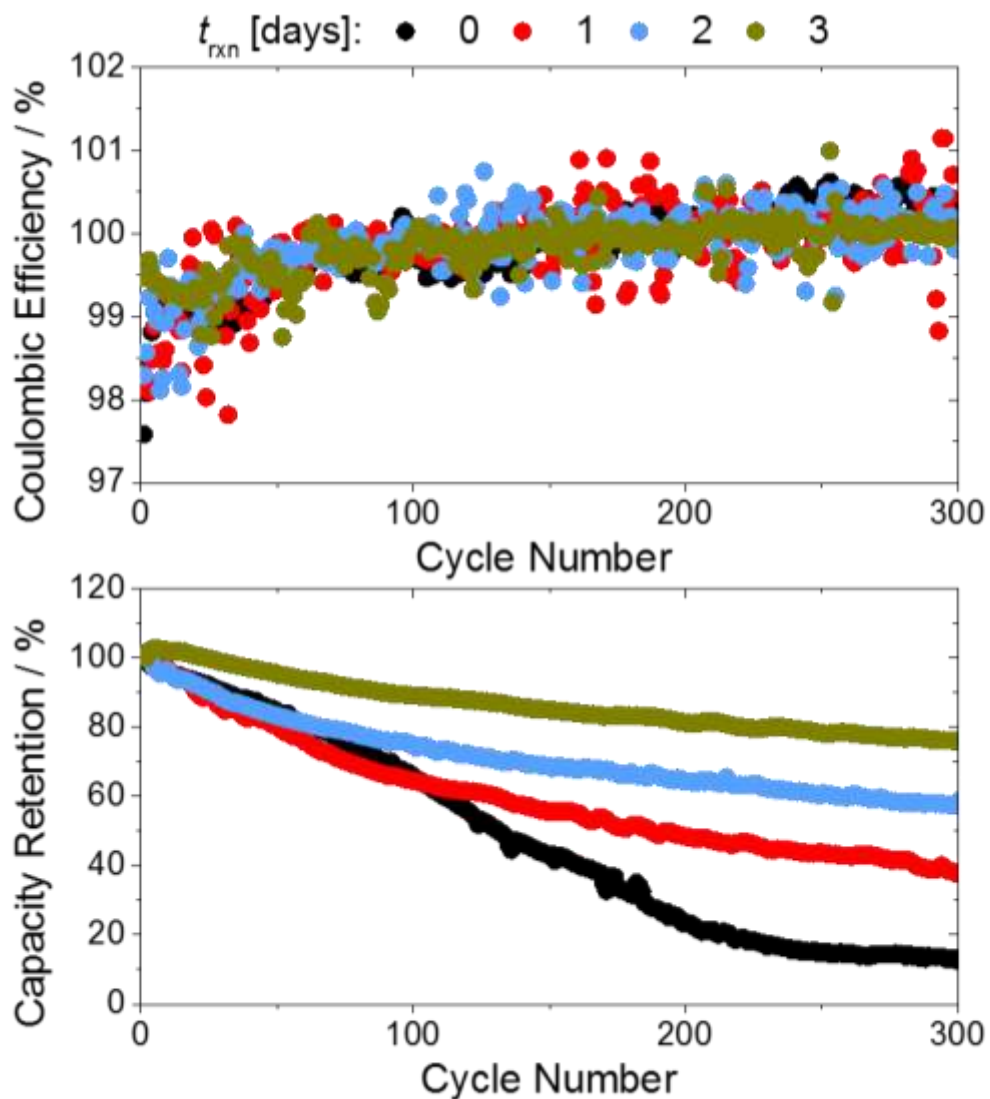


**Figure C10.** (a) Coulombic efficiencies (CEs) as a function of cycle number, which correspond to **Figure 6.9**. Average CEs for SiNP electrodes using guar + CB binders crosslinked for 0, 1, 2, and 3 days were 99.8, 99.9, 99.9, and 99.8%; (b) Capacity retention of SiNP electrodes using guar + CB binders, also corresponding to **Figure 6.9**; values are normalized to the second-cycle discharge capacity.

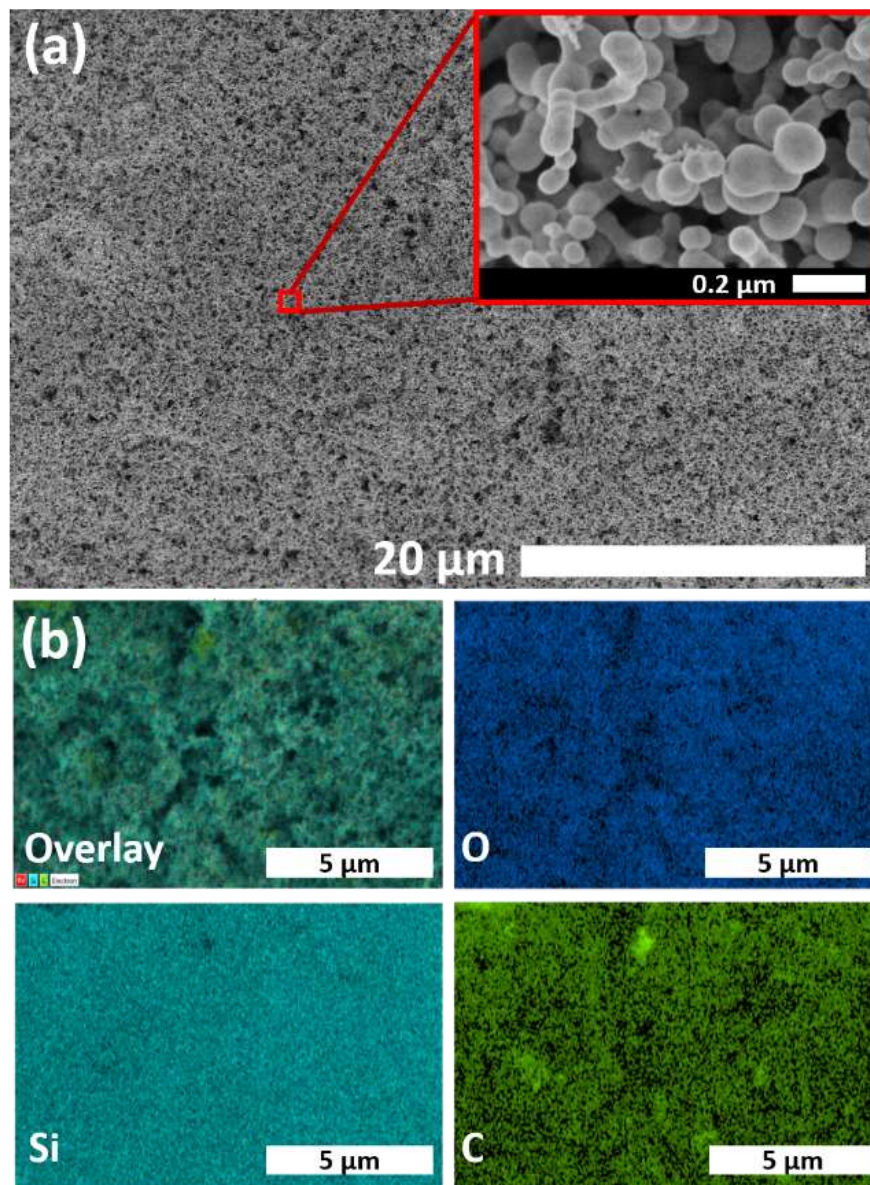


**Figure C11.** Characterization of SiNP electrode using guar + CB binder crosslinked for 2 days; (a) SEM image of top surface (inset shows porosity of the microstructure); (b) EDS analysis of the electrode with chemical symbol in bottom left.

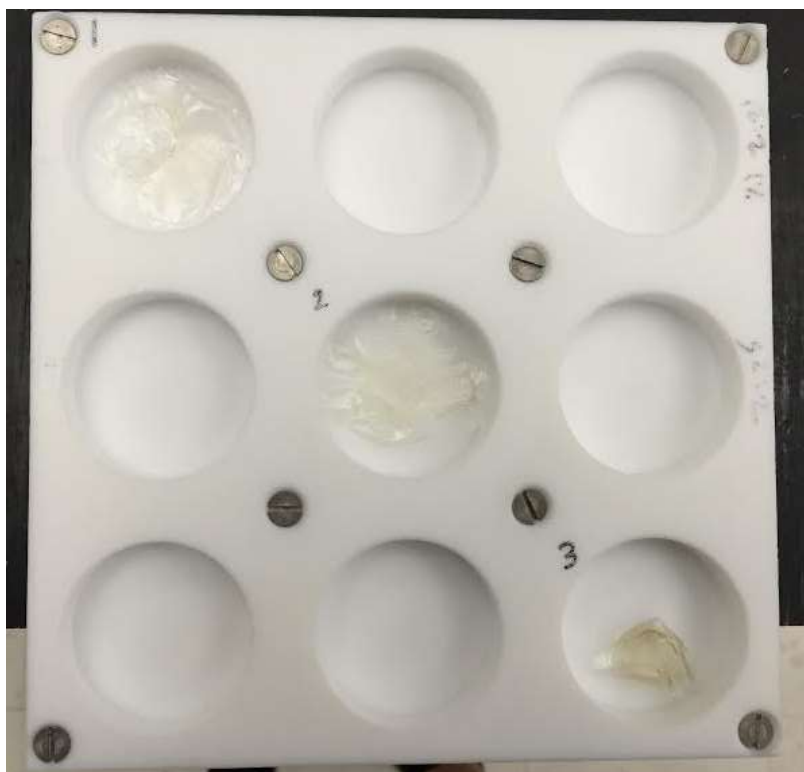


**Figure C12.** Photograph of films cast in Teflon molds showing guar crosslinked for 1 (top left), 2 (center), and 3 (bottom right) days.

## **Appendix D: Supporting Information for Chapter 7**

## D.1. Data Analysis

### D.1.1. Estimating mols Li on first lithiation.

$$x \frac{\text{mol}_{\text{Li}}}{\text{mol}_{\text{active}}} = C \left[ \frac{\text{mAh}}{\text{g}_{\text{active}}} \right] \cdot \frac{MW \left[ \frac{\text{g}_{\text{active}}}{\text{mol}_{\text{active}}} \right]}{F \left[ \frac{\text{mAh}}{\text{mol}_{\text{Li}}} \right]}$$

where:  $x$ : mols inserted on initial cycle  
 $C$ : capacity on initial cycle  
 $MW$ : molecular weight of **I**  
 $F$ : Faraday's constant

$$x \frac{\text{mol}_{\text{Li}}}{\text{mol}_{\text{active}}} = 1600 \left[ \frac{\text{mAh}}{\text{g}_{\text{active}}} \right] \cdot \frac{296.15 \left[ \frac{\text{g}_{\text{active}}}{\text{mol}_{\text{active}}} \right]}{2.6801e4 \left[ \frac{\text{mAh}}{\text{mol}_{\text{Li}}} \right]}; x \approx 17.7 \frac{\text{mol}_{\text{Li}}}{\text{mol}_{\text{active}}}$$

### D.1.2. Thermogravimetric analysis

Shown in **Figure D1**, **I** exhibited one weight-loss step for the structural water and the ammonium ion. Using a heating rate of  $5^{\circ}\text{C min}^{-1}$ , we observed removal of water and ammonium ions starting at  $\sim 200^{\circ}\text{C}$  to  $320^{\circ}\text{C}$ . After the removal of water and ammonia, **I** is decomposed into  $\text{MnV}_2\text{O}_6$  and  $\text{V}_2\text{O}_5$ , as confirmed by PXRD in the **Figure D10**. The overall reaction is:



(exp. 8.57%, calcd. 8.56%).

### D.1.3. Infrared spectra

The infrared spectrum of **I**, **Figure D2**, shows broad absorption bands in the 400 to  $1200 \text{ cm}^{-1}$  range, arising from V-O and Mn-O vibrations. Broad peaks around  $3300\text{-}3500 \text{ cm}^{-1}$  are consistent with the O-H stretching. Notably, two sharp peaks at  $1579 \text{ cm}^{-1}$  and  $1400 \text{ cm}^{-1}$  correspond to the bending mode of  $\text{H}_2\text{O}$  and  $\text{NH}_4^+$ , respectively, as confirmed with the infrared

spectra of  $\text{H}_2\text{O}$  and  $\text{NH}_3 \cdot \text{H}_2\text{O}$ .<sup>1</sup> Neither the characteristic peaks of  $\text{H}_3\text{O}^+$  at  $1715 \text{ cm}^{-1}$  and  $2150 \text{ cm}^{-1}$ , nor  $\text{NH}_3$  molecules at  $1205 \text{ cm}^{-1}$  were observed.<sup>1</sup> Therefore, **I** contains both coordinating water molecules and  $\text{NH}_4^+$  ions.

## D.2. Figures and Tables

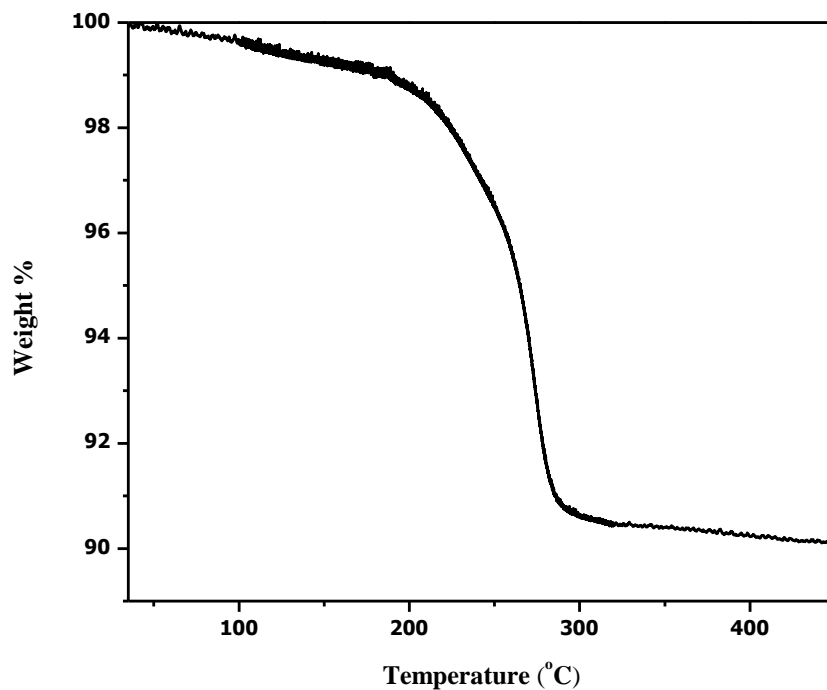


**Figure D1.** Thermogravimetric analysis for **I** in air plotted as weight (%) versus temperature (°C).

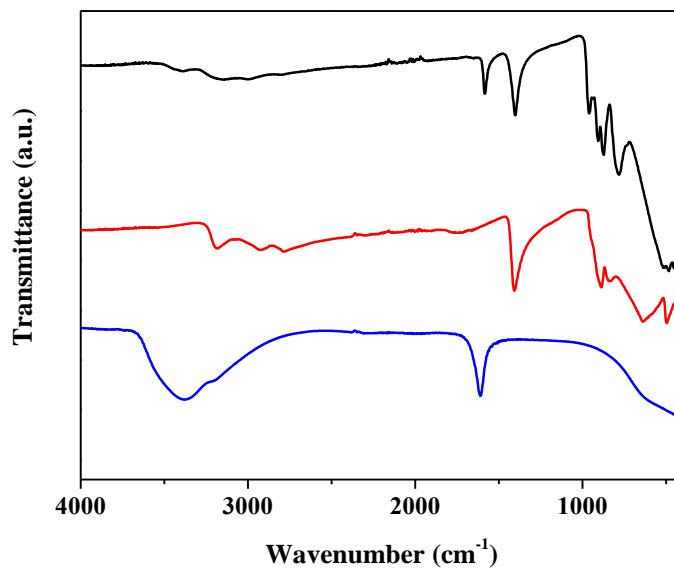


**Figure D2.** Infrared spectra of **I** (black), H<sub>2</sub>O (blue), and NH<sub>3</sub>H<sub>2</sub>O (red).

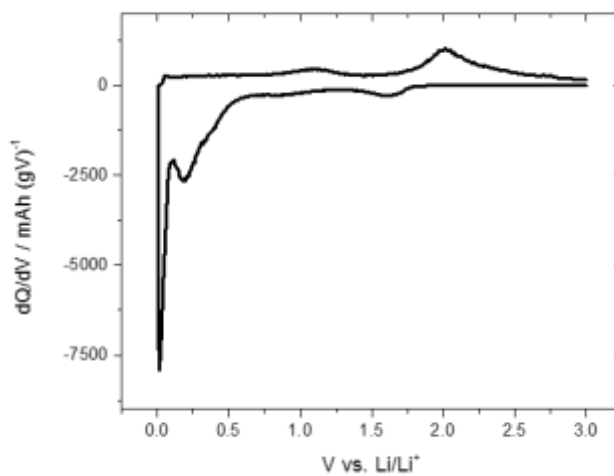


**Figure D3.** Typical (dis)charge capacity curve derivative profile from constant-current cycling at 10 mA g<sup>-1</sup>. Peaks denote phase changes that were used for *ex-situ* PXRD studies.

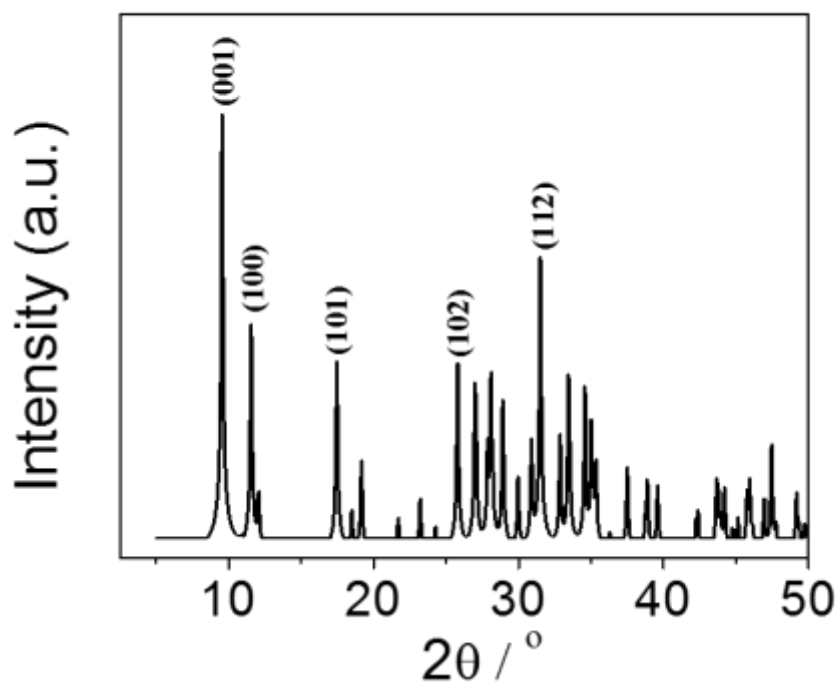


**Figure D4.** The calculated XRD spectrum of **I**, which agrees with the synthesized structure and proves we created a high-purity, single phase material.

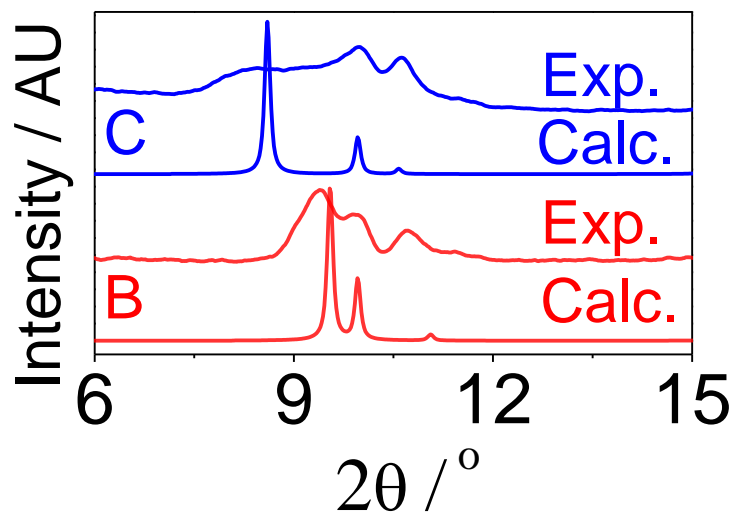


**Figure D5.** The empirical and simulated low-angle PXRD patterns for **I** electrodes that were lithiated to points **C** and **D**, as described in Chapter 7.

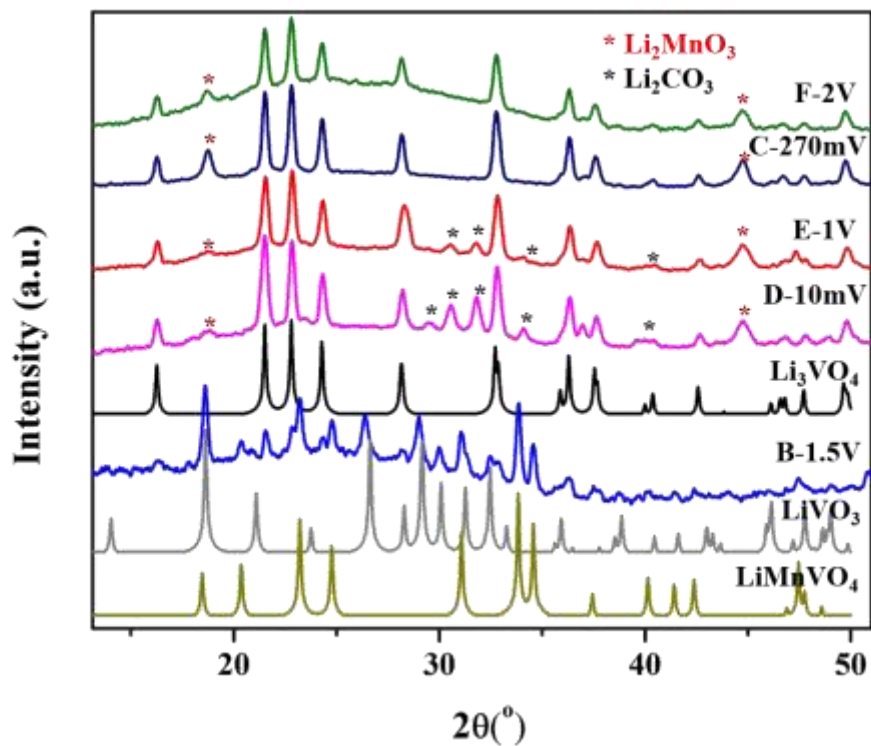


**Figure D6.** Powder XRD pattern of the thermogravimetric analysis residue for I electrodes after charge/discharge cycling and stopped at different voltages, and their assignments. The XRD pattern of D revealed a larger presence of  $\text{Li}_2\text{CO}_3$  (decomposed SEI material) at 10 mV than 270 mV, indicating that SEI formation occurred at low potentials vs.  $\text{Li}/\text{Li}^+$ .

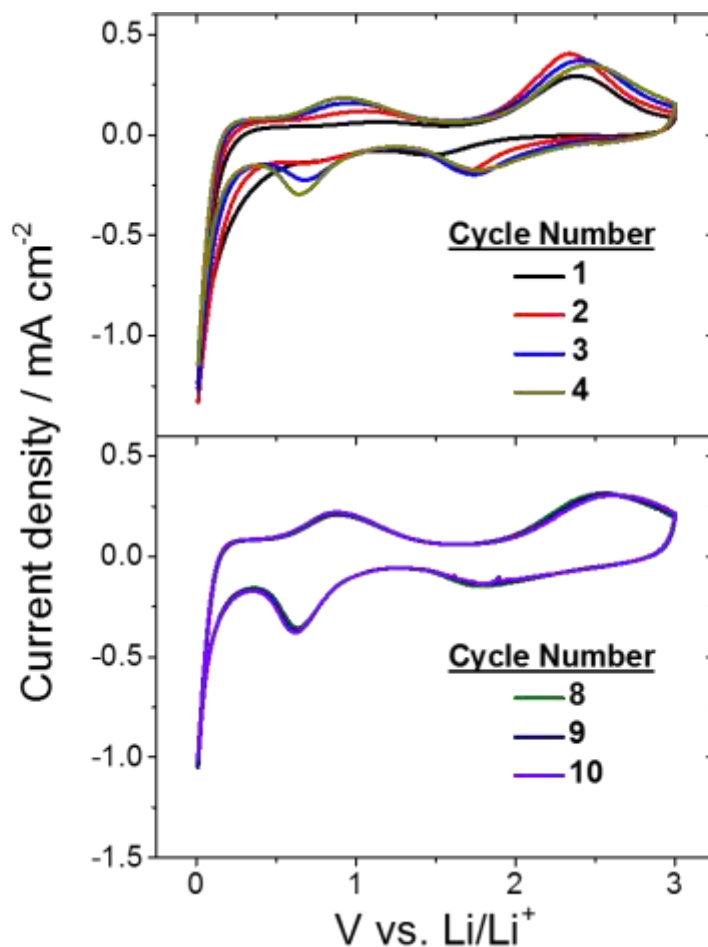


**Figure D7.** Cyclic voltammetry (CV) on **I** electrodes showing the initial cycling (top) and later cycles (bottom). The first cycle shows single cathodic polarization peak (intercalation) at a potentials near the onset of Li-ion reduction and a single anodic polarization peak (deintercalation) at 2.38 V vs. Li/Li<sup>+</sup>. As the cycling progresses, we see a changing voltammogram, as evidence of irreversible reactions and structural rearrangement within **I**; new cathodic peaks arise at ~1.71 and 0.65 V vs. Li/Li<sup>+</sup> and new anodic peaks arise at ~0.93 vs. Li/Li<sup>+</sup>. We also see a decrease in cathodic peak current as cycling progresses, which we attribute to Mn dissolution. Peak position becomes constant in later cycles (cycles 8-10) as **I** rearranges into a structure that is stable for (de)intercalation. A scan rate of 0.1 mV s<sup>-1</sup> was used.

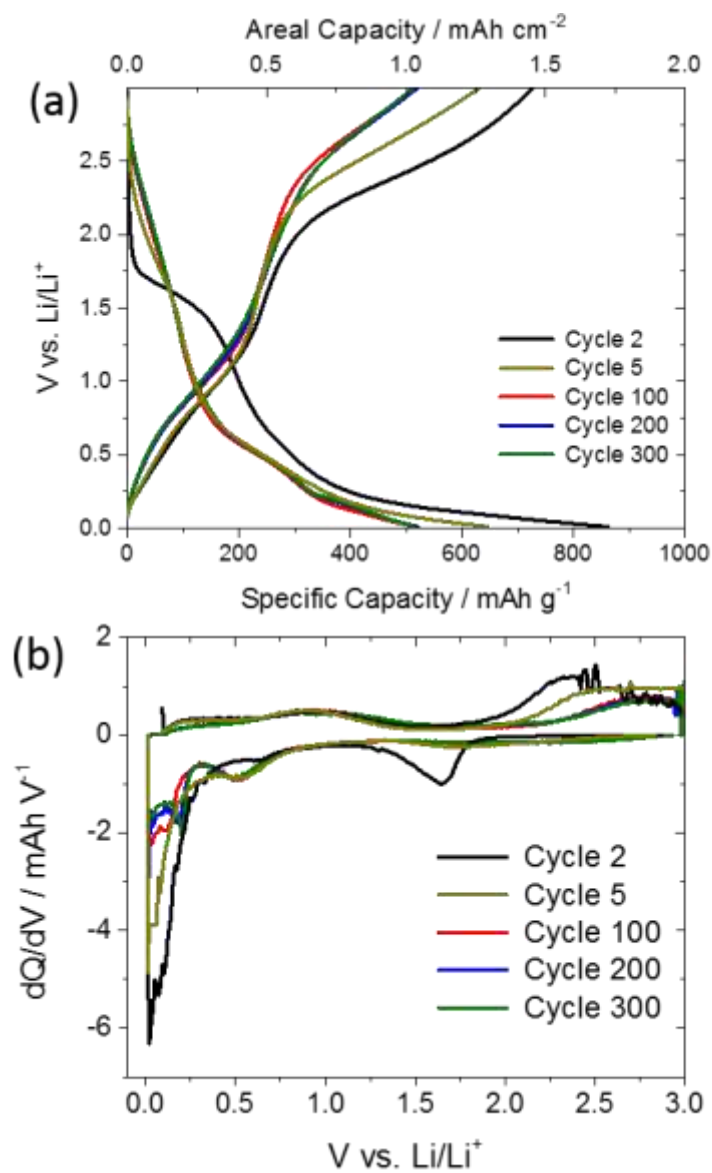


**Figure D8.** Select half-cell cycling profiles of **I** electrodes, showing (a) the charge/discharge curves and the corresponding (b) derivatives of the charge/discharge curves over 300 cycles. Low-voltage intercalation peaks in (b) decrease in magnitude due to Mn dissolution, however, we observed no significant decrease in low-voltage peak magnitude between cycles 100 and 300.

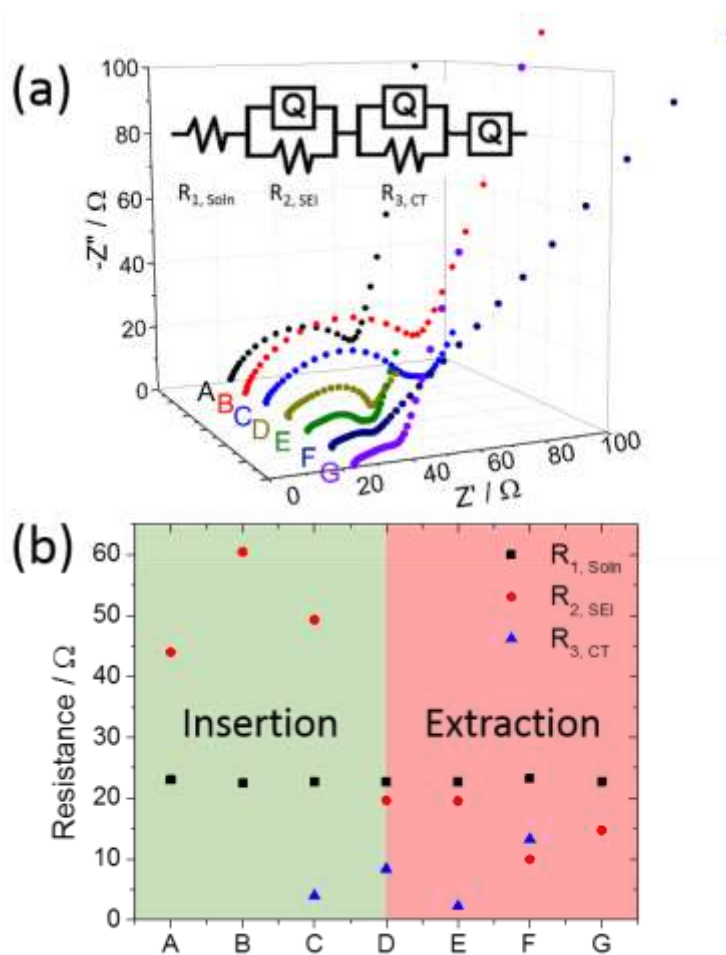


**Figure D9.** Impedance data for **I** electrodes showing a) Nyquist plots as a function of state-of-charge (SOC) with the equivalent circuit used to fit impedance data; b) values for the resistors when fitting the Nyquist plot to the model equivalent circuit. During the first cycle, the high-frequency resistance values stay constant, which indicates that Mn-ion that may have dissolved in the electrolyte, do not increase the solution resistance. The mid-frequency resistance, corresponding to film resistance from the SEI, decreased in half from points **C** to **D**, or from  $\sim 50 \Omega$  at 250 mV to  $\sim 19 \Omega$  at 10 mV. The reduction in  $R_2$  value with SOC may be associated with decomposition of electrolyte to form a more conductive SEI, as seen in graphite electrodes with similar electrolyte.<sup>2</sup> Upon delithiation, the SEI values do not increase beyond the fully charged state, indicating that a stable SEI has formed. Values of the low-frequency resistance,  $R_3$ , correspond to the charge transfer resistance. The charge transfer resistance is dependent on mols Li in **I** and diffusivity of Li in **I**. Since the concentration of Li in **I** is high at **D** (near full lithiation after chronoamperometry at 10 mV until C/100), we see the charge transfer resistance increase due to a lower driving force from the concentration gradient. Charge transfer resistances are large before major Li-insertion at **C** and near full Li-extraction at **G**, and therefore not shown in (b).

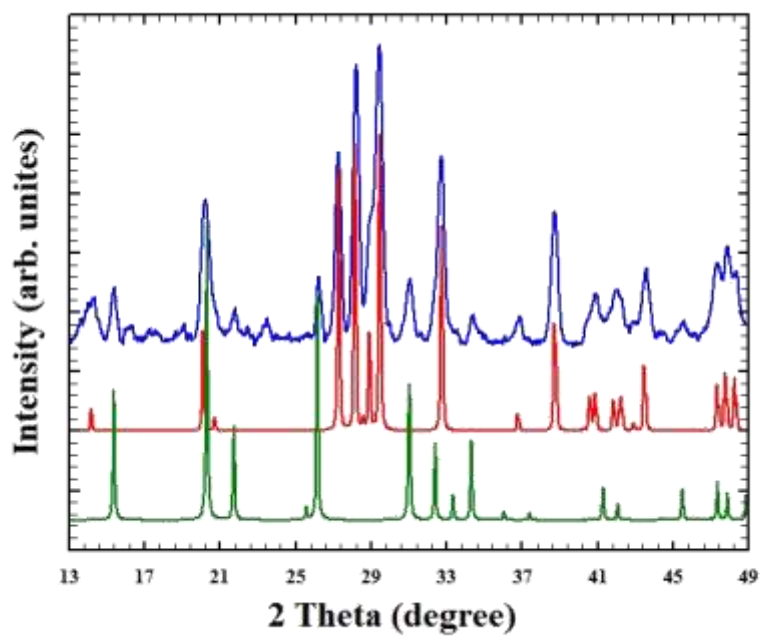


**Figure D10.** Powder XRD pattern of the TGA residue of **I** after heating in nitrogen (blue), and the calculated MnV<sub>2</sub>O<sub>6</sub> pattern (red) and the calculated V<sub>2</sub>O<sub>5</sub> pattern (green).

**Table D1.** Selected bond distances, angles, and bond valence sums for **I**<sup>a</sup>

Atom1	Atom2	Distance [Å]	Intra-Polyhedral Angle [°]	
Mn1	O6	2.281(1)	O6 – Mn1 – O7	95.54(9)
	O7	2.122(3)	O6 – Mn1 – O7'	84.46(9)
	ΣS <sub>ij</sub>	1.864	O7 – Mn1 – O7	180
Mn2	O2	2.235(1)	O5 – Mn2 – O2	88.84(8)
	O5	2.053(2)	O2 – Mn2 – O2'	103.88(9)
	ΣS <sub>ij</sub>	2.184		
V1	O3	2.131(2)	O3 – V1 – O4	73.03(7)
	O4	1.8642(8)	O3 – V1 – O5	151.2(1)
	O5	1.663(2)	O4 – V1 – O6	102.91(9)
	O6	1.652(3)	O4 – V1 – O5	100.52(8)
	ΣS <sub>ij</sub>	5.069	O5 – V1 – O6	103.5(1)
V2	O1	1.613(3)	O1 – V2 – O2	104.6(1)
	O2	1.709(2)	O1 – V2 – O3	105.02(8)
	O3	1.8784(8)	O2 – V2 – O3	99.25(8)
	O4	1.8642(8)	O2 – V2 – O4	152.4(1)
	ΣS <sub>ij</sub>	5.035	O3 – V2 – O4	73.40(7)

<sup>a</sup> S<sub>ij</sub> = exp[(R<sub>0</sub>-R<sub>ij</sub>)/B], B = 0.37, R<sub>0</sub> = 1.790 Å for Mn<sup>II</sup> – O, R<sub>0</sub> = 1.803 Å for V<sup>V</sup> – O.

**Table D2:** A review of Mn-V anodes in Li-ion half-cells, showing the superior cycling performance of **I** in this study compared to similarly prepared electrodes in literature

Reference in text	Capacity [mAh g <sup>-1</sup> ]	Max Cycle No.	Rate [mA g <sup>-1</sup> ]	Cutoff Voltage
11a <sup>3</sup>	460	50	100	3.4
11b <sup>4</sup>	245	70	0.27-C <sup>b</sup>	3.5
11c <sup>5</sup>	450	130	0.25-C <sup>b</sup>	3.9
11d <sup>6</sup>	500	50 <sup>a</sup>	100	3.5
13 <sup>7</sup>	500	9 <sup>a</sup>	?	3
This work	500	300	500	3

<sup>a</sup> capacity fading; <sup>b</sup> No basis capacity in text to relate C-rate to current

#### D.4. References

- (1) a) E. D. Dzyuba, L. N. Shchegrov and V. V. Pechkovskii, *Journal of Applied Spectroscopy* 14, 329-332 (1971); b) D. de Waal, A. M. Heyns, K. J. Range and C. Eglmeier, *Spectrochimica Acta Part A: Molecular Spectroscopy* 46, 1639-1648 (1990); c) J. Hetmańczyk, Ł. Hetmańczyk, A. Migdał-Mikuli and E. Mikuli, *Journal of Thermal Analysis and Calorimetry* 118, 1049-1056 (2014); d) J. Hetmańczyk, Ł. Hetmańczyk, A. Migdał-Mikuli and E. Mikuli, *Spectrochimica Acta Part A: Molecular and Biomolecular Spectroscopy* 136, 1515-1522 (2015).
- (2) S. Zhang, M. S. Ding, K. Xu, J. Allen, T. R. Jow. *Electrochemical and Solid-State Letters*, 4, 2001, A206-A208.
- (3) Zhang, S., Hu, R., Liu, L. & Wang, D. Hydrothermal synthesis of MnV<sub>2</sub>O<sub>6</sub> nanobelts and its application in lithium-ion battery. *Materials Letters* 124, 57-60, (2014).
- (4) Shuijin, L., Kaibin, T., Yi, J. & Chunhua, C. Preparation of aligned MnV<sub>2</sub>O<sub>6</sub> nanorods and their anodic performance for lithium secondary battery use. *Nanotechnology* 18, 175605 (2007).
- (5) Piffard, Y., Leroux, F., Guyomard, D., Mansot, J. L. & Tournoux, M. The amorphous oxides MnV<sub>2</sub>O<sub>6+δ</sub> (0 < δ < 1) as high capacity negative electrode materials for lithium batteries. *Journal of Power Sources* 68, 698-703, (1997).
- (6) Mario Simoes, Y. S., Songhak Yoon, Corsin Battaglia, Simone Pokrant, Anke Weidenkaff. Hydrothermal vanadium manganese oxides: Anode and cathode materials for lithium-ion batteries. *Journal of Power Sources* 291, 66-74, (2015).
- (7) Hara, D., Ikuta, H., Uchimoto, Y. & Wakihara, M. Electrochemical properties of manganese vanadium molybdenum oxide as the anode for Li secondary batteries. *Journal of Materials Chemistry* 12, 2507-2512 (2002).